Shape and Interactions of the Building Blocks of Biomolecular Architectures

Giulia Giubertoni

ISBN 978-94-92323-38-5

Cover: picture of Monte Rosa taken by Giovanni Chiocca from Cima Mutta, Valsesia, Italy.

Shape and Interactions of the Building Blocks of Biomolecular Architectures

ACADEMISCH PROEFSCHRIFT

ter verkrijging van de graad van doctor
aan de Universiteit van Amsterdam
op gezag van de Rector Magnificus
prof. dr. ir. K.I.J. Maex
ten overstaan van een door het College voor Promoties
ingestelde commissie,
in het openbaar te verdedigen in de Aula van de Universiteit
op vrijdag 16 oktober 2020, te 14:00 uur

door

Giulia Giubertoni

geboren te Borgosesia

Promotoren: Prof. dr. H.J.Bakker
Prof. dr. G.H.Koenderink

Overige leden: Prof. dr. D.Bonn
Prof. dr. M.L.Groot
Prof. dr. E.C. Garnett
Prof. dr. I.K.Voets
Dr. B. Ensing
Dr. R.Richter

Faculteit der Natuurwetenschappen, Wiskunde en Informatica

The work described in this thesis was performed at the Institute AMOLF, Science Park 104, 1098 XG Amsterdam, The Netherlands. This work is part of the industrial partnership program Hybrid Soft Materials that is carried out under an agreement between Unilever Research and the Netherlands Organisation for Scientific Research (NWO).

To Jud

Contents

1 Introduction

1.1 Molecular interactions as Human Interactions

Cogito ergo sum.

With these words Cartesius (René Descartes) seems to find his only certainty: humans exist, or at least exist as *res cogitans*, as a "*thinking thing*".[1] Is the thinking, our ability to logically use words to describe our thoughts and our feelings, enough to capture the human consciousness of our own existence? I honestly do not think so.

Cogito, et tracto ergo sum.
I think, I interact and thus I am.

We know that we exist, that we are not the result of a joke because we think, and because we interact. Interaction defined, defines, and will define who we are. No State, no village, no community, no family, no relationship can exist without reciprocal and dynamical interactions. Thereby, interactions define us, building and structuring what we are, and what we are part of. In a similar fashion, interactions act in molecules and in between

molecules, defining their conformation, their ability to cooperate, specifically and in a unique fashion. Every one of us is a building block of our society. The stability and the endurance of our community, or our relationships, strongly depend on how we interact with others. Similarly, small molecules are the building blocks of larger molecular systems, such as proteins that are the essential parts of cells and organs. As in the human world, if the interactions between the small molecules do not work properly, proteins will be altered, and cells and organs will not function.
Similar to psychologists, philosophers and sociologists who analyze human interactions to understand our complex behavior in society, we, as physical scientists study the intimate interactions between molecules. How can we do so? Psychologists can talk directly to their patients, but scientists hardly can do the same with molecules. Physicists can use light. Molecules are not static systems: they move, they rotate, and their atoms oscillate similar to a spring. Light, that is a special region of the electromagnetic spectrum, can induce these oscillations, and a physicist can record these molecular motions. Molecular interactions cause structural fluctuations in the molecule, perturbing the molecular oscillations. By measuring these oscillations, scientists can reconstruct molecular interactions, and also changes in molecular structure.

Using light, we can thus get access to the microscopic world of molecules, which enables us to understand the molecular mechanisms and the driving forces of biological processes. We will now introduce the subjects of this thesis, discussing the connection between the studied molecular structures, and their macroscopic biological functionalities.

1.2 Molecular structural diversity and biological functions

1.2.1 Proteins

Among the biological macromolecules, proteins are arguably the most important. Proteins perform many different biological tasks, such as oxygen transport in our blood[2] or converting light to biological fuels in plants[3]. Proteins are polymers composed of smaller building blocks, amino-acids

(Fig.1.1). The sequence of amino-acids is referred to as the primary structure. The local conformation of the protein is called the secondary structure, and mostly determines the function of the protein. Changes in the secondary structure can thus affect the biological functionality of the protein, leading to severe consequences.[4,5] Typical examples of secondary structures are the alpha-helix and the beta-sheet (Fig.1.1). An alpha-helix is formed when the chain of amino-acids twists into a spiral, while a beta-sheet is formed when the chain *zig-zags*, and when parallel strands of amino-acids form strong inter-amino-acid connections. Proteins often do not assume a unique secondary structure, but harbor different structural motifs.[6] The

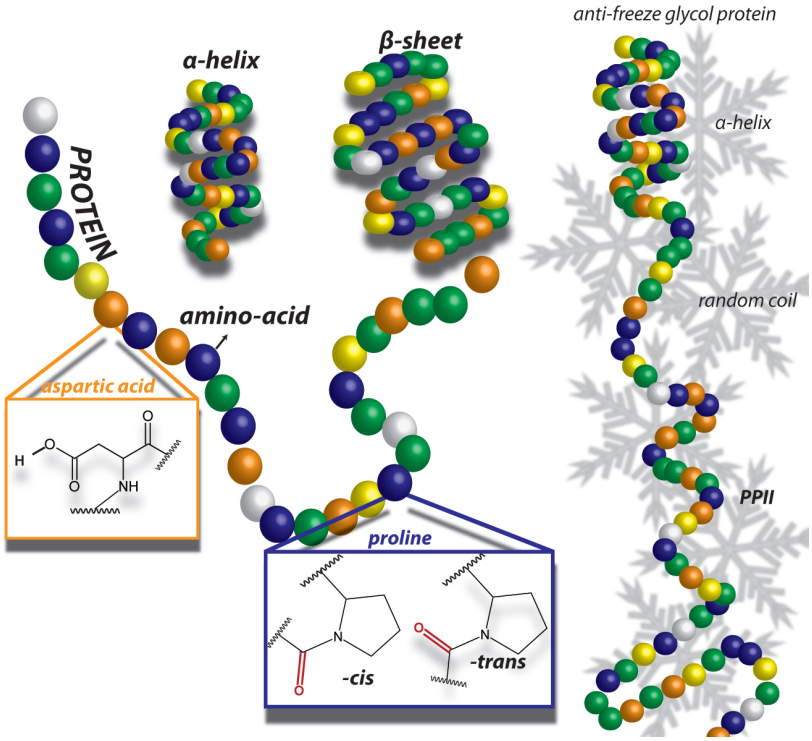

Figure 1.1: Schematic illustration of the possible secondary structures of a protein (left), and of the secondary structure of a disordered protein (right). The molecular structures of two different amino-acids, proline and aspartic acid, are shown in blue and orange rectangles, respectively.

three-dimensional conformation of a protein is not strictly determined by the sequence of amino-acids. Proteins can show conformational switches,

when containing proline residues, for example. The proline residue has two different conformations, depending on the orientation of the amide bond (*conformational isomerism*), and proteins can fold in different ways depending on the proline isomer.[7,8] The structure and function of a protein are also determined by functional groups (alcohol, thiols and carboxylic acid) contained in the side chains of the amino-acids of the protein sequence. The side-chain carboxylic acid group of aspartic acid, for example, is essential for protein folding[9,10], and for protein functions such as proton conduction[11,12].

In the last decades, it has also been found that proteins do not always adopt a specific conformation, and can have unordered domains, which can assume a specific secondary structure upon substrate binding. These structurally flexible proteins are crucial in many cellular mechanisms.[13] An example of flexible and unordered proteins is represented by anti-freeze glycol proteins, which enable the survival of animals at sub-freezing conditions.[14] By binding to the ice surface, anti-freeze proteins are able to inhibit the growth of ice crystals, which would be fatal for the organism.[15] A recent molecular study has proposed that the anti-freeze activity of anti-freeze glycoproteins is linked to the ability of the protein to segregate into a hydrophobic and a hydrophylic part, thus enhancing a particular secondary structure, called polyproline helix or PPII. PPII is formed when the protein twists into a loose spiral without the formation of intra-molecular bonds, which instead happens in α-helixes.[16] Anti-freeze glycoproteins thus represent a particularly interesting example of the functional biological role of a flexible and disordered protein structure.

1.2.2 Glycosaminoglycans

Polysaccharides are polymers composed of simple sugar units that repeat tens to thousands of times. In living systems, polysaccharides are subdivided in three classes. The first and second classes are storage and structure-related. A third class of polysaccharides is represented by glycosaminoglycans or mucopolysaccharides: heterogeneous polysaccharides, where the repeating unit is a disaccharide composed of an amino sugar and

an uronic acid. An example is hyaluronic acid, which is presented in Fig. 1.2. Glycosaminoglycans (GAGs) are negatively charged polymers (polyelectrolytes) at neutral pH, and their properties are heavily influenced by the pH and/or salt conditions. Glycominosoglycans are abundantly found in the three-dimensional network surrounding the cell, which we refer to as the extra-cellular matrix or ECM. GAGs are widely present in our bodies, and are associated with various physiological functions that are not always favorable.[18] For instance, heparin prevents the coagulation process in our body,[19,20] but can also promote amyloid formation, and hence amyloid diseases such as Alzheimer or Parkinson.[18,21,22] Glycosaminoglycans are also involved in the immune response to external pathogens[23], and can inhibit inflammatory response[24,25]. Interestingly, low-molecular weight hyaluronic acid has a pro-inflammatory role, while high-molecular weight hyaluronan has an anti-inflammatory role.[26] Since glycosaminoglycans, and hyaluronic acid in particular, are over-expressed in the presence of inflammation, they can be used as clinical predictors for some diseases, for example Dengue fever.[27,28] High concentrations and changes in the molecular weight of hyaluronic acid

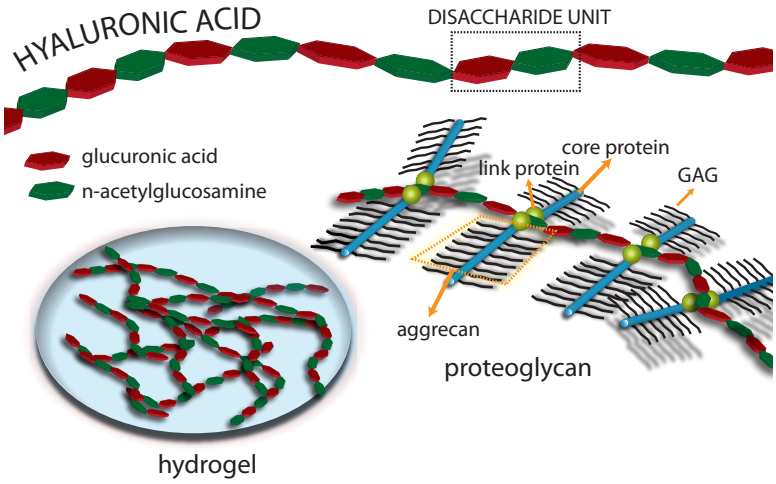

Figure 1.2: Schematic illustrations of the hyaluronic acid chain, and a proteoglycan, formed by aggrecans that bind to the hyaluronic acid chain via specific binding sites. Bottom left, a schematic illustration of hyaluronan hydrogel.[17]

have been also been linked to cancer initiation, metastasis, and therapy resistance.[29,30]

The diversity and the flexibility of the molecular structure of GAGs permit these molecules to interact with a large variety of biological macro-molecules. GAGs interact with proteins via precise binding mechanisms, forming protein-GAG complexes called proteoglycans (an example is reported in Fig. 1.2).[18] One class of proteoglycans, known as aggrecans, is responsible for the correct functioning of human cartilage.[17] The macromolecular structure of proteoglycans is often not unique. Since GAGs are strongly charged, their binding affinity to proteins depends on the pH and on the presence of cations.[18] For almost all GAGs, a covalent bond is formed between the GAG and the protein, but not in the case of hyaluronic acid.

Hyaluronan was discovered in the early 1930s by two researchers of Columbia University, and for a long time it was considered to be a simple GAG with limited biological functionalities.[31] However, nowadays the enormous physiological relevance of hyaluronan is widely acknowledged and among all the glycosaminoglycans, hyaluronan is arguably one of the most studied, also because of its broad application in the design of novel, biocompatible and responsive hydrogels,[32–34] elastic materials consisting of polymer networks and up to 90% of water. To capture and mimic the special properties of the extracellular matrix, stimuli responsiveness, biocompatibility, and tunability of mechanical properties are key. The extracellular matrix influences cellular processes via mechanical and biochemical signals, and in turn is influenced by the metabolism of the cell.[34] This gives rise to a dynamic reciprocity, which acts as a bidirectional and continuous flow of information that regulates different biological processes. Thanks to their high biocompatibility, hyaluronic acid polymers are widely used as a scaffold for responsive synthetic hydrogels.[35] Hyaluronan hydrogels are pH-responsive, showing dramatic changes in their mechanical properties. At pH=2.5, hyaluronan undergoes a liquid-to-gel transition, increasing its elasticity ten-fold.[36]This pH-responsive behavior is an interesting and important study case for gaining a comprehensive picture of the molecular interactions that drive hydrogel responsiveness, which plays a critical role in the dynam-

ical reciprocity between cell and extracellular matrix.

1.3 Infrared Spectroscopy

The molecular structures of bio-macromolecules, such as proteins and polysaccharides, are stabilized by molecular interactions. In biological systems, these molecular interactions usually involve the formation of a *hydrogen-bond* connecting two electronegative atoms or molecular groups. If these two molecular groups are part of the same chain, the hydrogen bond is intra-molecular, while, if they are part of different macro-molecules, the hydrogen bond is inter-molecular. In proteins and polysaccharides the molecular functional groups, which are involved in the formation of the hydrogen-bond, are usually amide and carboxyl groups. The frequencies of the molecular vibrational modes of the amide and carboxyl groups change when the inter- and intra-molecular interactions change in strength, and thus these modes mirror fluctuations of the structure and solvation of the macromolecule.

Molecular vibrations strongly absorb in a specific region of the electromagnetic spectrum, the infrared region. With infrared light, it is possible to observe light absorption at specific frequencies. These specific frequencies are resonant frequencies of molecular vibrational motions. In first approximation, the absorption frequencies depend on the strength of the chemical bonds and on the mass of the atoms. The investigation of the conformation of proteins and polysaccharides usually involves the molecular vibrations of the amide and carboxylic acid groups. The corresponding absorption lines are in the range from 1400 cm^{-1} till 1750 cm^{-1}, in the mid-infrared region (mid-IR). The amide group has two vibrational modes that are highly sensitive to the three-dimensional conformation: the amide I and the amide II vibrations. The vibrational frequencies of these amide modes shift upon the formation of a hydrogen bond, and the magnitude of this frequency shift depends on the secondary structure. For this reason, amide modes are considered to be precise structural markers. For example, the amide I vibration of a protein folded in an α-helical structure absorbs around 1660 cm^{-1}, and at 1620 and at 1680 cm^{-1} if the protein is folded in a β-sheet structure.[37]

1.3.1 Two-Dimensional Infrared Spectroscopy

The information extracted from infrared spectra is often insufficient to fully characterize the structure and solvation of the studied molecule. The spectra of proteins are usually highly congested, preventing the resolution of the vibrational frequencies of the amide I modes. Infrared spectroscopy thus often does not enable a trustworthy identification of the secondary structure. Changes in the solvation of the molecular groups are also difficult to observe in linear spectra since the linear spectral shape is often strongly broadened due to both homogeneous and inhomogeneous broadening mechanisms. Moreover, biological reactions often involve a change of the molecular interactions of only a small fraction of the molecular groups, and the

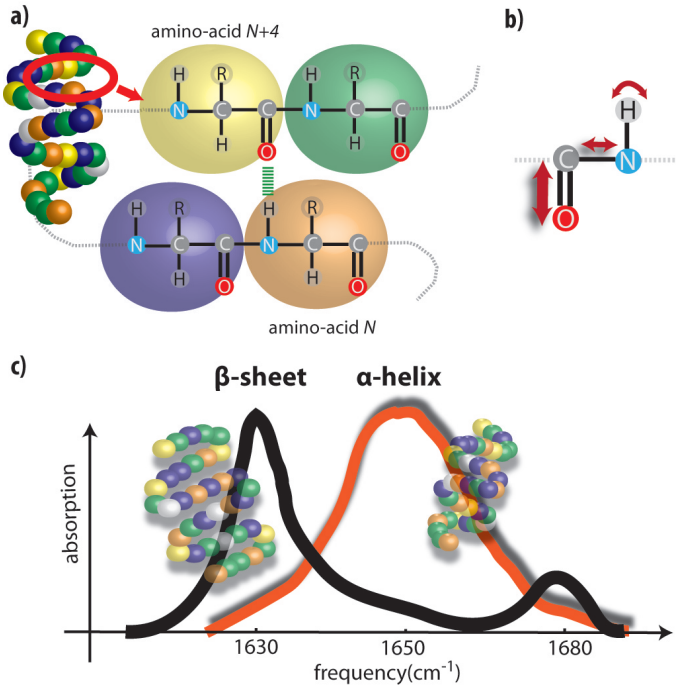

Figure 1.3: a) Schematic illustration of an α-helical structure, and b) of the amide group. The strongest vibrational motion is the amide I vibration, which mainly involves the C=O stretching mode, with minor contributions of the C-N stretching and N-H bending modes. c) Schematic illustration of the infrared absorption spectrum of the amide I mode in a $\beta - sheet$ and an $\alpha - helical$ structure.

effect on the linear spectrum can often not be resolved. The development of femtosecond infrared pulsed lasers[38] enabled a giant leap in spectroscopy, allowing researchers to circumvent many of the limitations of linear infrared spectroscopy. Proteins and other molecules change their local conformation on time scales that are on the order of picoseconds, and by using state-of-the-art lasers, which generate ultra-short pulses, one is capable of probing such fluctuations in molecular structure and solvation.[39]

Time-resolved two-dimensional infrared spectroscopy (2D-IR) is based on the use of two infrared femtosecond beams. The first (*pump*) is employed to excite molecular motions, whilst the second (*probe*), which has a tunable delay time with respect to the pump, is used to record the vibrational response at different times after the excitation. In 2D-IR we measure the signal as a function of both the pump and the probe frequency, thus yielding to

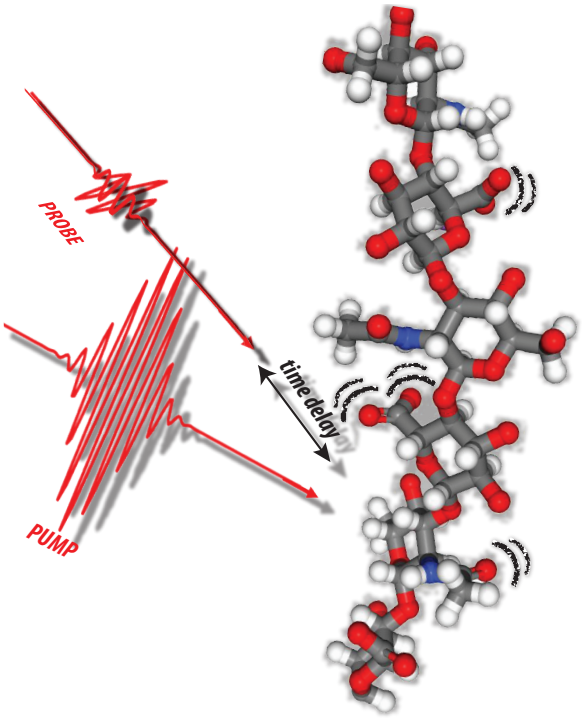

Figure 1.4: A strong infra-red pulse (*pump*) induces oscillatory motions in the molecular groups, and a second pulse (*probe*) is used to monitor the effect of the vibrational excitation.

a two-dimensional spectrum. The information contained in the line-shapes of the 2D-IR spectrum, and in their time-dependence, was recently used to study the structure of hydrated protons in bulk liquid water.[40] Molecular interactions between different molecular groups give rise to specific spectral features, called *cross-peaks*. Cross-peaks carry unique and precise information on the molecular interaction mechanism, which can be uncovered by analyzing their time dependence. The time dependence of cross-peaks, for example, allowed researchers to follow *in real time* the ultra-fast formation and disruption of a molecular complex of phenol/benzene.[41] Since cross-peaks require an interaction between specific molecular vibrations, the cross-peak signal can also greatly help in resolving the congested linear infrared spectra of proteins, identifying the presence of specific structures. Moreover, by examining the dependence of the cross-peak signal on the polarizations of the pump and probe beam, valuable information on the relative orientation of the interacting molecular groups, and thus on the molecular conformation is obtained. A nice recent example is the work of the group of M.Zanni, where the authors were able to identify amyloid fibers in human lenses, and to ultimately prove that cataract is an amyloid disease.[42] Here, they combined 2DIR with other techniques (transmission electron microscopy and light scattering measurements), showing the benefit of a multi-technique approach, which, due to the increasing complexity of the studied molecules, is now often necessary to uncover the connection between the macroscopic properties and the underlying molecular-scale interactions.

1.4 Outline of this thesis

This thesis focuses on the structure of bio-relevant molecules, and on their inter-/intra- molecular interactions. Chapter 2 presents the theory of linear and two-dimensional infrared spectroscopy, concentrating our discussion on molecular coupling mechanisms, and describes the setup employed in this thesis. Chapter 3 introduces basic principles of bio-polymer physics, describing their static and dynamic properties. Chapter 4 to 6 present our studies of the molecular structure of carboxyl groups, -COOH. We demonstrate the existence of distinct conformational isomers of carboxylic acid in formic

acid (Chapter 4), and in more complex bio-molecules, such as peptides, at room temperatures in aqueous environments (Chapter 5) and in hydrophobic environments (Chapter 6). Chapters 7 to 10 present the molecular conformation of hyaluronic acid in relation to its mechanical properties. First, the molecular conformation of the hyaluronan polymer chain at neutral pH is discussed. We study the intra-molecular hydrogen-bonds, which stiffen the polymer (Chapter 7), and the effect of calcium ions on the intra-molecular hydrogen-bonded network (Chapter 8). In Chapter 9 we identify the specific inter-molecular interactions that are activated by tuning the pH at 2.5, and that lead to a dramatic change of the viscoelastic behavior of hyaluronan solutions. The effects of temperature and nature of the side-chain on the inter-molecular interactions, which lead to the hydrogen-bonded network, are discussed in Chapter 10. Finally, in Chapter 11, we present an investigation of the molecular structure of anti-freeze glycoproteins in aqueous solution. We show that this largely disordered and flexible protein acquires a specific conformation at quasi-freezing conditions, enabling the protein to inhibit the growth of ice crystals.

2

Two-Dimensional Infrared Spectroscopy: from concepts to experiment

Abstract

The understanding of two-dimensional infrared spectroscopy requires a basic, but broad knowledge of physics and chemistry. Furthermore, the large content of information provided by a two-dimensional spectrum demands a careful and critical analysis of the spectral signatures. In this chapter, we will provide the reader with the basic knowledge required to understand and analyze two-dimensional infrared vibrational spectra based on previous works.[43–45] In the first part, we will treat the molecular vibration as a quantum oscillator, and we relate its properties to measurable spectroscopic observables. In the second part, we describe pump-probe and two-dimensional spectroscopy, and we introduce the coupling of molecular vibrations, which we again describe with a quantum formalism. We also describe the origins and mechanisms of molecular couplings. In the last part, we briefly describe the home-built set-up that we used to perform two-dimensional infrared spectroscopy.

2.1 Quantum description of molecular vibrational motion

To understand the principles of infrared spectroscopy, we need a description of the relative motions of the atoms within the molecule. In the following we will provide such a description within a quantum formalism.

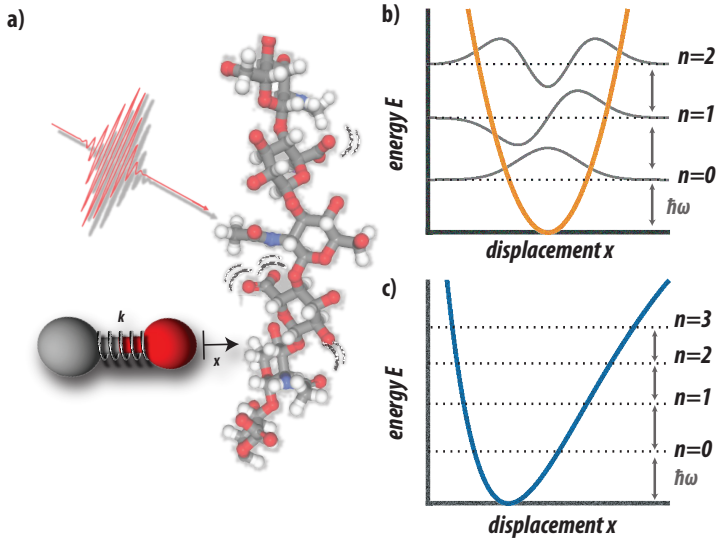

Figure 2.1: a) Schematic illustration of the molecular vibration of a carbonyl group. The interaction between the oxygen and carbon atoms can be described as a harmonic oscillator with elastic constant *k*. We refer to the displacement from the equilibrium position as *x*. b) The energy levels of the harmonic oscillator are equidistant and separated by an energy $\hbar\omega_0$, where ω_0 is the vibrational frequency of the harmonic oscillator. The eigenfunctions ψ are also shown. c) Energy levels of an anharmonic oscillator (*Morse oscillator*). In this case, the energy levels are not equidistant, and their separation decreases with increasing quantum number *n*.

The nuclei of molecules show oscillatory motions, which often have a vibrational frequency in the infrared spectrum. This means that the vibration can often be excited with infrared light. We will describe the vibration as a harmonic oscillator with elastic constant *k* (Fig.2.1) and reduced mass μ. In the simple case of a diatomic molecule of atoms with masses m_1 and m_2, the reduced mass $\mu = \frac{(m_1 m_2)}{m_1+m_2}$. The Hamiltonian, $\hat{H}_0$, which describes the

total energy of the system, is given by

$$\hat{H}_0 = \frac{\hat{p}^2}{2\mu} + \frac{1}{2}k\hat{x}^2 \tag{2.1}$$

where $\hat{p}$ and $\hat{x}$ are the momentum and position operators. The energy levels of the harmonic oscillator can be found by simply applying the Hamiltonian described in eq.2.1 to the time-independent Schrödinger equation:

$$\hat{H}\,|\psi\rangle = E\,|\psi\rangle \tag{2.2}$$

where E is the eigen-energy, and ψ denotes the wavefunction. By writing $\omega_0 = \sqrt{\frac{k}{\mu}}$ as the resonance frequency, and defining n as the vibrational quantum number, the eigen-values are given by:

$$E_n = \hbar\omega_0(n + \frac{1}{2}) \tag{2.3}$$

For the harmonic oscillator the energy levels are equidistant, with an energy separation of $\hbar\omega_0$. We also notice that at $n = 0$ (*ground state*) the energy is non-zero (*zero-point energy*). This result is related to the uncertainty principle, which states that it is not possible to know precisely both the position and the momentum of the oscillator ($\Delta x \Delta p \geqslant \hbar/2$).[46] This means that the expectation values of the square of the momentum and/or the position are non-zero, which directly implies that the energy cannot be zero.
Up to now we have considered a stationary system with a time-independent Schrödinger equation with a time-independent Hamiltonian. To enable transitions between the levels, we need to add a time-dependent term to the Hamiltonian. We thus add a time-dependent potential $V(t)$,

$$\hat{H} = \hat{H}_0 + \hat{V}(t) \tag{2.4}$$

The corresponding time-dependent Schrödinger equation has the following shape:

$$i\hbar\frac{\partial\,|\psi\rangle}{\partial t} = \hat{H}(t)\,|\psi\rangle \tag{2.5}$$

Here we consider the case that the time-dependent perturbation is given by the product of the electric field of infrared light multiplied by a dipole

moment. Hence, we express $\hat{V}(t)$ as a function of the electric dipole moment operator $\vec{\hat{\mu}}$ and an oscillating electric field $\vec{E}(t)$:

$$\hat{V}(t) = -\vec{\hat{\mu}} \cdot \vec{E}(t) \tag{2.6}$$

$\vec{\hat{\mu}}$ is dependent on the positions $\vec{\hat{x}}$ of all the charges q of the system:

$$\vec{\hat{\mu}} = \sum_i q_i \vec{\hat{x}}_i \tag{2.7}$$

By using the following form for the oscillating electric field:

$$\vec{E}(t) = \frac{1}{2}\vec{E}_0(e^{i\omega t} + e^{-i\omega t}) \tag{2.8}$$

we can rewrite eq.2.6 as follows:

$$\hat{V}(t) = -\frac{1}{2}\vec{\hat{\mu}} \cdot \vec{E}_0(e^{i\omega t} + e^{-i\omega t}) \tag{2.9}$$

In time-dependent first-order perturbation theory, the transition probability from level i to f induced by $\hat{V}(t)$ is given by Fermi's Golden Rule:

$$W_{fi} = \frac{2\pi}{\hbar^2}|\langle f|\hat{V}(t)|i\rangle|^2, \tag{2.10}$$

where W_{fi} represents the transition probability per unit time. By using eq.2.9, we obtain that

$$\begin{aligned} W_{fi} &= \frac{2\pi}{\hbar^2}|\langle f| - \frac{1}{2}\hat{\vec{\mu}} \cdot \vec{E}_0(e^{i\omega t} + e^{-i\omega t})|i\rangle|^2 = \\ &= \frac{\pi}{2\hbar^2}|\langle f|\hat{\mu}E_0 cos(\theta)|i\rangle|^2(\delta(\omega_{fi} - \omega) + \delta(\omega_{fi} + \omega)) \end{aligned} \tag{2.11}$$

where $\omega_{fi} = \frac{E_f - E_i}{\hbar}$, and θ is the angle between the electric field polarization and the dipole moment. The first delta function δ implies that the transition can only happen if the photon energy equals the energy difference between the initial and final states. Clearly, for a quantum harmonic oscillator, where the energy levels are equidistant, its spectrum will be limited to just one single frequency, ω_0. By taking $\omega = \omega_{fi}$, we can rewrite eq.2.11 to:

$$W_{fi} = \frac{\pi}{2\hbar^2}E_0^2 cos(\theta)^2|\langle f|\hat{\mu}|i\rangle|^2 = \frac{\pi}{2\hbar^2}E_0^2 cos(\theta)^2|\mu_{fi}|^2 \tag{2.12}$$

where μ_{fi} is defined as the *transition dipole moment*. We wrote this expression to describe the transition probability per unit of time to jump from $|i\rangle$ to the upper level $|f\rangle$.
We now expand the dipole moment $\hat{\vec{\mu}}$ as a function of the displacement operator $\hat{\vec{x}}$ around the equilibrium position x_0,

$$\hat{\vec{\mu}} \simeq \vec{\mu_0} + \hat{x}\frac{\partial \vec{\mu}}{\partial x} \tag{2.13}$$

By substituting this expression in eq.2.12, we obtain:

$$W_{fi} = \frac{\pi}{2\hbar^2} E_0^2 cos(\theta)^2 \left(\frac{\partial \vec{\mu}}{\partial x}\right)^2 |\langle f|\hat{x}|i\rangle|^2 \tag{2.14}$$

From eq.2.14, we see that a vibrational motion can only be excited by an infrared electric field if the transition dipole moment of the molecules changes as a function of the displacement x of the oscillator. The term $cos(\theta)$ represents the fact that the transition probability has its maximum if the electric field polarization is oriented parallel to the transition dipole moment. Moreover, the term $\langle f|\hat{x}|i\rangle|$ is only non-zero if $n_f = n_i \pm 1$.
For real molecules, this last rule is not as rigid because the potential is not harmonic, i.e. the potential contains third and higher orders of the displacement *x*. An empirical description of an anharmonic potential is provided by the *Morse* potential (Fig.1.2c),

$$V_0 = D(1 - e^{-a\hat{x}})^2 \tag{2.15}$$

were *a* and *D* are the curvature and the depth of the potential, respectively. The parameter *D* represents the energy necessary to break the bond of the diatomic molecule. By solving the time-independent Schrödinger equation, we find that

$$E_n = (n + \frac{1}{2})\hbar\omega_0 - (n + \frac{1}{2})^2 \frac{\hbar\omega_0^2}{4D} \tag{2.16}$$

with $\omega_0 = a\sqrt{2D/m}$. It follows from this expression that the energy separation of the levels decreases with increasing quantum number. As we will see, this dependence of the energy spacing on the vibrational quantum number is crucial in two-dimensional and pump-probe infrared spectroscopy.

2.2 Infrared Absorption

Both linear and pump-probe spectroscopy are based on the measurement of the attenuation of an infrared beam that travels through a sample (Fig.2.2). The attenuation of the infrared beam depends on the sample length *l*, on the molecule concentration *C* and on the ability of the molecule to absorb the incoming radiation. This last factor is determined by the transition probability expressed in eq.2.11.To relate the molecular properties previously described to the light attenuation, we start by considering an incoming beam with intensity I_0

$$I_0 = \frac{c\epsilon_0}{2} E_0^2 \tag{2.17}$$

where ϵ_0 is the dielectric constant in vacuum and *c* the speed of the light.

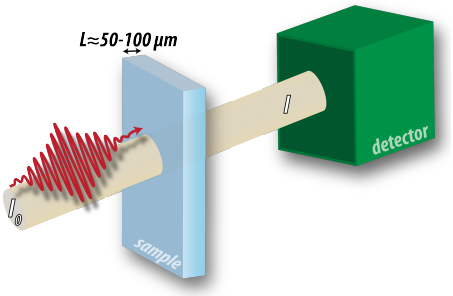

Figure 2.2: Schematic illustration of linear infrared spectroscopy, where we measure the attenuation of a beam with an intensity I_0 that travels through a sample for a distance L.

We find that

$$E_0^2 = \frac{I_0 2}{c\epsilon_0} \tag{2.18}$$

We substitute this expression for E_0^2 in eq. 2.11, which yields the following formula for the transition probability:

$$W_{fi} = \frac{\pi}{3\hbar^2} \frac{I_0}{c\epsilon_0} |\mu_{fi}|^2 \tag{2.19}$$

where we also replaced $cos(\theta)^2$ with its average value $\frac{1}{3}$ for an isotropic sample. We define now a new quantity, the *absortion cross-section*, σ, as

$$\sigma_{fi} = \frac{\pi\omega_{fi}}{3\hbar c\epsilon_0} |\mu_{fi}|^2 \tag{2.20}$$

The transition probability W_{fi} depends on the total amount of photons, which is proportional to I_0, and $W_{fi} = \sigma_{fi} I_0$.
The intensity reduction of the beam through a small distance dl can be written as

$$dI = -\sigma_{fi} I \cdot C \cdot dl \tag{2.21}$$

By integrating this expression we find that

$$\frac{I}{I_0} = -e^{-\sigma_{fi} C l} \tag{2.22}$$

This equation is referred to as the Lambert-Beer law. The exponential term can also be rewritten as $\alpha_{fi} = \sigma_{fi} C l$, which we refer to as the *absorbance*.

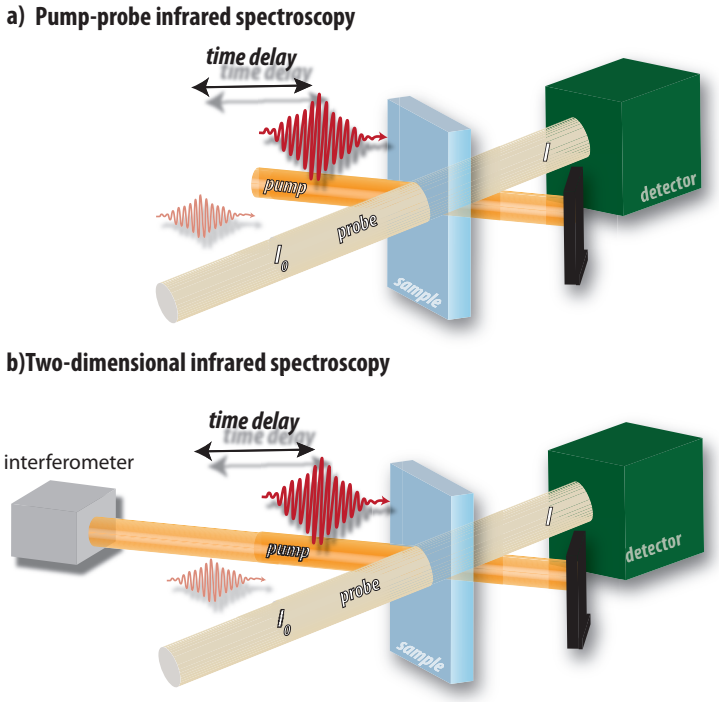

Figure 2.3: a) and b) schematic illustrations of pump-probe and two-dimensional infrared spectroscopy,respectively.

2.3 Two-Dimensional Infrared Spectroscopy (2DIR)

We have so far discussed about molecular motions, and how we can use a quantum formalism to describe them. We have then directly linked macroscopic measurements, light intensity, to molecular properties, such as the absorption cross-section. In the case of molecular vibrations in the condensed phase, the vibrational lifetime is typically on the order of hundreds of femtoseconds to a few picoseconds, and the relaxation dynamics contains information on the molecular structure, solvation and other molecular-scale interactions. Thanks to femtosecond lasers, we are able to access to these ultrafast dynamics by performing pump-probe or two-dimensional infrared spectroscopy. In both cases, we use an intense beam (*pump*) to excite the molecular vibrations from the ground state to the first excited state, and we use a second weaker beam (*probe*) to monitor the absorption of the probe pulse as a function of the probe frequency and the time delay between pump and probe beams. In two-dimensional infrared spectroscopy also the frequency of the pump beam is varied, and thus we record the absorption of the probe pulse as a function of pump and probe frequencies (Fig.2.3).

Pump-probe and two-dimensional infrared spectroscopies are non-linear spectroscopic techniques, which means that the signal measured is not linear with respect to the total electric field of the radiation. In this chapter, we will explain these two techniques by using a simple mathematical approach. If the reader is interested in non-linear theory response, we refer to the book of Hamm and Zanni for more details[43].

2.3.1 Transient Absorption Signal

Pump-Probe

In pump-probe spectroscopy the absorption of the probe pulse is recorded as a function of probe frequency in presence and in absence of the pump pulse. In case the pump is off, the absorbance of the sample is simply given by

$$\alpha_{off}(\omega_{probe}) = \sigma_{01}(\omega_{probe})N_0 \tag{2.23}$$

where N_0 is the number of molecules per area ($N_0 = CL$) in the ground state. In case the pump is on, the intense pump excites a significant fraction of the molecules, N_1, from the ground state $|0\rangle$ to the first excited state $|1\rangle$, and the probe absorption is modified because of three effects. Firstly, due to the pump excitation fewer molecules will be in the ground state, and thus less probe light is absorbed(*ground state depletion*) at the ω_{01} frequency, as shown in Fig.2.4b. Secondly, a fraction of the excited molecules can be stimulated back by the probe light to the ground state, leading to the enhancement of light at the ω_{01} frequency (*stimulated emission*). Thirdly, since the $|1\rangle$ state is populated, the probe radiation induces the transition from $|1\rangle$ to $|2\rangle$, and probe light at the ω_{12} frequency will be absorbed (*excited state absorption*). The resulting absorbance in the case of pump on takes the following form

$$\alpha_{on}(\omega_{probe}, t) = \sigma_{01}(\omega_{probe})(N_0 - 2N_1(t)) + \sigma_{12}(\omega_{probe})N_1(t) \qquad (2.24)$$

where σ_{12} is the absorption cross-section of the $|1\rangle$ to $|2\rangle$ transition. The factor of 2 takes into account that the cross-sections of ground state absorption and stimulated emission are the same. The signal measured is the difference between α_{off} and α_{on}

$$\begin{aligned} \Delta\alpha(\omega_{probe}, t) = \alpha_{on}(\omega_{probe}, t) - \alpha_{off}(\omega_{probe}) = \\ = (-2\sigma_{01}(\omega_{probe}) + \sigma_{12}(\omega_{probe}))N_1(t) \end{aligned} \qquad (2.25)$$

Usually, we refer to the negative term of the absorption difference as $bleach$ and to the positive term as *excited state absorption*. Further considerations about eq.2.25 are worthwhile:

- in the case of a harmonic oscillator, the absorption change is zero because $\omega_{01} = \omega_{12}$ and $2\sigma_{01} = \sigma_{12}$;
- as the excited state will relax, the absorption change will be time dependent, and should be referred to as *transient absorption signal*. The time dependence is introduced by the time dependence of the population N_1 of the first excited state, which has a certain lifetime τ. In many cases, the population decays exponentially, $N_1(t) = N_1(0)e^{-\frac{t}{\tau}}$

- although the bleach signal contains a factor 2 ($2\sigma_{01}$), the bleach and the excited state absorption will usually have similar amplitudes since in most cases $\sigma_{12} \approx 2\sigma_{01}$

Two-dimensional Infrared Spectroscopy

In two-dimensional infrared spectroscopy the absorption change of the probe is not only measured as a function of the probe frequency and the time delay between excitation and detection but also as a function of the pump frequency. To determine this dependence, the pump beam is sent through an interferometer (Mach-Zender (MZ) interferometer in our cur-

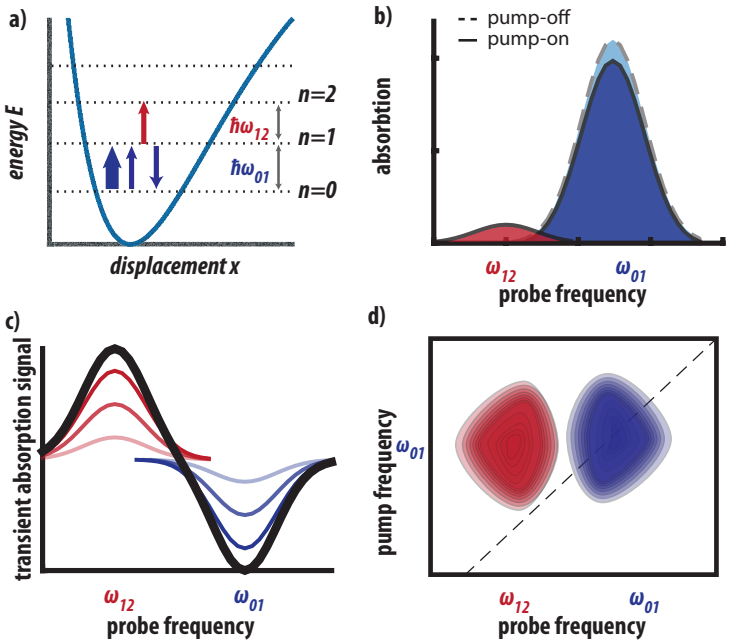

Figure 2.4: a) Anharmonic vibrational potential. An intense pump beam (blue bold arrow) excites a fraction of the population to the $|1\rangle$. The probe light experiences less absorption at $|0\rangle$-$|1\rangle$ frequency due to the partial depletion of the ground-state, and to stimulated emission. Because of the $|1\rangle$ is populated, the probe light can also excite a fraction of molecules to the $|2\rangle$ excited state, and thus part of the probe light is absorbed at the $|1\rangle$-$|2\rangle$ frequency. b) Absorption of probe in case of pump-on and pump off. c) Transient absorption signals at different time delay between pump and probe. d) 2DIR spectrum at a fixed pump-probe delay.

rent system) before entering the sample (Fig.2.3). The MZ interferometer converts the pump pulse into a pulse-pair with a tunable time separation τ_{in}. The intensity of the pump beam at the sample position is modulated, and hence also the pump-probe signal. The transient absorption signal is thus dependent on the probe frequency, on the time delay between pump-probe t_{pp}, and on the time-delay of the interferometer, $\Delta\alpha(\tau_{in}, t_{pp}, \omega_{probe})$. A Fourier transform is then applied along τ_{in}, yielding $\Delta\alpha(\omega_{pump}, t_{pp}, \omega_{probe})$, which is the two-dimensional infrared (2DIR) spectrum.

Fig.2.4d shows a typical 2DIR spectrum . The blue-colored diagonal signal is negative and referred to as bleach, whilst the red-colored diagonal signal is positive and referred to as excited state absorption. The shape of these 2DIR signals provides information on the line-shape broadening mechanisms of the excited molecular vibrations. The anti-diagonal width of the diagonal signals represents the homogeneous broadening and the diagonal width represents a convolution of the homogeneous and inhomogeneous broadening. Hence, 2DIR spectroscopy can disentangle the different line-broadening mechanisms, contrary to linear infrared spectroscopy.

2.3.2 Polarization dependence

The transient absorption signal is dependent on the time between the pump and probe pulses. However, the amplitude of the transient absorption signal is not only time-dependent because of the relaxation of the populated excited state. Other effects like molecular reorientation or resonant energy transfer can also lead to a time dependence of the measured signal. To determine these effects we perform polarization dependent pump-probe and two-dimensional infrared spectroscopy, where both pump and probe beams are linearly polarized. We measure the transient absorption signal in parallel ($\Delta\alpha(t)_{\parallel}$) and perpendicular ($\Delta\alpha(t)_{\perp}$) polarization with respect to the pump (Fig.2.5). By using $\Delta\alpha(t)_{\parallel}$ and $\Delta\alpha(t)_{\perp}$, we define the isotropic signal

$$\Delta\alpha_{iso}(t) = \frac{\Delta\alpha(t)_{\parallel} + 2\Delta\alpha(t)_{\perp}}{3} \tag{2.26}$$

which is an observable that is not affected by molecular reorientation or resonant energy transfer. The dynamics of these latter processes can be selectively monitored through the so called anisotropy parameter, which has the following form

$$R(t) = \frac{\Delta\alpha(t)_{\parallel} - \Delta\alpha(t)_{\perp}}{\Delta\alpha(t)_{\parallel} + 2\Delta\alpha(t)_{\perp}} \tag{2.27}$$

The anisotropy is the difference between the parallel and perpendicular transient absorption signals divided by the isotropic signal. As a result the decay of the anisotropy is independent from the vibrational lifetime.

The anisotropy parameter is related to the orientational correlation function of the excited molecule[47], i.e. given a transition dipole moment at an angle θ_r with respect to the pump polarization at time $t = 0$ which is the probability to preserve θ_r at $t > 0$. The anisotropy can be written as follows:

$$R(t) = \frac{2}{5}\langle P_2(\vec{\mu}(0) \cdot \vec{\mu}(t))\rangle \tag{2.28}$$

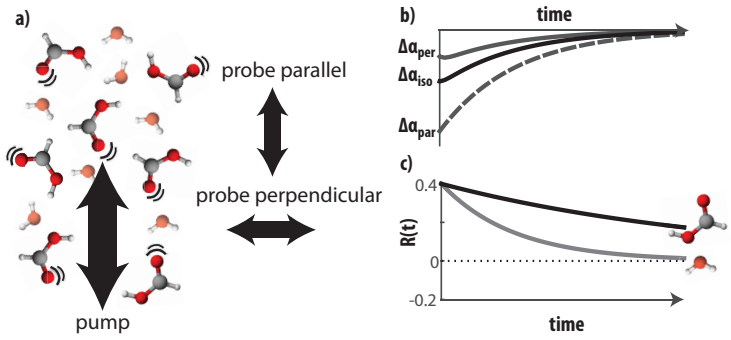

Figure 2.5: a) A linearly polarized pump pulse is used to excite the carbonyl vibration of simple acid molecules. The pump light is mainly absorbed by the molecules that have their transition dipole moment oriented parallel to the pump polarization, inducing an anisotropic distribution of the excited state. By using probe pulses with polarizations parallel and perpendicular to the pump polarization we measure a polarization dependent transient absorption signal. b) Parallel, perpendicular and isotropic transient absorption signals. c) Examples of anisotropy decay. The anisotropy decay of a carbonyl vibration molecule is slower than that of the hydroxyl vibration of a water molecule.

where $P_2(..)$ is the second order Legendre polynomial:

$$R(t) = \frac{2}{5}\langle\frac{1}{2}(3cos^2\theta_r(t) - 1)\rangle \tag{2.29}$$

This equation yields to the fact that the maximum of the anisotropy, obtained with $\theta_r(t) = 0$, is 0.4, whilst its minimum is -0.2, obtained with $\theta_r(t) = \frac{\pi}{2}$. In Fig.2.5 we report a schematic illustration of the anisotropy decay traces of a carbonyl vibration of formic acid and of a hydroxyl vibration of a water molecule. We observe that the anisotropy decay is much faster for the water molecule. This is because a water molecule is smaller than formic acid, thus showing a much faster orientational diffusion.[48,49] In addition, the anisotropy of the hydroxyl vibration of a water molecule can decay because of resonant energy transfer to nearby, differently oriented hydroxyl vibrations.[50]In this thesis, the majority of the studied molecular vibrations shows a constant anisotropy at 0.4, indicating that their reorientational diffusion happens on much larger time scales than the time interval over which we can probe the reorientation (typically 4-5 vibrational lifetimes).

2.4 Molecular couplings

Two-dimensional infrared spectroscopy can provide unique information on the structure of molecules, from small acids to proteins. Thanks to the pump-frequency resolution, 2DIR enables us to determine the couplings between different molecular vibrations, which provide information on the molecular structure. In Fig.2.6a we show the 2DIR spectrum of two uncoupled molecular vibrations, A and B. For both the diagonal peaks, the excited state absorption is red-shifted with respect to the bleach because of the anharmonicity of the potential, which leads to a difference (Δ) in energy between the bleach and the excited state (*diagonal anharmonic shift*). Next we consider the case that the molecular vibrations A and B are coupled. As a result, upon excitation of A (or B) a vibrational response will be observed at the vibrational absorption frequencies of B (or A). Hence, off-diagonal peaks called *cross-peaks* appear (Fig.2.6). Like the diagonal peaks, the cross peaks also consist of a bleach and a shifted induced absorption. The magnitude of this latter shift, the off-diagonal anharmonicity

(Δ_{AB}), is related to the coupling between the two modes. The amplitudes of the diagonal and off-diagonal also scale differently with the cross-section. The amplitude of the diagonal peaks scales with σ_{01}^2, whilst the cross-peak amplitude is proportional to the product of the absorption cross-sections of the A and B vibrations, $\sigma_{01}^A \sigma_{01}^B$.

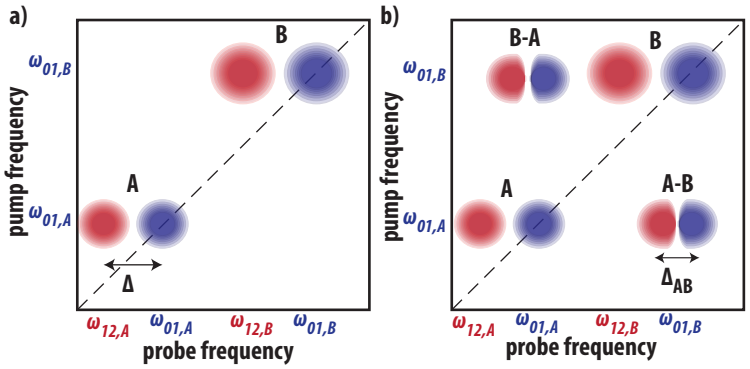

Figure 2.6: a) and b) 2DIR spectra for two uncoupled and coupled molecular vibrations, respectively.

2.4.1 System of coupled oscillators

In this section we will provide a more detailed description of the coupling mechanisms of two vibrations that give rise to cross peaks in the 2DIR spectrum. We consider a system composed by two coupled molecular vibrations, A and B. The total potential of the system is written as,

$$V(r_A, r_B) = V_1(r_A) + V_2(r_B) + \beta_{A,B} V(r_A, r_B) \tag{2.30}$$

where the $V_1(r_A)$ and $V_2(r_B)$ represent the vibrational potentials of the single oscillators A and B as a function of their vibrational coordinates, and $\beta_{A,B} V(r_A, r_B)$ the coupling terms. The β_{AB} is the coupling constant, and represents the strength of the coupling. We refer to the individual A and B molecular vibrations as *local modes*.

In first approximation, we assume the separate A and B oscillators to be harmonic. For a system of coupled harmonic oscillators the total Hamiltonian

takes the following form in second quantization:

$$\hat{H} = \hbar\omega_A(\hat{b}_A^\dagger \hat{b}_A + \frac{1}{2}) + \hbar\omega_B(\hat{b}_B^\dagger \hat{b}_B + \frac{1}{2}) + \beta_{AB}(\hat{b}_A^\dagger \hat{b}_B + \hat{b}_B^\dagger \hat{b}_A) \tag{2.31}$$

where $b^\dagger$ and b are creation and annihilation operators, respectively. The application of the creation operator increases the quantum number of the oscillator, $b^\dagger |n\rangle = \sqrt{(}n+1)\,|n+1\rangle$, and the annihilation operator decreases the quantum number $b\,|n\rangle = \sqrt{(}n)\,|n-1\rangle$. The last term of eq.2.31 originates from the bilinear term $q_A q_B$ of a Taylor expansion of the total potential $V(q_A, q_B)$, which we can rewrite in terms of annihilation and creation operators by using that $\hat{q} = \frac{1}{\sqrt{2}}(\hat{b}^\dagger + \hat{b})$. By ignoring the zero-point energy, eq.2.31 takes the following form

$$\hat{H} = \hbar\omega_A \hat{b}_A^\dagger \hat{b}_A + \hbar\omega_B \hat{b}_B^\dagger \hat{b}_B + \beta_{AB}(\hat{b}_A^\dagger \hat{b}_B + \hat{b}_B^\dagger \hat{b}_A) \tag{2.32}$$

By expressing the Hamiltonian of a coupled system in second quantization, the effect of the coupling mechanism becomes quite intuitive. The last term of eq.2.32 describes the coupling as a transfer of the excitation from one vibration to the other. Since molecular vibrations are better described by anhamornic oscillators, we consider an anharmonic expression for the potential, yielding the following Hamiltonian:

$$\hat{H} = \hbar\omega_A \hat{b}_A^\dagger \hat{b}_A + \hbar\omega_B \hat{b}_B^\dagger \hat{b}_B + \beta_{AB}(\hat{b}_A^\dagger \hat{b}_B + \hat{b}_B^\dagger \hat{b}_A) - \frac{\Delta}{2}\hat{b}_A^\dagger \hat{b}_A^\dagger \hat{b}_A \hat{b}_A - \frac{\Delta}{2}\hat{b}_B^\dagger \hat{b}_B^\dagger \hat{b}_B \hat{b}_B \tag{2.33}$$

where Δ is the anharmonicity shift, which we for simplicity assume to be the same for A and B. We now investigate the effect of this Hamiltonian within a limited set of basis functions, since the states accessible in 2DIR measurements are limited to the second level. This basis is given by the following set: $|00\rangle, |01\rangle, |10\rangle, |02\rangle, |20\rangle, |11\rangle$, where the first and second quantum numbers refer to the excitation of the A and B oscillators. In this

basis, the Hamiltonian takes the following form,

$$H = \begin{pmatrix} 0 & & & & & \\ & \hbar\omega_A & \beta_{AB} & & & \\ & \beta_{AB} & \hbar\omega_B & & & \\ & & & 2\hbar\omega_A - \Delta & 0 & \sqrt{2}\beta_{AB} \\ & & & 0 & 2\hbar\omega_B - \Delta & \sqrt{2}\beta_{AB} \\ & & & \sqrt{2}\beta_{AB} & \sqrt{2}\beta_{AB} & \hbar\omega_A + \hbar\omega_B \end{pmatrix} \tag{2.34}$$

The Hamiltonian in this form can be divided in three blocks: ground state, the one-exciton Hamiltonian and the second-exciton Hamiltonian. This Hamiltonian is block-diagonal, and every block or sub-matrix can be diagonalized separately. To find the vibrational levels of the one-exciton states, we can just consider the first-excited state Hamiltonian, $H^{(1)}$:

$$H^{(1)} = \begin{pmatrix} \hbar\omega_A & \beta_{AB} \\ \beta_{AB} & \hbar\omega_B \end{pmatrix} \tag{2.35}$$

By then calculating the determinant of the H_1 matrix to find the eigenvalues, we find the energy values for the first excited state of A and B

$$E^{(1)}_{A,B} = \frac{\hbar\omega_A + \hbar\omega_B \pm \sqrt{4\beta^2_{AB} + (\hbar\omega_A - \hbar\omega_B)^2}}{2} \tag{2.36}$$

We now consider the case of weak and strong couplings. For weak coupling, we have that $\beta_{AB} << \hbar\omega_A - \hbar\omega_B$, and thus we can reduce eq.2.36 to

$$E^{(1)}_{A,B} \sim \hbar\omega_{A,B} \pm \frac{2\beta^2_{AB}}{\hbar\omega_A - \hbar\omega_B} \tag{2.37}$$

In the case of weak coupling, the excitations are localized on single sites and the energy levels correspond to the uncoupled energies, slightly shifted.
For strong coupling, we have that $\beta_{AB} >> \hbar\omega_A - \hbar\omega_B$, and hence eq.2.36 is reduced to

$$E^{(1)}_{A,B} \sim \frac{\hbar\omega_A + \hbar\omega_B}{2} \pm \beta_{AB} \tag{2.38}$$

In the limit of strong coupling the energy levels of the two molecular vibrations A and B are strongly mixed.
The energy for the simultaneous excitation of both vibrations is given by

$$E^{(2)}_{AB} = E^{(1)}_A + E^{(1)}_B - \Delta_{AB} \tag{2.39}$$

Where the anharmonicity $\Delta_{AB}$is the off-diagonal anharmonicity, which we previously defined as the magnitude of the frequency separation between the bleach and the excited state absorption of a cross-peak. In the limit of weak coupling, it is possible to relate the off-diagonal anharmonicity Δ_{AB} to the coupling constant by using second order perturbation theory,

$$\Delta_{AB} = -\frac{4\Delta\beta_{AB}^2}{(\hbar\omega_B - \hbar\omega_A)^2} \tag{2.40}$$

We can observe that the diagonal and off-diagonal anharmonicities are accessible observables in 2DIR spectroscopies, and thus that in the weak coupling limit we can extract the coupling strength β_{AB}.

Above we considered the Hamiltonian for a system of two anharmonic oscillators. Though more complex, it is possible to expand this description to a system of *n* oscillators. In the case of identical molecules which display just nearest neighbor interactions, the Hamiltonian takes the following form

$$\hat{H} = \sum_i^n \hbar\omega_0 b_i^\dagger b_i + \sum_i^n \beta_i (b_i^\dagger b_{i+1} + b_i^\dagger b_{i-1}) \tag{2.41}$$

This expression can be used to study the vibrational excitations in secondary structures such as an α-helix, where amide vibrations are strongly coupled, and thus the vibrational motions are highly delocalized over the chain.

2.4.2 Energy Transfer

We have now described a system of two coupled vibrations, determining how the coupling mechanism affects and modifies the energy levels of the two vibrations in the cases of strong and weak coupling. Coupling interactions can lead to transfer of the vibrational excitation between the two coupled molecular vibrations if the energy difference is somehow compensated (*energy transfer*). In case this happens, the cross-peak signal follows a specific dynamics, i.e. the cross-peak signal is not instantaneous but increases with the delay time between the pump and probe (Fig.2.7c). Such energy transfer between coupled vibrations is enabled by fluctuations in the local environment that allow for a compensation of the energy mismatch between the

excited and accepting vibrations. Fluctuations lead to a time dependence of the coupling constant β and the site energies E_i, yielding to a temporal dependence which we express as $\beta(t) = \overline{\beta} + \delta\beta(t)$ and $E_i(t) = \overline{E_i} + \delta E_i(t)$. $\delta E_i(t)$ and $\delta\beta(t)$ represent the deviations of the site energies and coupling constant from their time average values, $\overline{E_i}$ and $\overline{\beta}$. By introducing the time dependence, the first-exciton Hamiltonian, which we previously found for a coupled dimer, can be written as:

$$H(t) = \begin{pmatrix} \overline{E_A} + \delta E_A(t) & \overline{\beta}_{AB} + \delta\beta_{AB}(t) \\ \overline{\beta}_{AB} + \delta\beta_{AB}(t) & \overline{E_B} + \delta E_B(t) \end{pmatrix} \tag{2.42}$$

where both the diagonal and off-diagonal elements are time dependent. A relatively simple expression for the transfer rate can be obtained by using a perturbative approach, in which the time dependence of the diagonal peaks is solely dependent on the fluctuations of the site energies (which is valid in the case of weak coupling ($\beta_{AB} << \Delta E$, with $\Delta E = \hbar(\omega_A - \omega_B)$), whilst the time dependence of the cross-peak depends only on the fluctuation of the coupling constant. The energy-transfer rate can be obtained from Fermi's golden rule:

$$P_{AB} = k_{AB}T \tag{2.43}$$

where P_{AB} represents the probability of a transition from A to B in a time T, and k_{AB} the transfer rate. This yields:[51]

$$k_{AB} = \frac{1}{\hbar^2}\int_{-\infty}^{+\infty} \langle \delta\beta(t)\delta\beta(0)\rangle e^{\frac{i}{\hbar}\Delta E t} dt \tag{2.44}$$

where $\langle ..\rangle$ denotes the ensemble average. Assuming that the fluctuations are Markovian and have a Gaussian distribution, $\langle \partial\beta(t)\partial\beta(0)\rangle = d^2 e^{-t/\tau}$ with d the amplitude of the fluctuations and τ the correlation time of the fluctuations, eq.2.44 yields:[51]

$$k_{AB} = \frac{2d^2\tau}{\hbar^2 + \Delta E^2\tau^2} \tag{2.45}$$

where we notice that the transfer rate scales as the square of the fluctuation amplitude, and is inversely proportional to the energy difference between the vibrations.

The dynamics of the cross-peak signals of modes A and B is given by $k_{AB} + k_{BA}$. In case the energy splitting of the states A and B is small compared to the thermal energy ($k_BT >> \Delta E$), $k_{BA} \approx k_{AB}$, and the rate at which the cross-peak rises is $\approx 2k_{AB}$. This is not always the case. In this thesis, for example, we will study cross-peaks among vibrations which lie more than 500 cm^{-1} from each other, and thus $k_BT < \Delta E$. In this case, the transfer rate downhill will be larger than the uphill rate (detailed balance), which will not lead to different dynamics of the cross-peak, but to different amplitudes of the cross-peak signals.

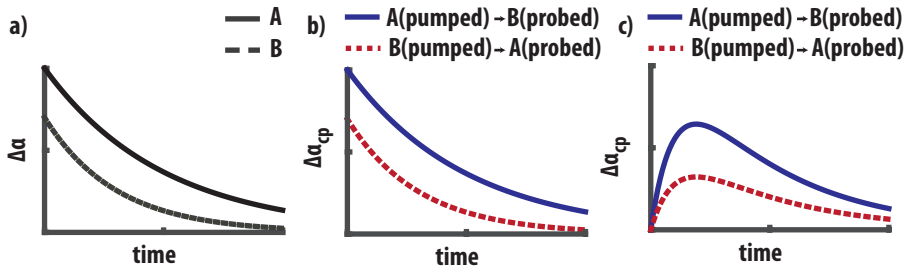

Figure 2.7: Examples of cross-peak dynamics for the coupling mechanisms studied in this thesis. a) Delay traces of uncoupled molecular vibrations A and B. b) Delay traces of the cross-peak signals $A(pumped) \rightarrow B(probed)$ and $B(pumped) \rightarrow A(probed)$ in case A and B are anharmonically coupled, as described in section 2.4.1. c) Delay traces for the cross-peaks $A(pumped) \rightarrow B(probed)$ and $B(pumped) \rightarrow A(probed)$ in case of fast energy transfer between the modes. After equilibration, the two cross-peak signals decay with the same rate that is a weighted average of the vibrational relaxation rates of A and B.

2.4.3 Transition dipole-dipole moment coupling model

The coupling constant β can find its origin in transition dipole-dipole coupling (TDC), meaning that the vibrations, A and B, are affected by the excitation of the other because A and B are electrically coupled via their transition dipole moments. In this case, the TDC coupling term has the following form:

$$\beta_{A,B} = \frac{1}{4\pi\epsilon_0}\left[\frac{\vec{\mu}_A \cdot \vec{\mu}_B}{r_{AB}^3} - 3\frac{(\vec{r}_{AB} \cdot \vec{\mu}_A)(\vec{r}_{AB} \cdot \vec{\mu}_B)}{r_{AB}^5}\right] \qquad (2.46)$$

where $\vec{\mu}_A$ and $\vec{\mu}_B$ are the transition dipole moments of the molecular vibrations A and B, respectively, and $\vec{r}_{AB}$ the vectors connecting the two sites. The coupling constant scales as $\frac{1}{r_{AB}^3}$ at large distance, and has its maximum in case that the two transition dipole moments are aligned parallel with respect to each other.

2.4.4 Chemical Exchange

The appearance of cross-peak signals can also be related to chemical exchange, which similarly to energy transfer mechanism is a time-dependent process. We can imagine that molecules can adopt two different states, with spectroscopic properties (i.e. vibrational frequencies) that depend on the adopted state. For example, a molecule can interconvert between a dimer state, absorbing at ω_A, and a monomer, absorbing at ω_B. Within a certain time, which is usually on the order of picoseconds if hydrogen-bonds are involved, the two states will interconvert. This chemical exchange will lead to the appearance of cross-peaks. At time 0 we tag molecules in a particular state by vibrationally exciting them. If during the vibrational lifetime the molecules chemically exchange (from monomer to dimer or vice-versa), the spectroscopic properties of this excitation change as well. Thus, a molecule, that at time 0 was excited at ω_A, will at time t have this excitation at ω_B, yielding to the appearance of a cross-peak, provided that the exchange does not lead to vibrational relaxation, and that the chemical exchange is the result of the spontaneous dynamic of the studied system (not excitation induced). The dynamics of the cross-peak signal will then be directly related to the chemical exchange rates $k_{AB} + k_{BA}$ between the two states.

2.4.5 Polarization dependence of a cross-peak

As for diagonal peaks, by using probe with parallel and perpendicular polarization with respect to the pump, we can determine the anisotropy of the cross-peaks. In this case, the anisotropy is given by

$$R = \frac{1}{5}\langle 3cos^2\theta_{AB} - 1\rangle \tag{2.47}$$

where θ_{AB} is the angle between the transition dipole moments of the A and B vibrational modes. Eq.2.47 provides a measurable observable of the relative orientation of the transition dipole moments of the interacting vibrations, providing important structural information. Though the anisotropy of cross-peak is a critical source of information, the measurement of the anisotropy of cross-peak can be easily perturbed. Cross-peaks most of the times overlap with diagonal peaks or an ingrowing heating signal, and thus the polarization dependence of the signal at the cross-peak vibrational frequencies can be highly perturbed. Molecular reorientation or the presence of resonant intermolecular energy transfer processes leading to a change of the anisotropy, must also be carefully considered.

2.5 Experimental set-up

Here, we provide for the reader's convenience a brief summary of the employed experimental set-up, based on previous work.[45]

2.5.1 Two-dimensional infrared set-up

As described before, the techniques of pump-probe and two-dimensional infrared spectroscopy are based on the measurement of the absorption of a probe pulse in presence and in absence of a pump beam,leading to an absorption change $\Delta\alpha$. The time delay t_{pp} between pump and probe can be varied, allowing to record the absorption change as a function of time, $\Delta\alpha(t)$. The transient absorption change is recorded as a function of wavenumber ($\overline{\nu} = \frac{1}{\lambda}$), where λ is the wavelength. In infrared spectroscopy, $\overline{\nu}$ is usually expressed in cm^{-1}. For example, amide vibrations absorb at 1600 cm^{-1} corresponding to a wavelength of $\sim 6\mu$m, water vibrations absorb at 3400 cm^{-1}, corresponding to a wavelength of $\sim 3\mu$m.

We measure the attenuation of the transmitted light of probe through the sample, normalized to a reference spectrum, $T = \frac{I_p}{I_r}$. The normalization to the reference spectrum is important to compensate for fluctuations in the laser spectrum. As a rule of thumb, the relative percent error between probe and reference spectrum should be lower than 0.3% to obtain measurements with a good signal-to-noise. In presence (*on*) or absence (*off*) of pump, the

absorption change takes the following form

$$\Delta\alpha(\overline{\nu}) = -\log_{10}\left(\frac{T_{on}(\overline{\nu})}{T_{off}(\overline{\nu})}\right) = -\log_{10}\left(\frac{I_{probe,on}(\overline{\nu})I_{ref,off}(\overline{\nu})}{I_{probe,off}(\overline{\nu})I_{ref,on}(\overline{\nu})}\right) \quad (2.48)$$

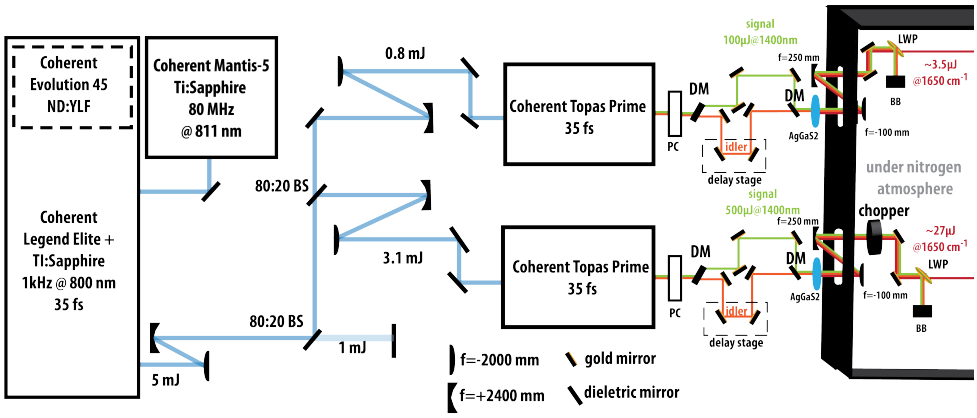

Figure 2.8: Scheme of the setup used for the generation of ultrashort infrared pulses. BS: beam splitter. $AgGaS_2$: silver-gallium-disulfide crystal. LWP: long-wave-pass filter. BB: beam block. DM:dichroic mirrors. PC: periscope.

Generation of ultrashort infrared pulses

To perform two-dimensional infrared spectroscopy, two infrared beams with a pulse duration of $\sim$ 100 femtoseconds are necessary. Since at this stage no laser is capable to produce directly ultrashort and intense pulses in the infrared region, the first part of the experimental setup (Fig.2.8) is used to convert the frequency of femtosecond near-infrared pulses to the infrared. The starting point of the setup is a commercial mode-locked Ti:Sapphire oscillator (Coherent, Mantis-5). The output is formed by broad band pulses @810 nm at a repetition rate of 80 MHz. The power output is $\sim$560 mW. The pulses are used to seed a Ti:Sapphire regenerative amplifier (Coherent, Legend Elite-USP-1K-HE+). To reduce the peak power, which could damage the optical components in the amplifier, the seed pulses are stretched to obtain a pulse duration of $\sim$100 picoseconds by a grating, and then 1 out of

80000 is coupled into the cavity of the amplifier via a Pockels cell. The amplification takes place as the pulse passes through the Ti:sapphire crystal in the regenerative cavity, which is pumped by a Nd:YLF laser (Coherent, Evolution, 44.1 Hz, 22mJ@input current=19.8 A). After 10 round-trips through the pumped crystal, the amplified pulse is extracted by using a second Pockels cell. After this, the 800 nm pulse is compressed back with a grating pair to a pulse with a duration of $\sim$35 fs. At this stage, the amplified pulses are horizontally polarized at 800 nm with a repetition rate of 1 kHz. A telescope is then placed in the pulse path to expand the diameter of the 800 nm beam to reduce the power density. Next, the 800 nm beam is split in three beams, with pulse energies of 1 mJ, 3.1 mJ, and 0.8 mJ. The second and third beams are used to generate the mid-infrared pump and probe pulses using two commercial optical parametric amplifiers (OPAs), after further expanding their diameters (by a factor 1.2). The use of different OPAs for the pump and probe allow us to independently tune the pump and probe infrared frequencies, and thus to perform *two-color experiments*.

The commercial OPAs produce two output beams, signal and idler. The wavelength of the signal can be tuned between 1200 to 1500 nm, and the wavelength of the idler between 1600 and 2400 nm. In both OPAs, the wavelength of signal and idler are selected via a software interface, upon careful calibration of all the rotational and translational motors of the delay stages and the mount of the nonlinear BBO crystal, which control the OPA parameters. Due to the lower input power for the probe path, the signal intensity is four times lower than for the pump path, also leading to somewhat larger pulse-to-pulse fluctuations.
After the OPA, the signal and idler, which are almost collinear with a small time difference, are separated with a dichroic mirror. The idler and signal are sent through separate delay stage, and sent at a small relative angle into a silver-gallium-disulfide (AGS) crystal. By carefully overlapping in space and in time, the signal and idler beams are difference-frequency mixed, generating a mid-infrared pulse that functions as pump or probe. The generated infrared beam is separated from the signal and idler beams with a germanium-based

long-wave-pass filter. The infrared beams of pump and probe are then expanded to beam sizes of 3.8 mm and 5 mm, respectively. Many of the experiments employ pulses near 6 μm, where the carbonyl vibrations absorb. Hence, to reduce absorption of the generated infrared by water vapor, the frequency-conversion stages are kept under nitrogen atmosphere.

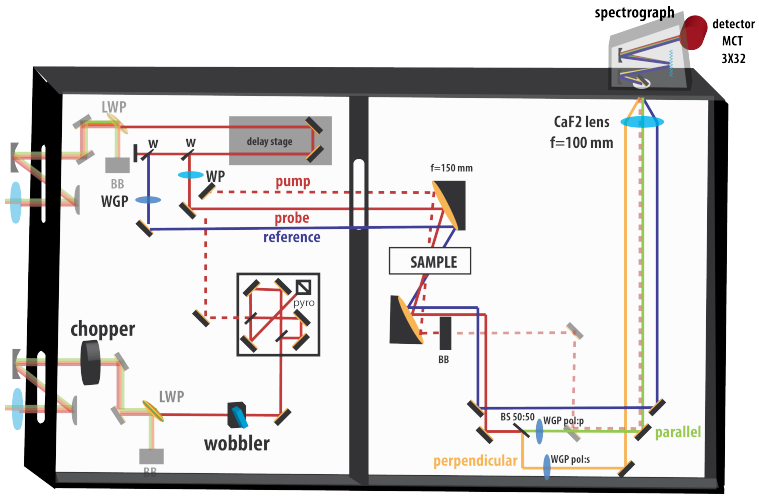

Figure 2.9: Scheme of the 2DIR set-up. WGP: wiregrid polarizer. WP: waveplate. W: ZnSe wedges. BB: beam block. P:parabolic mirrors.

Pump path

The pump beam passes through a chopper (Thorlabs, MC200), and a wobbler. The chopper and the wobbler are synchronized to the laser using a trigger signal from the amplifier. The chopper operates at 500 Hz, blocking every other shot. The wobbler is used to minimize artifacts caused by interference of scattered pump light with probe light in the detector, by introducing a small variable path-length change via an oscillating ZnSe-window. The presence of the wobbler reduces the power of the infrared beam by $\sim$20%. The pump beam is then guided onto a Mach-Zehnder interferometer, which is used to split the pump into two pulses, and to determine

the dependence of the signals on the pump frequency. The pump pulses are focused into the sample using an off-axis parabolic mirror (90°,f=15 cm). After the pump has traveled through the sample, it is blocked by a beam block. The beam block can be removed, and the pump can be guided by one fixed and one temporary routing mirror to the detector to analyse its spectrum.

Probe path

After the germanium-based long-wave-pass filter, the probe beam is guided into a delay stage, which is used to introduce a time delay between pump and probe (t_{pp}). Next, two ZnSe-wedges are used to split off two reflections from the beam to obtain separate probe and reference beam. The probe then travels through a wave-plate, which it is used to rotate the probe polarization to 45°with respect to the pump polarization. As a result, the parallel and perpendicular polarization components have similar intensities. Next, both probe and reference beams are focused into the sample by an off-axis parabolic mirror. The probe is aligned such that it overlaps with the pump beam, whilst the reference is displaced by a small distance.
After the sample, the probe travels through a beam splitter (50:50). The transmitted and reflected probe components are guided through two distinct polarizers to select either the parallel or the perpendicular polarization component. The reference, the parallel and the perpendicular probe beams are then sent into a spectrograph (Oriel, MS26oi), and the beams are detected by three lines of a mercury-cadmium-telluride detector (MCT), which is cooled with liquid nitrogen.

2.5.2 FTIR measurements

All samples that were studied with femtosecond pump-probe or 2DIR spectroscopy, were first characterized by measuring their linear Fourier Transform Infrared absorption spectrum. These measurements were performed using a Bruker Vertex 80v FTIR spectrometer, equipped with a liquid-nitrogen-

cooled mercury cadmium telluride (MCT) detector, which covers a spectral range between 12000 to 450 cm^{-1}. The linear spectra were recorded in transmission or in attenuated reflection modes under a nitrogen atmosphere with a frequency resolution of 3 or 2 cm^{-1}. For every spectrum, 50 to 100 scans were averaged. In all the measurements reported in this thesis, a standard sample cell with an optical length between 10-100 μm was used. In the attenuated reflection measurements the range of absorption is on the order of a few μm, depending on the infrared wavelength.

3

Concepts of Biopolymer Physics

Abstract

Drawing the connection between the molecular and macroscopic properties of a biopolymer is not-trivial. The mechanical properties result from various mechanisms that happen across different time- and size-scales. In particular, both the physical properties of the polymers, such as the rigidity of the chain, and of the solvent, such as pH and ionic strength, dictate the macroscopic properties. In this chapter, we provide for the reader's convenience a brief summary of basic concepts of polymer physics, basing our discussion on textbook knowledge.[52] We first introduce static properties of neutral biopolymers and charged biopolymers (polyelectrolytes). We then present the transport properties, viscosity and diffusion, for polymers in aqueous solution in the presence of salt.

3.1 Static Properties of Biopolymers

Polymers are chains that are composed of repeating blocks (monomers). In the case of polysaccharides, the repeating units are saccharide units that are linked with glycosidic bonds. Biopolymers, polymers essential in biological processes, constantly change their conformation in response to thermal fluctuations, but they maintain orientational correlations along their backbone for a certain distance termed the persistence length. In polysaccharides, one of the reasons for this local rigidity is the presence of intramolecular hydrogen-bonds, which are formed by the hydroxyl groups of the chain. An example is reported in Fig.3.1, where we show a schematic illustration of hyaluronic acid that is a linear polysaccharide composed of D-glucuronic acid and N-acetyl-D-glucosamine sugar units.

The rigidity of a biopolymer is an extremely important concept in biopolymer physics.[52] In order to introduce this concept, we start by discussing the worm-like chain. Contrary to simple models (ideal chain and Kuhn chain models) where the polymer chain is approximated to a sequence of $N+1$ monomers connected by N links with a step length *l*, in a worm-like model the biopolymer is approximated as a continuous chain, where the number of monomers *N* tends to infinity and the step length *l* to 0. Consider an elastic filament of length *s* with a constant curvature θ/s. By applying Hooke's law, we write the elastic energy as

$$\Delta U = \frac{1}{2} s \kappa_b \left(\frac{\theta}{s}\right)^2 \tag{3.1}$$

where κ_b is the bending rigidity constant.

By taking the thermal average over the angle, we calculate the mean square bending angle

$$\langle \theta^2 \rangle = 2 \frac{\int exp(-\Delta U/k_B T)\theta^2 d\theta}{\int exp(-\Delta U/k_B T) d\theta} = 2 \frac{s}{\kappa_b} k_B T \tag{3.2}$$

Similarly, we take the average of the cosine of the angle, $\langle cos\,\theta(s) \rangle$, between the tangent vectors along the polymer backbone separated by a distance *s* (Fig.3.1c). We define $\langle cos\,\theta(s) \rangle$ as the directional correlation of the worm-

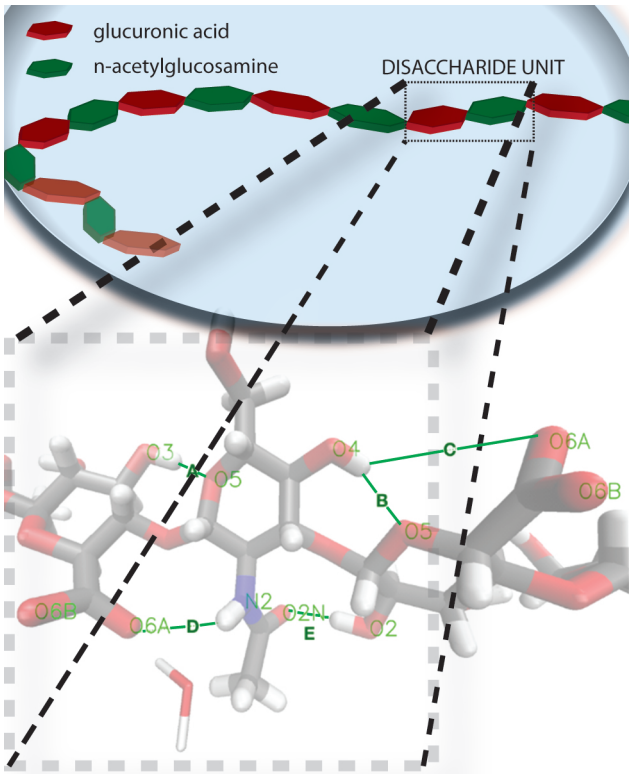

Figure 3.1: Schematic illustration of hyaluronic acid, a linear polysaccharide composed of D-glucuronic acid and N-acetyl-D-glucosamine. Green lines indicate the formation of intra-molecular hydrogen-bonds (listed by using letters A-E). Oxygen and nitrogen atoms involved in the formation of the intra-molecular hydrogen bonds are also indexed.

Figure 3.2: Schematic illustrations of an ideal chain a) and of a worm-like chain b). In c) a segment of length s and curvature θ. Adapted from *Introduction to Biopolymer Physics* by Johan R.C. Van der Maarel.[52]

like chain. We write that

$$\langle cos\,\theta(s)\rangle = exp\left(-\frac{|s|}{L_p}\right) \tag{3.3}$$

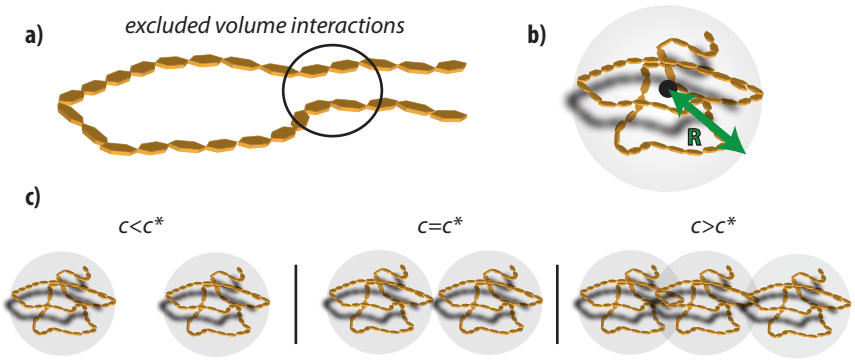

Figure 3.3: a) Illustration of excluded volume interactions between two chain segments, which are distant along the contour length but nevertheless close in space. b) Typical radius R of a coil-like polymer. c) Schematic representation of dilute and semi-dilute regime. In the dilute regime, the concentration is low enough such that polymers are spaced by distances larger than R. In the semi-dilute regime, the concentration is such that polymers start to interpenetrate. Adapted from *Introduction to Biopolymer Physics* by Johan R.C. Van der Maarel.[52]

where L_p is the persistence length, which indicates the length scale over which the orientational correlation of tangent vectors along the chain is lost. To relate the persistence length to the bending rigidity, we take a filament $s << L_p$, and we expand eq.3.3 up to the second order. We obtain that

$$\langle \theta^2 \rangle = 2\frac{s}{L_p} \tag{3.4}$$

By using eq.3.2, we obtain the following relation between the bending rigidity and the persistence length

$$L_p = \frac{\kappa_b}{k_B T} \tag{3.5}$$

In this view, the persistence length depends on the thermal energy required to bend the chain. We identify polymers as flexible if L_p is much smaller than the contour length L_c, as semi-flexible if $L_p/L_c \sim 1$, and as rigid if $L_p >> L_c$.

So far, we have only considered interactions between neighbouring segments. We did not consider the interactions between segments that are at larger distance than the persistence length, but in close proximity. In Fig.3.3a we present an illustration of a long-range interaction between two segments in the same chain. Between these two segments a repulsive force acts, since the first segment cannot occupy the space of the second segment. This concept is commonly referred to as *excluded volume*. We now consider a polymer with a typical size determined by the coil radius *R*. Let c be the concentration of the monomer. The average concentration inside the coil domain is thus

$$\langle c \rangle \simeq \frac{N}{R^3} \tag{3.6}$$

The repulsive forces are proportional to c^2. By applying a mean field approach, i.e. by neglecting fluctuations and correlations between monomers, we can write that

$$\langle c^2 \rangle = \langle c \rangle^2 \simeq \frac{N^2}{R^6} \tag{3.7}$$

The repulsive free energy per unit of volume is thus

$$F_{rep} \simeq \frac{1}{2} k_B T B \langle c^2 \rangle \tag{3.8}$$

where *B* is an excluded volume parameter with the dimension of a volume, and $\frac{1}{2}k_BT$ is the typical repulsive energy between a pair of segments. By using eq.3.7, after integration of the repulsive free energy over the chain volume R^3, we can express the repulsive force as a function of *R* as:

$$F_{rep}(R) \simeq \frac{1}{2} k_B T B \frac{N^2}{R^3} \tag{3.9}$$

The effect of this repulsive force is to swell the chain since a larger *R* means a lower energy. However, increasing *R* causes further restrictions in the configurational degrees of freedom, and thus the repulsive force is counterbalanced by entropy. In the case of an ideal chain, where the monomers do not interact, and thus the configurational energy is simply given by entropic contributions, we can write that

$$F_{elast}(R) \simeq k_B T \frac{R^2}{N l^2} \tag{3.10}$$

and we find the *R* (which is defined as Flory Radius R_F) for which the total energy ($F_{elast} + F_{rep}$) is minimized,

$$R_F \simeq \left(\frac{B}{l^3}\right)^{1/5} l N^{3/5} \tag{3.11}$$

The expression 3.11 is valid for an ideal chain, where excluded volume forces are only counterbalanced by entropic forces. A more general expression, which takes into account the solvent properties, for the typical radius R of the coil is given by

$$R \simeq l N^{\nu} \tag{3.12}$$

where ν depends on the solvent conditions. In a good solvent, the interactions between the polymer and the solvent are favorable, and thus the excluded volume forces are only counterbalanced by the entropic loss. In this case, ν takes the Flory value $3/5$.[53] In a bad solvent, the interactions between the polymer and the solvent are not favorable, and thus the polymer tends to contract: ν is, in this case, $1/3$.[52]

We have so far introduced the concept of rigidity of a single isolated chain, and seen that the typical size *R* of a polymer depends on the number of monomers. We now instead consider a solution of polymers in a good solvent. If the concentration is low enough such that the average coil distance exceeds the Flory radius R_F, so that the swollen chains do not interpenetrate, the solution is defined as dilute. Upon increasing the concentration of polymer, we reach a certain concentration c^* for which the average inter-coil distance approaches R_F, $(\frac{N}{c^*})^{\frac{1}{3}} \simeq R_F$. This concentration c^* is called the *overlap concentration*, and by using eq.3.12 for a good solvent, we find that $c^* \simeq N^{-4/5} l^{-3}$ (Fig.3.3c).[52] Above c^* the chains will start to interpenetrate, reaching the *semi-dilute* regime.[52]In Fig.3.4 we show the dependence of the polymer radius R and c^* on N by taking $l = 1$. We observe that the overlap concentration drastically decreases with increasing N. Solutions of polymers having a similar persistence length but different molecular weight will therefore exhibit quite different macroscopic behavior.

By further increasing the concentration, the chains start to be entangled,

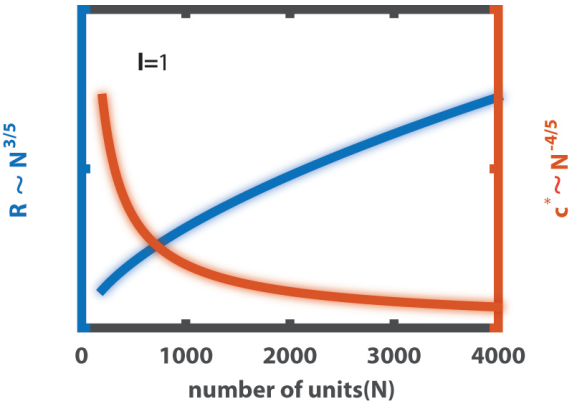

Figure 3.4: Dependence of the typical size R and of c^* on the numbers of monomers. We have here set the step length l (persistence length) to 1.

i.e. topological constraints are formed among the chains. This regime is called the semi-dilute *entangled* regime, and it is reached when the polymer concentration is:[52]

$$c > n^{8/5} c^* \simeq c_e \tag{3.13}$$

where n is the number of overlapping chains, which ranges between 3 and 10. Chain-entanglement has a strong effect on the dynamics of the polymers, as we will see in Chapter 10.

Static properties of polyelectrolyte in the presence of salt

Polyelectrolytes are polymers that carry ionizable charges. In case the charges are either positive or negative, the polyelectrolytes are defined as *homogeneous*, while in case both negative and positive charges are present, the polyelectrolytes are instead defined as *polyampholyte*. Since polyelectrolytes are charged, the above described parameters (persistence length, radius, and overlap concentration) must be adjusted to take into account the electrostatic forces existing among the chain segments and among the chains. We will start now by describing the polymer' properties in the presence of salt, where the dissociated ions are mobile and not condensed on the chain. This is the case when the distance between the charges is less than the Bjerrum length, l_B, which is the distance over which two elemen-

tary charges have an electrostatic energy comparable to k_BT. In aqueous solutions at room temperature, the Bjerrum length is 0.71 nm. In case the distance between the charges is less than l_B, ions can condense on the charged groups on the polymer to reduce the charge density along the chain. This phenomenon is referred to as Manning condensation.[54]

In our previous description of the persistence length, we have considered just correlations among sequential segments and excluded volume interactions. In case of homogeneous polyelectrolytes, we need to consider the electrostatic repulsion forces that act among the neighboring segments as well as among the segments that lie far apart along the chain but are nevertheless spatially close. Hence, the elastic energy must contain a second term,

$$\Delta U = \Delta U_0 + \Delta U_e \tag{3.14}$$

where $\Delta U_e = \frac{1}{2} k_B T L_p^e \frac{\theta^2}{s}$. The total bending energy can be then considered as the sum of the bare and electrostatic contributions, and the total persistence length the sum of the bare persistence length L_p^0 and of the electrostatic persistence length L_p^e. Clearly, repulsive electrostatic forces result in an increase of the persistence length. We treat the electrostatic interactions in the Debye-Hückel approximation, where dissociated charges interact simply through Coulomb potential, and no interactions with the solvent are considered. By taking an elastic filament with charge density $\rho = \nu_{eff} e$, where ν_{eff} represents the effective number of charges per unit length, and e the elementary charge, we find the following expression for L_p^e (also referred to as Odijk-Snolnick-Fixman expression):[52]

$$L_p^e = \frac{\nu_{eff}^2 l_B}{4\kappa^2} \tag{3.15}$$

where κ^{-1} is the Debye screening length, which is defined as $\kappa^2 = 8\pi\rho_s l_B$, where ρ_s represents the salt concentration. The electrostatic persistence length thus decreases as ρ_s^{-1} and increases with the square of the number of effective charges per unit length. By increasing the salt concentration, we thus expect that the persistence length decreases, and thus the chain flexibility increases (Fig.3.5).

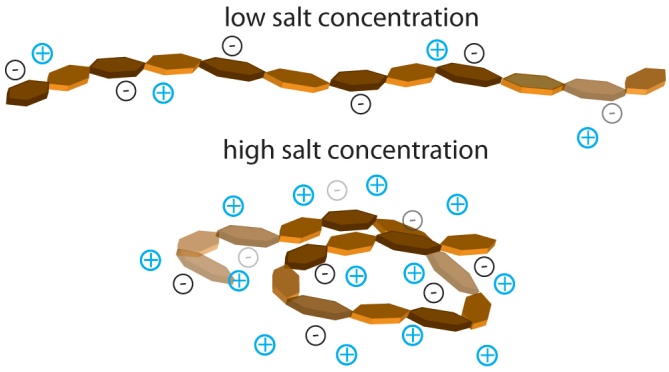

Figure 3.5: Schematic illustration of the conformation of a homogeneous polyelectrolyte in presence of low salt and high salt concentration. Black circles identify the negative charged groups of the polymers, while the light blue circles indicate the free positive cations.

3.2 Dynamic and Transport Properties

We now discuss some dynamic properties of biopolymers with a particular attention to transport properties such as viscosity. We consider polymers in a dilute solution so the polymer chains can be considered independent. Let R be the typical size of the polymer, which fluctuates due to thermal motion. Because of thermal energy, the value of R fluctuates in time with a certain relaxation time τ. At every time, the polymer will experience an elastic restoring force (f_{el}), and an hydrodynamic friction force f_{fr}. We write that

$$f_{el} = KR \tag{3.16}$$

where K is an elastic constant which depends on the solvent condition, and

$$f_{fr} = \zeta \frac{\partial R}{\partial t} \tag{3.17}$$

where ζ is the friction coefficient.
In a steady state, the sum of the elastic and friction forces must be equal to 0,

$$\zeta \frac{\partial R}{\partial t} + KR = 0 \tag{3.18}$$

and by integrating over R, we find that $\tau = \frac{\zeta}{K}$, which we refer to as global relaxation time. We now want to directly relate the dynamic properties of

Figure 3.6: Example of a viscoelastic solution of hyaluronic acid (M_w=1 MDa) dissolved at a concentration of 20 mg/ml in water at physiological salt conditions. The elastic state of hyaluronan (right) is reached by decreasing the pH from neutral to 2.5. By further decreasing the pH to 2, a liquid state is retrieved (left).

the polymer to τ. We first assume that the polymer chains are not freely drained, i.e. the solvent molecules cannot freely flow through the coil, but they are carried with the coil movement. Polymer dynamics under this condition is referred to as the *Zimm condition*. We write ζ by using the Stokes' law,

$$\zeta = 6\pi\eta_s R \tag{3.19}$$

where η_s represent the solvent viscosity and R is the characteristic size of the coil. As aforementioned, the elastic constant K depends on the solvent conditions. In case of a good solvent where the chain is swollen, $K^{-1} = R_F^2/k_BT$. In the Zimm condition, the global relaxation time thus takes the following form

$$\tau \simeq R_F^3\eta_s/k_BT \tag{3.20}$$

As expected, the relaxation time of a polymer chain in a good solvent is proportional to the size of the coil and to the solvent viscosity. By considering Brownian motion of the polymer, we can now use the global relaxation time to derive the self-diffusion coefficient, D. We assume that in the time τ, the polymer diffuses over a distance on the order of R, and we thus find

that: $D \simeq \frac{R^2}{\tau}$. Using eq.3.20 we find that

$$D \simeq \frac{k_B T}{R_F \eta_s} \tag{3.21}$$

In the case the solvent molecules are not carried by the coil movement (*Rouse* model), the elastic constant K assumes the following form:

$$K^{-1} \simeq \frac{N l^2}{k_B T} \tag{3.22}$$

By using $\zeta = \zeta_l N$, where ζ_l is the friction coefficient per link ($\zeta_l = 6\pi\eta_s l$), we find that the relaxation time in the Rouse model takes the form $\tau = \frac{N^2 l^3 \eta_s}{k_B T}$, and so the self-diffusion coefficient becomes:

$$D \simeq \frac{k_B T}{N l \eta_s} \tag{3.23}$$

A second transport property, which will be essential in this thesis, is the viscosity of the polymer solution. In order to calculate the viscosity we use the Einstein' equation, which describes the specific viscosity of a suspension of colloidal spheres with a volume fraction ϕ.

$$\frac{\eta - \eta_s}{\eta_s} = \frac{\Delta\eta}{\eta_s} = 2.5\phi \tag{3.24}$$

In the Zimm condition, $\phi = cR^3/N$, and, assuming a good solvent, we can thus write that the viscosity increment $\Delta\eta$ takes the form

$$\Delta\eta \simeq \frac{c}{N} k_B T \tau \tag{3.25}$$

The viscosity increment is directly proportional to the polymer concentration and the relaxation time.

Part I

Molecular Structure of -COOH group in formic acid and in peptides

Published as:

Giulia Giubertoni, Oleksandr O. Sofronov and Huib J. Bakker, Observation of Distinct Carboxylic acid Conformers in Aqueous Solution, *The Journal of Physical Chemistry Letters, 2019*

4

Observation of Distinct Carboxylic acid Conformers in Aqueous Solution

Abstract

We investigate the molecular geometry of the carboxyl group of formic acid in acetonitrile and aqueous solutions at room temperature with two-dimensional infrared spectroscopy (2DIR). We found that the carboxyl group adopts two distinct configurations: a configuration in which the carbonyl group is oriented anti-parallel to the hydroxyl (anti-conformer), and a configuration in which the carbonyl group is oriented at an angle of $\sim 60^{\circ}$ with respect to the hydroxyl (syn-conformer). These results constitute the first experimental evidence that carboxyl groups exist as two distinct and long-living conformational isomers in aqueous solution at room temperature.

4.1 Introduction

The chemical impact of conformational isomerism has been recognized for a long time.[55–60] The conformation change of a relatively small molecular group can have a large impact on the macromolecular structure. For example, the cis/trans-isomerization of the amino-acid proline can have a strong effect on the conformation of proteins.[7,61–64] Carboxyl groups play an important role in this respect, as they form strong inter- and intramolecular hydrogen bonds that govern and stabilize macromolecular structures.[65,66] As a consequence, the conformational isomerism of carboxylic acids has been intensely studied with different molecular simulations techniques.[67–70] These studies predicted the existence of distinct conformational isomers of the carboxylic acid group, both in the gas phase and in aqueous solution.

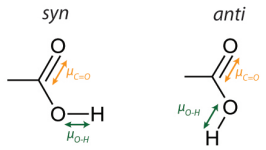

Figure 4.1: Schematic picture of syn- and anti-conformers. Orange and green arrows indicate the transition dipole moment of the carbonyl and hydroxyl vibrations,respectively.

Up to now, distinct carboxyl group conformers have only been experimentally observed in rare-gas matrices under cryogenic conditions.[71–73] The carboxylic acid group adopts two distinct planar geometries in rare gas matrices at low temperatures, as illustrated in Fig.4.1.[71,72,74,75] In the syn-conformer, the O-H group is oriented at $\sim 60^{\circ}$ with respect to the C=O, while in the anti-conformer the O-H is anti-parallel to the C=O. The anti-conformer is less stable than the syn-conformer, with the result that the chemical reactivity depends on the conformation.[76] Molecular dynamics simulations showed that the equilibrium concentration of the high energy anti-conformer is negligible in the gas phase at room temperature, but that this conformer stabilizes upon hydration.[69,70,77] In a rare-gas matrix at extremely low temperatures, the anti- and syn- configurations were identified with linear infrared spectroscopy, which was enabled by the fact that the carbonyl and hydroxyl

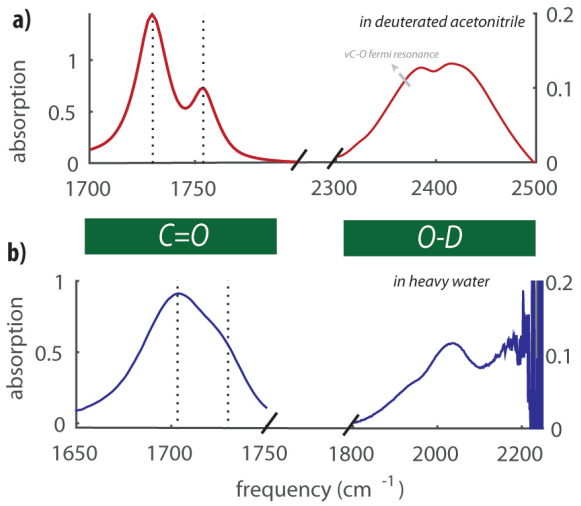

Figure 4.2: a) Linear infrared absorption spectrum of a 0.5 M solution of formic acid in deuterated acetonitrile. The spectrum shows two distinct narrow bands at 1730 cm^{-1} and 1754 cm^{-1}, and a broad band around 2430 cm^{-1} with a shoulder at 2380 cm^{-1}. b) Linear infrared absorption spectrum of a 0.3 M solution of formic acid in D_2O. The spectrum shows a C=O stretch band around 1700 cm^{-1} with a shoulder at 1724 cm^{-1}, and a band at 2030 cm^{-1} that is part of the broad and structured absorption spectrum of the O-D stretch vibration of formic acid. The solvent background absorption is subtracted in both cases.

stretch vibrations of the carboxyl group have narrow absorption lines in these conditions. In room-temperature solutions, in particular in water, the carbonyl and hydroxyl stretch vibrations are strongly affected by the interactions with the surrounding solvent molecules, leading to a strong broadening of the absorption bands. In addition, at acid concentrations above ~3 M, the vibrations will also be affected by dimer formation.[78–80] These effects preclude the study of conformational isomerism of carboxylic acids in aqueous media at room temperature with conventional linear infrared spectroscopy.

Here we use two-dimensional infrared (2DIR) spectroscopy to study the conformations of carboxyl group of formic acid molecules in room temperature solutions. We study the coupling between the carbonyl (C=O) and hydroxyl (O-D) stretch vibrations for deuterated formic acid dissolved in different solvents, including water. We found that the measurement of this

coupling reveals the relative orientation of the carbonyl and the hydroxyl groups, and thus forms a unique experimental test of the existence of conformational isomerism of carboxylic acids under bio-relevant conditions.

4.2 Results and Discussion

In Fig.4.2a and Fig.4.2b we show the linear infrared spectra of formic acid dissolved in deuterated acetonitrile and heavy water (0.5 and 0.3 M, respectively) in the frequency regions of the C=O ($\sim$1750 cm^{-1}) and the O-D ($\sim$2430 cm^{-1}) stretching vibrations. Acetonitrile is a weakly polar and aprotic solvent, and the measured response of formic acid in this solvent may be similar to that in an inert gas matrix, which was used in previous experiments.[71,74,75] Comparison of the response of formic acid in acetonitrile with the response in (heavy) water will reveal the effect of hydration on the carbonyl and hydroxyl stretch vibrations, and on the potential presence and relative abundance of different conformers. For formic acid in acetonitrile the absorption spectrum shows two distinct bands at 1730 cm^{-1} and 1754 cm^{-1}. The similarity of this spectrum with that of a more dilute solution (see Appendix Sec.4.4.1 and Fig.4.7a) indicates that the bands are unlikely to be the result of dimer formation. In the O-D stretch region we observe a broad band around 2430 cm^{-1} with an additional peak at 2380 cm^{-1}. The latter can be assigned to a Fermi resonance of the O-D stretch vibration with the overtone of the C-O stretch vibration.[72,74,81] For formic acid in water (Fig.4.2b), we observe a broad band for the carbonyl vibration around 1700 cm^{-1} with a shoulder around 1724 cm^{-1}. The absorption of the O-D vibrations is redshifted in heavy water[82] compared to acetonitrile solution. The band is broad and shows different subbands. Because of the strong absorption of the O-D stretch vibrations of D_2O, we cannot resolve the full O-D stretch spectrum of formic acid. However, the spectrum shows a distinct band at 2050 cm^{-1} corresponding to the O-D stretch vibration. The full O-D stretch absorption spectrum of formic acid can be seen in dimethyl sulfoxide (DMSO) solution (see Appendix Sec.4.4.1 and Fig.4.7c). The observed spectrum is broad (1900-2300 cm^{-1}) and has multiple peaks due to combined excitations of the O-D stretch vibration and the O-D...O

hydrogen bond. Since DMSO and water are hydrogen-bond acceptors of similar strength, the part of the formic O-D stretch absorption that we can observe in D_2O corresponds to the low-frequency part of the formic O-D stretch absorption spectrum observed in DMSO.

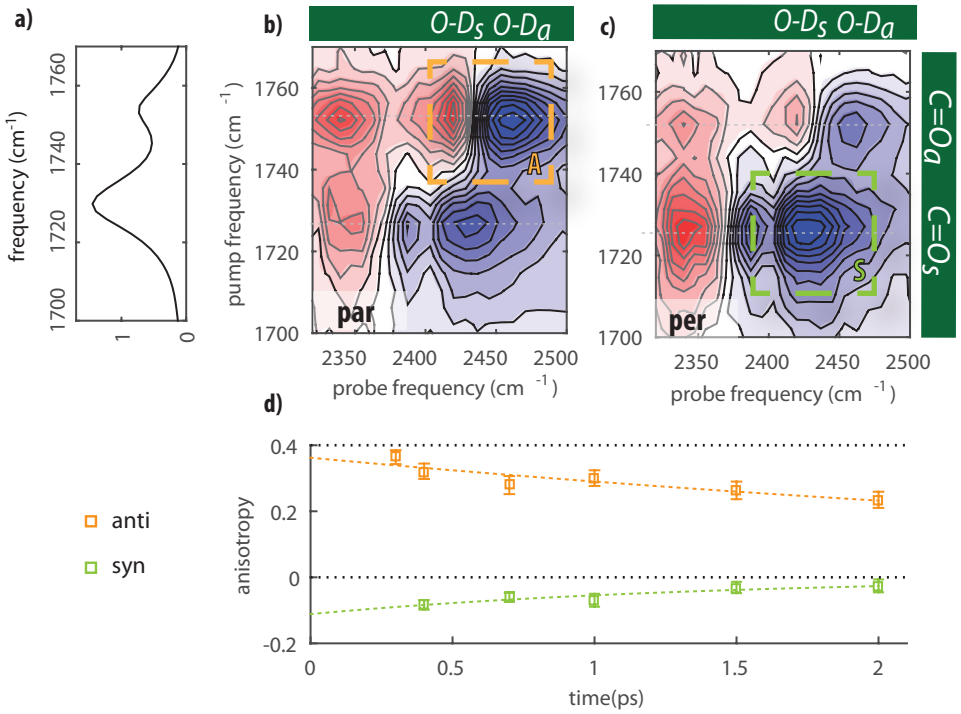

Figure 4.3: a) Linear spectrum of a 0.5 M solution of formic acid in deuterated acetonitrile in the region of the carbonyl stretch vibration. b) and c) 2DIR spectra at T_w=1 ps of the same solution when exciting the carbonyl stretching modes and probing the O-D stretching modes in parallel and perpendicular polarization configuration, respectively. d) Anisotropy of the A (anti) and S (syn) cross-peaks as a function of delay time between the excitation and detection pulses. The dashed lines are single exponential fits.

We study the vibrational response of the carbonyl and hydroxyl stretch vibrations and their coupling with 2DIR spectroscopy. The details of our 2DIR setup are reported in Chapter Section 2.5.[83] In brief, we excite the carbonyl stretching vibrations with a strong femtosecond infrared pulse pair (~100 fs,

5 μJ per pulse). This excitation induces transient absorption changes that are probed with a weaker (0.7 μJ) single femtosecond probing pulse that is delayed by a time T_w. In all experiments the excitation pulses are centred at 1720 cm^{-1} with a bandwidth of 200 cm^{-1}, in resonance with the carbonyl vibrations. The probe pulse is centred at 2450 cm^{-1} to measure the response of the O-D stretch vibrations in deuterated acenotrile, and at 2050 cm^{-1} to measure the response of the O-D stretch vibrations in heavy water solutions. The 2DIR signal is recorded simultaneously with the probe in parallel and perpendicular polarizations with respect to the pump, which allows us to extract information on the relative orientation of the excited C=O vibration and the probed O-D vibration. In Fig.4.3b and Fig.4.3c we show 2DIR spectra of formic acid in acetonitrile. The blue colored regions correspond to negative transient absorption changes (bleaching) and the red colored regions to positive transient absorption changes. The spectra contain several cross-peak signals corresponding to frequency shifts of the O-D stretch vibration that are induced by the excitation of the carbonyl vibration. In both the parallel and the perpendicular 2DIR spectra, we observe cross-peak bleachings at 2380, 2423, and 2463 cm^{-1}. We observe additional structure in the 2DIR spectrum at probe frequencies below 2400 cm^{-1}, namely a decreased absorption near 2380 cm^{-1}, and an enhanced absorption at 2340 cm^{-1}. These signals result from the frequency shift and/or bleaching of the aforementioned Fermi resonance of the O-D stretch vibration and the overtone of the C-O vibration, following the excitation of the carbonyl vibrations. The 2423 cm^{-1} and the 2463 cm^{-1} represent O-D stretching modes. It is clearly seen that the low-frequency carbonyl vibration at 1754 cm^{-1} shows a more intense cross-peak (which we denote as A) with the 2463 cm^{-1} O-D stretch mode in parallel polarization (Fig.4.3b). Similarly, the low frequency carbonyl vibration at 1730 cm^{-1} shows a more intense cross-peak (which we denote as S) with the 2423 cm^{-1} O-D stretch mode in perpendicular polarization (Fig.4.3c). To better illustrate the polarization dependence of the signals, we plot the anisotropy of the two cross-peaks as a function of the time delay between the excitation and probing pulses. Fig.4d shows that at all time delays between 0.3 and 2 ps the anisotropy

of the S-cross-peak is negative, indicating that the C=O at 1725 cm^{-1} is oriented at a large angle with respect to the O-D stretch vibration at 2423 cm^{-1}. The A-cross-peak shows a positive anisotropy, indicating that the C=O vibration at 1754 cm^{-1} is oriented almost parallel to the O-D stretching vibrating at 2463 cm^{-1}. The relative orientations indicate that there are two distinct species of formic acid in deuterated acetonitrile solution, with different relative orientations of the carbonyl and the O-D stretch modes. The anisotropy signals of Fig. 4.3d decay, probably as a result of the reorientation of the formic acid molecule. To extract the angle between the carbonyl and hydroxyl groups, we fit the anisotropy decays (Fig.4.3d) with a single exponential decay function. By extrapolating the fit to time delay zero, we determine the initial anisotropy R_0, from which we calculate the angle with the following expression: $\theta = \arccos(\sqrt{\frac{5R+1}{3}})$. The two angles extracted from the anisotropy values (15$\pm$5° and 65$\pm$10 $^\circ$) match well with the molecular geometries of the anti and syn configurations, respectively (Fig.4.1). Thereby these results demonstrate that formic acid exists in distinct anti and syn configurations in room temperature solution. The extracted angles are affected by the fast inertial (librational) motion of O-D bond,[84] which explains why the extracted angle for the anti-conformer is somewhat larger than expected (15° vs 0°).

We find that the syn-conformation of formic acid in deuterated acetonitrile has a low-frequency carbonyl vibration and a low frequency hydroxyl vibration, while the anti-conformation has high-frequency carbonyl and high-frequency hydroxyl vibrations. This finding agrees with the properties of formic acid in a low-temperature rare-gas matrix.[73] By comparing the linear infrared and 2DIR spectra (see Appendix Sec.4.4.2 and Fig.4.8), we find that the anti species accounts for 30%$\pm$5% of the total amount of carboxyl groups present in solution. The absence of a cross-peak signal between the different hydroxyl vibrations, which would indicate the transformation from syn to anti or viceversa, shows that the two species do not exchange within the lifetime of the vibrationally excited state ($\sim$6-8 ps). This finding is supported by the results of an experiment in which we excite and probe the carbonyl vibrations, and in which we also do not observe a cross-peak

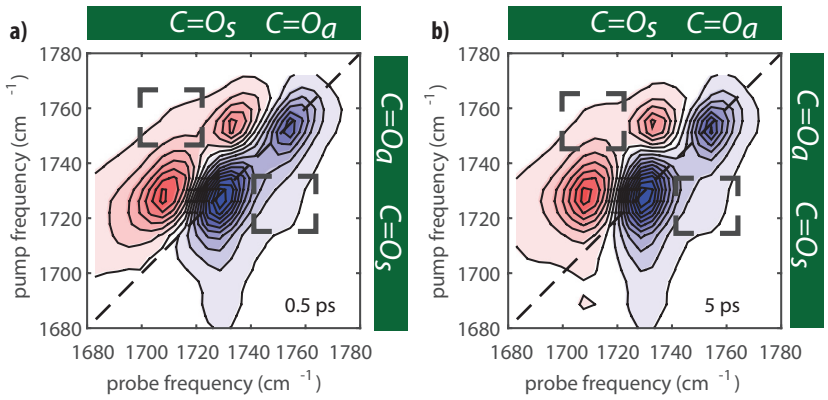

Figure 4.4: a) and b) isotropic degenerate 2DIR spectra of formic acid in deuterated acetonitrile at 0.5 and 5 ps, respectively. The dashed squares indicate the upward and downward cross-peak regions, where we do not observe any ingrowing spectral signatures.

signal of the two carbonyl vibrations (Fig. 4.4). This outcome agrees with the results of molecular dynamics simulations that showed the presence of a large energy barrier ($\sim$11 kcal/mol)[73,77] between the two species.

In Fig.4.5b-4.5c we show 2DIR spectra of formic acid in heavy water solution in the cross-peak region where the carbonyl stretching modes are excited and the O-D stretch modes around 2050 cm^{-1} are detected in a parallel and perpendicular polarization configuration with respect to the pump. The spectral features are much broader and not as distinct as in acetonitrile solution. However, we observe again that the cross-peak of the high-frequency shoulder of the carbonyl at 1724 cm^{-1} is stronger in parallel polarization (Fig.4.5b), while the cross-peak of the low-frequency carbonyl at 1694 cm^{-1} is stronger in perpendicular polarization (Fig.4.5c).

An interesting observation is that the high-frequency carbonyl vibration now has a cross-peak with a lower frequency O-D vibration while the low-frequency carbonyl vibration has a cross-peak with a higher frequency O-D vibration. In Fig.4.5d we plot the anisotropy of the A and S cross-peaks in water, and we observe that the A cross-peak corresponds to a positive anisotropy value while the S cross-peak corresponds to a negative anisotropy. We thus find strong evidence of the existence of two molecular geometries

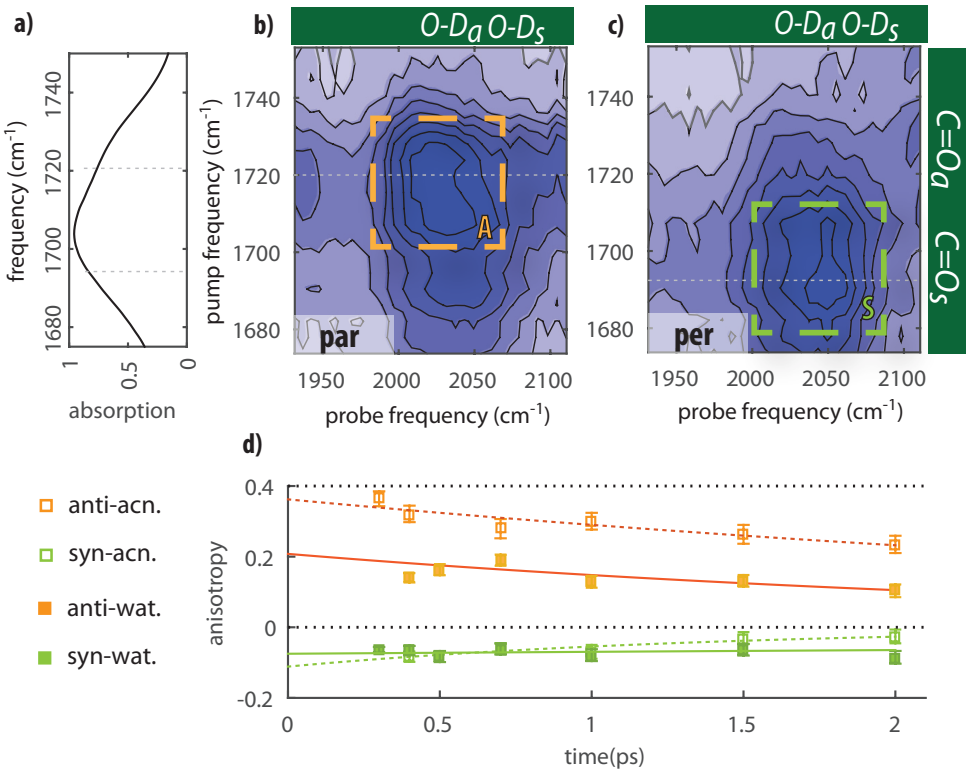

Figure 4.5: a) Linear spectrum of a 0.3 M solution of formic acid in D_2O in the region of the carbonyl stretch vibration. b) and c) 2DIR spectra at T_w=1 ps of the same solution when exciting the carbonyl stretching modes and probing the O-D stretching modes in parallel and perpendicular polarization configuration, respectively. d) Anisotropy of the A and S cross-peaks as a function of delay time between the excitation and detection pulses. For comparison for formic acid in acetonitrile also the results of Fig. 4.3d are shown. Dashed and continuous lines are single exponential fits.

of formic acid in aqueous solution: a configuration in which the carbonyl makes a small angle with the O-D vibration (A cross-peak and anti configuration), and a configuration where the carbonyl vibration makes a large angle with the O-D vibration (S cross peak and syn configuration). An interesting question is why the 1724 cm^{-1} carbonyl vibration shows a cross-peak with a lower frequency O-D stretch vibration, and the 1694 cm^{-1} carbonyl

vibration with a higher frequency O-D stretch vibration. This finding clearly deviates from what was observed for formic acid in acetonitrile (Fig.4.3) and in a rare-gas matrix at low temperature.[73] This observation can be explained from the difference in the strength of the hydrogen bonds between the O-D group of formic acid and the surrounding water molecules in the two configurations. In the anti configuration these hydrogen bonds are stronger than in the syn configuration. As a result, the O-D vibration undergoes a stronger red-shift in the anti configuration than in the syn configuration, which overcompensates the intrinsically higher frequency of the O-D stretch in the anti configuration that was observed for formic acid in deuterated acetonitrile and in a rare gas matrix. A similar reversal of the O-D stretch vibrational frequency is observed for a solution of formic acid in DMSO (which is a similarly strong hydrogen bond acceptor as water), as shown in Appendix Sec.4.4.3 and Fig.4.9. This explanation is also supported by molecular dynamics simulations of acetic acid hydrates, which show that the anti-conformer is more strongly hydrated than the syn-conformer.[77] In Fig. 4.5d we compare the anisotropy values obtained for formic acid in heavy water with the results obtained for formic acid in deuterated acetonitrile. We observe that the negative anisotropy of the S cross-peak does not show a significant change by changing the solvent while the positive anistropy of the A cross-peak is somewhat lower in heavy water than in deuterated acetonitrile. This difference likely results from the fact that the spectral features are much broader in heavy water than in deuterated acetonitrile. Hence, the signal observed in the region of the A cross-peak has some contribution of the stronger S cross-peak for which the anisotropy has a negative value. An additional effect may be that the stronger hydrogen bonding of the anti configuration to surrounding water molecules leads to a larger net deviation from a perfect parallel arrangement of the carbonyl and O-D groups. We estimate from the amplitudes of the cross peaks that $25\pm10\%$ of formic acid adopts an anti configuration in heavy water. Unfortunately, the precision of this estimation is low as a result of the strong broadening of the carbonyl absorption band. The analysis of the more narrow carbonyl spectrum of formic acid in DMSO yields a similar fraction for the anti configuration of

30±5%. It thus appears that the character of the solvent does not significantly change the concentration, and thus the relative stability of the two formic acid conformers. This result indicates that the stronger hydrogen bond donated by the formic acid O-D group in the anti configuration constitutes only a small contribution to the overall stabilization of this conformer, or that this contribution is compensated by counteracting solvation effects of the remainder parts of the molecule.

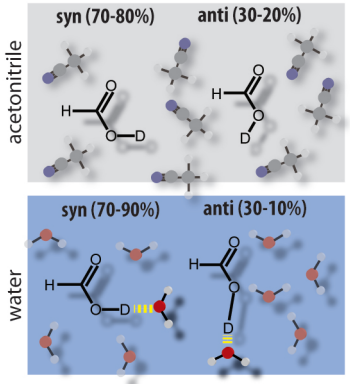

Figure 4.6: Illustration of the syn- and anti-conformers of formic acid in acetonitrile and in liquid water.

4.3 Conclusion

In summary, using femtosecond 2DIR spectroscopy we demonstrate that formic acid adopts two distinct, long-living conformations in deuterated acetonitrile and heavy water solutions, denoted as syn and anti (Fig.4.6). We observed that for formic acid in heavy water the frequency of the O-D stretch vibration is at a lower frequency in the anti configuration than in the syn configuration, which is opposite to what is observed for formic acid in deuterated acetonitrile. This difference indicates that the OD group of formic acid forms a stronger hydrogen bond to surrounding water molecules in the anti-conformer than in the syn-conformer. We observe that the fractions of anti-conformer syn-conformer are 20-30% and 80-70 %, respectively, both in deuterated acetonitrile and in heavy water solution. The observation of distinct conformers of the carboxylic acid and their slow exchange at room

temperature shows that these conformers are separated by high energy barriers. As a result, the presence of these conformers can have a large effect on the structure and dynamics of (bio)molecular systems.

4.4 Appendix

4.4.1 Assignment of absorption peaks to carbonyl and O-H/O-D vibrations

Solutions of formic acid in d-acetonitrile show two absorption peaks in the carbonyl vibrational region. The most intense is around 1730 cm^{-1}, while the second is at 1760 cm^{-1}. To discard the possibility that one of the peak is due to dimer formation, we measure the linear spectra of formic acid at 0.05 M and 0.5 M. Fig.4.7a shows the spectra normalized to the absorption of the 1730 cm^{-1} peak. We observe that the relative intensity between the two peaks does not change by increasing the concentration, strongly suggesting that these two peaks are associated to two structurally different monomers.

The spectrum of D_2O strongly absorbs between 2200 to 2600 cm^{-1}, partially overlapping with the vibrational region of the acid O-D modes around 2100 cm^{-1}. To corroborate the assignment of the absorption peaks at 2050 cm^{-1} to the O-D modes of the acid and not of the D_2O, we add different concentrations of NaOD to formic acid solutions. By gradually deprotonating the -COOD groups, we observe that the intensities of the absorption peaks at 2050 cm^{-1} decrease (Fig.4.7b). This indicates that the peaks observed at 2050 cm^{-1} are due to the absorption of the vibrational modes of the acid O-D. This assignment is corroborated by measuring the vibrational spectrum of formic acid in dimethyl sulfoxide. In Fig.4.7c we observe that the spectrum of HCOOD in dimethyl sulfoxide contains a broad structured band around 2100 cm^{-1}. In the case of HCOOH this broad band is shifted to higher frequency (2600 cm^{-1}), confirming that the broad band at 2100 cm^{-1} HCOOD is due to the absorption of the acid O-D modes.

4.4.2 Relative concentration of syn- and anti- conformers

The relative concentration of the conformers cannot be determined from the linear infrared spectrum, as the cross-sections of the carbonyl vibrations

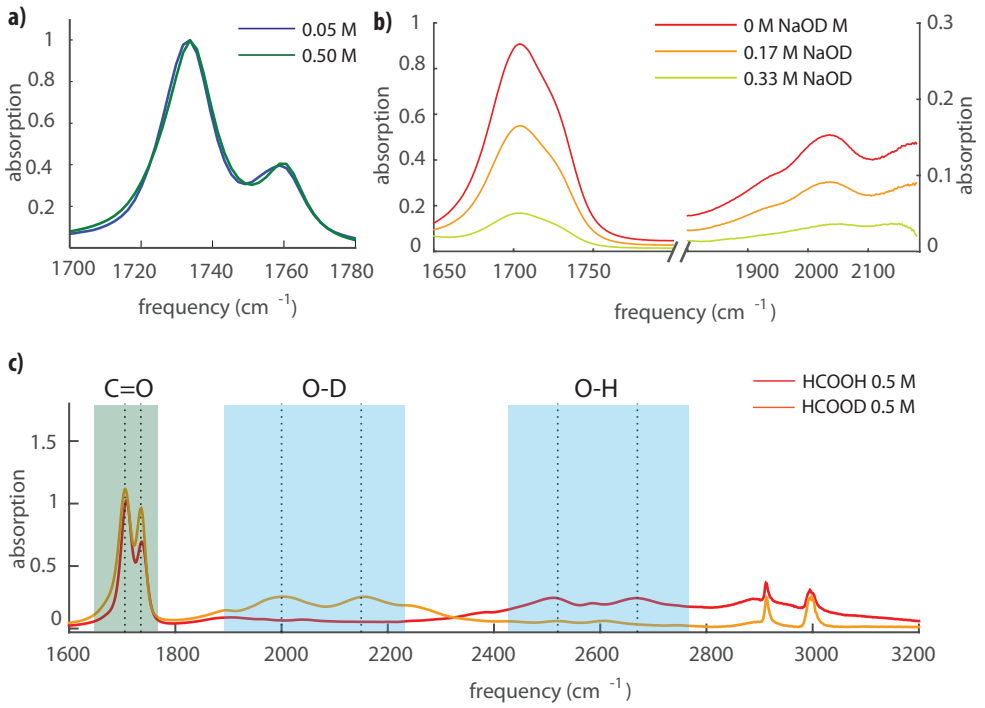

Figure 4.7: a) Scaled linear infrared spectra of 50 and 500 mM solution of formic acid in acetonitrile-d3. b) Linear infrared spectra of 0.5 M formic acid in heavy water with different amounts of added NaOD (D_2O background is subtracted). We observe a strong decrease in absorption at 2050 cm^{-1}, which supports the assignment of this band to the O-D stretch vibration of formic acid. c) Linear infrared spectra of 0.5 M solutions of deuterated and non-deuterated formic acid in DMSO (solvent background is subtracted). In both solutions the double-peak structure of the carbonyl band is clearly observed. The broad structured bands at 1900-2300 cm^{-1} and 2400-2800 cm^{-1} are assigned to O-D and O-H stretch vibrations of deuterated and non-deuterated formic acid, respectively.

of the two conformers are not known. However, we can make use of the fact that the linear infrared absorption spectrum scales as μ^2 (where μ is the vibrational transition dipole moment), while the 2DIR spectrum scales as μ^4, thus providing an additional relation between the measured signals, cross-sections and relative concentrations of the conformers. The linear IR spectrum and the diagonal 2DIR spectrum (pump frequency = probe

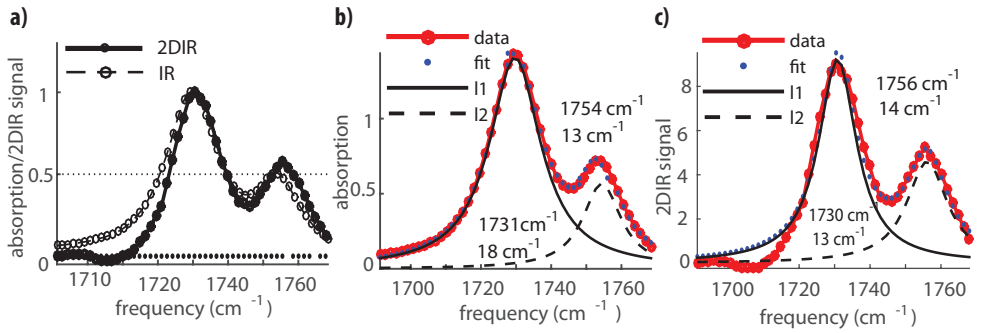

Figure 4.8: a) Linear infrared spectrum and a diagonal slice of the 2DIR spectrum of formic acid in acetonitrile-d3. The similar shapes of the spectra indicate that the carbonyl stretch vibration has a similar absorption cross section for the syn- and anti-conformers. b) and c) Decomposition of the linear infrared spectrum (b) and 2DIR diagonal slice (c) of formic acid in acetonitrile-d3 into two Lorentzian-shaped bands, corresponding to two formic acid conformers.

frequency) are shown together in Fig.4.8a.

The diagonal 2DIR spectrum (and in fact all presented 2DIR spectra) is normalized with respect to the pump spectrum. We observe a very similar ratio of the two bands in the linear IR spectrum and the diagonal 2DIR spectrum, which indicates that the two bands have similar cross-sections. To obtain the precise ratio between the cross-sections of the peaks, we fit the linear spectrum and the 2DIR slice with two Lorentzian-shaped bands (Fig.4.8b-c). We find that the ratio of the two cross-sections is close to 1. We then calculate the areas under the bands of the two carbonyl vibrations by fitting the linear spectrum. The ratio of these areas represents the fractions of the two conformers.

4.4.3 Syn- and anti- conformers in DMSO solution

Fig.4.9a-b show the parallel and perpendicular 2DIR spectra obtained by exciting the carbonyl modes at 1730 cm^{-1}, and probing the O-D vibrational modes around 2100 cm^{-1}. Similarly to formic acid in heavy water and in acetonitrile, we notice that in parallel polarization configuration the strongest cross-peak signal is observed when pumping the carbonyl vibration at 1730

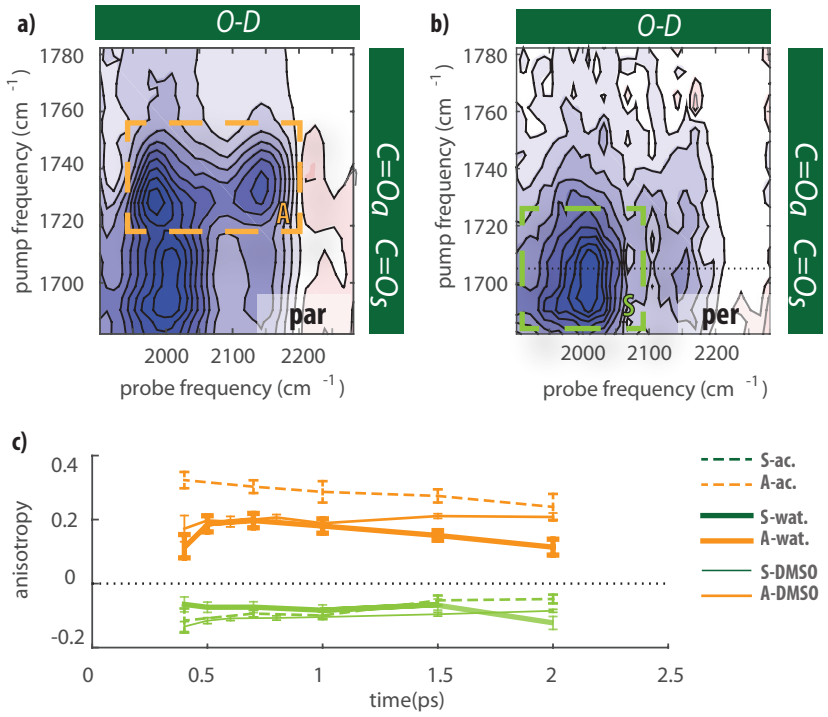

Figure 4.9: 2DIR spectra of 0.5 M of formic acid in DMSO obtained by excitation of the carbonyl stretch vibration and probing of the O-D stretch modes with a) parallel and b) perpendicular probe polarization; c) Comparison of the anisotropy values of the O-D/C=O cross-peaks of formic acid in acetonitrile-d3, heavy water, and DMSO solution.

cm^{-1}, while in perpendicular polarization configuration the strongest cross-peak signal is obtained when pumping at 1710 cm^{-1}. The dependence of the amplitude of the cross-peak signal on the probe polarization suggests that in DMSO two different species of formic acid are present. We find that the anisotropy of the cross-peak obtained by exciting at 1730 cm^{-1} is around 0.2, similar to the value that we observe when exciting the higher frequency carbonyl mode of formic acid dissolved we find in water. This anisotropy value corresponds to an angle between the transition dipole moments of the O-D and C=O vibrations of $\sim$35°. The anisotropy of the cross-peak at lower pump frequency is -0.1, corresponding to an angle of $\sim$70°.

Published as:

Oleksandr O. Sofronov, Giulia Giubertoni,A. Pérez de Alba Ortíz, B. Ensing, Huib J. Bakker, Peptide side-COOH groups have two distinct conformations under bio-relevant conditions , *The Journal of Physical Chemistry Letters, 2020*

5

Peptide side-COOH groups have two distinct conformations under bio-relevant conditions

Abstract

The carboxyl (COOH) side-chain groups of amino acids, such as aspartic acid, play an important role in biochemical processes, including enzymatic proton transport. In many theoretical studies it was found that the (bio)chemical reactivity of the carboxyl group strongly depends on the conformation of this group. Interestingly, up to now there has been no experimental investigation of the geometry and the stability of different COOH conformers under bio-relevant conditions. Here, we investigate the conformational isomerism of the sidechain COOH-group of N-acetyl aspartic acid amide using polarization-resolved two-dimensional infrared spectroscopy. We find that the carboxyl group shows two distinct near-planar conformers (syn and anti) when dissolved in water at room temperature. Both conformers are significantly populated in aqueous solution ($75\pm10\%$ and $25\pm10\%$ for syn and anti, respectively). Molecular dynamics simulations show that the anti-conformer interacts more strongly with water molecules than the syn-conformer, explaining why this conformer is present in significant amounts in aqueous solution.

5.1 Introduction

Carboxyl groups and carboxylate anions are widely present in proteins, both as part of the side chain of amino acids glutamic and aspartic acid, and as C-terminal groups. Under physiological conditions, the carboxyl groups are usually deprotonated, but in specific microenvironments they can still be found in protonated form.[85–88] The side-chain carboxyl groups of aspartic acid and glutamic acid residues are essential for enzymatic catalysis, protein folding,[9,10] proton conduction in protein nanochannels,[11,12] and gating of pH-sensing ion channels[89,90].

For simple carboxylic acids (formic, acetic and propionic acid) dissolved in rare-gas matrices under cryogenic conditions, the carboxyl group can adopt two distinct conformations with a planar structure.[71,91,92] In the so-called syn-conformer, the hydroxyl group is at an angle of $\sim 60^{\circ}$ with respect to the carbonyl group, while in the so-called anti-conformer the hydroxyl group is oriented anti-parallel to the carboxyl group. Recently, we showed for formic acid that distinct long-living syn and anti carboxyl conformers exist also in aqueous solutions at room temperature, with relative abundances of 70-80% and 20-30%, respectively(see Chapter 4).

The conformational isomerism of carboxyl groups in molecules that are more complex than propionic acid has not been studied yet.[93] The potential presence of the anti conformer is often neglected, especially in X-ray diffraction studies in which proton positions cannot be determined accurately. As a consequence, only 2% of the carboxyl groups found in the Cambridge Structural Database are depicted in an anti-conformation.[94] Nevertheless, the presence of side-chain COOH-groups of aspartic and glutamic acid residues in an anti-conformation is expected to play an important role in enzymatic reactions and polypeptide structure stabilization.[94–101]

Here we use polarization-resolved two-dimensional infrared (2DIR) spectroscopy and molecular dynamics simulations to study the conformational isomerism of the side-chain carboxyl group of N-acetylaspartic acid amide (Fig.5.1), as a model for the aspartic acid residue. In the 2DIR experiments we measure the response of the hydroxyl vibration upon the excitation of

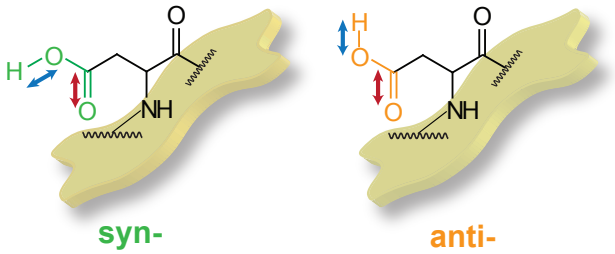

Figure 5.1: Syn and anti conformers of N-acetylaspartic acid amide. Red and blue arrows indicate the transition dipole moments of the carbonyl and of the hydroxyl vibrations, respectively.

the carbonyl vibration of the same carboxyl group. The polarization dependence of this signal provides unique information on the molecular geometry of the carboxyl group. We observe two distinct conformations of the carboxyl group with different orientations of the hydroxyl group with respect to the carbonyl group. We also determine the fractions of the two conformers in dimethyl sulfoxide (DMSO) solution and in aqueous solution. Finally, we use molecular dynamics simulations to explain the structures and relative abundances of the two conformers from their interactions with the solvent molecules.

5.2 Results and Discussion

First, we measure the 2DIR spectra of N-acetylaspartic acid amide in DMSO solution (0.4 M) by exciting the carbonyl stretch vibration and probing the hydroxyl stretch vibration (Fig.5.2a). The good solubility of this amino acid in DMSO and the absence of solvent absorption bands in the spectral regions of the carbonyl and hydroxyl groups allow for an accurate measurement of the 2DIR cross-peak signals of these two groups. The carbonyl vibration has an absorption band centered at 1720-1730 cm^{-1}. Upon excitation of this vibration, cross-peak signals appear at 2500-2800 cm^{-1} resulting from the excitation-induced frequency shift of the hydroxyl vibration (see Chapter 4).In the probed frequency region 2500-2800 cm^{-1} this shift results in a negative absorption change (colored in blue). The cross-peak signal has

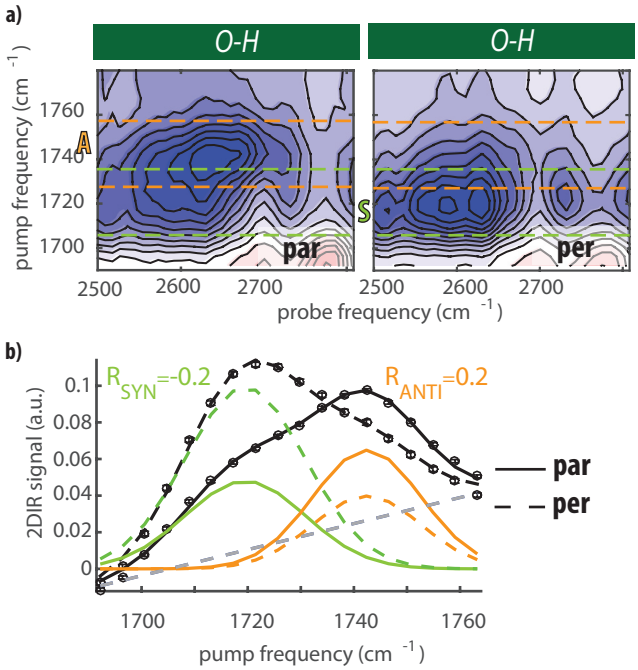

Figure 5.2: a) 2DIR spectra in the C=O/O-H cross-peak region measured in parallel and perpendicular polarization configuration at a time delay T_w=0.5 ps. The green and the orange bars highlight the responses of the syn- and anti-conformers, respectively. b) Parallel (solid) and perpendicular (dashed) transient absorption signals obtained by integrating the corresponding 2DIR signal over the probe frequency in the range between 2500 and 2750 cm^{-1}. The green and the orange colours indicate, respectively, the vibrational responses of the syn and anti conformers. The grey dashed line represents the correction for the isotropic background.

the form of a series of subbands, which is typical for OH-stretch vibrations of strongly hydrogen bonded systems, and results from the strong coupling of the OH-stretch vibration to the low-frequency vibrations of the hydrogen bonds.[102,103] These subbands are also observed in the linear infrared absorption spectrum of the hydroxyl vibration (see Appendix Sec.5.4.1 and Fig.5.7).

The amplitude of the cross-peak signal is observed to depend on the excitation frequency and the polarization configuration. Excitation of the low-frequency part of the carbonyl vibration ($\sim$1720 cm^{-1}) results in a stronger

hydroxyl cross-peak signal in perpendicular polarization, whereas excitation of the high frequency part of the carbonyl peak ($\sim$1745 cm^{-1}) yields a cross-peak signal that is more pronounced in parallel polarization.

In Fig.5.2b we show the 2DIR signals in parallel and perpendicular polarizations integrated over a probe frequency range of 2500-2750 cm^{-1} as a function of the carbonyl excitation frequency. We fit this integrated cross-peak signal with two Gaussian-shaped bands. For each band, we calculate the anisotropy $R = \frac{\Delta\alpha_{\mathsf{par}} - \Delta\alpha_{\mathsf{per}}}{\Delta\alpha_{\mathsf{par}} + 2\Delta\alpha_{\mathsf{per}}}$, where $\Delta\alpha_{\mathsf{par}}$ and $\Delta\alpha_{\mathsf{per}}$ are the transient absorption changes (cross-peak signals) measured in parallel and in perpendicular polarization configuration, respectively. The anisotropy represents the relative orientation of the hydroxyl transition dipole moment with respect to the carbonyl transition dipole moment, and can be used to calculate the angle between the carbonyl and the hydroxyl groups following $\theta = \arccos\sqrt{\frac{5R_0+1}{3}}$. We find that the cross-peak of the higher carbonyl vibration has a positive anisotropy of $\sim$0.2 (35°) and the lower carbonyl peak has a negative anisotropy of $\sim$-0.2 (90°). These anisotropy values clearly indicate that the two carboxyl group species comprise distinctly different relative orientations of the O-H group and C=O group. Based on these angles, we assign the cross-peak signal with positive anisotropy and a high frequency of the carbonyl vibration to the anti-conformer, and the cross-peak signal with a negative anisotropy and a low frequency of the carbonyl vibration to the syn-conformer. This result demonstrates that the carboxyl group shows distinct syn- and anti-conformers, not only for simple carboxylic acids, but also for more complex molecules like amino acids. We observe these distinct conformers also for the terminal carboxyl groups of other amino acids in DMSO solution (see Appendix Sec.5.4.2 and see Fig.5.8-5.9).

The obtained angles between the carbonyl and hydroxyl groups differ from the ideal values of 0° (for a perfect in-plane anti-parallel configuration) and 60° (for an in-plane syn configuration). Similar deviations have been observed for formic acid in DMSO solution (see Chapter 4). These deviations can be explained from the fact that the extracted anisotropy values can be affected by out-of-plane rotations of the O-H or C=O group.

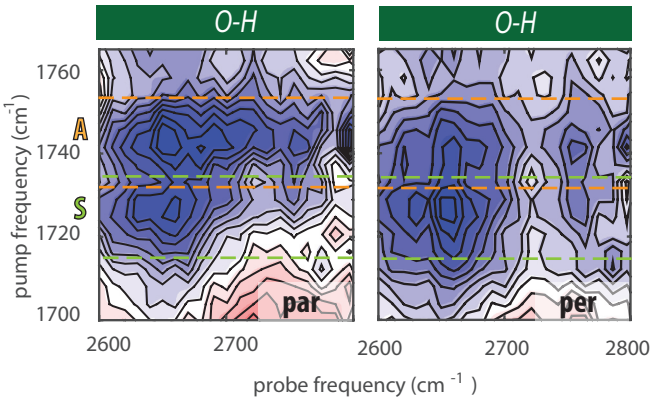

Figure 5.3: Cross-peak 2DIR spectra of N-acetylaspartic acid amide in aqueous solution. 2DIR spectra of N-acetyl aspartic acid amide in the C=O/O-H cross-peak region measured in perpendicular and parallel polarization configuration at T_w=0.3 ps. The green and the orange bars highlight the responses of the syn- and anti-conformers, respectively.

Such a rotational distortion can explain an increase of the ideal angle of the anti-configuration from 0° to 35°, and an increase of the ideal angle of the syn configuration from 60° to ∼90°. Indeed, analysis of the Cambrige Structural Database shows that the O-C-O-H dihedral angle can deviate by 10-30° from the ideal value for both the syn and anti conformers.[104] In addition, the anisotropy values may be affected by fast inertial (librational) motion of O-H bond, which leads to an ultrafast or even pulse-width limited partial decrease of anisotropy.[84]

To mimic the properties of aspartic acid residues under biological conditions, we study the conformational isomerism of N-acetylaspartic acid amide in aqueous solution. In Fig.5.3 we show 2DIR spectra of N-acetylaspartic acid amide dissolved in water, obtained by exciting the carbonyl vibration at ∼1730 cm^{-1} and probing the O-H stretching vibration at ∼2700 cm^{-1}. For this solution, a strong absorption band of the solvent, i.e. the water HOH-bending vibration, overlaps with the carbonyl band of the acid. Therefore, to increase the contrast between the carbonyl and the water absorption, and to obtain a significant carbonyl-hydroxyl cross-peak signal, we used a 1 M aqueous solution of N-acetylaspartic acid amide. The cross-peak signals that we

observe in parallel and perpendicular polarization configurations for this solution are qualitatively the same as those measured for N-acetylaspartic acid amide dissolved in DMSO. Again we observe a stronger cross-peak signal in perpendicular polarization at a low excitation frequency of 1725 cm^{-1} of the carbonyl vibration. At this excitation frequency, we extract an anisotropy of ∼-0.1, from which we derive an angle between the O-H and C=O groups of ∼65°. In parallel polarization we observe a stronger cross-peak signal at a relatively high frequency of the carbonyl vibration. We find that in parallel polarization the maximum of the cross-peak intensity is at 1745 cm^{-1}. At this excitation frequency we extract an anisotropy of ∼0.25, corresponding to an angle between O-H and carbonyl of ∼30°.

In order to quantify the populations of the anti- and syn-conformers, we also measured degenerate 2DIR spectra, in which the carbonyl vibrations are both excited and probed. The 2DIR signal is proportional to the concentration and the square of the vibrational cross-section, whereas the linear IR absorption scales with the concentration and the vibrational cross-section. Hence, from the combination of the degenerate 2DIR spectrum and the linear IR absorption spectrum we can determine the ratio of the vibrational cross-sections and the relative concentrations of the two carboxylic acid conformers. Fig.5.4a shows the 2DIR spectrum of N-acetylaspartic acid amide in aqueous solution at a concentration of 1 M. Because of the low cross-section of the water bending vibration and its fast relaxation dynamics, its impact to the 2DIR signal at delay time 0.3 ps is negligible.[105] We observe that the diagonal peak is centered at 1725 cm^{-1} and is elongated at the high frequency side.

In Fig.5.4b we plot a diagonal cut (probe=pump frequency) of the degenerate 2DIR spectrum as a function of the pump frequency. The resulting transient absorption spectrum shows a peak centered at 1725 cm^{-1}, and a shoulder around 1745 cm^{-1}. These two vibrational frequencies match with the excitation frequencies found in Fig.5.3 for the syn- and anti-conformers. We fit the 2DIR signal with two Voigt profiles, representing the carbonyl stretching vibrations of the syn- and anti-conformers. A third Voigt-shaped band centered at 1680 cm^{-1} was added to account for the contribution

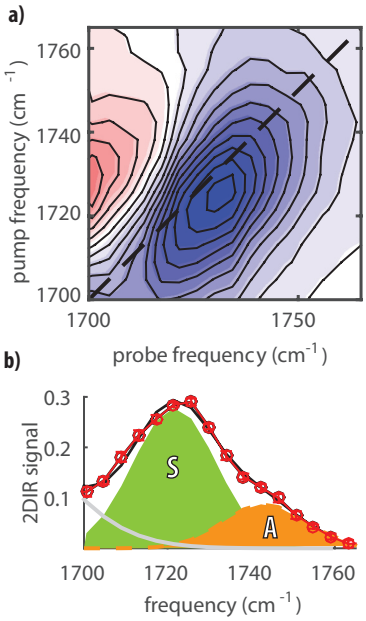

Figure 5.4: Degenerate 2DIR spectrum of N-acetylaspartic acid amide in aqueous solution. a) Isotropic degenerate 2DIR spectrum of a solution of 1 M N-acetylaspartic acid amide in water, measured at T_w=0.3 ps. b) Transient absorption signal obtained by taking the diagonal slice of the bleach signal of the 2DIR spectrum plotted as a function of pump frequency. The green and orange coloured bands represent the 2DIR signals of the syn and anti conformers obtained from a fit of the measured spectrum with Voigt profiles.

of the amide vibration (grey line). We find that the relative area of the anti-conformer band in the diagonal 2DIR signal amounts to ∼25%. Unfortunately, we cannot determine the relative area of the absorption band of the anti-conformer in the linear infrared absorption spectrum, because of the strong overlap with the bending mode of the water. However, for N-acetylaspartic acid amide dissolved in DMSO we can analyze both the diagonal negative absorption change of the degenerate 2DIR spectrum and the linear infrared absorption spectrum (see Appendix Sec.5.4.3 and in Fig.5.10). We find similar areas for the bands of the syn- and anti-conformers in the linear spectrum and the 2DIR spectrum, which implies that the vibrational cross-sections of syn- and anti- carbonyls are similar, as was found before for

formic acid (see Chapter 4). Based on this quite general result, we assume that the cross-section ratio of the carbonyl vibrations of the two conformers is also similar in water solution, which implies that the relative area of the anti-conformer in the 2DIR spectrum directly represents the relative fraction of this conformer. We thus find the populations of the syn- and anti-conformer to be 75$\pm$10% and 25$\pm$10%, respectively. These populations are similar to those found for formic acid in water (see Chapter 4). Hence, we conclude that the relative abundances of the syn- and anti-conformers of carboxyl groups in polar solvents such as DMSO or water depend only weakly on the rest of the molecule.

A.Pérez de Alba Ortíz et al. performed molecular dynamics (MD) simulations to study the intermolecular interactions of the syn- and anti-conformers of N-acetylaspartic acid amide in water. The MD simulations are done with full atomistic resolution and at the force field level of theory. Two MD simulations of aqueous solvated N-acetylaspartic acid amide have been performed in the two different planar configurations of the –COOH group, syn and anti. The angles between C-O and O-H, and the dihedral C-O-C-H, are not restrained in these simulations.

From the simulations of both conformers, they obtained the density histograms of the hydrogen and oxygen atoms of water molecules closest to the hydrogen and oxygen atoms of the carboxyl group as a function of the hydrogen bond distance and the angle between the hydrogen bond and the corresponding covalent O-H bond (Fig.5.5). We see that in all cases for distances larger than 2.45 Å the angle becomes ill-defined. Thus, we define 2.45 Å as a cut-off distance for hydrogen-bond formation between the carboxyl group and the water molecules.

The radial distribution functions of water oxygens forming a hydrogen bond with the acid hydrogen of the two conformers (Fig.5.6a) show clear differences. We find that the strongly polar OH-group of the carboxylic acid donates $\sim$1.0 hydrogen bonds for both conformers. However, the density of water oxygen atoms at a short distance ($\sim$1.8Å) is about 10% higher for the anti-conformer than for the syn-conformer. This result shows that the

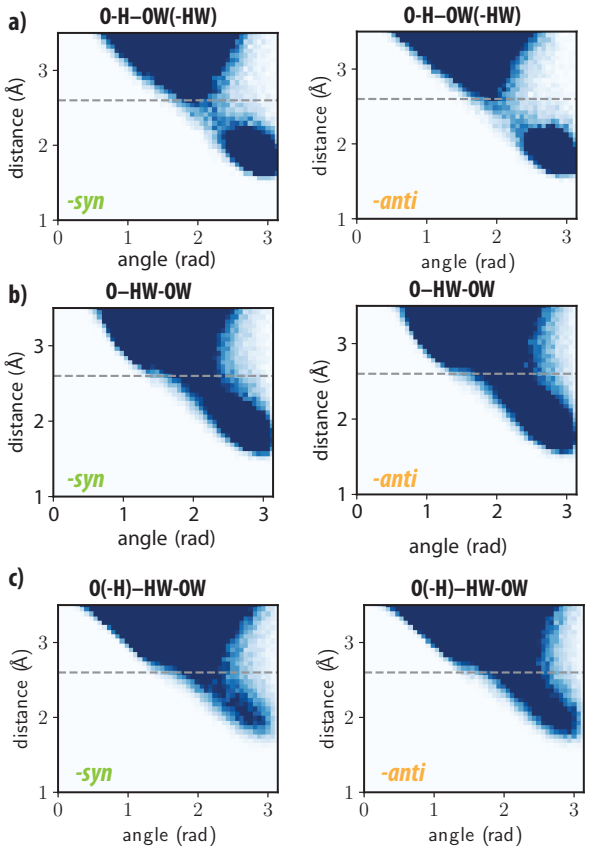

Figure 5.5: Density histograms of the water oxygen and hydrogen atoms closest to the hydrogen and oxygen atoms of the carboxyl group of N-acetylaspartic acid. a) Density of water oxygens closest to the hydrogen atom of the carboxyl group as a function of the $H_c \cdots O_w$ distance and O_c–$H_c \cdots O_w$ angle. b, c) Densities of the water hydrogens closest to the carbonyl (b) and hydroxyl (c) oxygen atoms of the carboxyl group as a function of the $O_c \cdots H_w$ distance and $O_c \cdots H_w$–O_w angle. The index c stands for the carboxyl group and the index w for a water molecule.

hydrogen bonds donated by the carboxyl group of the anti-conformer are shorter and stronger than those of the syn-conformer. This finding reflects that the hydroxyl group is more polar for the anti-conformer than for the syn-conformer, in accordance with earlier theoretical work.[77,104]

The hydration number of the oxygen atoms is rather different for the

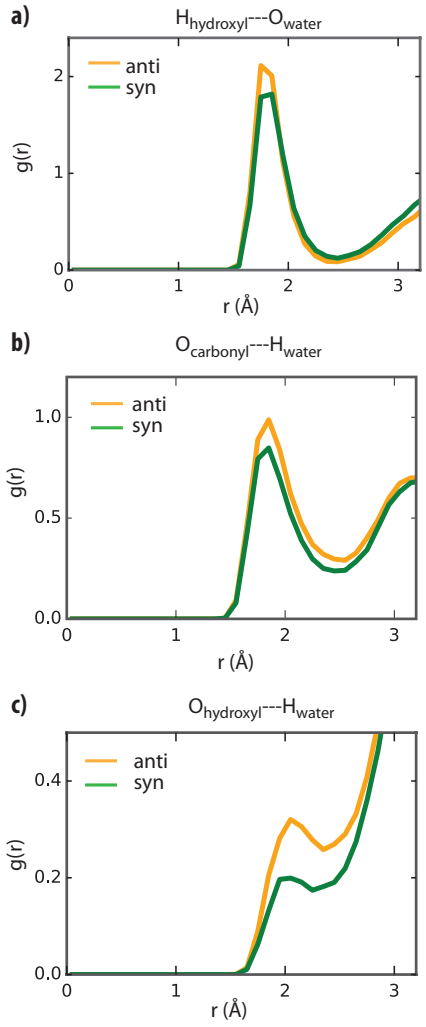

Figure 5.6: Molecular dynamics simulations of the interaction of the carboxyl group of N-acetylaspartic acid amide in syn- and anti-conformation with water. a) Radial density function of the water oxygens closest to the hydrogen atom of the carboxyl group. b,c) Radial density functions of the water hydrogens closest to the carbonyl (b) and hydroxyl (c) oxygen atoms of the carboxyl group.

two carboxyl group conformers (Fig.5.6b,c). The oxygen atom of the carbonyl group accepts ∼1.7 hydrogen bonds from water molecules for the

anti-conformer, and only $\sim$1.4 hydrogen bonds for the syn-conformer. The same trend is observed for the hydroxyl group, its oxygen atom accepts $\sim$0.7 hydrogen bonds from water molecules for the anti-conformer and $\sim$0.5 hydrogen bonds for the syn-conformer. The anti-conformer is thus much better hydrated than the syn-conformer. These differences are captured at the classical level of MD simulations, which means that they are due to exposure and steric effects and not the result of differences in the basicities of the oxygen atoms in the syn- and anti-conformers.

The better hydration of the anti-conformer explains why we observe this conformer to be significantly present in aqueous solution while it is nearly absent in the gas phase. The $25\pm10\%$ fraction of anti-conformer in aqueous solution suggests a free energy difference between the anti- and syn-conformer of 0.6 ± 0.3 kcal/mol. This value will also determine the difference in equilibrium constants of chemical reactions involving the carboxyl group such as acid dissociation. We calculate a difference in acidity of syn- and anti-conformers of $\Delta pK_a=0.5\pm0.3$. Hence, in spite of its better hydration, the anti-conformer of the carboxyl group is still more acidic than the syn-conformer, which can play an important role in intermolecular interactions and chemical equilibria inside polypeptide structures. The difference in acidity between the two conformers is much smaller than the $\Delta pK_a=4$ that was obtained in calculations of the two conformers without any solvent present .[95,106,107] This latter value for ΔpK_a is widely accepted in enzyme studies.[96,98,100,108] The energy gap we estimate from our experiment is in fact even smaller than the 1.5-1.7 kcal/mol that has been calculated for acetic acid conformers in aqueous solution.[69,70,77] Hence, the anti-conformer of the side-chain carboxyl group of N-acetylaspartic acid amide is more acidic than the syn-conformer, but this difference in acidity could strongly depend on the degree of solvation. Variation of the local environment of the amino-acid, i.e. within a protein, can thus lead to a strong change of the acidity of the aspartic acid side group.

5.3 Conclusion

We showed with polarization-resolved two-dimensional infrared spectroscopy that the side-chain carboxyl group of N-acetylaspartic acid amide exists in two distinctly different conformations, both in DMSO solution and in aqueous solution. In one of these conformations the carbonyl stretch vibration has a relatively low frequency of $\sim$1720 cm^{-1}, and the angle between the carbonyl and hydroxyl groups of the carboxylic acid side group amounts to $\sim$90°. For the other conformer the carbonyl stretch vibration has a relatively high frequency of $\sim$1745 cm^{-1}, and the angle between the carbonyl and hydroxyl groups of the carboxylic acid side group is $\sim$35°. In line with earlier work we assign these conformers to nearly-planar syn- and anti-conformers, where we explain the deviations from the ideal values of 60° (syn) and 0° (anti) from small angle out-of-plane rotations of the hydroxyl and carbonyl groups.

We find that the anti-conformer of N-acetylaspartic acid amide has a relative abundance of $\sim$25%, both when dissolved in DMSO and in water, which is significantly higher than the $<$1% observed in gas-phase studies. Molecular dynamics simulations show that the increase of the relative abundance of the anti-conformer upon dissolution in water can be explained by the more favourable hydration of this conformer in comparison to the syn-conformer. The lower relative abundance of the anti-conformer in comparison to the syn-conformer implies that this conformer is more acidic in water than the syn-conformer, corresponding to a ΔpK_a of 0.5$\pm$0.3. The acid dissociation is only one of the chemical properties of the carboxyl group that depends on the molecular conformation. Hence, the fact that both the syn- and the anti-conformers are present under biological conditions must be carefully taken into account when studying biochemical processes of polypeptides.

5.4 Appendix

5.4.1 Infrared spectra of N-acetylAspartic acid amide

The linear spectra of N-acetylaspartic acid in DMSO and water solutions are shown in Fig.5.7 . For our purpose, we focus on the carbonyl and hydroxyl regions around 1700 cm^{-1} and 2700 cm^{-1}, respectively. In the carbonyl region, we observe the carbonyl stretching modes at 1720 cm^{-1}, and the amide I vibrations at 1680 cm^{-1}. We observe that in water the amide I and C=O vibrations are broader with respect to in DMSO solutions because of the strong interactions with the water molecules. In the hydroxyl region, we observe both in DMSO and in water solutions the broad structured band of the stretching mode of the hydroxyl group.

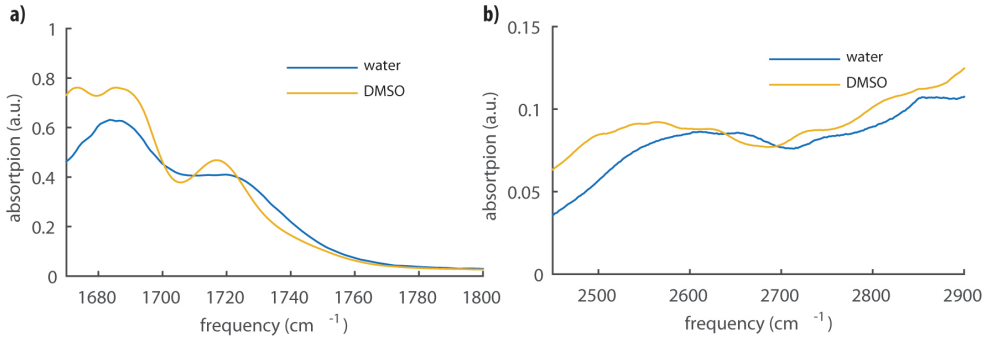

Figure 5.7: Linear infrared spectra of N-acetylaspartic acid amide in dimethyl sulfoxide and in aqueous solution in the frequency regions of the carbonyl a) and the hydroxyl b) vibrations. The absorption background of the solvent has been subtracted.

5.4.2 Syn-and anti- conformers in terminal –COOH groups of N-AcetylLeucine and N-AcetylPhenylalanine

To investigate the existence of distinct conformers of the –COOH groups of amino-acids, we studied N-acetylleucine and N-acetylphenylalanine. For N-acetylphenylalanine the sidechain is a benzyl group, and for N-acetylleucine an isobutyl group. In Fig.5.8a we show 2DIR spectra obtained by exciting the carbonyl vibrations and probing the hydroxyl vibration of the–COOH group of

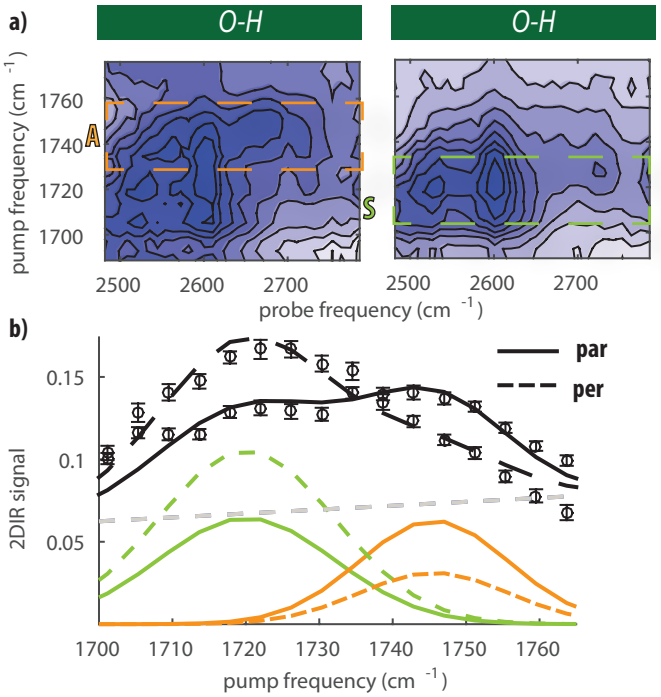

Figure 5.8: a) 2D-IR spectra of N-acetylleucine in DMSO solution in the C=O/O-H cross-peak region measured in parallel (left) and perpendicular (right) polarization configuration at a time delay T_w=0.5 ps. b) Parallel (solid) and perpendicular (dashed) transient absorption signal obtained by averaging the corresponding 2DIR signal over the probe frequency in the range between 2550 and 2750 cm^{-1}. The green and the orange colours indicate, respectively, the vibrational responses of the syn- and anti-conformers. The extracted anisotropy values are 0.25 and -0.15 for the anti- and syn-conformers, respectively.

N-acetylleucine, measured in parallel and perpendicular polarization configuration. We observe that in parallel polarization configuration the cross-peak is more intense at an excitation frequency of 1740 cm^{-1}, while in perpendicular polarization configuration the signal is most intense at an excitation frequency of 1720 cm^{-1}. To extract the anisotropy of the signals, we average over the probe region between 2500 and 2700 cm^{-1}. Fig.5.8b shows the averaged parallel and perpendicular 2DIR signals as a function of the pump frequency. We fit the spectra with two Gaussian-shaped bands to extract

their anisotropy values. We find that the cross-peak at the higher excitation frequency has a positive anisotropy ($R = 0.25$), while the one at the lower excitation frequency has a negative anisotropy ($R = -0.15$). Similar results are obtained for N-acetylphenylalanine (Fig.5.9). We assign the cross-peak signal with an excitation frequency of 1740 cm^{-1} and a positive anisotropy value to the anti-conformer, and the cross-peak signal with an excitation frequency of 1720 cm^{-1} and a negative anisotropy to the syn-conformer.

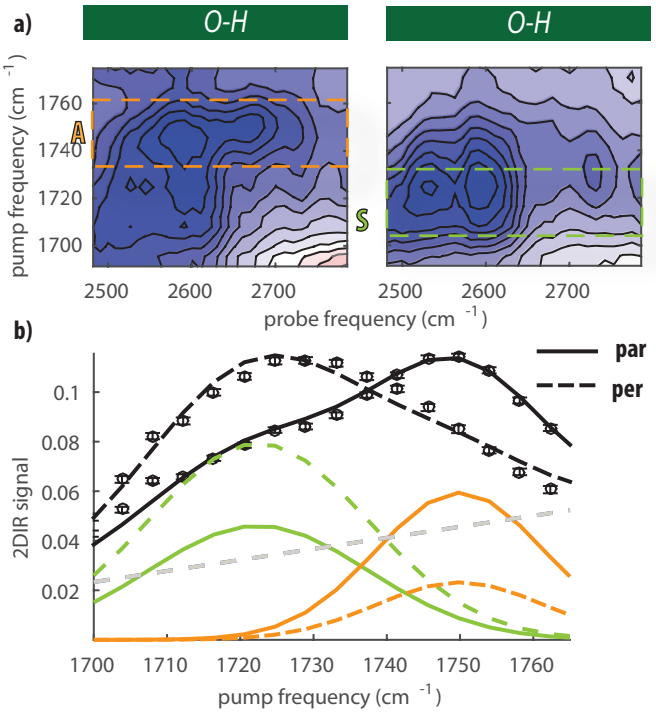

Figure 5.9: a) 2D-IR spectra of N-acetylphenylalanine in DMSO solution in the C=O/O-H cross-peak region measured in parallel (left) and perpendicular (right) polarization configuration at a time delay T_w=0.5 ps. b) Parallel (solid) and perpendicular (dashed) transient absorption signals obtained by averaging the 2DIR signals of Figure a) over the probe frequency in the range between 2550 and 2750 cm^{-1}. The green and the orange colours indicate, respectively, the vibrational responses of the syn- and anti-conformers. The extracted anisotropy values are 0.25 and -0.15 for the anti- and syn-conformers, respectively.

5.4.3 Concentration of syn and anti conformers in DMSO

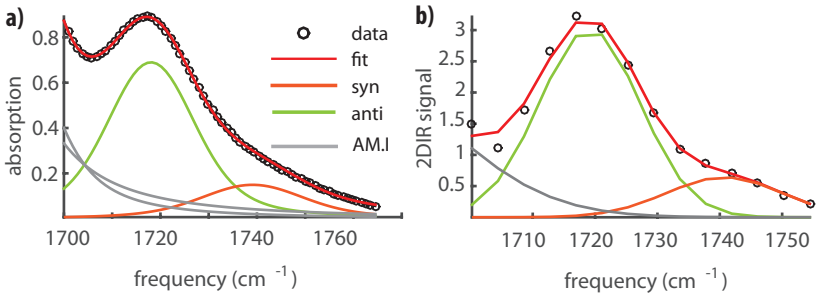

Figure 5.10: Fit of the linear infrared spectrum (a) and 2DIR diagonal slice (b) of N-acetylaspartic acid amide in DMSO solution with two Voigt-shaped bands corresponding to the syn- and anti-conformers. The extracted fraction of the anti-conformer is 20±10%. The additional Voigt bands (grey) represent the vibrational responses of the two amide groups, which are clearly observed in the linear infrared spectrum.

The relative abundances of the anti- and syn-conformers can be determined from the combination of the linear absorption spectrum and the diagonal 2DIR signal of the carbonyl vibrations. In this determination we make use of the fact that the linear infrared absorption spectrum scales with σ (where σ is the absorption cross-section), while the 2D-IR spectrum scales with σ^2, thus providing an additional relation between the measured signals, cross-sections and concentrations of the conformers. Fig.5.10a-b show the linear spectrum and the diagonal slice of the negative absorption change peaks as a function of pump frequency of N-acetylaspartic acid amide in DMSO. We fit the 2DIR signal by using two Voigt-shaped peaks, which represent the carbonyl stretching vibrations of syn and anti conformers. These two peaks are represented in Fig.5.10 by the green and orange colored peaks, respectively. We find that the *anti* area of the 2DIR signal is 20±10%, similarly to the linear spectrum, and that the cross-section ratio of the two conformers is 1±0.2.

Published as:

Giulia Giubertoni,Oleksandr O.Sofronov and Huib J.Bakker Effect of intramolecular hydrogen-bond formation on the molecular conformation of amino-acids, *Communications Chemistry, 2020*

6

Effect of intramolecular hydrogen-bond formation on the molecular conformation of amino-acids

Abstract

The molecular conformation of carboxyl group can be crucial for its chemical properties and intermolecular interactions, especially in complex molecular systems as polypeptides. We study the conformational variety of the model amino acid N-acetylproline in solutions at room temperature with two-dimensional infrared spectroscopy. We find that the carboxyl group of N-acetylproline adopts two distinctly different conformations, *syn*- and *anti*-. In the *syn*-conformer the O-H group is oriented at $\sim 60^{\circ}$ with respect to the C=O and in the *anti*-conformer the O-H is anti-parallel to the C=O. In hydrogen-bond accepting solvents such as dimethyl sulfoxide or water, we observe that, similar to simple carboxylic acids, around 20% of the -COOH groups adopt an *anti*-conformation. However, when N-acetylproline is dissolved in a weakly hydrogen-bond accepting solvent (acetonitrile), we observe the formation of a strong intramolecular hydrogen bond between the carboxyl group in *anti*-conformation and the amide group, which stabilizes the *anti*-conformer, increasing its relative abundance to $\sim 60\%$.

6.1 Introduction

Amino acids fulfill diverse roles in living systems as protein building blocks, neurotransmitters and metabolic intermediates, thereby making them one of the most important classes of organic molecules.[109–111] In view of its low pK_a values of $\sim$2 in aqueous solution, the carboxyl group of the amino-acid will usually be deprotonated. However, under specific conditions, like the nonpolar microenvironments of polypeptides, the side-chain carboxyl groups of aspartic and glutamic acids, and the carboxyl groups of C-terminal amino acids can exist in their protonated form,[85–87] and can participate in enzymatic processes or the stabilization of protein tertiary structure.[112,113] Recently, we showed that the carboxyl group of simple carboxylic acids in room temperature solution adopts two distinct nearly planar conformations, *syn*- (70-80% fraction) and *anti*- (20-30%).[114] In the *syn*-conformation the hydroxyl group is oriented at an angle of 60° with respect to the carbonyl, and in the *anti*-conformation the hydroxyl group is oriented anti-parallel with respect to the carbonyl group.[104,115] It has also been shown that the reactivity of the carboxyl group, and more general the strength of the intra- and intermolecular interactions, strongly depends on the conformation of the carboxyl group.[94,97]

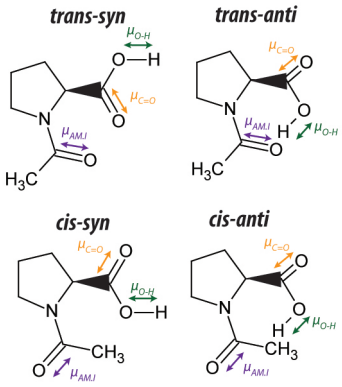

Figure 6.1: Schematic illustration of the different conformational isomers of N-acetylproline as determined by the conformations of the amide and carboxyl groups. Green and yellow arrows indicate the orientation of the transition dipole moments of the hydroxyl and carbonyl stretch vibrations. The purple arrow indicates the transition dipole moment of the amide I vibration.

Here we study the conformational isomerism of the carboxyl group of the model acetylated amino acid N-acetylproline in weakly and strongly interacting solvents with polarization-resolved two-dimensional infrared spectroscopy (2DIR). Fig.6.1 shows all the possible structures of N-acetylproline considering the conformational isomerism of both the amide (cis/trans) and the carboxyl group (*syn/anti*). It is seen that the trans-*anti* conformation offers the possibility of forming an intramolecular hydrogen bond between the C=O group of amide and the O-H group of carboxyl. N-acetylproline thus represents an ideal system to study the competition of inter- and intramolecular interactions on the molecular conformation in solvents that resemble hydrophobic and hydrophilic environments. The amide and hydroxyl vibration are usually not as strongly coupled as the carboxyl and hydroxyl vibrations since they are few atoms apart. Nevertheless, in the presence of an intramolecular hydrogen-bond, the two molecular groups are interacting, and thus the two molecular vibrations can be coupled leading to the observation of a cross-peak signature.

6.2 Results

6.2.1 Linear infrared spectroscopy

Fig. 6.2 shows the linear infrared spectra of N-acetylproline dissolved in acetonitrile, dimethyl sulfoxide (DMSO), and water in the frequency regions of the amide I, carboxyl C=O stretch and carboxyl O-H stretch vibrations. We observe that the maximum frequency of the carboxyl C=O stretch absorption shifts from 1752 cm^{-1} in acetonitrile to $\sim$1720 cm^{-1} in DMSO and water. The same trend is observed for the amide I vibration, which shifts from 1648 cm^{-1} in acetonitrile to 1643 cm^{-1} in DMSO and to $\sim$1600 cm^{-1} in water. When N-acetylproline is dissolved in acetonitrile, two additional amide peaks appear at 1585 cm^{-1} and 1605 cm^{-1}. The absorption band at 1605 cm^{-1} is found to be concentration dependent and can be assigned to the amide I vibration of the N-acetylproline dimer (see Appendix Section 6.5.1 and Fig.6.8).

The absorption spectrum of the carboxyl O-H stretch vibrations is also strongly solvent dependent. When N-acetylproline is dissolved in acetoni-

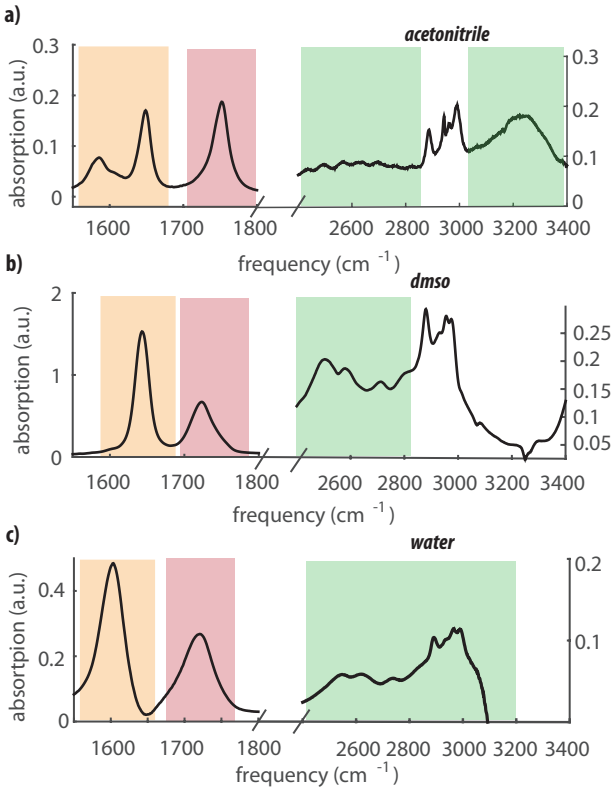

Figure 6.2: Fourier transform infrared spectra of N-acetylproline in a) acetonitrile (0.08 M), b) DMSO (0.4 M) and c) water (1 M). The solvent background is subtracted. The orange, red and green shaded areas indicate the frequency regions of the amide I, the carboxyl C=O stretch, and the carboxyl O-H stretch vibrations, respectively.

trile, the carboxyl O-H stretch spectrum extends to frequencies up to 3400 cm^{-1}. The observed broad absorption spectrum can be subdivided into a broad continuous absorption below 2900 cm^{-1} and a broad band centered around 3250 cm^{-1}. When N-acetylproline is dissolved in DMSO or water, a strong absorption is observed in the frequency region 2400-2900 cm^{-1} due to strongly hydrogen-bonded acidic OH-groups. For N-acetylproline dissolved in water the spectrum at frequencies $>$3000 cm^{-1} is not accessible due to strong absorption of water molecules. Due to coupling of the OH-stretch vibrations to low-frequency hydrogen bond modes, the absorption spectrum

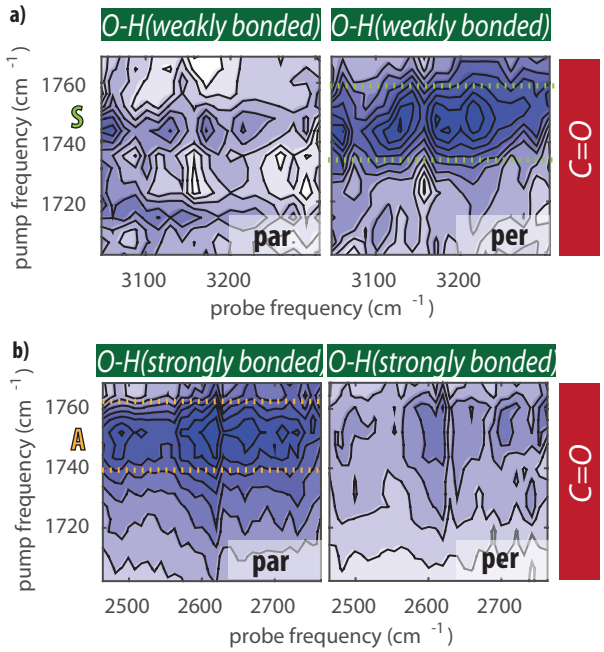

Figure 6.3: 2DIR spectra of N-acetylproline dissolved in acetonitrile measured by exciting the carboxyl C=O vibration and probing a) high frequency and b) low frequency carboxyl O-H vibrations. The spectra are measured in parallel polarization configuration (left panel) and perpendicular polarization configuration (right panel). The concentration of N-acetylproline is 0.2 M (a) and 0.08 M (b). The spectra are measured at a time delay of 0.5 ps. The color scale is normalized to the maximum intensity of the perpendicular signal in a), and to that of the parallel signal in b).

contains a series of subbands.[102,103]

6.2.2 Conformers of N-acetylproline in different solvents

Fig.6.3 shows 2D-IR measurements for N-Acetylproline dissolved in acetonitrile, where we excite the carbonyl modes, and we probe the hydroxyl modes. The coupling between the carbonyl and the hydroxyl vibrations results in a negative absorption change (*bleach*). The cross-peak intensity is strongly dependent on the polarization. Fig.6.3a shows the cross-peak signal ob-

tained by exciting the carbonyl near 1750 cm^{-1}, and probing the OH stretch vibration near 3200 cm^{-1}. The cross-peak signals have their maximum at an excitation frequency 1748 cm^{-1}, and a broad frequency range of the O-H stretch vibration. By extracting the cross-peak intensity measured in parallel ($\Delta\alpha_{par}$) and perpendicular ($\Delta\alpha_{per}$) polarization configuration, we determine the angle between the transition dipoles moments of the carbonyl and hydroxyl vibrations. We thus find an angle of $75\pm10^{\circ}$. This angle is in good agreement with the angle that we have found before for the carboxylic acid group of formic acid in syn conformation (Chapter 4). We thus conclude that at an excitation frequency of 1748 cm^{-1}, mainly carbonyl groups of *syn*-conformers absorb. Fig. 6.3b shows the 2DIR spectrum obtained

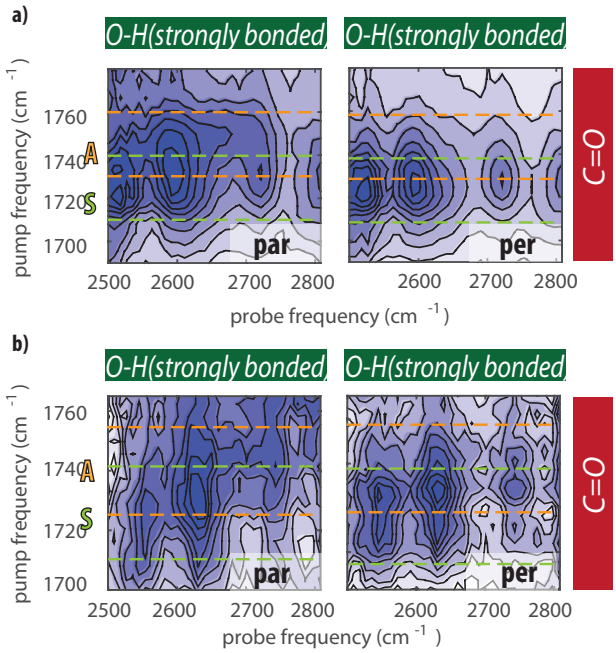

Figure 6.4: 2DIR spectra in the C=O/O-H cross-peak region measured in parallel polarization configuration (left panel) and perpendicular polarization configuration, for solutions of N-acetylproline dissolved in (a) DMSO at a time delay of 0.5 ps, and in (b) water at a time delay of 0.3 ps.

when exciting the carbonyl vibrations and probing the low-frequency hy-

droxyl vibrations around 2600 cm^{-1}. We observe that the largest cross-peak signal is obtained in parallel polarization configuration with a maximum at an excitation frequency of 1755 cm^{-1}. From the signals measured in parallel and perpendicular polarization configuration we find that the angle between the carbonyl and the hydroxyl transition dipole moments amounts to $17\pm10^{\circ}$. This value is in good agreement with a carboxyl group in an *anti*-conformation.[114]

In Fig.6.4 we show C=O/O-H cross-peak 2DIR spectra of N-acetylproline dissolved in DMSO and in water, measured in parallel and perpendicular polarization configurations. The excitation of the high frequency carbonyl vibrations near 1745 cm^{-1} results in a stronger response of the OH-stretch vibrations in parallel polarization configuration, while excitation of the low frequency carbonyl vibrations near 1730 cm^{-1} leads to a stronger cross-peak signal of the O-H vibrations in perpendicular polarization configuration. Hence, in DMSO and in aqueous solution the O-H stretch vibrations of both the *syn*- and the *anti*- conformer of the N-acetylproline carboxyl group absorb in the same broad frequency range (2400-2900 cm^{-1}), and we observe a significant difference in the carbonyl stretch frequency between the two conformers.

The large difference between the frequencies of the O-H stretch vibrations of the *syn*- and *anti*-conformers observed for N-acetylproline dissolved in acetonitrile indicates a large difference in the strength of the hydrogen bond donated by the OH-group. The O-H stretch vibration has a high frequency of $\sim$3200 cm^{-1} when the carboxyl group has a *syn*-conformation, and decreases to $\sim$2600 cm^{-1} when carboxyl group acquires an *anti*-conformation. This finding indicates that the O-H group of the *anti*-conformer forms a strong intramolecular hydrogen bond within the N-acetylproline molecule, while the O-H group of the *syn*-conformers is only weakly hydrogen bonded to the solvent. This notion is supported by the relatively low vibrational frequency of the C=O vibration of the *anti*-conformer in acetonitrile. In previous work we observed that the carbonyl vibration of the *anti*-conformer of formic acid in acetonitrile solution absorbs at a frequency that is 20-30 cm^{-1} higher than the carbonyl vibration of the *syn*-conformer (Chapters 4-5). However, the frequency of the carbonyl vibration can decrease by 20$\sim$30

cm^{-1} upon strong hydrogen bonding of the O-H group. We clearly see this effect when we compare the C=O vibrational spectrum of N-acetylproline in acetonitrile and DMSO solutions (Fig. 6.2). For N-acetylproline dissolved in acetonitrile the frequency difference between the carbonyl vibrations of the *anti*-conformer and *syn*-conformer is much smaller than for N-acetylproline in DMSO or water, because the usual blueshift of the carbonyl vibration of the *anti*-conformer in comparison with the *syn*-conformer gets largely compensated by the redshift that results from the strong intramolecular hydrogen bond formed by the *anti*-conformer.

The only moiety of N-acetylproline that can accept a strong hydrogen bond from the carboxyl O-H group is the amide group. To investigate the formation of an intramolecular hydrogen bond between the carboxyl O-H group and the C=O group of the amide group in more detail, we measured 2DIR spectra in which we tune the excitation pulses to the frequency range of the amide I vibration and the probing pulses to the frequency region low-frequency O-H stretch vibrations (Fig. 6.5). When N-acetylproline is dissolved in acetonitrile, we observe a strong cross-peak signal at an excitation frequency of 1585 cm^{-1} and probing frequencies near 2600 cm^{-1}. We assign the excitation frequency of 1585 cm^{-1} to the amide I vibration of N-acetylproline. The frequency of this vibration is strongly red shifted compared to its usual value of $\sim$1650 cm^{-1} as a result of the formation of the strong intramolecular hydrogen bond with the carboxyl OH group. This redshift is comparable to that of similar systems forming strong intra- and intermolecular hydrogen bonds.[116–118] The formation of this strong intramolecular hydrogen bond is further confirmed by the observation of an instantaneous cross-peak signal of the amide I vibration at 1585 cm^{-1} upon excitation of the carboxyl C=O vibration (see Appendix Section 6.5.2). This signal demonstrates that the strong intramolecular hydrogen bond between the carboxyl O-H group and the amide group also leads to a coupling of the carbonyl vibration of the carboxyl group and the amide I vibration.

In Fig. 6.5b and c we show 2DIR spectra obtained by exciting in the frequency region of the amide I vibration and probing in the frequency region

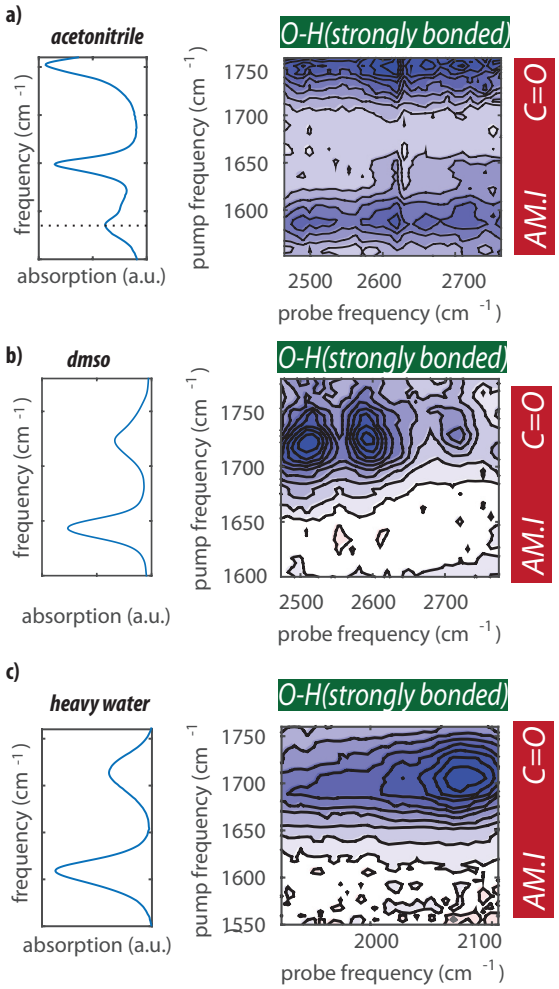

Figure 6.5: Isotropic 2DIR spectra obtained by exciting amide I vibration, and probing the hydroxyl stretch vibration of N-acetylproline dissolved in acetonitrile (a), DMSO (b) and heavy water (c). All 2DIR spectra were collected at 0.5 ps. For the solution of heavy water the hydroxyl (O-D) vibrations were probed around 2050 cm^{-1}

of the O-H stretch vibrations in DMSO solution (probing around 2600 cm^{-1}) and in heavy water solution (probing around 2050 cm^{-1}). The latter experiment was performed in heavy water to prevent absorption of the excitation pulses by the bending mode of H_2O. For N-acetylproline dissolved in DMSO

and in heavy water, we still observe a strong cross-peak signal between the C=O and the O-H vibrations of the carboxyl group, but no cross-peak signal of the amide I and the O-H stretch vibration. The absence of this cross-peak signal confirms that there is no strong intramolecular hydrogen bond formed between the amide and carboxyl groups when N-acetylproline is dissolved in DMSO solution or in water. This finding agrees with results of previous work.[119–121]

6.2.3 Relative abundance of the different conformers of N-acetylproline

To quantify the relative abundances of the *syn*- and *anti*-conformers, we measure both linear infrared absorption spectra and degenerate 2DIR spectra of the carbonyl vibrations. In Fig. 6.6a we show the linear infrared absorption spectrum in the frequency region of the carboxyl C=O vibration for a solution of 0.08 M N-acetylproline in acetonitrile. We fit this spectrum with three Voigt-shaped bands. Two of these bands are centered at the frequencies where we found the strongest *syn* and *anti* cross-peak signals (1747 and 1753 cm^{-1}). The third band at 1728 cm^{-1} is assigned to the N-acetylproline dimer (see Appendix Section 6.5.1). At 0.08 M the relative area of the *anti*-conformer band is $60\pm10\%$. Fig. 6.6b reports the spectrum of N-acetylproline in DMSO, which we fit with two Voigt-shaped bands centered at 1723 and 1749 cm^{-1}. We find that in DMSO the relative area of the *anti*-conformer is only $15\pm10\%$, which is thus much lower than in acetonitrile solution. We measure degenerate 2DIR spectra by tuning the excitation and probing pulses both to the frequency region of carbonyl vibrations (Fig. 6.10). We fit the diagonal slices of these spectra in the frequency region of the carbonyl vibration with two Voigt-shaped bands (Fig.6.7). With the band areas obtained from the linear and 2DIR spectra, we are able to determine the relative populations and cross-sections (see Appendix Section 4.4.2). We find that the fractional area of the *anti*-conformer band in the 2DIR signal amounts to $65\pm15\%$ in acetonitrile solution and to $20\pm10\%$ in DMSO solution. These areas are similar to the areas found in the linear spectra, indicating that the carboxyl C=O vibration has a similar cross-section

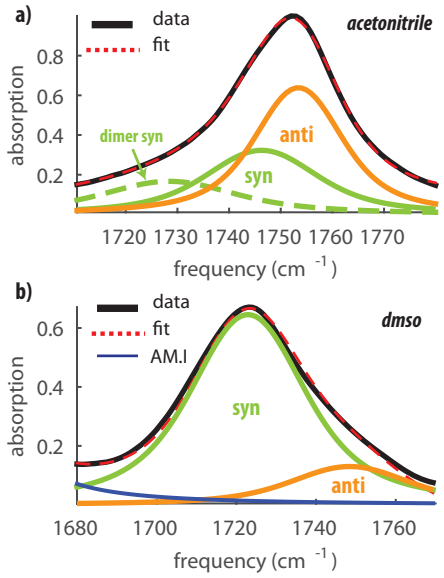

Figure 6.6: a) Linear spectrum of the carboxyl C=O vibration of N-acetylproline in acetonitrile (0.08 M). We fit the spectrum with 3 Voigt-shaped bands to describe the response of the *anti*-conformer ($\nu_0 = 1753$ cm^{-1}, $\sigma = 6.1$ cm^{-1}, $\Gamma = 6.3$ cm^{-1}), of the *syn*-conformer ($\nu_0 = 1746$ cm^{-1}, $\sigma = 8$ cm^{-1}, $\Gamma = 8$ cm^{-1}) and of the *syn*-dimer ($\nu_0 = 1728$v, $\sigma = 8$, $\Gamma = 12$ cm^{-1}). b) Linear spectrum of the carboxyl C=O vibration of N-acetylproline in DMSO (0.4 M). We fit the spectrum with 2 Voigt-shaped bands to describe the response of the *anti*-conformer ($\nu_0 = 1748$ cm^{-1}, $\sigma = 11$ cm^{-1}, $\Gamma = 11$ cm^{-1}) and of the *syn*-conformer ($\nu_0 = 1723$ cm^{-1}, $\sigma = 10$ cm^{-1}, $\Gamma = 11$ cm^{-1}).

in the *anti* and *syn* conformation.[114] Unfortunately, we cannot analyze the data obtained for N-acetylproline in water in a similar manner, since the two carbonyl bands are broadened by strong interactions with the surrounding water molecules, and thus, overlap too strongly.

6.3 Discussion

We find that the *anti*-conformer is much more abundant in acetonitrile solution than in DMSO and water solution. The relative fraction of the *anti*-conformer in acetonitrile solution is $\sim$60%, whereas in DMSO solution it

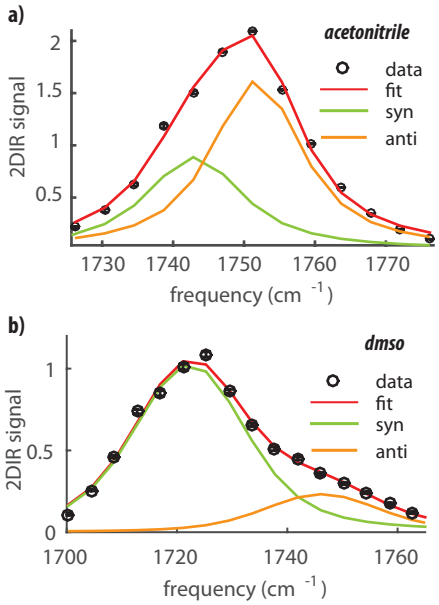

Figure 6.7: a) Diagonal slice of the 2DIR spectrum of N-acetylproline in acetonitrile (0.08 M). We fit the spectra with 2 Voigt-shaped bands to describe the response of the *anti*-conformer (ν_0=1722 cm^{-1}, σ=9 cm^{-1}, Γ =6 cm^{-1}), and of the *syn*-conformer (ν_0 =1746 cm^{-1}, σ =9 cm^{-1}, Γ = 7 cm^{-1}). b) Diagonal slice of the 2DIR spectrum of N-acetylproline in DMSO (0.4 M). We fit the spectra with 2 Voigt-shaped bands to describe the response of the *anti*-conformer (ν_0 = 1752 cm^{-1}, σ = 8.2 cm^{-1}, Γ = 6.5 cm^{-1}), and of the cm*syn*-conformer (ν_0 = 1743 cm^{-1}, σ = 9 cm^{-1}, Γ = 5 cm^{-1}).

is only $\sim$20%. This difference can be explained from the formation of a strong intramolecular hydrogen bond between the C=O group the amide in a trans conformation and the O-H group of the carboxyl group in an *anti* conformation in acetonitrile solution. This hydrogen-bond formation is energetically sufficiently favorable to make the trans-anti conformational isomer the most abundant in this solution. In DMSO and water this intramolecular hydrogen bond is not formed and the *syn*-conformer of the carboxyl group prevails. This latter finding agrees with previous work on simple carboxylic acids like formic acid (Chapter 4) and acetic acid.[71,73] The *syn*-conformer is usually the more stable conformer, unless there exist specific interactions that strongly stabilize the *anti*-conformer.

An interesting question is why the intramolecular hydrogen bond would only be formed in acetonitrile solution and not in DMSO or water. We observe that the redshift of the O-H stretch vibration due to the formation of the amide-hydroxyl intramolecular hydrogen bond is similar to the redshift of the O-H stretch vibration observed upon dissolving N-acetylproline in DMSO or water. This finding indicates that the intramolecular hydrogen bond is of similar strength as the intermolecular hydrogen bonds to DMSO and water molecules, which makes it all the more surprising that there is no sign of the formation of an intramolecular hydrogen bond for N-acetylproline in DMSO and water. This observation indicates that other factors, such as a better solvation of the amide group and other parts of the molecule, also play a role, thereby making a configuration of N-acetylproline without intramolecular hydrogen bond much more favorable in a polar solvent like DMSO or water.

The stabilization of the *anti*-conformer of the carboxyl group of amino-acids by the formation of an intramolecular hydrogen bond between the carboxyl OH group and the amide C=O group may be a more general phenomenon. We found that the formation of this intramolecular hydrogen bond, and thus the relative abundance of the *anti*-conformer of the carboxyl group, strongly depends on the polarity of the surroundings of the amino acid. In a weakly polar environment, as mimicked here by acetonitrile, such an intramolecular hydrogen bond is likely formed, leading to a strong increase of the relative abundance of the *anti* conformer. Hence, for C-terminal amino acids and aspartic and glutamic acid residues that are located in the hydrophobic micro-environment of a folded protein, the *anti* conformer of the (side-chain) carboxyl group may be much more abundant than in a polar, aqueous environment, which may affect the secondary and tertiary structure of the protein.

6.4 Conclusions

We studied the molecular structure of the model acetylated amino acid N-acetylproline using linear infrared spectroscopy and two-dimensional infrared

spectroscopy. N-acetylproline shows both amide and carboxyl conformational isomerization, and thus forms an interesting model system to study how the interaction of these groups influences the relative abundances of the different conformers of the carboxyl group of amino acids in peptides. When N-acetylproline is dissolved in acetonitrile, we observe a strong redshift of the O-H stretch vibrational frequency and a strong vibrational coupling of the amide vibration with both the C=O and O-H vibrations of the carboxyl group. These observations point at the formation of a strong intramolecular hydrogen bond between the amide C=O group and the carboxyl O-H group. This intramolecular hydrogen-bond formation is possible only in the trans-*anti*-configuration of N-acetylproline (Fig. 6.1). Due to the formation of a strong intramolecular hydrogen bond, the *anti*-conformer of the carboxyl group of N-acetylproline in acetonitrile has a relatively high abundance of $65\pm15\%$, which is much higher than is observed for the carboxyl group of simple carboxylic acids like formic acid or acetic acid. If N-acetylproline is dissolved in a hydrogen-bond accepting solvent, like DMSO or water, the intramolecular hydrogen bond between the carboxyl and amid groups is not formed. In these latter solvents the relative abundance of the *anti*-conformer is only $\sim$20%, similar to what has been observed for simple carboxylic acids.

6.5 Appendix

6.5.1 Dimer formation of N-acetylProline in acetonitrile

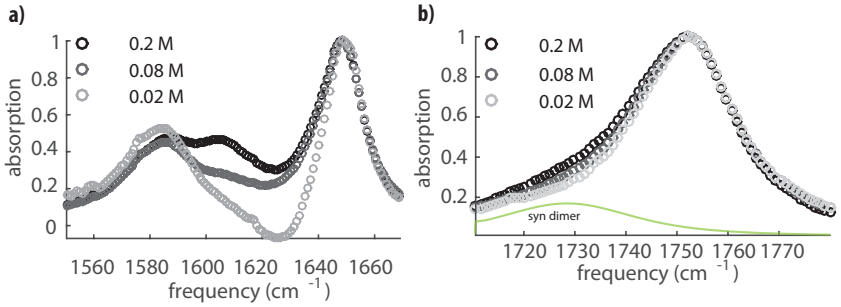

Figure 6.8: Normalized linear spectra of N-acetylproline at concentrations of 0.02, 0.08, and 0.2 M in the amide I (a) and carboxyl C=O stretch (b) vibrational regions. In a) we observe an increase of absorption at 1606 cm^{-1} with increasing N-acetylproline concentration, and in b) we observe an increase of absorption around 1725 cm^{-1} with increasing N-acetylproline concentration.

Fig. 6.8 shows that the increase of the concentration of N-acetylproline leads to the rise of an additional amide I absorption band at 1605 cm^{-1} and an additional carboxyl C=O stretch absorption band at 1728 cm^{-1}. The additional carboxyl C=O stretch is also observed in the 2DIR spectrum, as illustrated in Fig. 6.9a. The rise of these bands indicates the formation of dimers of N-acetylproline. At a concentration of 0.2 M, a second C=O/O-H cross-peak appears in the 2DIR spectrum at a relatively low excitation frequency of $\sim$1728 cm^{-1}. This signal is stronger for the perpendicular polarization configuration than for the parallel polarization configuration, which indicates that this C=O vibration corresponds to a dimer of *syn*-conformers. Excitation of the amide vibration of the N-acetylproline dimer at 1605 cm^{-1} gives rise to a cross-peak signal with strongly hydrogen-bonded hydroxyl vibrations (Fig. 6.9). This observation shows that the dimer formation involves the interaction between the carboxyl group of one N-acetylproline molecule and the amide group of another N-acetylproline molecule. Since in this dimer the hydroxyl group is strongly hydrogen bonded to the amide group of the second molecule, both the carbonyl and hydroxyl vibrations

shift to lower frequencies.

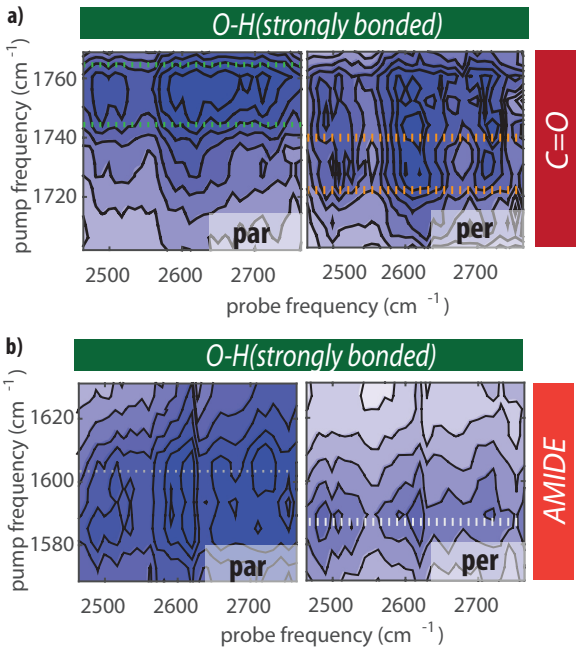

Figure 6.9: 2DIR spectra of N-Acetylproline in acetonitrile at a concentration of 0.2 M, obtained by exciting in the frequency region of the carboxyl C=O vibrations (a) and in the frequency region of the amide I vibrations (b). In both case we probe in the frequency region of the OH stretch vibrations around 2600 cm^{-1}. The 2DIR spectra are recorded in parallel (left panel) and perpendicular (right panel) polarization configurations. In a) the green bar shows the cross-peak between the carbonyl and the OH vibration of the *anti*-conformer, while the orange bar shows the cross-peak of the carbonyl and the OH vibration of the dimer. In b) the white lines show the central frequencies of the amide I vibration in the dimer (left) and in the trans-*anti* conformer (right) of N-acetylproline

6.5.2 Cross-peak between amide I and COOH of N-AcetylProline in acetonitrile

To study the interaction between the amide and the carboxyl groups in more detail, we also measured 2DIR spectra in the C=O/amide I cross-peak region. In Fig. 6.10a we observe that excitation of the carboxyl C=O

vibration at 1750 cm^{-1} leads to cross-peak signatures of two amide I modes at 1650 and 1585 cm^{-1}. To understand the origin of these cross-peaks, we resolve their dynamics. In this analysis we average over the pump frequency region between 1700 and 1770 cm^{-1} to obtain 2DIR signals as a function of probe frequency for time delays between 0.3 and 10 ps (Fig.6.10b). We then fit the resulting transient absorption spectra with a cascade kinetic model (A→B→C). We observe that the spectral signature of state A contains a cross-peak signal at a probe frequency of 1585 cm^{-1}, showing that this cross-peak is instantaneous. This means that the carboxyl C=O and the amide I vibrations are anharmonically coupled, as a result of the strong hydrogen bond that is formed between the carboxyl O-H group and the amide C=O group. The signature of the cross-peak at ν_{probe} =1650 cm^{-1} is not present in the initial spectral component A, and is part of component B that rises with a time constant of 0.6 ps (Fig.6.10c). This finding indicates that the cross-peak at ν_{probe} =1650 cm^{-1} results from intramolecular energy transfer.

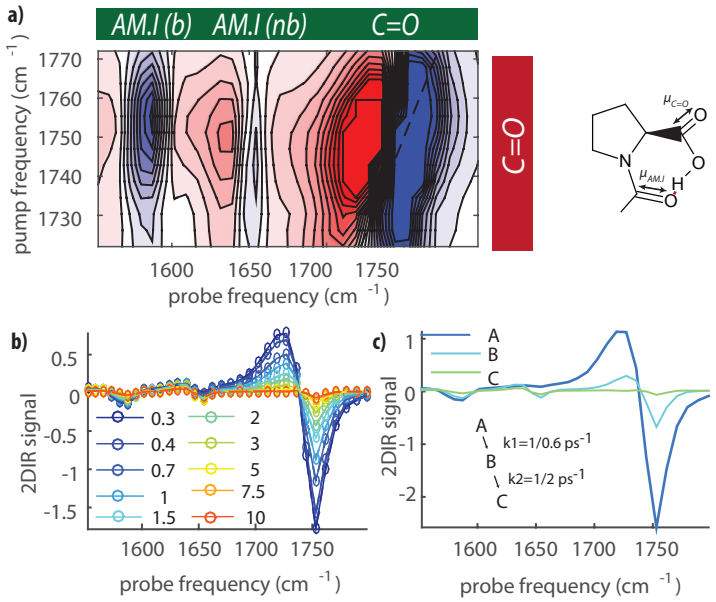

Figure 6.10: a) 2DIR spectrum of N-acetylproline in acetonitrile at a concentration of 0.08 M measured by exciting in the frequency region of the carboxyl C=O vibrations and by probing in the frequency region of the amide I and carboxyl C=O vibrations at a waiting time T_w of 0.5 ps. b) 2DIR probe slices obtained by averaging over the pump frequency region 1700-1770 cm^{-1} at different waiting times. c) The spectral signatures and interconversion time constants of the three states used to fit the spectral dynamics.

Part II

Molecular Structure of Hyaluronic Acid and Anti-Freeze Glycol Protein

Published as:

Giulia Giubertoni, G.H.Koenderink and Huib J.Bakker,
Direct Observation of Intrachain Hydrogen Bonds in
Aqueous Hyaluronan , *The Journal of Physical Chemistry A*
2019

7

Direct Observation of Intrachain Hydrogen Bonds in Aqueous Hyaluronan

Abstract

We use two dimensional-infrared spectroscopy (2DIR) to study the interactions between the amide and carboxylate anion groups of hyaluronan polymers at neutral pH. The spectra reveal the presence of intrachain hydrogen bonds between the amide and carboxylate anion groups in aqueous solution. We determine the relative orientation of the amide and carboxylate anion groups when forming this hydrogen bond and quantify the fraction of amide groups that participate in hydrogen bonding. We find that a variation of the pH and/or temperature has a negligible effect on this fraction, whereas the persistence length of the hyaluronan chains and the associated viscosity of hyaluronan solutions is known to change significantly. We conclude that the hydrogen bonding between the amide and carboxylate anion groups does not significantly contribute to the chain rigidity of hyaluronan polymers.

7.1 Introduction

Hyaluronan is a natural polysaccharide in the human body with important biological functionalities, and accordingly it also has many biomedical applications[36,122]. Since the 1940s, hyaluronan has been the subject of numerous studies, investigating its physico-chemical properties and their role in biological functions such as stem cell fate determination and tissue lubrication[123–126]. The viscoelastic properties of aqueous solutions of hyaluronan were found to strongly depend on the concentration and on the molecular weight of the polysaccharide, in accordance with semiflexible polymer models[127]. The mechanical properties also strongly depend on the nature and concentration of added salts and the pH of the solution[36,128–130], a phenomenon that is much less well understood. The physico-chemical conditions likely influence the conformation of hyaluronan polymers and their interactions, but direct experimental evidence is lacking. Hyaluronan polymers show an exceptionally large bending rigidity under physiological conditions, with a persistence length between 4 to 7 nm, corresponding to approximately 4 to 7 monomers.[131,132] This feature has been interpreted as a strong indication for the presence of intramolecular hydrogen-bonds, which locally stiffen the chain by limiting the rotation of the disaccharide units around the glycosidic bonds[133]. Indeed, for solutions of hyaluronan tetra-saccharides in dimethyl sulfoxide (DMSO), strong evidence for the existence of specific intrachain hydrogen bonds between the amide and the carboxylate anion groups has been found by means of NMR. Based on this observation, it was proposed that the secondary conformations of long chains of hyaluronan polymers, such as helical stuctures, could be stabilized by intrachain hydrogen bonds between amide and carboxylate groups.[134] Several molecular dynamics studies indicated that direct hydrogen bonds between amide and carboxylate anion groups should be formed also in aqueous solution under physiological conditions.[135] However, some other NMR and molecular dynamics studies suggested that the probability of forming this type of hydrogen bond is smaller than 10%.[130,136–138] In fact, up to now, there has been no direct experimental evidence for the existence of intrachain hydrogen-bonds between the amide and carboxylate anion groups.

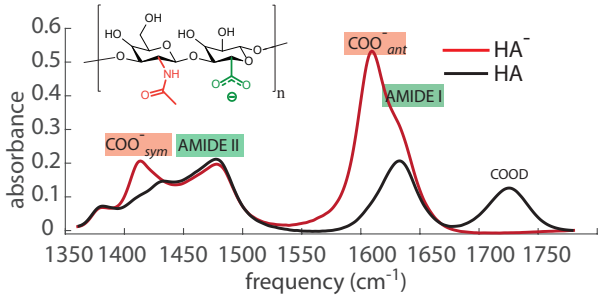

Figure 7.1: Linear infrared spectra of protonated –COOH (HA) and deprotonated -COO^- (HA^-) hyaluronan dissolved at a concentration of 20 mg/ml in heavy water. The linear spectra are obtained by decomposing the measured linear spectra as explained in the Appendix Sec.7.4. We observe that the main difference between the HA and HA- spectra is the presence of –COO^- molecular vibrations at 1400 and 1600 cm^{-1}. In the inset, a schematic of the molecular structure of the repeating units of hyaluronan. The disaccharide contains N-acetyl-glucosamine linked to glucuronate via a glyosidic bond.

Two-dimensional infrared (2DIR) spectroscopy is one of the few techniques capable of directly probing interactions such as hydrogen-bonding at the molecular scale in aqueous (bio)molecular solutions.[43] Similar to two-dimensional nuclear magnetic resonance (2D-NMR), 2DIR can resolve molecular couplings and dynamics, but at a much shorter time scale. Molecular interactions such as hydrogen-bonds or electrostatic forces usually change on a time scale of picoseconds,[139] and 2DIR is ideally suited to take snapshots of these interactions with sub-picosecond time resolution. Here we apply polarization-resolved 2DIR spectroscopy to study the interaction and relative orientation of the amide and carboxylate anion groups of hyaluronan in aqueous solutions and as a function of ionic strength and temperature.

7.2 Results and Discussion

Linear Infrared Spectroscopy

Hyaluronan is a linear polysaccharide whose basic structure is a repeating unit composed of N-acetyl-glucosamine and glucuronic acid (inset in Fig.7.1). Fig.7.1 shows the linear infrared spectra for protonated (HA) and

deprotonated (HA^-) hyaluronan in heavy water solutions at a concentration of 20 mg/ml.

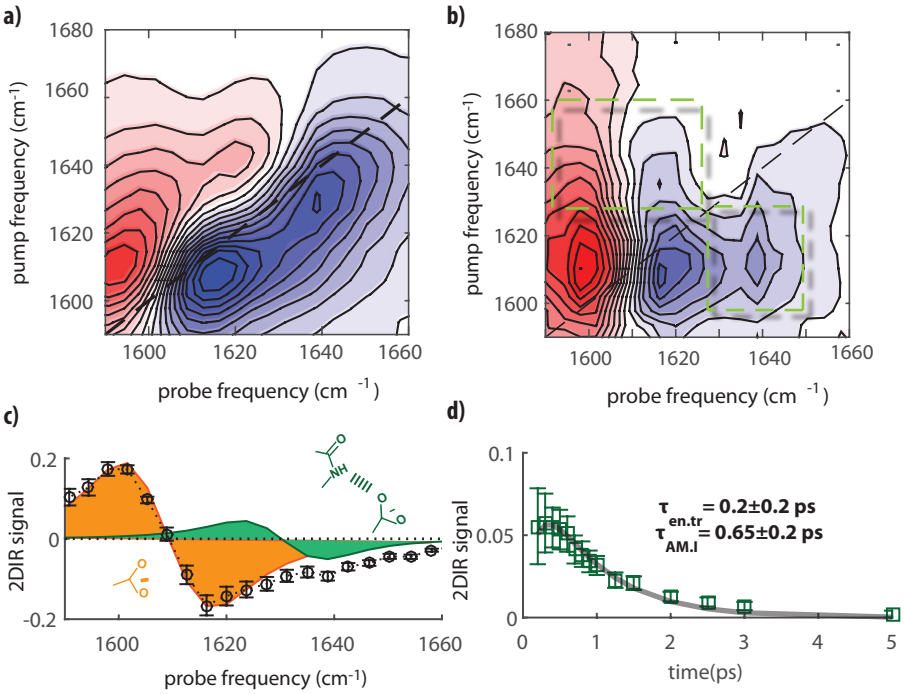

Figure 7.2: a) Isotropic 2DIR spectrum for a solution of 20 mg/ml hyaluronan in heavy water at pH = 6.8. b) 2DIR spectrum obtained by subtracting the parallel signal from three times the perpendicular signal. The green rectangles indicate the off-diagonal regions, which reveal cross-peak signals arising from the vibrational coupling between amide I and COO- modes. c) 2DIR absorption signal as a function of probe frequency obtained by averaging over the pump-frequency range between 1600 and 1615 cm^{-1}. The orange spectral signature represents the anti-symmetric stretching vibration of the carboxylate anion group, and the green spectrum represents the cross-peak signal of this vibration and the amide I vibration. d) Dependence of the cross-peak signal on the waiting time T_w between the probing pulses and the two excitation pulses (symbols), fitted to a double exponential decay (green line). The fit reveals a rise time constant ($t_{en.tr}$) of 0.2 ± 0.2 ps and a decay time constant ($t_{AM.I}$) of 0.6 ± 0.2 ps.

The spectra of the two species are extracted by fitting linear infrared spectra measured for hyaluronan in different solutions with a pH ranging from 1.5 to 6.9 (see Appendix Section 7.4 and Fig.7.6). The HA^- infrared spec-

trum shows strong absorption bands centered around 1400 cm^{-1} and 1600 cm^{-1} due to the molecular vibrations of the carboxylate anion: the symmetric stretching and anti-symmetric stretching modes, respectively. Under acidic conditions, these bands give way to a new band at 1725 cm^{-1} representing the carbonyl stretch vibration of the carboxylic acid group. For both HA and HA^- we observe a band at 1633 cm^{-1}, which corresponds to the amide I mode, and a band around 1480 cm^{-1}, corresponding to the amide II mode[82].

Intramolecular Interaction between Amide and Carboxylate Anion Groups

Fig.7.2a shows the 2DIR spectrum measured for a solution of hyaluronan at 20 mg/ml at pH $= 6.8$ at room temperature for a waiting time T_w of 0.7 ps. This spectrum represents the isotropic response, and it is obtained by adding the 2DIR spectrum measured with parallel polarization to two times the 2DIR spectrum measured with perpendicular polarization[43]. We observe the presence of two pairs of diagonal peaks. Upon excitation at 1607 cm^{-1}, we observe a strong bleach (blue coloured) and induced absorption (red coloured) peaks, representing the spectral response of the fundamental transition and the excited-state absorption of the anti-symmetric stretching mode of the carboxylate anion. Similarly, we observe upon excitation at a pump frequency of 1633 cm^{-1} bleach and excited state absorption signals arising from the excitation of the amide I vibration. In the 2DIR spectrum, similarly to the linear infrared spectrum, the two vibrations strongly overlap. This spectral overlap obscures the off-diagonal regions of the 2DIR spectrum that contain information on the coupling of the different vibrations in the form of so-called cross-peak signals, and thus on potential molecular interactions. To reduce the diagonal signals of the amide and carboxylate modes, we subtract the parallel 2DIR spectrum from three times the perpendicular 2DIR spectrum.[140] Nevertheless, in Fig.7.2b we still observe a significant diagonal signal for the anti-symmetric stretching mode and a signal corresponding to the $1 \rightarrow 2$ transition of this mode. It follows from the time-dependent anisotropy of these signals that the carboxylate anion rapidly reorients over a limited angle with a time constant of $\sim$ 250 fs (see

Appendix Section 7.4.2 and Fig.7.7a). In addition to the residual diagonal signal, we observe cross-peak signals for an excitation frequency of 1610 $cm^{-1}$and a probing frequency of 1640 cm^{-1}(upward cross-peak), and for an excitation frequency of 1640 $cm^{-1}$and a probing frequency of 1610 cm^{-1}(downward cross-peak). These off-diagonal features signal the presence of a vibrational coupling between the amide I vibration and anti-symmetric stretch vibration of the carboxylate anion group. To study the origin of the cross-peak, we measure the temporal dynamics of the upward cross-peak. It is difficult to study this dynamics for the downward cross-peak, as this signal is strongly obscured by the diagonal signal of the anti-symmetric stretch vibration of the carboxylate anion. The cross peak signal (excitation at 1614 cm^{-1}, detection at 1637 cm^{-1}) shows a rise followed by a slower decay (see Appendix Sec.7.4.2 and Fig.7.7b) which indicates that it results from energy transfer between the excited anti-symmetric stretching mode of COO^- and the probed amide I vibration. Hence, the cross-peak signal is expected to have a similar spectral shape as the diagonal signal of the amide I vibration, showing a positive excited-state absorption signal and a negative bleaching signal. Fig.7.2c shows the transient spectrum at Tw of 0.7 ps obtained by averaging the 2DIR spectrum over the excitation frequency interval between 1605 and 1615 cm^{-1}. In this figure we also show a decomposition of the transient spectrum in spectral components that can be assigned to the diagonal signal of the anti-symmetric stretching mode of the carboxylate anion and the cross-peak signal of the amide I vibration, represented by the orange and green spectral components, respectively. These spectral components are obtained from a global fit of the transient spectra to Lorentzian functions representing the excited-state absorption and bleaching signal of the anti-symmetric stretching mode of COO^-, and Lorentzian functions defining the positive and negative part of the cross-peak signal of the amide I vibration. We perform a global fit to the transient spectra measured at different delay times in which the widths, center frequencies, and amplitudes of the Lorentzians are global parameters (see Appendix Section 7.4.3). We find that the bleach of the cross-peak has its maximum at 1637 cm^{-1}. In Fig.7.2d, we show the amplitude of the decomposed spectrum of the cross-

peak as a function of delay. The cross-peak signal shows a fast rise, followed by a slower decay. We fit these data to a double exponential function, with a rise time constant of 0.2±0.2 ps and a decay time constant of 0.6±0.2 ps. We assign the decay to the vibrational relaxation of the amide I vibration. The occurrence of fast energy transfer between the carboxylate anion and the amide group indicates that these groups are in close contact with each other. This molecular interaction must be of intramolecular origin, since there is no interchain aggregation in aqueous solution at neutral pH, as evidenced by AFM imaging and by rheology measurements.[114] Hence, the fast rise of the cross-peak signal constitutes a strong indication that the amide and carboxylate group interact via an intrachain hydrogen bond: O=C-N-H·····O-C=O .[135]

Relative Orientation of the Carboxylate and Amide Groups

To study the molecular interaction between the amide and carboxylate anion groups in more detail, we also measured the coupling between the amide II vibration of the amide group and the anti-symmetric stretch vibration of the carboxylate anion (Fig.7.3a). The amide II vibration absorbs at 1490 cm^{-1}, and is mainly formed by a C-N vibration. Its transition dipole moment is at an angle of $\sim 70^{\circ}$ with respect to the transition dipole moment of the amide I mode in heavy water solutions.[141,142] Fig.7.3a shows the 2DIR spectrum in the frequency region of the amide II spectral region, measured with a parallel polarization configuration of the excitation and probing pulses, at a waiting time Tw=0.3 ps. We observe a clear cross-peak signal for excitation frequencies between 1600 and 1640 cm^{-1} and probing frequencies around 1490 cm^{-1}. This cross-peak signal shows an anti-diagonally elongated lineshape, which is typical for the cross-peak of the amide I and amide II vibrations.[141] We also observe that the nodal line slope is substantially larger for high excitation frequencies than for low excitation frequencies, which suggests the presence of an additional cross-peak signal at lower excitation frequencies, i.e. of the amide II vibration and the anti-symmetric stretch vibration of the carboxylate anion. Indeed, this difference in nodal

line slope between high and low excitation frequencies is not observed in the 2DIR spectrum of N-acetyl-glucosamine, which only exhibits a cross-peak between the amide I and amide II vibrations (Fig.7.3b). In Fig. 7.3c we plot the parallel signal as a function of excitation frequency obtained by averaging over a narrow probe-frequency interval between 1488 and 1492 cm^{-1}(Fig.7.3d shows the perpendicular signal). We observe that this signal shows a significant absorption between 1600 and 1615 cm^{-1}, confirming the presence of significant vibrational coupling between the amide II vibration and the anti-symmetric stretch vibration of the carboxylate anion.

The polarization dependence of the 2DIR measurements provides information on the angles between the transition dipole moments of the amide I mode (which is largely parallel to the C=O bond of the amide group), the amide II mode (which is largely parallel to the C-N bond), and the anti-symmetric stretching vibration of the carboxylate anion group (which lies close to a line connecting the two oxygen atoms), as illustrated in Fig.7.4c. We thus decompose the parallel and perpendicular transient spectra obtained by pumping and probing in the amide I region (Fig.7.4a-b). By measuring the ratio between the parallel and perpendicular signals of the cross-peak, we find an angle between the transition dipole moments of the amide I and the anti-symmetric stretching mode of the carboxylate anion of $15 \pm 10^{\circ}$.

The angle between the transition dipole moments of the amide I and of the amide II is expected to be $67 \pm 5^{\circ}$(Fig.7.4c). Hence, we expect that the transition dipole moments of the amide II and of the anti-symmetric stretching vibrations will be at an angle of 50°, provided that all vibrations are in the same plane. By extracting the ratio between the parallel and perpendicular signals, measured for excitation frequencies between 1600 and 1615 cm^{-1} and for a detection frequency around 1490 cm^{-1}, we find that the angle between the transition dipole moments of the amide II vibration and the anti-symmetric stretch vibration of the carboxylate anion is $45 \pm 10^{\circ}$. The obtained angles between the transition dipole moments of the vibrations of the amide and the carboxylate anion groups indicate that the orientation of these groups is highly constrained, which points at the formation of a direct intrachain O=C-N-H·····O-C=O hydrogen bond. In this hydrogen bond,

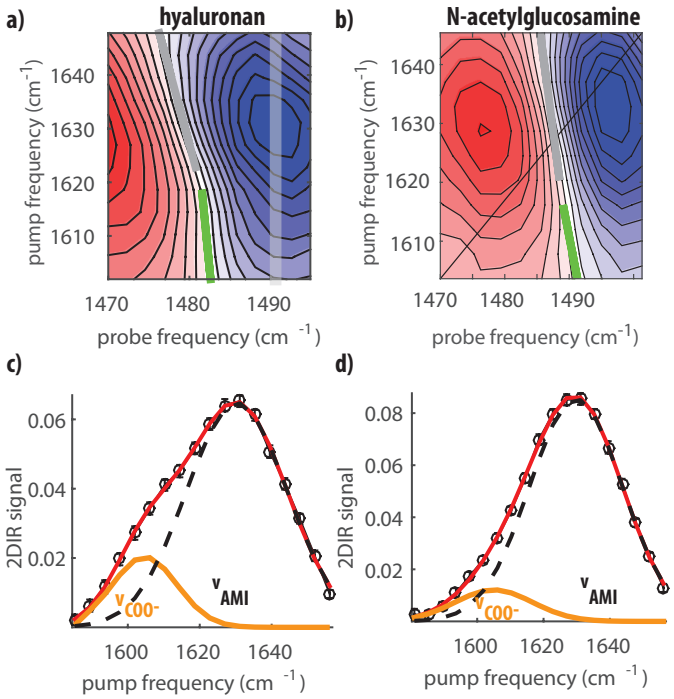

Figure 7.3: a) 2DIR spectrum measured in parallel polarization for a solution of hyaluronan at pH=6.8 at a waiting time T_w=0.3 ps. Grey and green lines represent the nodal lines. b)2DIR spectrum in parallel polarization of N-acetyl-glucosamine in D_2O at a concentration of 8% wt at a pH 7 at a waiting time of 0.3 ps. c) and d) Transient spectra as a function of pump-frequency obtained by averaging the 2DIR spectra over the probe-frequency range between 1488 and 1492 cm^{-1}, measured for hyaluronan with parallel and perpendicular polarization configuration of the pump and probe pulses, respectively. The orange Gaussian-shaped peak represents the cross-peak upon excitation of the anti-symmetric stretching mode of the carboxylate anion group.

the hydrogen atom is located close to the line that connects the two oxygen atoms of the carboxylate anion (Fig.7.4d). Since the formation of this hydrogen-bond causes a direct vibrational coupling between the amide I and the anti-symmetric stretching modes, we can retrieve the fraction of amide and carboxylate anion groups that are bonded. We thus decompose the transient spectrum (see Appendix 7.4.3 and Fig.7.8) obtained from the isotropic 2DIR spectrum into a diagonal signal $\Delta\alpha_{iso}^{COO^-}(t)$ of the anti-symmetric ν_{COO^-} vibration and a $\Delta\alpha_{iso}^{cp}(t)$ cross-peak signal. After the energy trans-

fer is complete, we find $\Delta\alpha_{iso}^{cp}(t)/\Delta\alpha_{iso}^{COO^-}(t) \sim 0.1$. This ratio provides information on the fraction ($f_{en.tr}$) of the excited anti-symmetric stretching vibrations of carboxylate anions that relax via energy transfer to the amide I vibration. We use $\Delta\alpha_{iso}^{cp}(t)/\Delta\alpha_{iso}^{COO^-}(t) = f^{en.tr}(t)\sigma_{AM.I}/\sigma_{COO^-}$, where $\sigma_{AM.I}$ and σ_{COO^-} are the cross-sections of the $\nu_{AM.I}$ and anti-symmetric

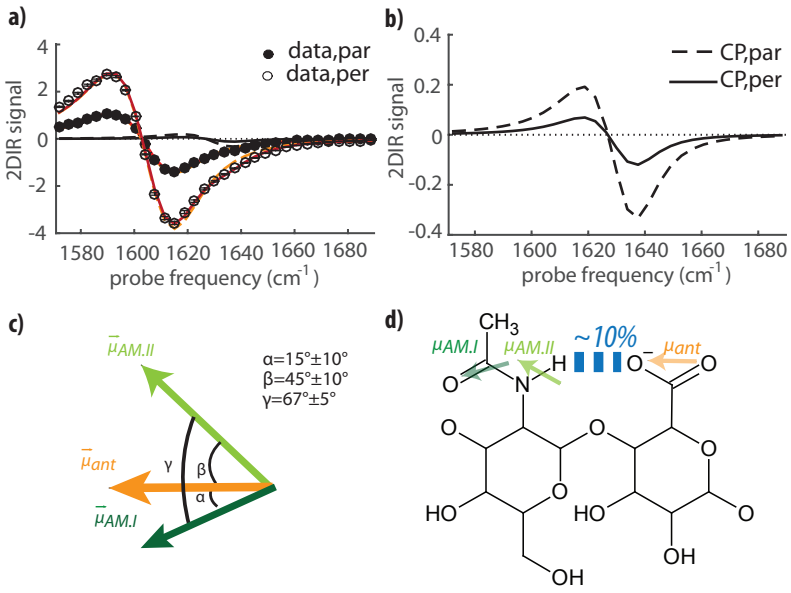

Figure 7.4: a) Measured transient absorption spectra for a pump frequency of 1607 cm^{-1} for parallel (blue circles) and perpendicular (red circles) polarization together with fits (blue and red solid lines) , for a solution of 20 mg/ml hyaluronan in heavy water at pH=6.8. The waiting time is 0.3 ps. The contributions of the cross-peak signal with the amide I vibration to the parallel and the perpendicular transient absorption spectra are represented with the dashed and continuous black lines. b) Cross-peak signals obtained from the fits to the transient absorption spectra shown in a). From the ratio of the parallel and perpendicular cross-peak signals, we obtain an anisotropy of $R = 0.32 \pm 0.05$. From this anisotropy value, we can extract the angle between the transition dipole moments of the amide I and anti-symmetric stretching using $\theta = arcos(\sqrt{(5R+1)/3})$. We thus obtain an angle of $15 \pm 10^{\circ}$. c) Schematic representation of the relative orientation of the transition dipole moments of amide I ($\vec{\mu}_{AM.I}$), amide II ($\vec{\mu}_{AM.II}$) and anti-symmetric stretching ($\vec{\mu}_{ant,}$) vibrations upon formation of a hydrogen-bond between amide and carboxylate anion groups. d) Illustration of the intra-molecular hydrogen-bond between amide and carboxylate anion groups in one single disaccharide unit.

ν_{COO^-} vibrations, respectively. The ratio $\sigma_{AM.I}/\sigma_{COO^-}$ is close to 1 (see Appendix Section 7.4.3 and Fig.7.8), which implies that $10 \pm 5\%$ of the anti-symmetric ν_{COO^-} oscillators decays via energy transfer to the amide I vibration, as a consequence of the formation of a strong hydrogen-bond between the amide and carboxylate anion groups.

Effect of pH and Temperature

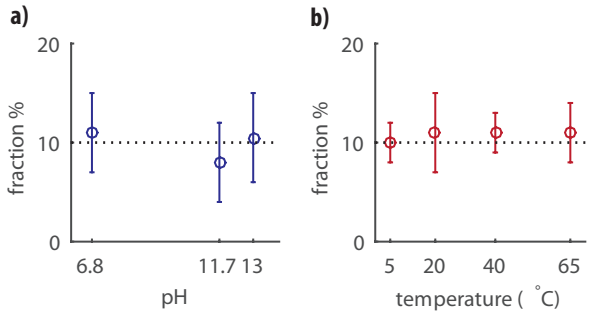

Figure 7.5: a) Fractions of carboxylate groups that decay via energy transfer to the amide I at pH=6.8, 11.7 and 13. b) Fractions of carboxylate groups that decay via energy transfer to the amide I at different temperatures. In both cases, the fractions are obtained by fitting the isotropic transient spectra at different pHs and temperatures as described in Appendix Sec.7.4.3.

It has been observed that the stiffness of hyaluronan chains drops down drastically $(30 - 50\%)$ when the pH is increased from neutral pH to alkaline pH.[143,144] To understand the effect of the pH on the hydrogen-bond between the amide and carboxylate anion groups, we measured 2DIR spectra at different pH values, and we calculate the fractions of carboxylate groups that relax via energy transfer to the amide I vibration. In Fig.7.5a we show the fractions as a function of pH. We observe that an increase in pH from 6.8 up to 13 does not lead to a change of the fraction of bonded carboxylate anion groups. The fact that an increase of pH leads to a decrease in stiffness of the hyaluronan polymers but not to a change of the fraction that relaxes via energy transfer, indicates that the intrachain hydrogen bond between the carboxylate anion group and the amide group is not a major determinant of chain stiffness. This conclusion supports a hypothesis put forward in the

literature that the main source of chain stiffness is formed by the hydrogen bonds/water bridges to the oxygen rings.[127,143,145] It has also been reported that the viscosity of a hyaluronan solution drops significantly when the temperature is increased, likely also because of a reduction of the stiffness of the polymer chains.[146–148] We measured 2DIR spectra at different temperatures in the range between 5°C and 65°C, which has been observed to lead to a decrease in viscosity of $\sim 25\%$.[147] In Fig.7.5 we compare the fractions of bonded carboxylate as a function of temperature. Again we do not observe a significant change in the fraction when varying the temperature in the range between 5° and 65°C. The absence of an effect of temperature on the fraction of intra-chain O=C-N-H·····O-C=O hydrogen bonds between the amide and the carboxylate anion group is somewhat unexpected. If this fraction would have been dependent on a single hydrogen-bond binding energy, and if this binding energy would not have been too high, the fraction of intra-chain bonds would have been expected to decrease when the temperature is raised. However, the situation for the hyaluronan polymers is more complex, as is illustrated by the fact that only $\sim 10\%$ of the intra-chain O=C-N-H·····O-C=O hydrogen bonds that could be formed are actually formed. This fraction relies on a detailed balance of solvation interactions, configurational entropy, and different intra-chain interactions. With increasing temperature all these contributions to the free energy will change. With respect to the fraction intra-chain O=C-N-H·····O-C=O hydrogen bonds, temperature is observed to have little effect, suggesting that some effects may compensate each other. For instance, it could be that at low temperatures the fraction of formed intra-chain hydrogen bond is limited because a higher fraction would have a high associated energy penalty due to unfavourable solvation interactions. At higher temperatures this energy penalty is reduced, which may compensate the tendency for the intra-chain hydrogen bonds to break up, thus yielding a fraction of intra-chain hydrogen bonds that is more or less temperature independent. The independence of the connected fraction on temperature indicates that this interaction does not play an important role for the stiffness of the polymer chains, that does strongly depend on temperature.[146–148] The observed decrease of the vis-

cosity with temperature is thus likely caused by a decrease of the stiffness of the polymer chains induced by a reduction of hydrogen bonds/water bridges formed by the oxygen rings.[127,143,145]

7.3 Conclusion

We studied the intramolecular interactions of hyaluronan polymers in aqueous solution using two-dimensional infrared (2DIR) spectroscopy. The measured 2DIR spectra provided clear evidence for the existence of a direct intrachain O=C-N-H·····O-C=O hydrogen bond between the amide and the carboxylate anion groups of the hyaluronic polymer units. From the amplitude of the cross-peak signal in the 2DIR spectra we concluded that this hydrogen bond is only formed for 10% of the amide groups. This finding agrees with previous results of NMR measurements and molecular dynamics simulations.[136–138] By measuring 2DIR spectra with different polarization configurations for the excitation and the probing pulses, we also determined the relative orientation of the transition dipole moment of the amide I and amide II vibrations with respect to the transition dipole moment of the anti-symmetric stretch vibration of the carboxylate anion group, when these groups are connected by a direct hydrogen bond. We find that these transition dipole moments are at relative angles of $15 \pm 10^\circ$ and $45 \pm 10^\circ$, respectively. These angles indicate that the intrachain hydrogen bond possesses the molecular structure that is illustrated in Fig.7.4d. Variations in the solution pH or in the temperature did not change the fraction of anti-symmetric carboxylate anion vibrations showing energy transfer to the amide group, whereas the persistence length of hyaluronan and the associated viscosity of hyaluronan solutions is known to change significantly. Therefore, our findings indicate that the intrachain hydrogen bond between the carboxylate anion group and the amide group does not play an important role in the stiffness of hyaluronan polymers.

7.4 Appendix

7.4.1 pKa of low molecular weight hyaluronan

Fit of the linear infrared absorption spectra at different DCl concentrations

We fit the linear infrared spectra using a global fitting procedure as a function of frequency and concentration of added DCl ($[D^+_{added}]$), which is based on the minimization of the square error E

$$E = \sum_{i,j}(S(\omega_j, [D^+_{added}]_i) - S^{exp}(\omega_j, [D^+_{added}]_i))^2 \tag{7.1}$$

where S is the fitted spectrum and S^{exp} the experimental spectrum. Assuming that the experimental spectra are a linear combination of the spectra at neutral (S_n) and acidic (S_a) pH, we expect that

$$\begin{aligned} &\forall i,\ for\ \omega_{min} \leqslant \omega_J \leqslant \omega_{max} \\ S(\omega_j, [D^+_{added}]_i) &= c_n S_n(\omega_j, [D^+_{added}]_i)^{neutral} + c_a S_a(\omega_j, [D^+_{added}]_i)^{acid} \end{aligned} \tag{7.2}$$

where c_n and c_a are the coefficient for the neutral and acid spectra, respectively.

Calculation of the pK_a value in heavy water

We determine the pD and the fraction of protonated/depronated carboxylic acid groups of hyaluronan as a function of added DCl using the acid-base equilibrium and mass balance equations:

$$\begin{cases} c_a = [DA] + [A^-] \\ [D^+_{added}] = [DA] + [D^+] \\ pK^D_a = pD^+ - log_{10}([A^-]/([DA]) \\ pK^D_w = pD^+ + pOD^- \end{cases} \tag{7.3}$$

The first equation represents the conservation of the total concentration c_a of hyaluronan, which is the sum of neutral hyaluronan $[DA]$ and nega-

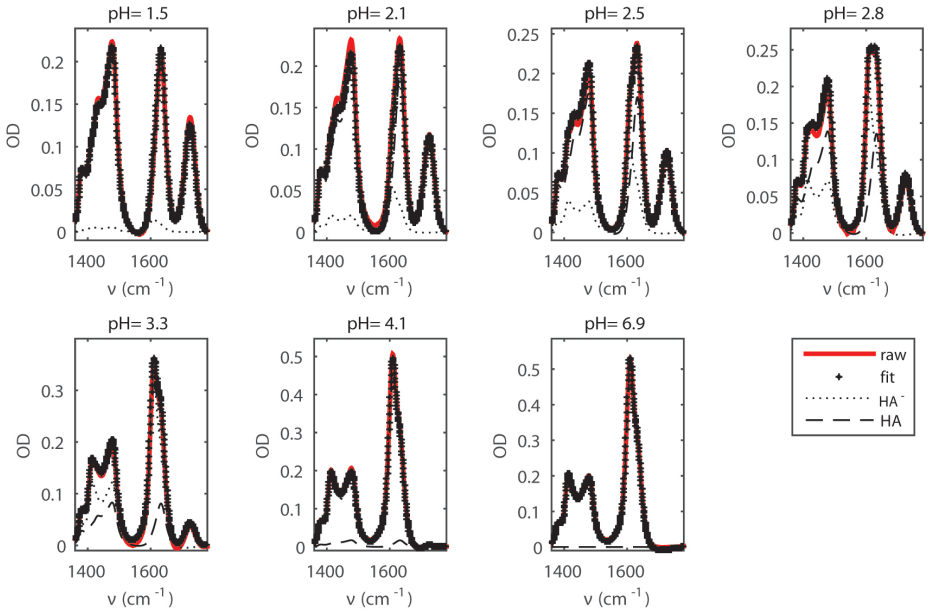

Figure 7.6: Measured raw linear spectra (red) with fits (symbols) of hyaluronan at 20 mg/ml at different pH values (see legends) in heavy water solutions, and the resulting inferred spectra for HA and HA-.

tively charged hyaluronan $[A^-]$. The second equation represents the conservation of the total concentration of added D^+, which equals the sum of free D^+ and D^+ that gets bonded to the added negatively charged hyaluronan $[A^-]$. The third equation is the acid-base equilibrium equation for hyaluronic acid. The fourth equation is the heavy water dissociation equilibrium, where pK_w^Dindicates the heavy water dissociation constant. Note that the acid dissociation constant in heavy water solutions, pK_a^D, is different from that in water solution. In order to determine the pK_a^D, we fit the fractions of $[DA]^{ext}$ and $[A^-]^{ext}$ (extracted from the global fit of the linear spectra), by using a global fitting procedure as a function of added DCl, $[D^+_{added}]$. This procedure is based on the minimization of the least-square error E of the

following expression:

$$E = \sum_i ([DA]^{ext}([D^+_{added}]_i) - [DA]([D^+_{added}]_i, pK_a^D))^2 + \sum_i ([A^-]^{ext}([D^+_{added}]_i) - [A^-]([D^+_{added}]_i, pK_a^D))^2 \quad (7.4)$$

where pK_a^D is the only free parameter. $[DA]$ and $[A^-]$ are obtained by solving the system of equations in Eq.7.3. Using $pK_w^D = 14.95$, we obtain from the fit a value of $pK_a^D = 3.3 \pm 0.2$, which is in good agreement with the expected value from literature assuming a pK_a in water of 2.9.

pD to pH conversion

We determine the pH* of a heavy water solution with a glass electrode. As the pH-meter is calibrated with water buffers for which the activity on the surface of the glass electrode differs from heavy water, we use the following correction to obtain the pD:$pD = pH^* + 0.44$. Next the pD values are converted to the pH values of a solution of water of similar acidity using: $pH = pD \times 0.929$.[149]

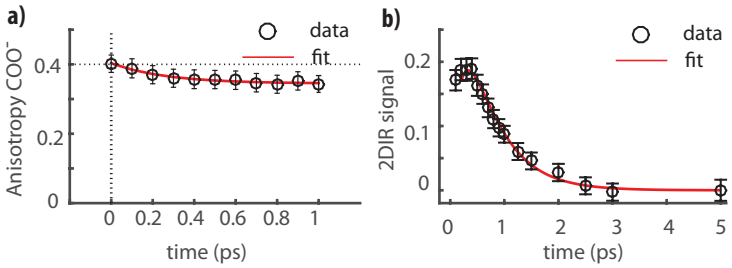

Figure 7.7: a) Anistropy decay of the anti-symmetric stretching vibration of the carboxylate anion group. The data are fitted to an exponential decay with an offset. We obtain a decay time constant of 0.250 ± 0.150 ps, and an offset of 0.37 ± 0.04. b) 2DIR signal obtained from the 2DIR spectrum reported in Fig.2b at the cross-peak frequencies (excitation at 1614 cm^{-1}, detection at 1637 cm^{-1}). The data are fitted to a double exponential function with a rise time constant of 0.2 and a decay time constant of 0.6 ps.

7.4.2 Fast orientational reorientation of the carboxylate and cross-peak dynamics

Fig.7.2b shows a difference 2DIR spectrum, obtained by subtracting parallel signal from three times the perpendicular signal. This difference 2DIR spectrum shows the spectral signature of the cross-peak signal of the amide I vibration and the anti-symmeteric stretch vibration of the carboxylate anion group. In addition, the difference 2DIR spectrum also shows a residual signal of the latter vibration on the diagonal. The presence of this residual signal indicates that the ratio between the parallel and perpendicular signals of this vibration is not exactly 3, and thus that the anisotropy is less than 0.4. In Fig.7.7a we show the anisotropy decay of the anti-symmetric stretching vibration of the carboxylate. We observe that the anisotropy shows a rapid partial decay, reaching an offset of $\sim$0.37. By fitting the dynamic to an exponential decay with offset, we find a time constant of $\sim$0.250 ps, suggesting that excitation of the transition dipole moment of the anti-symmetric stretch vibration of carboxylate anion shows a rapid wobbling motion within a small cone.

To identify the origin of the cross-peak, we extract the dynamics of isotropic signal at the cross-peak pump and probe frequencies (Fig.7.7b). We observe that the signal quickly rises and slowly decays. We fit the data to a double exponential function, and we find a rise time constant of 0.2 ps and a decay time of 0.6 ps, which is similar to the vibrational relaxation time of the amide I vibration. The dynamics, thus, strongly suggest that the cross-peak results from ultrafast energy transfer from the anti-symmetric stretch vibration of the carboxylate anion to the amide I vibration.

7.4.3 Calculation of the fraction hydrogen-bonded -COO^-

Fit of the 2DIR slices.

We fit the 2DIR spectrum using a global fitting procedure as a function of probe frequency and time which is based on the minimization of the square error E

$$E = \sum_{i,j} (S(\omega_j, t_i) - S^{exp}(\omega_j, t_i))^2 \tag{7.5}$$

where S is the fitted spectrum and S_{exp} the experimental spectrum. Assuming that the experimental spectra are a linear combination of the diagonal signal, S_{COO^-} , the cross-peak signal, S_{cp}, and the heating signal $S_{heating}$ we can write:

$$\forall i,\ for\ \omega_{min} \leqslant \omega_j \omega_{max}$$
$$S(\omega_j, t_i) = c_{COO^-}(t_i) S_{COO^-}(\omega_j) + c_{cp}(t_i) S_{cp}(\omega_j) + c_{heating}(t_i) S_{heating}(\omega_j) \quad (7.6)$$

where c_{COO^-} , c_{cp} and $c_{heating}$ are the time-dependent amplitudes of the diagonal, cross-peak and heating signals, respectively. The heating signature $S_{heating}(\omega_j)$ corresponds to the 2DIR signal at late time delay (T_w= 10 ps). The spectral signatures S_{COO^-} and S_{cp} are described as the sum of two Lorentzian-shaped peaks that correspond to the bleach and the excited state absorption (esa) of the diagonal peak ($l^{bleach}_{COO^-}$ and$l^{esa}_{COO^-}$) and of the cross-peak (l^{bleach}_{cp} and l^{esa}_{cp}),

$$S_{COO^-}(t_i, \omega) = c_{COO^-}(t_i)[-l^{bleach}_{COO^-}(\omega) + a_{COO^-} l^{esa}_{COO}(\omega)] \quad (7.7)$$

And

$$S_{cp}(t_i, \omega) = c_{cp}(t_i)[-l^{bleach}_{cp}(\omega) + a_{cp} l^{esa}_{cp}(\omega)] \quad (7.8)$$

where a_{cp} and factor a_{COO^-} represent the relative amplitude of the excited state absorption with respect to the bleaching signal.

We thus rewrite equation 7.4.3 as follows:

$$E = \sum_{i,j} (c_{cp}(t_i)[-l^{bleach}_{cp}(\omega_j) + a_{cp} l^{esa}_{cp}(\omega_j)] +$$
$$+ c_{COO^-}(t_i)[-l^{bleach}_{COO^-}(\omega_j) + a_{COO^-} l^{esa}_{COO^-}(t_i)(\omega_j)] +$$
$$+ c_{heating}(t_i) S_{heating}(\omega_j) - S^{exp}(\omega_j, t_i))^2$$

(7.9)

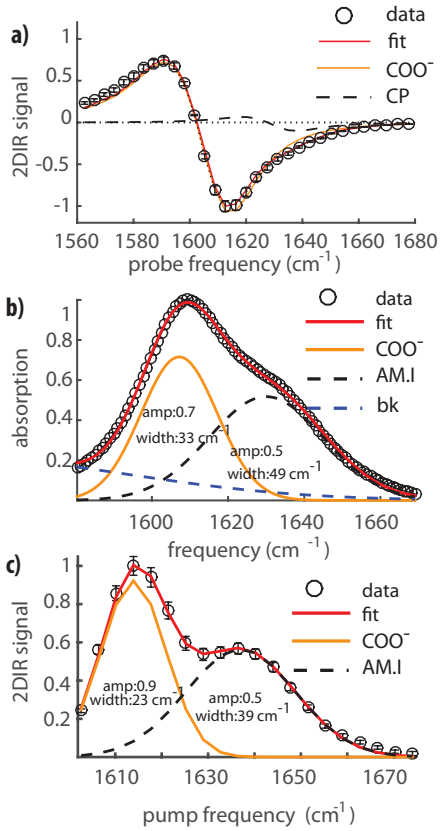

Figure 7.8: a) Measured transient absorption spectrum obtained for a pump frequency of 1607 cm^{-1} (black circles) together with a fit (red line), for a solution of 20 mg/ml hyaluronan in heavy water at pH=6.8. The waiting time is 0.3 ps. The solid orange line represents the diagonal response of the anti-symmetric vibration of COO^-, and the dashed line represents the spectral response of the cross-peak signal of this vibration and the amide I vibration. b) Normalized measured linear IR spectrum of a solution of hyaluronan at 20 mg/ml at pH=6.8. c) Normalized isotropic transient absorption spectrum of a solution of 20 mg/ml hyaluronan in heavy water at pH=6.8. The waiting time is 0.3 ps. The similarity of the shape of the spectra of b) and c) indicates that the amide I vibration and the anti-symmetric stretch vibration of COO^- have a similar absorption cross section.

Where the widths, centre frequencies, and the relative amplitude factors of the esa are global parameters.

Cross-section ratio of the amide I vibration and the anti-symmetric stretch vibration of -COO^-

By applying the fit procedure previously described, we are able to extract the ratio $r = \Delta\alpha_{iso}^{cp}/\Delta\alpha_{iso}^{COO^-}$ between the transient absorption signals of the cross-peak and the anti-symmetric stretching vibration of COO^- (Fig.7.8a). This ratio r is also equal to $r = f_{en,tr}\frac{\sigma_{AM.I}}{\sigma_{COO^-}}$, where $f_{en,tr}$ is the fraction of carboxylate groups bonded to the amide through an intra-molecular hydrogen bond, and $\sigma_{AM.I}$ and σ_{COO^-} the absorption cross-sections of the amide

I and anti-symmetric stretch vibrations, respectively. As we previously discussed in Appendix Section 5.4.3, the ratio between the two cross-sections $\frac{\sigma_{AM.I}}{\sigma_{COO^-}}$ can be found by comparing the linear and 2DIR spectra, because the linear signal scales with σ, while the 2DIR signal scales with as σ^2. Fig.7.8b and c show the normalized linear IR spectrum and the normalized isotropic 2DIR signal along the diagonal (pump=probe). We observe that in both the cases the relative amplitude between the amide I and the anti-symmetric stretching is $\sim$0.5, indicating that the absorption cross-sections are similar. Hence, we assume that $\frac{\sigma_{AM.I}}{\sigma_{COO^-}} \sim 1$, which implies that the fraction $f_{en,tr}$ can be directly obtained from the ratio of the transient absorption signals of the cross-peak signal of the amide I and the COO^- anti-symmetric stretch vibration, and of the diagonal signal of the latter vibration.

In preparation as:

G.Giubertoni, A. Pérez de Alba Ortíz, F.Bano, D.Green,P. DeAngelis, G.H.Koenderink, R.Richter, B.Ensing, and H.J.Bakker, Strong reduction of the chain rigidity of hyaluronan by selective binding of Ca^{2+} ions

8

Strong reduction of the chain rigidity of hyaluronan by selective binding of Ca^{2+} ions

Abstract

The biological functionalities of natural polyelectrolytes are strongly influenced by the presence of ions, which bind to the polymer chains and thereby modify their properties. Though the biological impact of such modifications is largely recognized, a detailed molecular picture of the binding process and of the mechanisms that drive the subsequent structural changes in the polymer is lacking. Here we study the molecular mechanism of the condensation of divalent cations (calcium) on hyaluronan, a ubiquitous polymer in human tissues. By combining measurements with two-dimensional infrared spectroscopy and molecular dynamics simulations, we find that calcium specifically binds to hyaluronan at millimolar concentrations. Because of its size and charge, the calcium cation can bind simultaneously to the strongly negatively charged carboxylate group and the uncharged amide group of adjacent saccharide units. We find both with simulations and AFM-force spectroscopy measurements that the binding of the calcium ions weakens the intramolecular hydrogen-bond network of hyaluronan, increasing the flexibility of the polymer chain. We also observe that binding of calcium to hyaluronan saturates at a maximum binding fraction of $\sim$10%. This saturation indicates that the binding of Ca^{2+} strongly reduces the probability of subsequent binding of Ca^{2+} at neighboring binding sites, probably as a result of enhanced conformational fluctuations and/or electrostatic repulsion effects. Our findings provide a detailed molecular picture of ion condensation, and reveal the severe effect of a few, selective and localized

electrostatic interactions on the rigidity of a polyelectrolyte chain.

8.1 Introduction

Polyelectrolytes are charged polymers, which are widely present in Nature and in man-made materials for applications ranging from wound dressing to oil-recovery.[150,151] Because of their charged nature, the polyelectrolyte chains strongly depend on the solution pH and on the salt conditions. Usually, dissolved ions are mobile, and can thus screen the charges along the chain, thereby reducing the persistence length that is a measure of the chain rigidity.[52] Nevertheless, localized electrostatic interactions between ions and the charges on the chain (which we refer to as Manning condensation) can happen if the distance between the charges on the chain is less than the Bjerrum length (λ_b).[54] In this case, ions bind to the charges on the chain, causing the polymer to wrap around the ions.[152,153] Multivalent ions can also condense without creating local wrapping of the chain, but still reducing significantly the persistence length by forming local ion "jackets".[154] Though the effect of condensation on the configuration of polyelectrolytes has been thoroughly studied in previous work[152–155], the molecular details of the complexes formed between cations and polyelectrolytes, and the molecular mechanisms underlying the conformational changes that follow from the ion binding, are still unknown.

Among all the natural polyelectrolytes, a specific class of charged polysaccharide, glycosaminoglycans (GAG), is arguably one of the most studied. In the human body, GAGs are critically important in many biological processes, such as anti-coagulation[19,20], inflammatory response[24,25] and the immune response to external pathogens[24]. The GAG hyaluronan plays an especially important role in many biological processes, facilitating skin hydration and tissue lubrication and mediating cell-matrix and cell-cell communication[124,125]. As part of the extracellular matrix (ECM), hyaluronan together with collagen governs the mechanical properties of the ECM, which, together with biochemical cues, guides cell behavior[156,157]. Many clinical studies have also shown that diseases such as cancer or osteoarthritis are correlated with changes in the average molecular weight and concentration of hyaluronan[30,158,159]. Thanks to its biocompatibility, hyaluronan is also widely applied as a building block for responsive and biocompatible hydro-

gels[34,160,161].

An interesting feature of hyaluronan is the sensitivity of its mechanical properties to a particular divalent cation, calcium. At a concentration of a few mM of calcium, hyaluronan hydrogels show a decrease in viscosity that is much more drastic than in the presence of a similar concentration of sodium or magnesium[162,163] Furthermore, calcium ions have been found to show an unusually strong effect on the thickness of hyaluronan brushes grafted to a surface to emulate the glycocalyx of cells[164]. Interestingly, a previous study also showed that low concentrations of calcium cause a reduced translational diffusivity of small solutes, such as glucose and lysine, in hyaluronan polymer solutions.[165]. These findings suggest that hyaluronan polymers change their molecular conformation when interacting with calcium ions. The distance between negative charges in hyaluronan is $\sim$ 1nm, which is smaller than the Bjerrum length for divalent cations (around 1.4 nm),[154,164] and thus ion condensation processes may occur, leading to a reduction of the charge density along the chain.

Here we investigate the interaction between hyaluronan and calcium ions at the molecular level, with force spectroscopy measurements using an atomic-force microscope, linear infrared spectroscopy, femtosecond two-dimensional infrared (2DIR) spectroscopy, and molecular dynamics simulations. We find that calcium ions strongly bind to hyaluronan, forming complexes with the carboxylate anion group and amide groups. We further find that the formation of only a few of these complexes suffices to change the intramolecular hydrogen bond network and, as a result, the persistence length of the hyaluronan polymers. We thus obtain a direct molecular picture of the binding mechanism between calcium and hyaluronan, and a molecular explanation of the change in flexibility of the polymer upon the interaction with the calcium ions.

8.2 Results

8.2.1 Complexation of calcium ions with hyaluronan

We used linear and nonlinear IR spectroscopy to characterize the interaction between calcium ions and HA. HA is composed of repeating disaccha-

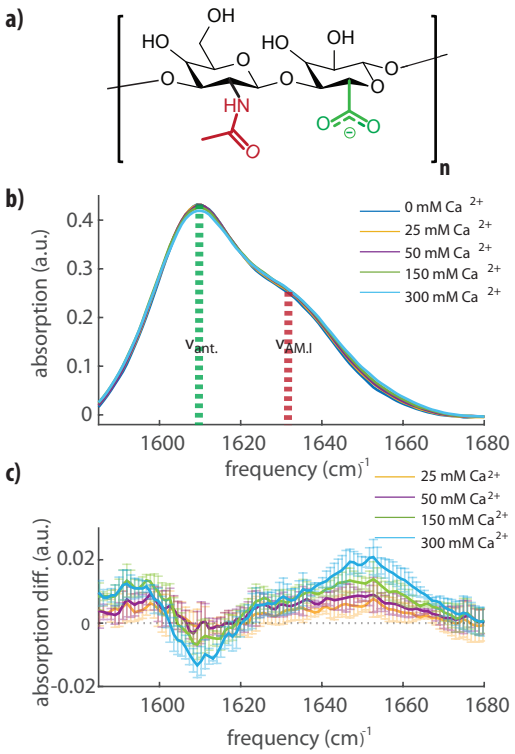

Figure 8.1: a) Molecular structure of a disaccharide unit of hyaluronan containing amide (red) and carboxylate (green) groups on adjacent saccharide units. b) Linear FTIR infrared spectra for a solution of hyaluronan at 20 mg/ml in water containing 0, 25, 50, 150 or 300 mM of calcium ions (as indicated). In the shown region, we observe the absorption peaks of the anti-symmetric stretching mode of the carboxylate anion group (ν_{ant}), and of the amide I vibration ($\nu_{AM.I}$). c) Differential FTIR infrared spectra obtained by subtracting the infrared spectrum in pure water (0 mM Ca^{2+}) from the other spectra shown in b).

ride units (Fig.8.1a). The disaccharide unit contains N-acetylgalactosamine linked by a glycosidic bond to glucuronic acid. In Fig.8.1b we report linear infrared absorption spectra of a solution of HA at a concentration of 20 mg/ml, where we vary the $CaCl_2$ concentration from 0 to 300 mM. In the frequency region between 1580 and 1685 cm^{-1}, we observe two bands, at 1609 cm^{-1} and at 1633 cm^{-1}. Following the literature, we assign the band at 1609 cm^{-1} to the absorption band of the anti-symmetric stretching mode

of the carboxylate anion group (ν_{ant}), and the band at 1633 cm^{-1} to the absorption band of the amide I vibration ($\nu_{AM.I}$) of the amide group.[82] Upon addition of $CaCl_2$, we observe a small increase of the absorption around 1590 cm^{-1} and 1620 cm^{-1}, and a significant decrease of the absorption near 1607 cm^{-1}.

With increasing calcium concentration we also notice an enhanced absorption in the high-frequency region of the spectrum, corresponding to the high-frequency wing of the amide I band (1650 cm^{-1}). In the absence of calcium, the amide group is hydrated in average by 2 water molecules, and each hydrogen-bond induces a red-shift of the amide I absorption band of 10 to 20 cm^{-1}.[166,167] The observed blue shift of the amide I band from $\sim$1633 cm^{-1} to 1650 cm^{-1} when adding calcium ions suggests therefore that the amide group gets (partly) dehydrated. Computational studies have shown that in simple model systems containing a single amide group, calcium ions have a significant probability to be located close to the carbonyl oxygen ($<$ 2.5 Å), and thus to be in direct contact with the amide group.[166–168] The creation of such a cation-amide pair induces a red-shift in the amide I vibration with respect to the frequency of this mode in the gas phase, but this red-shift is smaller than the red-shift of the amide I vibration that results from the formation of hydrogen bonds with water molecules. In a previous study, calcium was found to bind to the amide oxygen in a collinear fashion, displacing both water molecules[166], thus corroborating that the observed blue-shift of the amide vibration results from the binding of calcium ions.

At calcium concentrations below 150 mM, there is no clear difference between the linear absorption spectra with and without added salt. Nevertheless, based on previous measurements, we do expect already a significant effect of calcium ions on the hyaluronan structure in this concentration regime.[163–165]

We study the molecular-scale effect of calcium at low concentration with two-dimensional infrared (2DIR) spectroscopy. 2DIR is a nonlinear technique in which molecular vibrations are excited from the ground state ($\nu = 0$) to the first excited level ($\nu = 1$) with an intense femtosecond mid-infrared light pulse. This excitation leads to a change of the absorption of the excited and

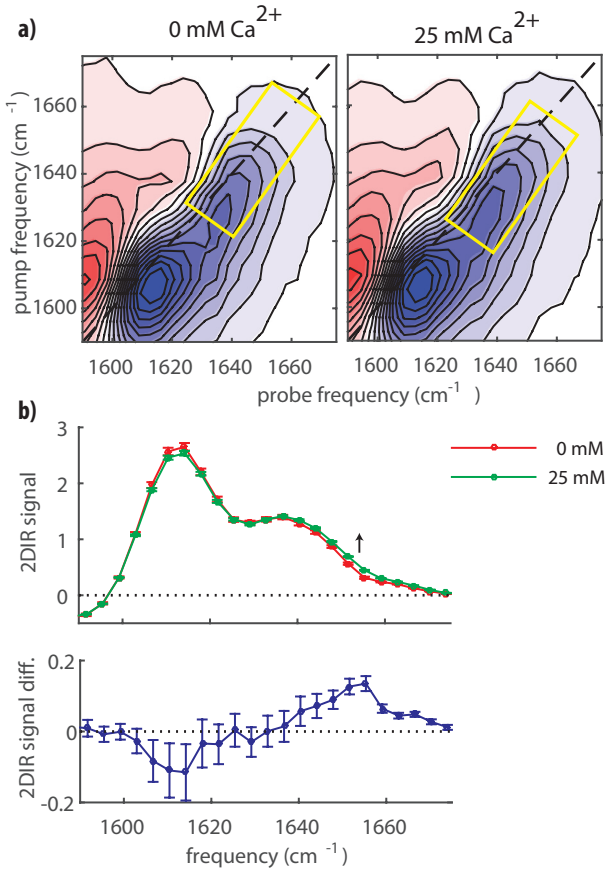

Figure 8.2: a) 2DIR spectra of hyaluronan at a concentration of 20 mg/ml in heavy water at neutral pH containing 0 (left) and 25 mM (right) calcium ions. The waiting time between the pump and probe pulse is 0.3 ps. The yellow rectangles indicate the regions with the largest changes in absorption change. b) Top: transient absorption 2DIR signals taken along the dashed lines in (a). Bottom: Differential spectrum obtained by subtracting the spectrum measured for a solution without calcium from the spectrum of a solution with 25 mM calcium ions.

other vibrations that we probe with a second, weaker, broadband, femtosecond mid-infrared light pulse (probe pulse). 2DIR spectroscopy has as an advantage over linear infrared spectroscopy that the signal, the absorption change $\Delta\alpha$, is proportional to the square of the vibrational cross-section, σ, ($\Delta\alpha \sim \sigma^2$), while in linear infrared spectroscopy the signal is linearly propor-

tional to the vibrational cross-section ($\alpha \sim \sigma$). 2DIR is thus ideally suited to distinguish species with high cross-sections and low concentration from a background of species with low cross-sections and high concentrations.

In Fig.8.2a we present 2DIR spectra measured at 0 mM and at 25 mM

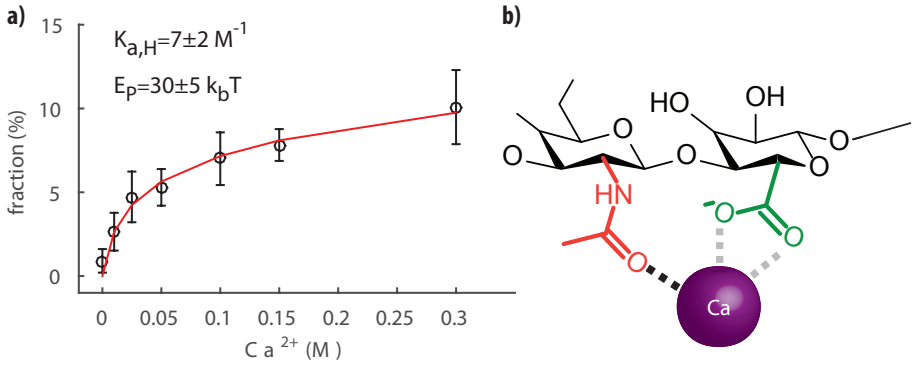

Figure 8.3: a) Fraction of complexed amide groups as a function of calcium concentration. The data (symbols with error bars) are fitted with a model that includes an increasing energy penalty with increasing occupation of the amide groups (the details are described in the Appendix Section 8.5.3). The experimental values and error bars are obtained by averaging over three different experiments. b) Illustration of the complex formed. The grey dashed line shows the bidentate binding of the carboxylate anion group to Ca^{2+}.

of calcium ions. In both spectra we observe a strong signal when exciting at 1607 cm^{-1}, which extends to higher frequencies and shows a shoulder at 1630 cm^{-1}. The peak colored in blue represents a decrease in absorption due to bleaching of ν_{ant} and the signal at lower probe frequency colored in red represents the induced absorption of the $\nu = 1$ to $\nu = 2$ transition. Upon addition of calcium ions, we observe an enhanced absorption at higher frequencies around 1660 cm^{-1}, which can be seen more clearly in the lower part of Fig.8.2b where we show the difference between the two slices taken along the diagonal of the bleach, illustrating the enhanced absorption. We observe a significantly increased absorption in the blue wing of the amide vibration at a calcium concentration of 25 mM. In line with the linear absorption spectra, we assign this enhanced absorption to the complexation of the amide carbonyl to the calcium ion, which we will indicate as $\nu_{AM.I-Ca(2+)}$. In order to extract the relative area of the $\nu_{AM.I-Ca(2+)}$ amide band at

different concentrations of calcium ions, we fit the 2DIR data with three Gaussian-shaped peaks. In this fit we use two Gaussian-shaped peaks to describe the ν_{ant} and $\nu_{AM.I}$ vibrational bands in the absence of calcium, and we use a third Gaussian-shaped peak to describe $\nu_{AM.I-Ca(2+)}$ (Appendix Section 8.5.1). The central frequencies and the widths of the three bands are global parameters in the fit, meaning they are fixed at all studied calcium concentrations, and only the amplitudes of the three bands are allowed to be different at each calcium concentration. Examples of the fits are reported in Appendix Section 8.5.1. We assume that $\nu_{AM.I-Ca(2+)}$ and $\nu_{AM.I}$ have the same cross-section, and thus we obtain the fraction of amide groups bonded to calcium ions directly from the area of the $\nu_{AM.I-Ca(2+)}$ peak (see Fig.8.3a). We observe that already at a low calcium concentration of 10 mM a significant fraction of amide groups is bonded to calcium ions. The fraction of amide bonded groups rises quickly with increasing calcium concentration but saturates at a fraction of just 10%.

The observed saturation implies that the binding between Ca^{2+} and hyaluronan is best described with a model that accounts for a high affinity for calcium at low concentrations, but an energetic penalty upon complex formation. This penalty energy E_p depends on the fraction of formed complexes, and can be accounted for by using an expression for the association equilibrium constant that contains an exponential term containing a penalty energy E_p divided by k_BT and proportional to the fraction of occupied sites:

$$K_{a,H}(f) = K_{a,H_0} e^{-\frac{E_p}{k_B T} f} = \frac{[Ca^{2+}HA]}{[Ca^{2+}]\,[HA]} \tag{8.1}$$

with

$$f = \frac{[Ca^{2+}HA]}{[HA] + [Ca^{2+}HA]} \tag{8.2}$$

where $[HA]$ is the concentration of unoccupied binding sites and $[Ca^{2+}HA]$ the concentration of occupied binding sites. Using $[Ca^{2+}] + [Ca^{2+}HA] = [Ca^{2+}]_i$ with $[Ca^{2+}]_i$ the total concentration of calcium ions in the solution, and $[HA] + [Ca^{2+}HA] = [HA]_0$ with $[HA]_0$ the total concentration of

binding sites, we can write the equilibrium expression 8.1 as:

$$K_{a,H} = \frac{x}{\left(\left[Ca^{2+}\right]_i - x\right)\left([HA]_0 - x\right)} \tag{8.3}$$

where $x = [Ca^{2+}HA]$. Solving Eq.8.3 for x and using Eq.8.2 we obtain:

$$f = \frac{1}{2} + \frac{\frac{1}{K_{a,H}} + \left[Ca^{2+}\right]_i}{2[HA]_0} - \frac{\sqrt{\left(\frac{1}{K_{a,H}} + \left[Ca^{2}+\right]_i + [HA]_0\right)^2 - 4\left[Ca^{2+}\right]_i [HA]_0}}{2[HA]_0} \tag{8.4}$$

To extract the zero-concentration limit binding constant $K_{aH,0}$, and the penalty energy E_p, we globally minimize:

$$\sum_i \left(f^{\exp}\left(\left[Ca^{2+}\right]_i\right) - f\left(\left[Ca^{2+}\right]_i\right)\right)^2 \tag{8.5}$$

Where the $f^{exp}([Ca^{2+}]_i)$ are obtained from the 2DIR experiments, and the $f([Ca^{2+}]_i)$ follow from solving the coupled equations 8.1 and 8.4.The details are reported in the Appendix Section 8.5.3. We fit the fraction of bonded amide, and we find $K_{a,H0} = 7 \pm 2$ M^{-1} and $E_p = 30 \pm 5\ k_BT$. We thus find that the binding constant in the limit of zero concentration is one order of magnitude larger than in the case of amide:calcium complexes in other simple model systems containing single amide group.[167] The obtained binding constant is equivalent to a binding energy of around 1.7 k_BT.

8.2.2 Effect of calcium ions on the persistence length of hyaluronan

To assess the effect of ions on the persistence length and flexibility of HA at the level of individual chains, we devised an atomic force microscopy assay to probe the stretching of individual HA chains under tensile force, as schematically illustrated in Fig.8.4a. Briefly, HA polysaccharide chains were anchored via a thiol label (site-specifically introduced at the non-reducing end) to a gold-coated AFM probe. The AFM probe was brought into contact with a planar support displaying the HA receptor CD44, which acted as a bait to capture an HA chain dangling from the AFM tip. Pulling the AFM probe away from the planar support generated a tensile force that was monitored as a function of the probe-support distance, as exemplified in Fig.8.4b. Care

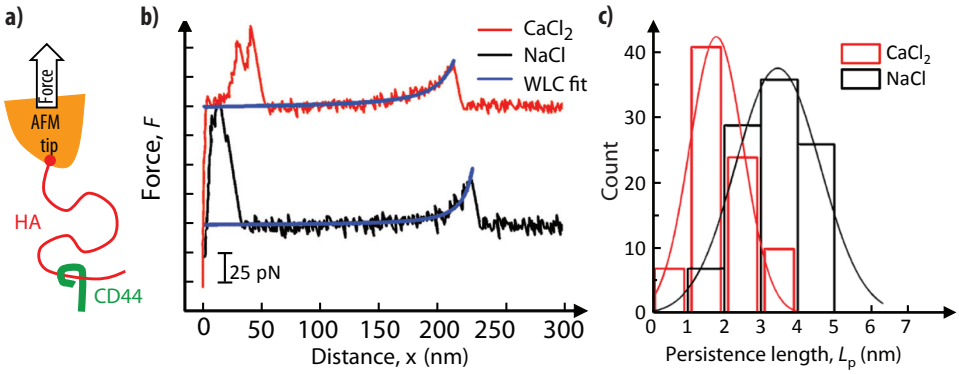

Figure 8.4: a) Illustration of the setup to measure the persistence length of HA by single molecule force spectroscopy: HA polysaccharide chains (MW = 647 kDa) were grafted via their non-reducing end to an AFM tip; extracellular domains of the HA receptor CD44 were anchored via their C-terminal end (i.e. recapitulating their orientation on the cell membrane) to a planar support, and served as baits to capture HA chains. b) Representative force curves obtained for stretching a single HA chain in $CaCl_2$ (red curve) and NaCl (black curve; offset by 100 pN along the y axis for clarity). Except for a region of non-specific binding at small separations ($<$ 50 nm), the data are well-fit by the worm-like chain (WLC) model (blue curves).c) Histograms of persistence lengths Lp determined from WLC model fits for $CaCl_2$ (red bars) and NaCl (black bars). These are well-fit by Gaussian-shaped curves (lines in matching colors), giving mean and standard deviations of 3.5 $\pm$ 1.2 nm in NaCl and 1.8 $\pm$ 0.8 nm in $CaCl_2$. Conditions: retract velocity – 1 μm/s, 150 mM NaCl or 50 mM $CaCl_2$.

was taken to adjust the surface densities of HA and CD44 such that the rupture of individual HA·CD44 bonds, and thus the stretching of individual HA chains, could be resolved. The force vs. extension curves could be well-fitted with the worm-like chain (WLC) model (Fig.8.4b), as expected for flexible and sufficiently long polymer chains. Histograms of the persistence lengths L_p extracted from these fits (Fig.8.4c) show that calcium ions decrease the persistence length of HA. At physiological concentrations of monovalent salt (150 mM NaCl), we found $L_p = 3.5 \pm 1.0$ nm, in reasonable agreement with previous work.[169] In the presence of 50 mM of $CaCl_2$ the persistence length was reduced almost two-fold, to 1.8 ± 0.8 nm. Such a marked decrease in persistence length, or equivalently, increase in chain flexibility, indicates that calcium ions strongly affect the molecular conformation of hyaluronan.

8.2.3 Effect of calcium ions on the conformation of hyaluronan

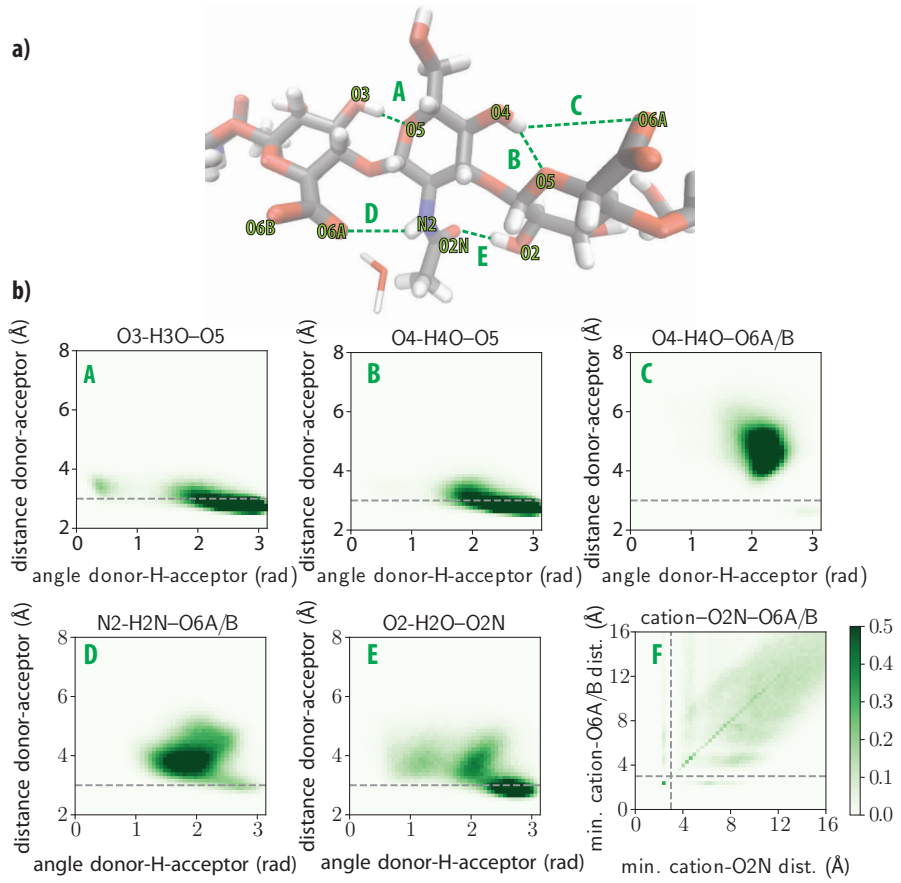

Figure 8.5: a) Key hydrogen bonds (labeled A to E) of a hyaluronan oligomer. b) 2D histograms of the hydrogen-bond distances and angles (labeled A to E) and of the cation-amide (O2N)-carboxylate (O6A/B) complex (labeled F). c) 2D Histograms of the differences for contacts A to F for hyaluronan between the $CaCl_2$-OPLS environment and the NaCl environment.

We observed that calcium ions specifically bind to hyaluronan, leading to a significant reduction of the persistence length. To correlate the calcium complex formation to the increased chain flexibility, we perform force field-based molecular dynamics (MD) simulations with atomistic resolution and an explicit description of the solvent molecules. We use specialized and previously tested force field parameters for a short HA oligomer dissolved in NaCl

and $CaCl_2$ solvent environments. We perform MD simulations of aqueous solvated HA at a concentration of 50 mM $CaCl_2$ which is the same as used in the AFM experiments. We employ two different force-fields for Ca^{2+}, referred to as $CaCl_2$-Deublein and $CaCl_2$-OPLS, since the treatment of divalent cations is known to be challenging at the classical level of theory.[166,170] We run unbiased MD simulations starting from a straight-chain state, i.e. without chain bending, in the presence of either calcium or sodium ions, and we studied the effect of cations on the properties of several hydrogen-bonds within the HA oligomer.

In Fig.8.5a we show the structure of the oligomer, in which we also

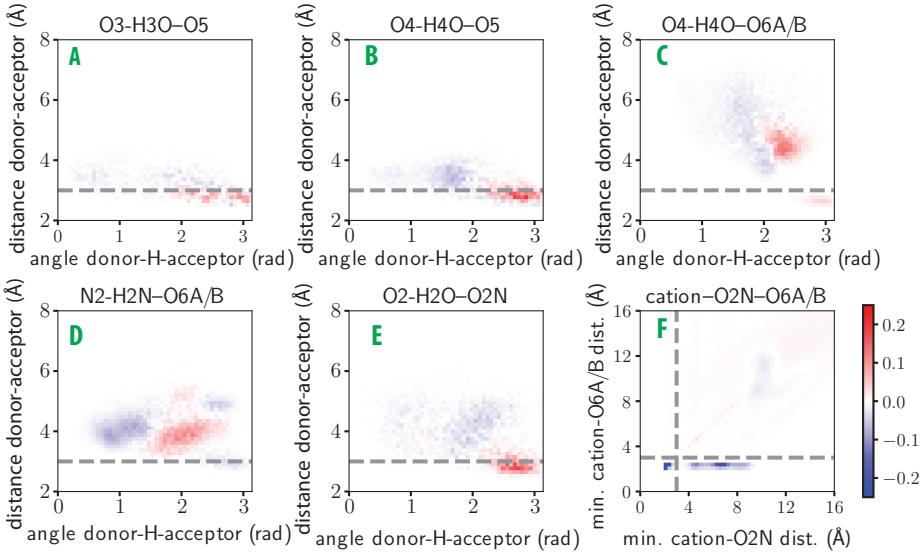

Figure 8.6: 2D Histograms of the differences for contacts A to F for hyaluronan between the $CaCl_2$-OPLS environment and the NaCl environment.

indicate the five studied hydrogen bonds (labeled A to E). In addition, we also study the geometry of the complex formed with the cation (labeled F). In Fig.8.5b, we show 2D histograms of the donor-acceptor distances and angles of the hydrogen bonds A-E and the amide/carboxylate/cation complex in a NaCl environment. Strong hydrogen bonds are characterized by donor-acceptor distances <3 Å and angles >2.5 rad, the latter implying

Probability of close contact (<3 Å) with cation	O2N	O6A/B	O2N & O6A/B
HA in NaCl	2%	1%	0.3%
HA in $CaCl_2$-OPLS	17%	43%	17%
HA in $CaCl_2$-Deublein	18%	26%	10%

Table 8.1: Probability of close contact of Na^+ or Ca^{2+} cations with the single carboxyl (O6A/B) and amide oxygens(O2N), and with both the two oxygens (OA/B & O2N).

a high degree of alignment between the acceptor, the hydrogen and the donor. We find that hydrogen bonds A and B display a close and aligned hydrogen bond (<3 Å, >2.5 rad), while C shows a longer distance and a smaller angle. Contacts D and E show both close and far contacts, with a wide range of angles, as they compete for the amide group, with contact E being somewhat favored over contact D. The cation-complex F does not show a well-defined structure. The short (<3 Å) and long (>3 Å) distance contacts between the amide and carboxylate groups and the closest cation become apparent only after magnification of the probability scale, i.e. when changing the maximum value from 0.5 to 0.05 normalized units.

In Fig.8.6, we show the changes in the 2D histograms (blue for increasing, red for decreasing) when NaCl is replaced by $CaCl_2$. For contacts A to E, we observe positive peaks at longer distances and smaller angles, which indicate a weakening of these hydrogen bonds. Only hydrogen bond D also shows a small positive peak at a distance of 3 Å and an angle of 2.8 rad. The largest difference is observed for the complex F. The Ca^{2+} cations form close contacts with the carboxylate (<3 Å) and both close (<3 Å) and far contacts with the amide (> 3 Å), in agreement with the 2DIR experimental results of Fig.8.3. The positive signal at a distance of around 10 Å observed for both the amide and the carboxylate groups can be explained from cations located on neigboring monomers. The MD results thus confirm that Ca^{2+} cations have a high propensity to bind to the carboxylate and amide groups, and show that this binding results in a weakening of the intramolecular hydrogen bonds of hyaluronan.

Table 8.1 shows the probabilities of the formation of close contacts between the cation and the amide or the carboxylate group, and with both groups. For both force-fields for Ca^{2+}, we find that the $CaCl_2$ environment

yields much greater probabilities of close contacts than the NaCl environment. The $CaCl_2$-OPLA and $CaCl_2$-Deublein yield similar values for the probability of close contacts with the amide (17 and 18%, respectively), which is somewhat larger than the 10% extracted from the 2DIR experiments. In Table 1 we also observe that the probabilities of close contacts between the cation and the carboxylate differ between the two Ca^{2+} force fields. Previous literature reports that OPLS overestimates the Ca^{2+} carboxylate affinity[171] and possibly points to $CaCl_2$-Deublein being more realistic.

We then calculate the chain end-to-end distance, and we observe that it remains around 70 Å for all cases, which suggests that the amide/carboxylate/calcium complex does weaken the hydrogen-bond network, but that large deformation events do not occur within the computational time scale and for this small polymer size. In order to estimate the effect of Ca^{2+} on the flexibility of hyaluronan, we calculate the bending free energy of the octamer in NaCl, $CaCl_2$-Deublein and $CaCl_2$-OPLS environments. This is achieved by means of a variation of the constrained MD method[172]. The resulting bending free energy profiles, spanning end-to-end lengths from a slightly stretched hyaluronan octamer (75 Å) to a half-bent U-shaped one (35 Å), are shown in Fig.8.5a. The two environments with Ca^{2+} are consistent with each other and present significantly lower free energies at more flexed configurations than the Na^+ environment, indicating a higher flexibility of hyaluronan in the presence of Ca^{2+}, in agreement with the AFM experiments (Fig.8.4). In flexible polymers, the bending free energy is linearly related to the persistence length[173], and to the bending elastic modulus[174]. The bending free energy thus offers a good alternative to calculate the persistence length from the decay of tangent correlations, for which the statistics are poor in the simulated short octamer. In Fig.8.7b, the differences in the five key hydrogen bonds are analyzed for the bent configuration with an end-to-end length of 35 Å for both $CaCl_2$-OPLS and NaCl. There is a general weakening of all contacts, even more considerable than the weakening observed for the unbiased chains of Fig.8.6. Contacts B to E shift to either longer distances ($>$4

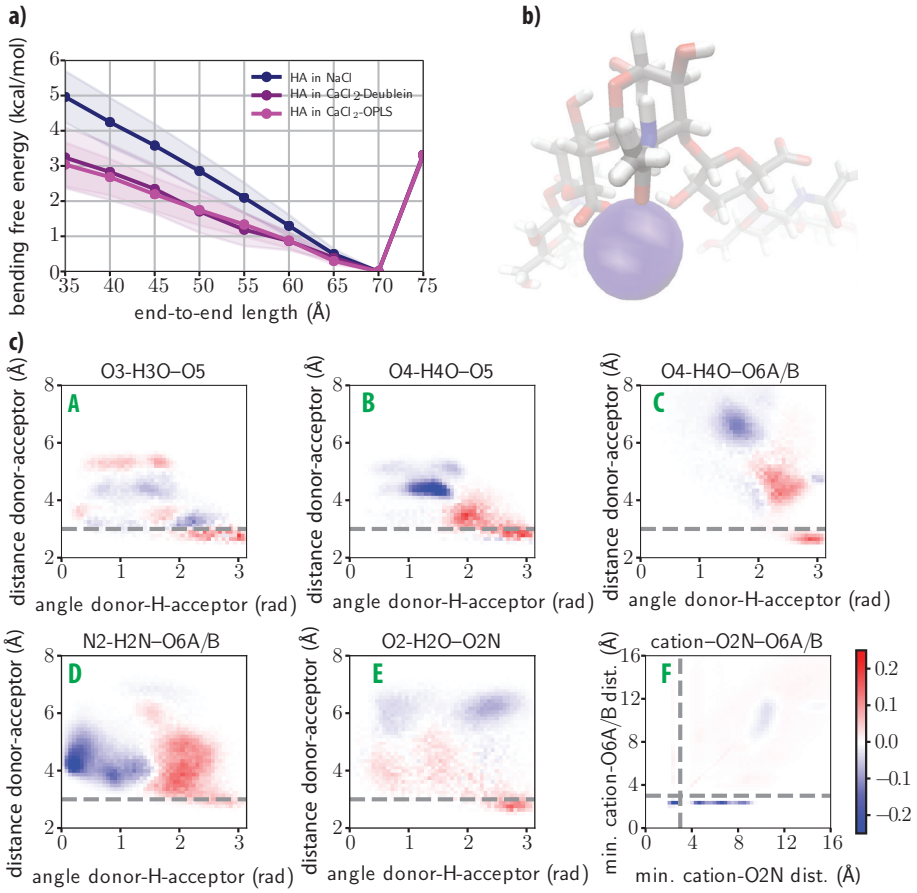

Figure 8.7: a) Bending free energy profile of hyaluronan for the three different simulation environments described in the text. The shaded regions refer to one standard deviation, as determined from a blocking analysis. b) Visualization of the amide/carboxylate/cation complex rendered by averaging atomic positions during the last 25 ns of the $CaCl_2$-OPLS run constrained at an end-to-end length of 35 Å. The picture is centered at the middle of the chain. c) 2D histograms of the differences in the key hydrogen-bond distances and angles (labeled A to E) and in the cation-amide (O2N)-carboxylate (O6A/B) complex (labeled F) for hyaluronan between the $CaCl_2$-OPLS simulation environment and the NaCl simulation environment with both systems constrained at an end-to-end length of 35 Å.

Å) or smaller angles (<2 rad), showing a clear weakening of these hydrogen bonds. Contact A is the only hydrogen bond with a small positive change

at close distances. The bending is thus accompanied by a weakening of all hydrogen bonds with the exception of hydrogen bond A, thereby reducing the stiffness of the polysaccharide.

8.3 Discussion

The 2DIR results and the MD results show that the HA polymer chains have a high affinity for calcium ions at low concentrations, leading to the formation of specific calcium complexes with amide and carboxylate groups of adjacent saccharide units. The single polymer stretching experiments measurements show that in a solution with 50 mM Ca^{2+} the persistence length decreases by 50%, while the calculations with the constrained MD method show that at this Ca^{2+} concentration the free energy required for bending decreases by 40%. The combination of the three techniques thus shows that Ca^{2+} binds with high affinity to hyaluronan and that this binding leads to a drastic increase of the flexibility and thus to a decrease of the persistence length.

The 2DIR results show that the association constant of Ca^{2+} and hyaluronan has a relatively high value of 7 M^{-1} at low Ca^{2+} concentrations. This association constant is much higher than the association constant for the binding of Ca^{2+} to amide groups, for which an association constant has been reported of of $\sim$0.1 M^{-1} [167]. We observe a similar association constant for Ca^{2+} and N-acetylglucosamine (see Appendix Sec.8.5.2). This difference can be explained from the fact that in hyaluronan the Ca^{2+} not only binds to an amide group but at the same time to a nearby carboxylate anion group. The binding with the latter group will be rather strong, thus explaining the much larger association constant of Ca^{2+} to hyaluronan compared to that to isolated amide groups. It is also interesting to compare the association constant of Ca^{2+} and hyaluronan with that of Ca^{2+} and glucuronic acid, which represents the binding affinity of a monomeric unit of hyaluronan for Ca^{2+}. For glucuronic acid we find an association constant of 1.2 ± 0.2 M^{-1} (see Appendix Sec.8.5.2), which is thus approximately five times smaller than that of hyaluronan and Ca^{2+}. This finding indicates that in hyaluronan the relative position and orientation of the amide group and the carboxylate

anion are more favorable for binding of Ca^{2+} than in glucuronic acid, which probably can be explained from the larger conformational fluctuations of glucuronic acid in comparison to hyaluronan.Due to these larger conformational fluctuations, the molecular geometry to bind Ca^{2+} is on average much less favorable for glucoronic acid than for hyaluronan.

We find that the high affinity of hyaluronan for Ca^{2+} rapidly drops when the concentration of Ca^{2+} increases, i.e. we observe that the occupation of the binding sites saturates at a bound fraction of only $\sim$10%.This strong saturation is not observed for glucuronic acid. It thus appears that the binding of a calcium ion at a particular binding site of HA hinders the binding of other Ca^{2+} ions at nearby binding sites. This hindrance may be due to a conformational effect, i.e. the binding leads to a change of the conformation of the hyaluronan, with the result that the neighboring binding sites no longer possess the highly favorable conformation of the carboxylate and amide groups that caused the initial high association constant of 7 M^{-1} of hyaluronan. This explanation is supported by MD simulations that show that the binding of Ca^{2+} induces a weakening of the hydrogen bonds and increases the flexibility of the polymer chain. The increase of the flexibility, which is also borne out by the force measurements, implies that the conformational fluctuations increase in amplitude. As a result, the time fraction in which the conformation of the binding site is favorable for binding Ca^{2+} is reduced, thereby decreasing the association constant. An additional contribution to the decrease of the affinity for Ca^{2+} may be an electrostatic effect, i.e. the positive charge of Ca^{2+} repels the binding of other Ca^{2+} at nearby binding locations. This effect is obviously much more important for hyaluronan than for glucuronic acid, as the polymer structure of hyaluronan enforces the binding sites to be closely spaced.

The MD simulations showed that the free energy cost of bending hyaluronan is consistently lower in the presence of Ca^{2+} than in the presence of Na^{+}. This lower energy cost potentially also affects other mechanical properties of hyaluronan. For instance, it has been observed that calcium ions are 10-fold more potent than sodium ions in regulating the thickness of HA brushes[164]. Based on simple charge screening one would expect only a roughly 3-fold in-

crease in potency of Ca^{2+}, compared to Na^{+}. In view of the present findings, the anomalously strong effect of Ca^{2+} can be explained from the specific binding of Ca^{2+} to HA, causing a decrease of the persistence length of HA.

8.4 Conclusion

We studied the interaction between hyaluronan polymers and Ca^{2+} ions with a combination of linear infrared spectroscopy, two-dimensional infrared spectroscopy, molecular-scale force measurements and molecular dynamics simulations. We find that hyaluronan binds Ca^{2+} with high affinity, with an association constant of 7 ± 2 M^{-1} at millimolar Ca^{2+} concentrations. The molecular dynamics simulations confirm that hyaluronan has a high affinity for Ca^{2+} ions, forming complexes in which the Ca^{2+} ion is bound to both the amide and the carboxylate anion groups. Upon binding to the carboxylate, Ca^{2+} is able to inner chelate with the amide oxygen. This favorable binding is enabled by the stereochemical arrangement of the carboxylate and amide groups on adjacent saccharides. The force measurements show that the binding of Ca^{2+} leads to a large decrease of the persistence length of the hyaluronan polymers which amounts to $\sim$50% at a calcium concentration of 50 mM. The molecular dynamics simulations show that this decrease of the persistence length can be explained from a weakening of several of the intramolecular hydrogen bonds, induced by the formation of complexes of Ca^{2+} with the carboxylate and amide groups.

The association constant of hyaluronan and Ca^{2+} is $\sim$5 times higher than that of glucuronic acid, which contains the same carboxylate anion and amide motif as hyaluronan, in the form of a monomer. This finding indicates that in hyaluronan the relative position and orientation of the amide group and the carboxylate anion are on average more favorable for binding of Ca^{2+} than in glucuronic acid, probably because of the larger conformational fluctuations of the latter molecule. When the concentration of Ca^{2+} is increased, we observe a saturation of the binding of Ca^{2+} to hyaluronan, reaching a maximum fraction of only $\sim$10%. This effect shows that the binding of Ca^{2+} strongly reduces the probability of subsequent binding of Ca^{2+} at neighboring binding sites. The saturation effect can be well modeled

with a free-energy penalty that scales with the fraction of bound Ca^{2+}. The reduction of the association constant with increasing fraction of bound Ca^{2+} can be explained from the weakening of several intramolecular hydrogen bonds of hyaluronan and an increase of the flexibility of the hyaluronan polymers upon the binding of Ca^{2+}, as shown by the molecular dynamics simulations. An additional contribution to the saturation effect may be formed by electrostatic repulsion, i.e. the positive charge of Ca^{2+} repels the binding of other positive charges at nearby binding locations.

Hence, by using a multi-technique approach, we show that selective cation binding takes place between calcium and hyaluronan polymers, leading to the formation of specific complexes. The formation of these complexes significantly affects the flexibility of the hyaluronan polymers. Our findings provide a detailed molecular picture of ion condensation, and reveal the severe effect of a few, selective and localized electrostatic interactions on the rigidity of a polyelectrolyte chain.

8.5 Appendix

8.5.1 Fit of the 2DIR diagonal slices

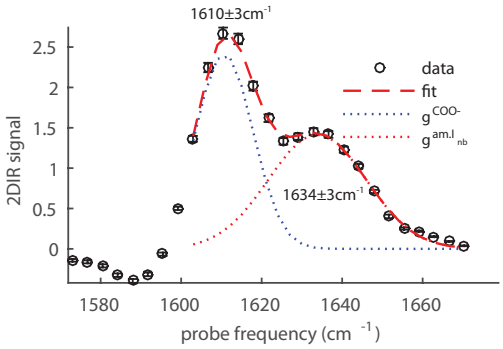

Figure 8.8: Fit of the diagonal slice of the isotropic 2DIR signal as a function of probe frequency for a solution of 20 mg/ml hyaluronan and 0 mM calcium. The fit is obtained by using two Gaussian-shaped bands describing the anti-symmetric stretching vibration of the carboxylate anion group (g^{COO^-}), and the amide I vibration of the amide group that is not bonded to calcium ($g_{nb}^{AM.I}$). We find that $\omega_0^{COO^-}$=1610±3 cm^{-1},Γ^{COO^-}=24±2 cm^{-1} and $\omega_{0,nb}^{AM.I}$=1634±3 cm^{-1},$\Gamma_{nb}^{AM.I}$=40±3 cm^{-1}.

In order to extract the fraction of amide groups bonded to Ca^{2+} ions, we take the isotropic 2DIR signal along the diagonal in the 2DIR spectra as a function of the probe frequency at a waiting time of 0.3 ps. All 2DIR spectra were reproduced at least three times at each Ca^{2+} concentration. We fit the linear infrared spectra and diagonal slices of the 2DIR spectra using a global fitting procedure based on the minimization of the following square error:

$$E = \sum_i (S^{\text{fit}}([Ca^{2+}]_i) - S^{\text{exp}}([Ca^{2+}]_i))^2 \tag{8.6}$$

where $[Ca^{2+}]_i$ is the total added concentration of calcium ions to the solution. We define S^{fit} as the sum of three Gaussian-shaped bands describing the anti-symmetric stretching vibration of the carboxylate anion group (g_{COO}^-), the amide I vibration of the unbonded amide group ($g_{nb}^{AM.I}$), and the amide I vibration of the amide group bonded to the calcium ion ($g_b^{AM.I}$).

We thus write,

$$\forall_i, S^{fit}\left(\left[\mathrm{Ca}^{2+}\right]_i\right) = \\ = c^{COO-}\left(\left[\mathrm{Ca}^{2+}\right]_{\mathrm{i}}\right) g^{\mathrm{COO}-}\left(\omega_0^{\mathrm{COO}^-}, \Gamma^{\mathrm{COO}^-}\right) + c_{nb}^{AM.I}\left(\left[\mathrm{Ca}^{2+}\right]_{\mathrm{i}}\right) g_{nb}^{AM.I}\left(\omega_{0,\mathrm{nb}}^{AM.I}, \Gamma_{\mathrm{nb}}^{AM.I}\right) \\ + c_b^{AM.I}\left(\left[\mathrm{Ca}^{2+}\right]_{\mathrm{i}}\right) g_b^{AMI}\left(\omega_{0,b}^{AM.I}, \Gamma_{\mathrm{b}}^{AM.I}\right) \tag{8.7}$$

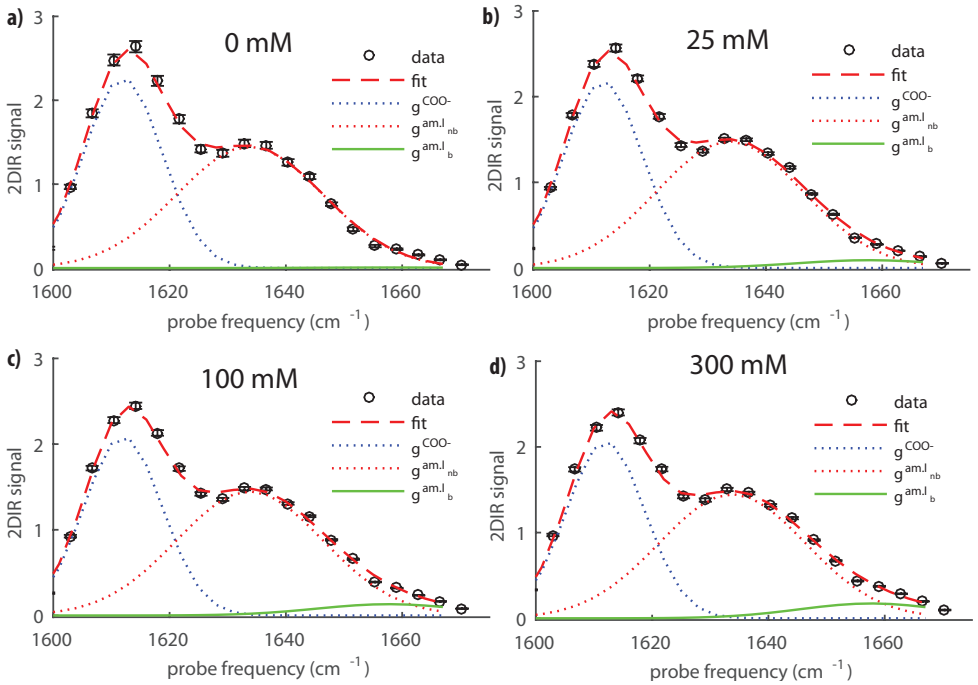

Figure 8.9: Fit of the diagonal slices of the isotropic 2DIR signals as a function of probe frequency for a solution of 20 mg/ml hyaluronan and different calcium concentrations. The fit is obtained by using three Gaussian-shaped bands as described in the text. The first two Gaussians correspond to the bands shown in Fig.8.8 for a solution without calcium. The third Gaussian band represents the amide I vibrational spectrum of amide groups that are bonded to calcium. For this band we find that $\omega_{0,b}^{AM.I} = 1658 \pm 3$ cm^{-1},$\Gamma_b^{AM.I} = 42 \pm 3$ cm^{-1}.

where $c^{\mathrm{COO}-}$, $c_{nb}^{AM.I}$ and $c_b^{AM.I}$ are the amplitudes of the three Gaussians-

shaped peaks that depend on the calcium concentration.
$\omega_0^{COO^-}, \Gamma^{COO^-}$ represent the center frequency and the width of the anti-symmetric stretching, respectively. $\omega_{0,nb}^{AM.I}, \Gamma_{nb}^{AM.I}$represent the centre frequency and the width of the unbonded amide I band, respectively, and $\omega_{0,b}^{AM.I}, \Gamma_{b}^{AM.I}$represent the centre frequency and the width of the bonded amide I band,respectively. We constrained the center frequencies and the widths of the g^{COO^-} and $g_{nb}^{AM.I}$ bands to differ maximally by ± 3 cm^{-1} from the values obtained by fitting the 2DIR signal with no added salt (Fig.8.8). The center frequency and width of the $g_b^{AM.I}$ band are completely free parameters. We took all these parameters to be the same for all calcium concentrations, meaning that only the amplitudes of the bands are allowed to change as a function of calcium concentration. The values of the parameters are obtained with a global fit of all the data-sets measured at different calcium concentrations. In Fig.8.9 we show the results of the fit at a few calcium concentrations with the amplitudes and widths of the $g_{nb}^{AM.I}$ and $g_b^{AM.I}$. bands, and assuming that the amide I vibration of an amide group bonded to calcium has the same cross-section as the amide I vibration of a non-bonded amide group, we can determine the fraction f of amide groups that are bonded to a calcium ion from the following ratio:

$$\forall_i, f([Ca^{2+}]_i) = \frac{\Gamma_b^{AM.I} c_b^{AM.I}([Ca^{2+}]_i)}{\Gamma_{\mathrm{b}}^{AM.I} c_b^{AM.I}([Ca^{2+}]_i) + \Gamma_{\mathrm{nb}}^{AM.I} c_{nb}^{AM.I}([Ca^{2+}]_i)} \tag{8.8}$$

8.5.2 Model for the binding of calcium ions to N-acetyl-glucosamine and glucuronic acid

We describe the binding of calcium to an amide or carboxylate group of N-acetyl-glucosamine and glucuronic acid:

$$Ca^{2+} + M \overset{K_{a,M}}{\rightarrow} Ca^{2+}M \tag{8.9}$$

Where M represents the amide and/or carboxylate group. The equilibrium equation of this reaction is given by:

$$K_{a,M} = \frac{[Ca^{2+}M]}{[Ca^{2+}]\,[M]} \tag{8.10}$$

By using

$$\left[Ca^{2+}\right] + \left[Ca^{2+}M\right] = \left[Ca^{2+}\right]_i \tag{8.11}$$

where $\left[Ca^{2+}\right]_i$is the total added concentration of calcium ions to the solution, and

$$[M] + \left[Ca^{2+}M\right] = [M]_0 \tag{8.12}$$

where $[M]_0$ is the total concentration of molecular groups to Ca^{2+}. We can write eq.8.10

$$K_{a,M} = \frac{x}{(\left[Ca^{2+}\right]_i - x)([M]_0 - x)} \tag{8.13}$$

where $x = [Ca^{2+}M]$.

Solving eq.8.13 for x yields

$$x = \frac{\frac{1}{K_{a,M}} + \left[Ca^{2+}\right]_i + [M]_0}{2} \pm \frac{\sqrt{\left(\frac{1}{K_{a,M}} + \left[Ca^{2+}\right]_i + [M]_0\right)^2 - 4\left[Ca^{2+}\right]_i [M]_0}}{2} \tag{8.14}$$

with the only physical solution

$$x = \frac{\frac{1}{K_{a,M}} + \left[Ca^{2+}\right]_i + [M]_0}{2} - \frac{\sqrt{\left(\frac{1}{K_{a,M}} + \left[Ca^{2+}\right]_i + [M]_0\right)^2 - 4\left[Ca^{2+}\right]_i [M]_0}}{2} \tag{8.15}$$

To extract the binding constant $K_{a,M}$, we globally minimize

$$\sum_i \left(\mathrm{x}\left(\left[Ca^{2+}\right]_i\right)/[\mathrm{M}]_0 - f^{exp}\left(\left[Ca^{2+}\right]_i\right)\right)^2 \tag{8.16}$$

where f^{exp} is the experimentally determined fraction of bonded amide or carboxylate that can be obtained from equation 8.8. Fig.8.10 and 8.11 show the fit obtained for glucuronic acid and N-acetyl-glucosamine, respectively.

8.5.3 Saturation model for the binding of calcium ions to hyaluronan

We describe the binding of calcium binds to hyaluronan with a binding constant $K_{a,H}$

$$Ca^{2+} + HA \overset{K_{a,H}}{\rightarrow} Ca^{2+}HA \tag{8.17}$$

The fraction of binding sites of hyaluronan that gets occupied with calcium rapidly saturates with increasing added calcium concentration, which indicates that the binding process is anti-cooperative, i.e. the binding of Ca^{2+} leads to a penalty energy that increases with increasing fraction of occupied sites. To describe this effect, we take the equilibrium equation:

$$K_{a,H} = \frac{[Ca^{2+}HA]}{[Ca^{2+}]\,[HA]} \tag{8.18}$$

and we set the equilibrium constant $K_{a,H}$ equal to its value in the limit of no binding K_{a,H_0} multiplied with an exponential term containing a penalty energy E_p that is proportional to the fraction of occupied sites:

$$K_{a,H}(f) = K_{a,H_0} e^{-\frac{E_p}{k_b T} f} \tag{8.19}$$

with

$$f = \frac{[Ca^{2+}HA]}{[HA] + [Ca^{2+}HA]} \tag{8.20}$$

Similar as in the previous model for monomers we can rewrite eq.8.18 to:

$$K_{a,H} = \frac{x}{([Ca^{2+}]_i - x)([HA]_0 - x)} \tag{8.21}$$

Where $x = [Ca^{2+}HA]$. Solving eq.8.21 yields:

$$x = \frac{\frac{1}{K_{a,H}} + [Ca^{2+}]_i + [HA]_0}{2} \pm \frac{\sqrt{\left(\frac{1}{K_{a,H}} + [Ca^{2+}]_i + [HA]_0\right)^2 - 4\,[Ca^{2+}]_i\,[HA]_0}}{2} \tag{8.22}$$

with the only physically meaningful solution:

$$x = \frac{\frac{1}{K_{a,H}} + [Ca^2+]_i + [HA]_0}{2} - \frac{\sqrt{\left(\frac{1}{K_{a,H}} + [Ca^2]_i + [HA]_0\right)^2 - 4\,[Ca^{2+}]_i\,[HA]_0}}{2} \tag{8.23}$$

By using $[HA] + [Ca^{2+}HA] = [HA]_0$ and $f = x/[HA]_0$ we obtain that

$$f = \frac{1}{2} + \frac{\frac{1}{K_{a+1}} + [Ca^2]_i}{2[HA]_0} - \frac{\sqrt{\left(\frac{1}{K_{a,H}} + [Ca^{2+}]_i + [HA]_0\right)^2 - 4\,[Ca^{2+}]_i\,[HA]_0}}{2[HA]_0} \tag{8.24}$$

To extract the binding constant $K_{H,0}$ and the penalty energy E_p, we globally minimize

$$\sum_i \left(f^{ext}\left(\left[Ca^{2+}\right]_i\right) - f\left(\left[Ca^{2+}\right]_i\right)\right)^2 \tag{8.25}$$

where f^{ext} is obtained from equation eq.8.10, and $f([Ca^{2+}]_i)$ is obtained by solving the following system of two coupled equations

$$\begin{cases} f\left(\left[Ca^{2+}\right]_i\right) - \\ \frac{1}{2} - \frac{\frac{1}{K_{a,\bar{H}}} + [Ca^{2+}]_i}{2[HA]_0} + \frac{\sqrt{\left(\frac{1}{K_{a,H}} + [Ca^{2+}]_i + [HA]_0\right)^2 - 4\,[Ca^{2+}]_i\,[HA]_0}}{2[HA]_0} = 0 \\ \log K_{a,H} - \log K_{a,H_0} + \frac{E_p}{k_b T} f\left(\left[Ca^{2+}\right]_i\right) = 0 \end{cases} \tag{8.26}$$

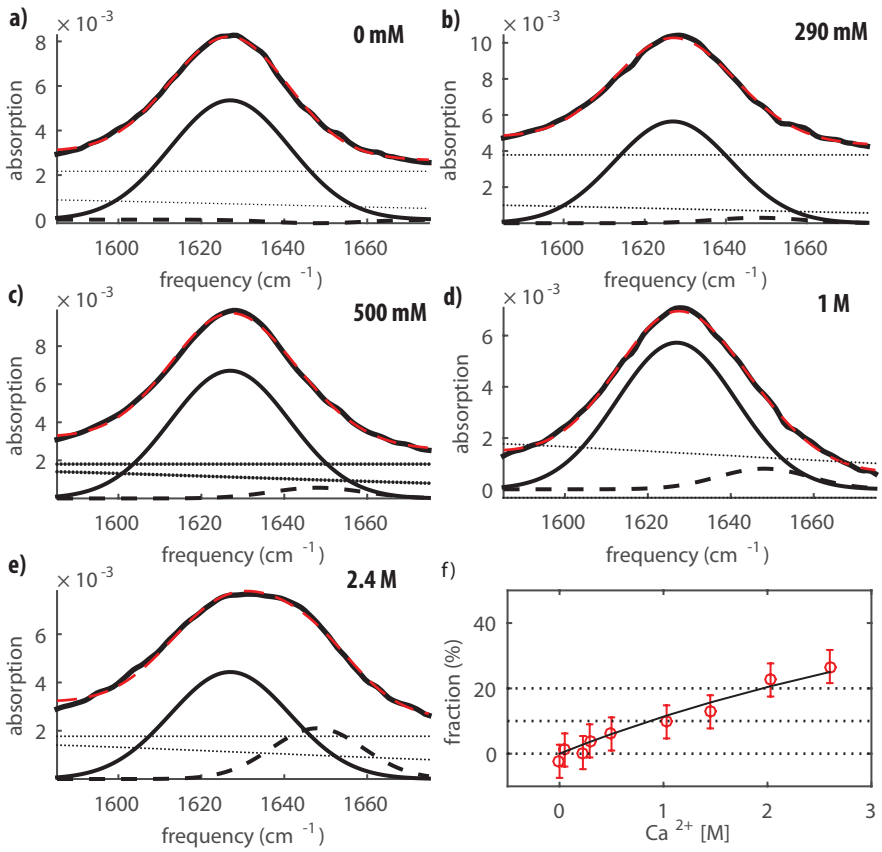

Figure 8.10: a), b) , c) ,d) and e) ATR spectra of N-acetyl-glucosamine at a concentration of 10 mg/ml for five different added calcium concentrations. Upon addition of calcium, we observe a broadening and a blue shift of the band. The spectra are fitted with two Gaussians-shaped bands, which represent the amide I mode of the amide groups that are not bonded to calcium ions and the amide groups that are bonded to calcium ions. In addition to the Gaussian-shaped bands, the fit of the spectra also contains the spectrum of heavy water and a straight line to compensate for the offset due to experimental issues encountered in the background subtraction. The Gaussian band of the not-bonded amide groups is centered at 1627 $\pm$2 cm^{-1} and has a width of 37 $\pm$3 cm^{-1}, and the Gaussian band of the bonded amide groups is centered at 1648 $\pm$3 cm^{-1} and has a width of 48 $\pm$3 cm^{-1}. The amplitudes of the Gaussians are free parameters, that are optimized at every added calcium concentration. e) Fraction of bonded amide as a function of calcium concentration. The experimental fraction (red dots) is obtained by fitting the linear spectra at different concentrations, and by taking the areas of the two Gaussian-shaped bands. The error bars are obtained by propagation of the experimental errors and the fit errors. The data are fitted to the equilibrium model described in Sec.8.5.2. We found $K_{a,M} = 0.125 \pm 0.05$ M^{-1}.

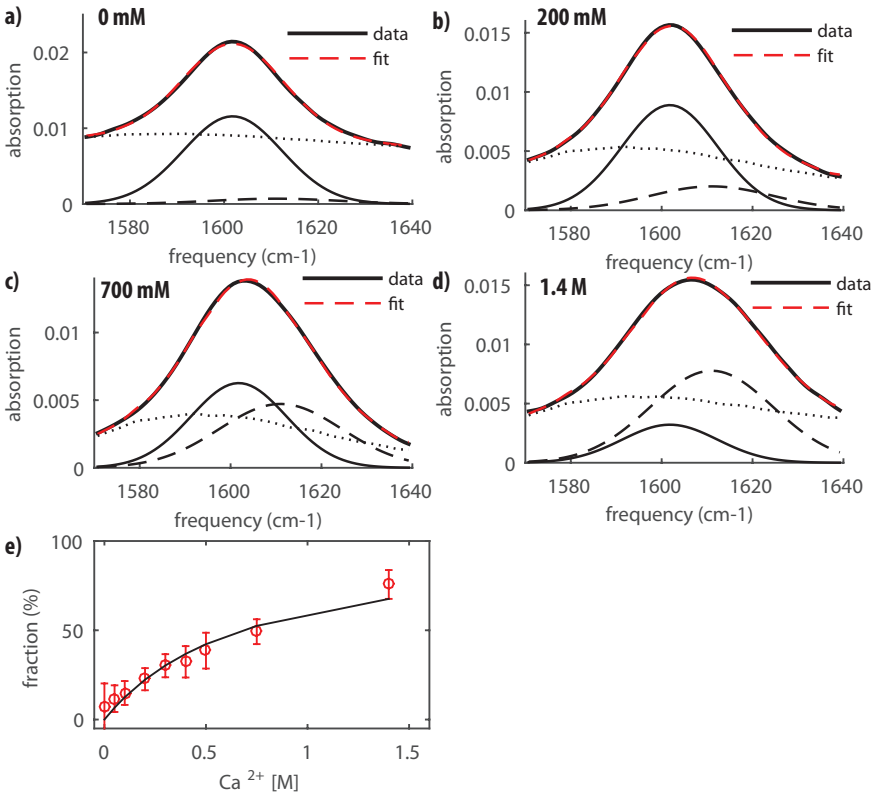

Figure 8.11: a), b) , c) and d) ATR spectra of glucuronic acid at a concentration of 10 mg/ml for four different calcium concentrations. Upon addition of calcium, we observe a broadening and a blue shift of the band. The spectra are fitted with two Gaussian-shaped bands, which represent the anti-symmetric stretching modes of the carboxylate anion groups, the carboxylate groups not-bonded to Ca^{2+} and the carboxylate groups that are bonded to Ca^{2+}. In addition to the Gaussian-shaped bands, the fit of the spectra also contains the spectrum of heavy water, which shows a broad band centered around 1550 cm^{-1}, to compensate for the offset due to experimental issues encountered in the background subtraction. The Gaussian band of the carboxylate group that is not bonded is centered at 1601 $\pm$2 cm^{-1} and has a width of 35 $\pm$2 cm^{-1}, and the Gaussian of the carboxylate group that is bonded is centered at 1611 $\pm$3 cm^{-1} and has a width of 45 $\pm$3 cm^{-1}. The amplitudes of the Gaussians are the only parameters that are allowed to vary with the added calcium concentration.e) Fraction of bonded -COO^- as a function of added $[Ca^{2+}]$. The experimental fraction (red dots) is obtained by fitting the linear spectra measured at different calcium concentrations, and by taking the areas of the two Gaussians-shaped bands. The error-bars are obtained by propagation of the experimental errors and the fit errors. The data are fitted with the equilibrium model described in Sec.8.5.2. We found that $K_{a,M} = 1.2\pm0.2$ M^{-1}.

Published as:

Giulia Giubertoni, Federica Burla, Cristina Martinez-Torres,Biplab Dutta, Galja Pletikapic, Eddie Pelan, Yves L. A. Rezus, Gijsje H. Koenderink,and Huib J. Bakker, Molecular Origin of the Elastic State of Aqueous Hyaluronic Acid, *Journal of Physical Chemistry B, 2019*

9

Molecular Origin of the Elastic State of Aqueous Hyaluronic Acid

Abstract

The macroscopic mechanical properties of biological hydrogels are broadly studied and successfully mimicked in synthetic materials, but little is known about the molecular interactions that mediate these properties. Here, we use two-dimensional infrared spectroscopy to study the pH-induced gelation of hyaluronic acid, a ubiquitous biopolymer, which undergoes a transition from a viscous to an elastic state in a narrow pH range around 2.5. We find that the gelation originates consisting of a double amide -COOH hydrogen bond and an N-D-COO^- hydrogen bond on the adjacent sugars of the hyaluronan disaccharide unit. We confirm the enhanced interchain connectivity in the elastic state by atomic force microscopy imaging.

9.1 Introduction

Hydrogels regulate the mechanical properties of cells and tissues and thereby play an important role in many biological and pathophysiological processes, ranging from stem cell differentiation and the degradation of aging cartilage to wound healing.[34,126,160,175–177] An important feature of natural hydrogels is their ability to tune their viscoelastic properties in response to environmental stimuli such as the solution pH, temperature and salt conditions. Up to now, it has been difficult to connect the macroscopic response of hydrogels to the underlying molecular interactions, e.g. hydrogen-bond and hydrophobic interactions, thus limiting the capability to predict and tune the properties of hydrogels.

One of the few techniques able to track interactions at the molecular scale is two-dimensional infrared spectroscopy (2DIR).[43] 2DIR shares with two-dimensional nuclear magnetic resonance (2D-NMR) the ability to resolve molecular couplings and dynamics, but 2DIR can resolve these interactions at a much shorter time scale. Molecular interactions such as hydrogen-bonds or electrostatic forces usually change on a time scale of picoseconds, and with 2DIR snapshots of these interactions can be taken with femtosecond time resolution.[139]

Here we use 2DIR to identify the molecular interactions that drive the pH-triggered gelation of hyaluronic acid, a natural polyelectrolyte that has received widespread attenion, being one of the main components of the extracellular matrix. It is important for cell-cell communication and also plays an important role in many biological processes such as joint lubrication, skin hydration and cell migration[122], while its dysregulation contributes to cancer development.[30] Due to its biocompatibility, hyaluronic acid is also widely used as a scaffold for cell culture and drug delivery.[123,178–181]Hyaluronic acid is a paradigmatic example of a responsive natural hydrogel: it displays a sharp transition in mechanical behavior at pH 2.5, switching from a viscous state to an elastic gel denoted as the 'putty state'.[36] The mechanism underlying this remarkable liquid-to-gel transition has been investigated for over almost a century with macroscopic techniques that map the dependence of the viscoelastic properties on pH, temperature and ionic strength.[128–130]

Based on these studies, it has been proposed that at pH=2.5, the net charge of the polyelectrolyte chains may be sufficiently suppressed to enable the formation of inter-chain hydrogen-bond interactions that would act as crosslinks.[137,163,182–186] This principle was suggested to be applicable to the wider class of polysaccharides[187], but there has been no direct evidence for this putative pH-triggered hydrogen-bonding mechanism.

9.2 Results

9.2.1 Rheology and Linear Infrared Spectroscopy

Hyaluronic acid has a relatively simple linear structure and homogeneous composition with repeating disaccharides composed of N-acetyl-glucosamine and glucuronic-acid (illustrated in the inset of Fig. 9.1b. The pH-dependent viscoelastic behavior of hyaluronic acid solutions stands out clearly in tube inversion assays, as shown in Fig.9.1a.. While the sample prepared in a solution state ("s") at pH 1.6 readily flows, the sample prepared in the "putty state" ("p") at pH 2.5 only flows on a time scale of minutes. This large difference in time scales originates from a pH-triggered transition in rheological properties from liquid to gel. To study the pH dependence of this transition in quantitative detail, we performed rheological experiments on semi-dilute solutions of high and low molecular weight hyaluronic acid. We studied solutions in heavy water (D_2O), since heavy water is used as a solvent in 2DIR studies of the amide and carbonyl vibrations. 2DIR cannot be applied to solutions in H_2O, as the amide and carbonyl vibrations of hyaluronic acid absorb in the same infrared frequency region as the bending vibration of H_2O (between 1600 and 1700 cm^{-1}). In all experiments, the pD values are converted to pH values (see Appendix Section 7.4).[149] Fig. 9.1b shows that the elastic and the viscous moduli sharply increase in a narrow range around a pH of 2.5, revealing a liquid-gel transition. This transition occurs at a pH value just below the pK_a, which is about 2.9.[129,137,178]

We studied the protonation state of hyaluronan as a function of pH with linear IR spectroscopy (Fig.9.1c). The relative intensities of the carboxylic acid and carboxylate anion bands of hyaluronan directly reflect the protonation state of hyaluronan.The anti-symmetric vibration of the carboxylate

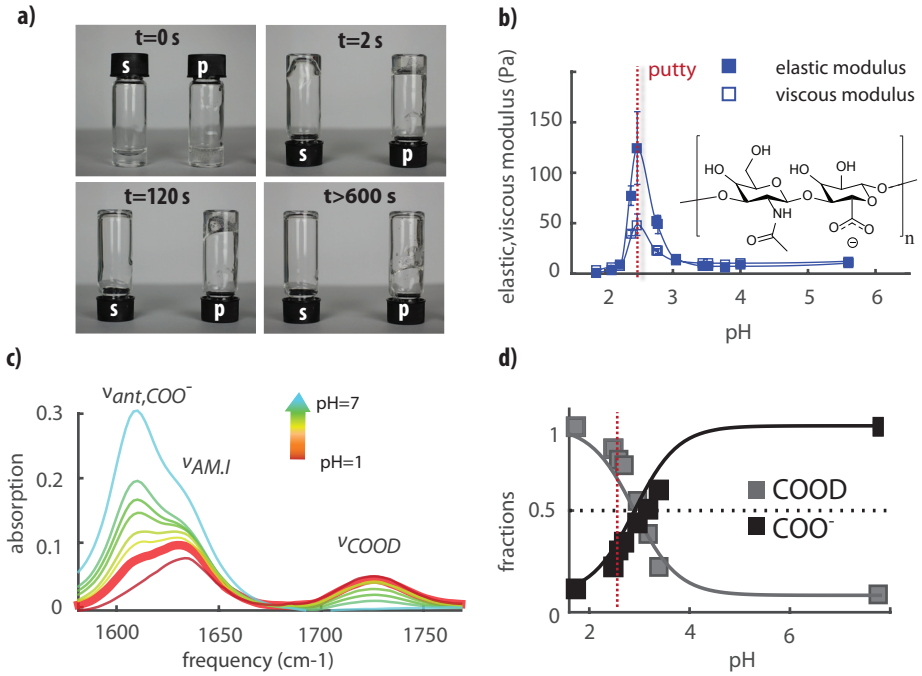

Figure 9.1: Hyaluronic acid solutions undergo a sol-gel transition in a narrow pH range. a) A tube inversion assay shows that hyaluronic acid solutions prepared at pH 1.6 exhibit viscous flow (s), whilst solutions prepared at pH 2.5 form a viscoelastic gel (p) that flows only on time scales beyond 2 min. b) The pH dependence of the viscous and elastic modulus of hyaluronic acid in heavy water solutions. We observe a sharp peak in the elastic shear modulus at pH 2.5. Inset shows that hyaluronic acid is a polymer of disaccharides, themselves composed of D-glucuronic acid and N-acetyl-D-glucosamine. c) Linear infrared spectra for hyaluronic acid solutions in D_2O at pH values ranging between 1.6 and 7. The infrared spectrum at pH=2.5 is represented by the thick solid line. Between 1550 and 1760 cm^{-1} we observe three bands: the anti-symmetric stretching mode of the carboxylate anion group, $\nu_{ant,COO-}$, at 1607 cm^{-1} , the amide I vibration, $\nu_{AM.I}$, at 1633 cm^{-1} and at 1726 cm^{-1} the carboxylic acid stretching mode, ν_{COOD} . d) Fractions of COO- and COOD groups determined from the IR spectra as a function of pH. Thick lines represent the expected fractions based on acid-base equilibrium equations (see Chapter 7 Appendix Section 7.4) assuming a pK_a=2.9. We find good agreement between the measured and expected carboxylic and carboxylate fractions, with about 25% deprotonation of the carboxyl groups at pH=2.5.

anion, $\nu_{ant,COO-}$, absorbs at 1607 cm^{-1}, and the amide I band, $\nu_{AM.I}$absorbs at 1633 cm^{-1}. The C=O vibration of the COOD group, that will be denoted

as ν_{COOD}, absorbs around 1726 cm^{-1}. At pH = 2.5, the COO- and COOD groups are present in a ratio of 1:4 (inset in Fig.9.1c), which corresponds to a pK_a of 2.9, as reported in literature.[178]

9.2.2 Two-Dimensional Infrared Spectroscopy

We use 2DIR spectroscopy to study the intermolecular interactions among hyaluronic acid chains that lead to the sol-gel transition. We excite the amide and the carboxyl vibrations with a strong femtosecond infrared pulse pair ($\sim$100 fs, 4 μJ per pulse). This excitation induces transient absorption changes that are probed with a weaker (0.35 μJ) single femtosecond probing pulse that is delayed by a time T_w. The excitation and probe pulses are centered at 1680 cm^{-1} with a bandwidth of 200 cm^{-1}. The excitation and probe spectra thus have sufficient spectral width to cover the ν=0 to ν=1 transition (bleach) and the ν=1 to ν=2 transition (excited state absorption, or esa) of the $\nu_{ant,COO-}$, the ν_{COOD}, and the $\nu_{AM.I}$vibrations.

Fig.9.2a and Fig.9.2b compare the 2DIR spectra measured for the solution (pH=1.6) and the putty state (pH=2.5), both for T_w =1.5 ps. Bleaching (increased transmission) is indicated in blue, while increased absorption (esa) is indicated in red. The bleach of the v=0 to v=1 transition, and the esa of the $\nu_{AM.I}$ are centered at 1639 cm^{-1} and 1619 cm^{-1}, respectively, along the probe frequency axis, while for the ν_{COOD} these signals are centred at 1731 cm^{-1} and 1703 cm^{-1}, respectively. The bleaching and esa of the $\nu_{ant,COO-}$ mode are in the low-frequency wing of the bleaching and esa of the amide I vibration, and lead to an elongation of the bleaching and the induced absorption signals to the lower-left corner of the 2DIR spectrum. We observe additional signals in the off-diagonal regions of the 2DIR spectrum, indicating that the carboxyl and amide modes are coupled. In the upper pump-frequency region, the cross-peak signal represents the effect of the excitation of the ν_{COOD} vibration on the spectrum of the $\nu_{AM.I}$ mode. In the lower pump-frequency region, the spectral shape of the carboxylic acid vibration is elongated along the pump axis.This effect reduces the visibility of the upward cross-peak, which represents the effect of the excitation of the $\nu_{AM.I}$ vibration on the spectrum of the ν_{COOD} vibration. For this reason,

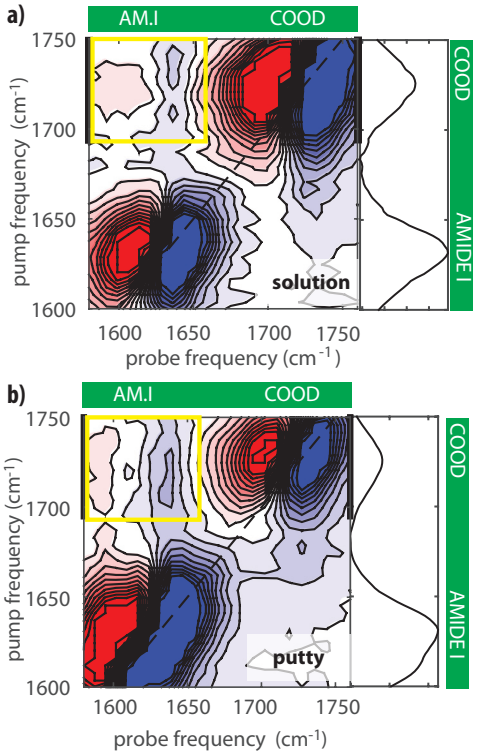

Figure 9.2: Isotropic two-dimensional infrared spectra of solutions of hyaluronic acid in D_2O at a concentration of 20 mg/ml in the spectral region of the carboxylic acid (ν_{COOD}) and the amide I ($\nu_{AM.I}$) vibrations. 2D IR spectra (a) for the solution state (pH=1.6), and (b) for the putty state (pH=2.5). The corresponding linear spectra are shown on the right-hand side of the 2DIR spectra. The spectra were collected at a delay time Tw of 1.5 ps. The cross-peaks are indicated by the yellow rectangles and show the presence of vibrational interactions between $\nu_{AM.I}$and ν_{COOD}. The thick black lines represent the integrated pump-region used for the fitting. The pump and probe spectra are centred at 1680 cm^{-1}.

we focus our analysis on the downward cross-peak that represents the effect of the excitation of the carboxylic acid vibration on the $\nu_{AM.I}$ vibration.

The excitation of the ν_{COOD} vibration also affects the spectrum of the amide II mode ($\nu_{AM.II}$) around 1490 cm^{-1}, as illustrated in Fig.9.3a. We observe the presence of off-diagonal signals at two different probe frequencies, around 1435 cm^{-1} (which we assigned to the bending modes of the –COH and –CH groups of the N-acetyl-galactosamine and glucurononic acid moieties) and 1490 cm^{-1} (corresponding the amide II vibration). At the amide II probe frequency, we observe a cross-peak at the excitation frequencies of the amide I and carbonyl stretching mode. Fig.9.3b shows the integrated cross-peak signal of the ν_{COOD} and $\nu_{AM.II}$ vibrations as a function of time delay. We observe that the ν_{COOD} -$\nu_{AM.II}$ cross-peak is not instantaneous: the maximum of the intensity is reached after $\sim$1.5 ps. The observed dynamics

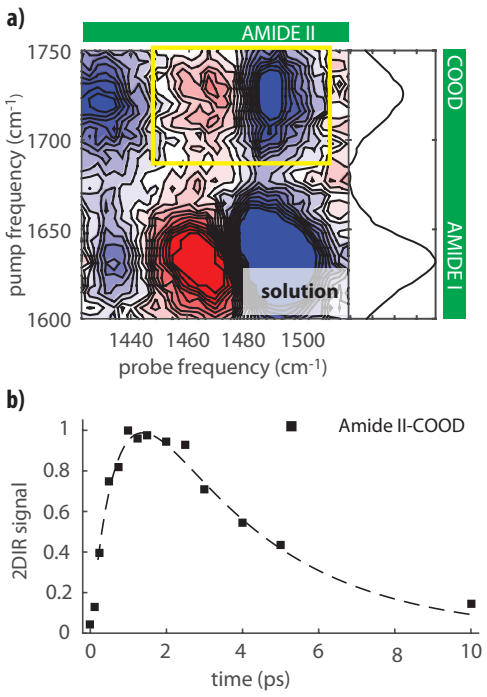

Figure 9.3: a) Isotropic 2DIR spectrum for hyaluronic acid in D_2O solutions at a concentration of 15 mg/ml in the solution state. Spectrum was collected at a delay time of 1.5 ps. The pump and probe spectra are centered at 1680 cm^{-1} (AMIDE I region)and 1450 cm^{-1} (AMIDE II region) respectively. The cross-peak, which appears in the region indicated by the yellow rectangle, reveals a vibrational interaction between $\nu_{AM.II}$ and ν_{COOD}. Due to the low signal-to-noise at pH 2.5, it was not possible to perform the same experiment in the putty state. b) Decay trace for the cross-peak in the $\nu_{AM.II}$ vibrational region normalized to the minimum intensity. The decay is fit to a two-step consecutive reaction model, shown by the dashed line. The time constants are 0.7 ps for the initial signal growth and 3.3 ps for the decay. The build-up time constant is comparable to the vibrational relaxation time $T1_{COOD}$ of the COOD parent-mode of 0.65$\pm$0.1 ps.

can be well described with a double exponential function with a build-up time constant τ_1 of $\sim$0.7 ps and a decay time constant τ_2 of $\sim$3 ps. The build-up time constant is comparable to the vibrational relaxation time $T_{1.LFM}$ of the COOD parent-mode of 0.65$\pm$0.1 ps. The decay time τ_2 is much longer than the vibrational lifetimes of the COOD, amide I, and amide II vibrations. This result indicates that the ν_{COOD} -$\nu_{AM.II}$ cross-peak results from the transient excitation of low-frequency modes within the hyaluronic acid chain that affect the absorption spectrum of the amide II vibration. The low-frequency modes become excited as a result of the vibrational relaxation of ν_{COOD}, thus explaining the build-up of the cross-peak signal with τ_1 of $\sim$0.7 ps. The cross-peak signal decays when the low-frequency modes transfer their energy to other modes, for instance to the modes of water. The time constant τ_2 thus represents the time constant $T_{1.LFM}$ of the relaxation of the

low-frequency modes.

To learn more about the mechanism that underlies the cross-peak sig-

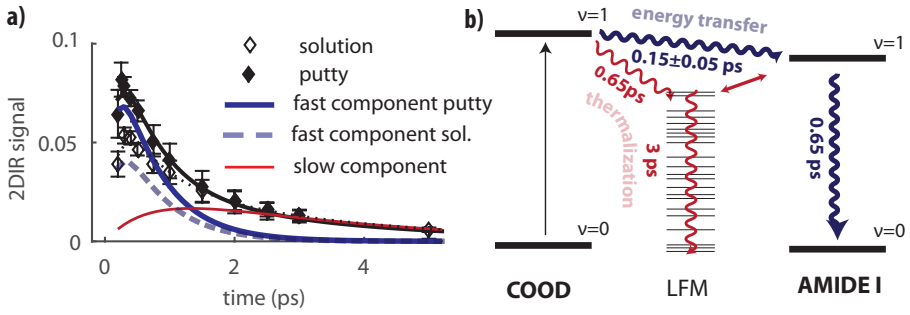

Figure 9.4: a) Decay traces of the cross-peak in the $\nu_{AM.I}$ vibrational region extracted by fitting the isotropic signal (see Appendix Section 9.5.1) for hyaluronic acid at a concentration of 20 mg/ml in the solution and putty states . The decay traces are normalized to the carboxylic acid intensity at early time delay. The solid and dashed black lines are fits to the relaxation model (see the Appendix Section 9.5.3), for the putty and solution states, respectively. The initial amplitude of the fast component (indicated with c_{ent}) is nearly two times larger in the putty state ($c_{ent} = 0.13 \pm 0.01$) than in the solution state($c_{ent} = 0.077 \pm 0.005$). The red line represents the contribution of the slow component, whose initial amplitude $c_{thputty} \sim c_{thsol.} = 0.024 \pm 0.004$. b) Schematic of the relaxation model describing the cross-peak dynamics. Red and blue lines refer, respectively, to the slow component (due to thermalization) and fast component (due to energy transfer) of the cross-peak dynamics. Values shown are the average with standard deviation for 6 independent measurements.

nals of the amide I modes following excitation of the COOD vibration, we compare the dependence on time delay for the solution and the putty states (Fig. 9.4a). We normalized the transients to the bleaching signal of the carboxylic acid vibration at early time delay (~0.2 ps). From ~1.5 ps on, the decay of the transients is quite similar to that of the ν_{COOD} - $\nu_{AM.II}$ cross-peak, showing a time constant of ~3 ps. However, the transients of the ν_{COOD} - $\nu_{AM.I}$cross-peak signals have their maximum at 0.3-0.5 ps, a much earlier delay time than the one observed for the ν_{COOD} - $\nu_{AM.II}$ cross-peak (~1-1.5 ps). In addition, the transients of the ν_{COOD} - $\nu_{AM.I}$cross-peak show an additional faster decay component with a time constant of ~0.6 ps. Interestingly, the transient of the ν_{COOD} - $\nu_{AM.I}$ cross-peaks has a much higher intensity at early delay times for the putty state than for the solution

state. This observation, together with the dynamics observed for the ν_{COOD} - $\nu_{AM.II}$ cross-peak, indicates that the ν_{COOD} - $\nu_{AM.I}$cross-peak signal contains contributions from two distinct mechanisms: 1) energy transfer from the excited COOD vibration to the amide I vibration; 2) anharmonic coupling to low-frequency modes that affect the vibrational spectrum of the amide I mode. The relaxation model corresponding to these two mechanisms is illustrated in Fig.9.4b. The cross-peak signal arising from the energy transfer rises with a time constant T_{ent}, representing the time scale of energy transfer from the excited COOD vibration to the accepting amide I vibration, and decays with the vibrational lifetime $T_{1.AM.I}$ of the amide I vibration. This direct energy transfer does not occur for the amide II mode because there is a rather large energy difference between the ν_{COOD} and $\nu_{AM.II}$ vibrations. We extract the value of $T_{1.AM.I}$ from the diagonal signal of the amide I mode in the 2DIR spectrum. We find that $T_{1.AM.I}$ is comparable to the vibrational lifetime of the COOD vibration: $T_{1.AM.I}$ = 0.65$\pm$0.1 ps. The time constants of the second mechanism involving anharmonic coupling to low-frequency modes can be extracted from a fit to the transient of the ν_{COOD} - $\nu_{AM.II}$ cross-peak (Fig.9.3b). We thus fit the transients of the ν_{COOD} - $\nu_{AM.I}$ cross-peak to the following expression containing the lifetimes of the COOD vibration, $T_{1.COOD}$, the amide I vibration, $T_{1,AM.I}$, and the low-frequency-modes, $T_{1.LFM}$:

$$\begin{aligned}\frac{\Delta\alpha_{CP}(t)}{\Delta\alpha_{COOD}(t)} = c_{anh}\frac{T_{1LFM}}{T_{1COOD}-T_{1LFM}}(e^{\frac{-t}{T_{1COOD}}}-e^{\frac{-t}{T_{1LMF}}}) \\ +c_{ent}\frac{T_{1AM.I}}{T_{ent}-T_{1AM.I}}(e^{\frac{-t}{T_{ent}}}-e^{\frac{-t}{T_{1AM.I}}})\end{aligned} \tag{9.1}$$

Here $\frac{\Delta\alpha_{CP}(t)}{\Delta\alpha_{COOD}(t)}$ is the intensity of the cross-peak normalized to the intensity of the ν_{COOD} vibration at early time delay, t=200 fs. The parameters $c_{anh}$and c_{ent} represent the cross-peak amplitudes associated with the anharmonic coupling and direct energy transfer mechanisms, respectively. T_{ent},c_{anh} and c_{ent} are the only free parameters. As shown in Fig.9.4a, c_{ent} is nearly twofold larger for the putty state than for the solution state, whereas $c_{anh}$is comparable for the two states. For the time constant T_{ent} we obtain a value of 150 $\pm$50 fs. The energy transfer to the amide I mode constitutes

an additional channel for vibrational relaxation of the COOD mode. The fact that we do not observe a significant difference in T_{1COOD} between the putty and the solution state indicates that this energy transfer process only occurs for a minor fraction of the COOD groups. From the values of c_{ent}, we estimate this fraction to be $13\pm2\%$ for the putty state and $7\pm2\%$ for the solution state. The time constant T_{ent} also does not change upon the formation of the putty state which shows that the efficiency of the energy transfer remains the same. Hence, upon formation of the putty state only the number of COOD groups showing energy transfer increases.

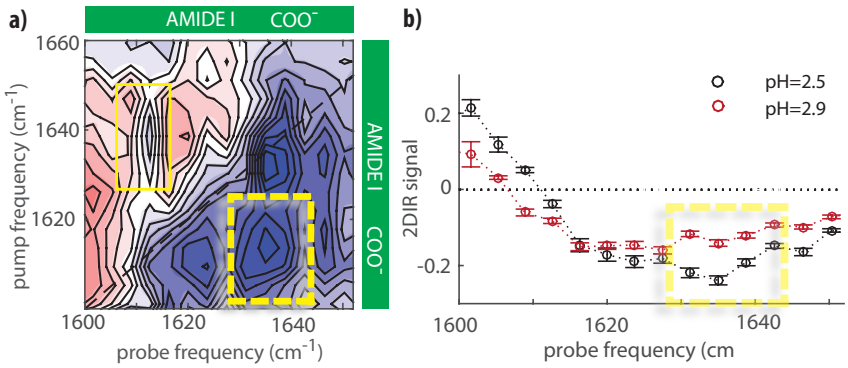

Figure 9.5: a) Difference 2DIR spectrum for a solution of hyaluronic acid at pH 2.5 at a concentration of 20 mg/ml. The difference 2DIR spectrum was obtained by subtracting the parallel signal from three times the perpendicular signal. The yellow rectangles indicate the cross-peak signals of the amide I and COO- modes. b) Transient absorption spectra obtained by averaging over the pump frequency region between 1600 and 1620 cm^{-1} at pH 2.5 and 2.9, and normalized with respect to the pure anti-symmetric stretching signal of the carboxylate anion group (Fig.9.10-9.11).

The ultrafast energy transfer between the C=O vibration of the COOD group and the amide I vibration of the amide group can be well explained from the presence of a hydrogen bond between the COOD and the amide groups.[188] To get more information on the nature of this hydrogen bond, we compared the intensity of the ν_{COOD}-$\nu_{AM.I}$ cross-peak signal for polarizations of the probing pulse parallel and perpendicular to the polarization of the excitation pulse. The ratio of these two signals reveals the relative orientation of the transition dipole moments of the excited and probed vibrations

that form the cross-peak signal.[189] From the ratio of the signals at T_w between 0.3 and 1 ps (where the energy transfer mechanism is predominant), we find that the angle between the transition dipoles of ν_{COOD} and $\nu_{AM.I}$is $\sim 20^\circ$ (see Appendix Section 9.5.2 and Fig.9.9). As the transition dipole moment of $\nu_{AM.I}$is at an angle of $\sim 20^\circ$ relative to the C=O bond of the amide group,[37] we conclude that the hydrogen-bond configuration involves a parallel (or anti-parallel) alignment between the C=O groups of the carboxylic acid and amide, forming two closely spaced intermolecular hydrogen bonds between the amide and carboxylic acid groups, i.e. C=O-OD...O=C-ND and -N-D...O=C-OD...O=C-. This geometry, in which the amide and carboxylic acid groups act both as hydrogen-bond donor and acceptor stabilizing the hydrogen-bonded structure formed by these two molecular groups, constitutes a strong inter-chain connection. We conclude that the putty state at pH=2.5 contains a two-fold higher density of these strong double hydrogen-bonds than the solution state at pH=1.6.

To study the role of the COO- groups in the formation of the putty state, we also measure 2DIR spectra where we excite and probe the $\nu_{ant,COO-}$ and the $\nu_{AM.I}$vibrations. Since the absorption bands of these two vibrations overlap, we subtract the parallel signal from three times the perpendicular signal. In the resulting difference spectrum, the diagonal peaks are strongly suppressed since the corresponding parallel signal is ~ 3 times larger than the perpendicular signal. This procedure is thus ideally suited to reveal the presence of cross-peak signals of vibrations that are differently oriented. This strategy has been extensively used in 2DIR experiments on proteins to resolve vibrational couplings.[140] Fig.9.5a reports the resulting difference 2DIR spectrum at pH= 2.5 (putty state). On the diagonal, we observe some residual signal due to orientational relaxation of the COO- and amide molecular groups.[190–192] In addition, we also see clear off-diagonal signals (indicated by the yellow rectangles). In Figure 9.5b we plot the transient absorption spectrum at pH=2.5 (black cirkles) obtained from Fig.9.5a by averaging the signals with pump frequencies between 1600 and 1620 cm^{-1}, corresponding to the excitation of the $\nu_{ant,COO-}$ vibration. The resulting spectrum is compared with the transient absorption spectrum at pH=2.9

that is obtained using the same procedure (see Appendix Section 9.5.4 and Fig. 9.11). The transient absorption spectrum at pH 2.5 clearly shows an enhanced absorption signal around the amide I vibrational frequency, which implies that excitation of the $\nu_{ant,COO-}$ vibration yields an enhanced response of the $\nu_{AM.I}$ vibration at pH=2.5. This means that in the putty state (pH=2.5) the interaction between the COO- and amide molecular groups is enhanced. A similar enhancement is observed for the other cross-peak signal, i.e. exciting the amide I vibration and probing the COO- mode (see Appendix Section 9.5.4 and Fig. 9.10f). Hence, our results show that the formation of single N-D-COO- hydrogen bonds is enhanced in the putty state, in addition to the enhanced presence of double amide-COOH hydrogen-bonds in this state.

9.2.3 Atomic Force Spectroscopy (AFM)

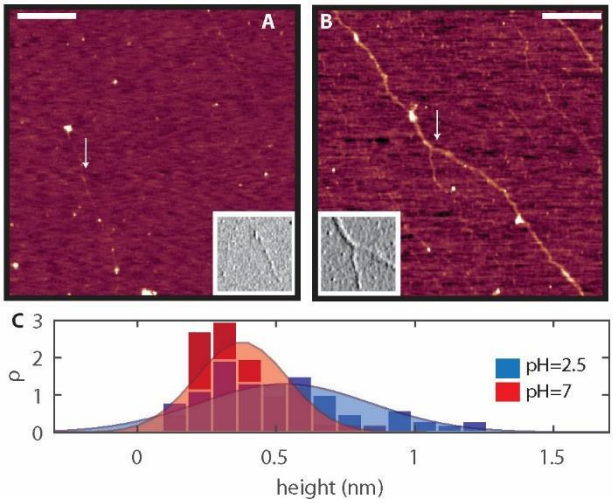

Figure 9.6: On the top, AFM height images of HA filaments at pH 7 and pH 2.5, respectively, colour coded from 0 nm (dark red) to 1.2 nm (white). The insets show amplitude images of smaller areas of 500x500 nm^2, indicated by the arrows. Scale bar: 500 nm. On the bottom, filament height distributions with Gaussian fits.

We also perform atomic force microscopy (AFM) imaging of hyaluronic acid solutions at different pH values to investigate to what extent the ad-

ditional hydrogen bonds in the putty state are formed within or between hyaluronic acid chains (Fig.9.6a,b). At pH=7 we mainly observe pearl-necklace conformations: thin chains alternating with thicker globular configurations. The globular portions are likely due to the low affinity for mica.[193] At pH=2.5 the AFM images clearly show a much larger density of thick filaments than at pH=7, indicative of inter-chain interactions. To quantify the extent of lateral association of hyaluronan polymers, we measured the heights of the filaments at pH=7 and pH=2.5 (Fig.9.6c). At neutral pH, we find a Gaussian height distribution centered at an average filament height h_0 =0.37 μm. This value is consistent with the expected thickness of a single hyaluronan chain.[193] At pH=2.5 we find a much broader distribution, and h_0=0.53 μm, meaning that the filaments are thicker. Since the length of the filaments at pH=2.5 is not changed compared with pH=7, we conclude that this thickening is mainly due to enhanced inter-chain interactions that laterally associate the strands.

9.3 Discussion

The two-dimensional infrared (2DIR) spectroscopy measurements show that the remarkable pH-triggered gelation of hyaluronic acid at pH 2.5 involves the enhanced formation of double hydrogen bonds between carboxylic acid and amide groups, and of strong single hydrogen bonds between carboxylate anion (which is a stronger hydrogen-bond acceptor) and amide groups. The enhanced formation of hydrogen bonds is intimately related and even enabled by changes in the structure and electrostatic interactions of the hyaluronan polymer chains. An important question is why the gelation only occurs in a narrow pH range. In particular, one may wonder why the gelation does not occur for a larger pH range below 2.5, as at lower pH there will be even more carboxylic acid groups and thus potentially even more strong double hydrogen bonds with the amide groups located on a different chain. The answer to this question can be found in the special structure of the hyaluronic acid disaccharide unit, which contains a carboxylic acid group and an amide group on neighboring sugar units (see inset of Fig.9.1b). The formation of a double amide-carboxylic acid hydrogen-bond structure involves a quite

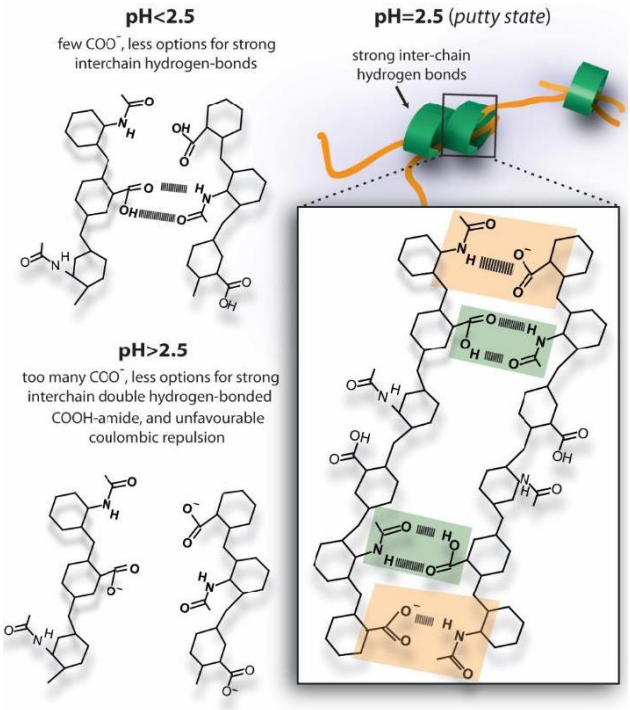

Figure 9.7: Schematic images showing the transition from a weakly hydrogen-bonded network of hyaluronan at pH$\leqslant$2.5 (top left) to a strongly hydrogen-bonded network at pH=2.5 values (right), to isolated single chains at pH$\geqslant$2.5 (bottom left). At pH=2.5 the balance between hydrogen-bond and Coulomb repulsion interactions is optimal, and allows the formation of hydrogen-bonds between the carboxyl acid and amide groups observed as the fast time component in the cross-peak dynamics in 2D IR. Green shaded squares indicate the formation of hydrogen-bonds between amide and protonated carboxyl groups, whilst orange shaded squares depict the formation of hydrogen-bonds between amide and deprotonated carboxyl groups.

strict local positioning of the hyaluronic acid chains, which prevents the formation of a second double hydrogen-bond structure at the adjacent saccharide units. Hence, the following mechanistic picture arises (Fig.9.7): at pH=2.5, the partial deprotonation of the carboxylic acid groups allows for a high probability of forming a strong double amide-COOH hydrogen-bond (green box) and an adjacent strong N-D-COO- hydrogen bond (orange box), together forming a very strong inter-chain connection. In the single N-D-

COO- hydrogen bond, the N-D of an amide group acts as the hydrogen bond donor and the COO- anion group as the hydrogen-bond acceptor. For a sufficient length and concentration of the hyaluronic acid chains, this enhanced hydrogen-bond formation will yield a long-range connected network that behaves as an elastic solid, the putty state. This state is not formed at lower pH, because at these pH values very few carboxylic acid groups are deprotonated and the strong double amide-COOH hydrogen-bond can only be combined with a relatively weak single N-D-COOH or single COOH-amide hydrogen bond on the neighboring sugar units, thus forming a weaker inter-chain connection. As a result, less inter-chain connections are formed (ca. two-fold less at pH=1.6) and the overall connectivity is too low to form an elastic gel. At pH values above 2.5, the putty state is also not formed, because a large fraction of the carboxylic acid groups is deprotonated, which implies that no double amide-COOH hydrogen-bonds can be formed. In addition, Coulomb repulsion will prevent the formation of N-D...-O-C hydrogen bonds on neighboring sugar units. As a result, the density of inter-chain connections is again too low to allow for gel formation.

9.4 Conclusion

In summary, we studied the molecular origin of the 'putty state' of the biologically important polysaccharide hyaluronic acid, which undergoes a sol-gel transformation only in a narrow range around pH=2.5. Using two-dimensional infrared (2DIR) spectroscopy, we find that this remarkable transition is accompanied by the enhanced formation of strong inter-chain connections that consist of a strong double amide-COOH hydrogen-bond (green box in Fig.9.7) and a strong N-D-COO- hydrogen bond (orange box in Fig.9.7) on the adjacent sugar groups of the hyaluronan disaccharide unit. These strong collective inter-chain connections can only form when the carboxylic acid groups are partially deprotonated, which explains why the putty state is observed in a narrow pH range only. The enhanced inter-chain connectivity in the putty state is confirmed by AFM measurements that reveal the association of hyaluronan into thick strands in this state.

The present study illustrates that the combination of 2DIR spectroscopy,

AFM and rheology constitutes a unique tool to identify the molecular mechanisms by which hydrogels respond to environmental stimuli. This combined multiscale approach has great potential to investigate the molecular origin of the biological functionalities of other natural polyelectrolytes, and to assist in the rational design of supramolecular biomaterials with life-like functionalities.[180]

9.5 Appendix

9.5.1 Fit of the transient absorption signal

The partial overlap of the –COOH diagonal peak with the cross-peak hinders a straightforward determination of the dynamics of the cross-peak. Specifically, the positive excited state absorption (esa) band of the diagonal peak obscures the negative bleach signal of the cross-peak. Furthermore, heating signals originating from the relaxation of the excited vibrations will obscure the cross-peak signal. Therefore, it is important to deconvolute the signal in order to extract the dynamics emanating solely from the cross-peaks. The

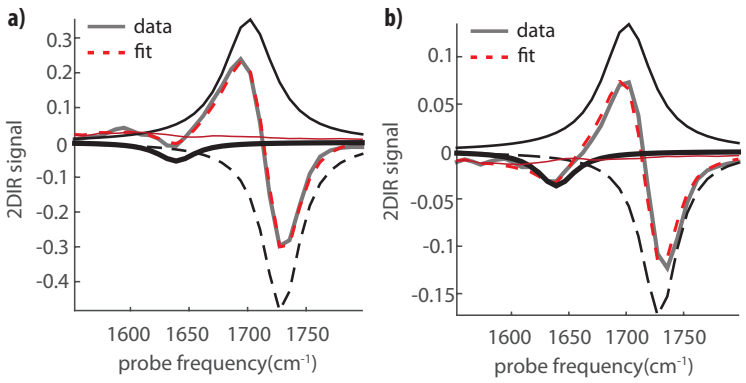

Figure 9.8: a) and b) examples of the fit of the transient absorption signal for solution of hyaluronan at 20 mg/ml at pH=2.5 at T_w=0.2 ps and T_w=0.9 ps, respectively. Thick black line represents the cross-peak' bleach, whilst continuous and dashed lines the esa and the bleach of the diagonal peak,respectively. The red continuous line represents the spectral response of the heating effect, which is taken from the transient absorption spectrum at 50 ps, when the vibrational dynamics are complete.

transient absorption spectrum following excitation of the ν_{COOD} vibration is

obtained by averaging the signals obtained with pump frequencies between 1700 and 1760 cm^{-1} (ν_{COOD} pump-region). The transient absorption spectrum following excitation of the ν_{COOD} mode is expected to be a linear combination of five band: two describing the bleach and induced absorption of the cross-peak, two describing the bleach and esa of the diagonal signal, and one describing the effect of heating on the transient absorption spectrum. However, the heating signal strongly diminishes the visibility of the esa band. Therefore, our fitting routine is not able to disentangle the contribution of the induced absorption of the cross-peak. Hence, we describe the transient absorption spectrum with three Lorentzians for the bleach and esa of the diagonal signal, and the bleach signal of the cross-peak, and a spectral signature representing the heating signal:

$$\begin{array}{c} \forall i,\ \text{for } \omega_{\min}^{\text{probe}} \leqslant \omega_j^{\text{probe}} \leqslant \omega_{\max}^{\text{probe}} \\ S\left(\omega_j^{\text{probe}}, t_i\right) = \sum_{k=1}^{3} c_k\left(t_i\right) l_k\left(\omega_j^{\text{probe}}\right) + c_h\left(t_i\right) h\left(\omega_j^{\text{probe}}\right) \end{array} \tag{9.2}$$

The heating spectrum is taken directly from the transient absorption spectrum at 50 ps, when the vibrational dynamics is over. The width and center position of the cross-peak and the width of the bleach of the diagonal peak are constrained in a global fit to the transient absorption spectra at all delays following excitation of the ν_{COOD} mode. The global fitting procedure is performed as a function of probe frequency and delay time and it is based on the minimization of the least-square error using the following expression

$$\sum_{ij}\left(S\left(\omega_j^{probe}, t_i\right) - S^{exp}\left(\omega_j^{probe}, t_i\right)\right)^2 \tag{9.3}$$

where S^{exp} represents the measured transient absorption spectrum. Examples of the fit are reported in Fig.9.8. The central frequencies and widths of the Lorentzians are presented in Table 9.1.

9.5.2 Cross-peak anisotropy

The aforementioned global fitting routine is used to determine the amplitudes of the Lorentzians in the 2DIR spectra measured with the polarization of the probe pulses parallel and perpendicular with respect to the pump

mode	Center Frequency (cm^{-1})	FHWM (cm^{-1})
ν_{COOD}^{esa}	1703 ± 1	47±2
ν_{COOD}^{bleach}	1731 ± 3	37±3*
$\nu_{AM.I}^{esa}$	1619 ± 2	48 ± 6
$\nu_{AM.I}^{bleach}$	1639 ± 2	39±4*
ν_{CP}^{bleach}	1639±3	39±4

Table 9.1: Parameters of the five Lorentzians representing the bleaching of the ν_{COOD} mode and of the $\nu_{AM.I}$ mode, the excited-state absorption of the ν_{COOD} mode and of the $\nu_{AM.I}$ mode, and the bleaching of the cross peak signal between the ν_{COOD} mode and the $\nu_{AM.I}$ mode in the transient absorption spectrum following excitation of the ν_{COOD} mode. The errors are the standard deviations computed by averaging over at least three different independent measurements. *To reduce the number of free parameters in the fit, we set the widths of the Lorentzians representing the bleach signals of the carbonyl vibration of the COOD group and the amide I vibration equal to the widths of the corresponding bands obtained from a fit of the linear infrared absorption spectrum.

pulse. By using the Lorentzian amplitudes of each mode extracted at every time t_i for parallel - $c_j^{par}(t_i)$ - and perpendicular - $c_j^{per}(t_i)$ - polarizations, we can then calculate the anisotropy $R_j(t_i)$, which is defined as:

$$R_j\left(t_i\right) = \frac{c_j^{par}\left(t_i\right) - c_j^{per}\left(t_i\right)}{c_j^{par}\left(t_i\right) + 2c_j^{per}\left(t_i\right)} \tag{9.4}$$

Fig.9.9 reports the obtained anisotropy values. We can extract the angle between the direction of the transition dipole moments at time 0 and time t_i woththe following relation between anisotropy value and the angle:

$$R\left(t_i\right) = \frac{3\cos^2\theta\left(t_i\right) - 1}{5} \tag{9.5}$$

For the cross-peak signal, the extracted angles reflect the relative orientation between the transition dipole moment of the carbonyl vibration of the carboxylic acid group and that of the amide I vibration at different delay times T_w (inset Fig.9.9). By averaging over 6 different measurements, we obtain an angle of 20± 5°.

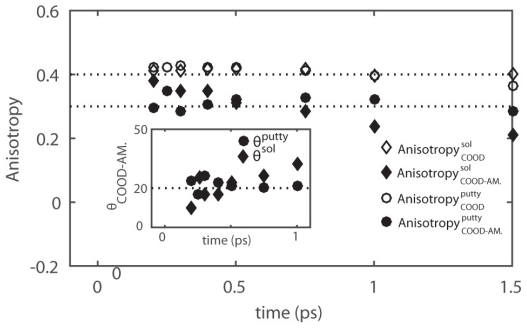

Figure 9.9: Anisotropy of the bleach of the cross-peak and of the diagonal peak of the carbonyl vibration of the –COOD group extracted by fitting the transient absorption spectra obtained by averaging over the pump frequency region between 1700 and 1760 cm^{-1} measured in parallel and perpendicular polarization configuration. In the inset, the extracted angles of the cross-peak anisotropy are plotted as a function of the delay time T_w.

9.5.3 Relaxation Model

We model the delay-time dependence of the cross-peak of the ν_{COOD} mode and the $\nu_{AM.I}$ mode (amide I mode) as the result of the relaxation of two carboxylic acid species. One species, with population $N_{th}(t)$, relaxes by energy transfer to lower-frequency modes. These lower-frequency modes are anharmonically coupled to the amide modes. The other carboxylic acid species, with population $N_{ent}(t)$, relaxes via energy transfer to a nearby amide I vibration. We thus write the cross-peak transient signal as:

$$\Delta\alpha_{cp}\left(\omega^{probe},t\right) = -2\sigma_{AM.I}\left(\omega^{probe}\right)\left(w\left(\beta_{AM.I,LFM}\right) * N_{th}(t) + N_{ent.}(t)\right) \tag{9.6}$$

where $\sigma_{AM.I}$ is the amide I cross-section and $w(\beta_{AM.I,LFM})$ is a coupling-dependent weighting factor that represents the effect of the excitation of the low-frequency modes on the spectrum of the amide I vibration. $N_{th}(t)$ and $N_{ent}(t)$ can be described as follows:

$$N_{th}(t) = N_{th}(t=0)\left(\frac{T_{1.LFM}}{T_{1.COOD} - T_{1.LFM}}\right)\left(e^{-t/T_{1.COOD}} - e^{-t/T_{1.LFM}}\right) \tag{9.7}$$

and

$$N_{ent}(t) = N_{ent}(t=0)\left(\frac{T_{1.AM.I}}{T_{ent}-T_{1.AM.1}}\right)\left(e^{-t/T_{ent}}-e^{-t/T_{1.AM.I}}\right) \quad (9.8)$$

where $T_{1.COOD}$ is the lifetime of the carboxylic acid mode (0.65±0.1 ps), $T_{1.AM.I}$ is the lifetime of the amide I mode (0.65±0.1 ps) and T_{1LFM} (∼3 ps) is the lifetime of the low frequency modes extracted from a fit to the cross-peak signal of the ν_{COOD} mode and the $\nu_{AM.II}$ mode (amide II mode). By normalizing the $\Delta\alpha_{cp}(\omega^{probe},t)$ to $\Delta\alpha_{COOD}(\omega^{probe},t=200fs)$ we obtain from eq.9.6 that

$$\frac{\Delta\alpha_{cp}\left(\omega^{probe},t\right)}{\Delta\alpha_{COOD}\left(\omega^{probe},t=200fs\right)} = \frac{-2\sigma_{AM.L}\left(\omega^{probe}\right)\left(w\left(\beta_{AM.I,LFM}\right)N_{th}(t)+N_{ent}(t)\right)}{-2\sigma_{COOD}\left(\omega^{probe}\right)N_{COOD}(t=200fs)} =$$
$$=\frac{\sigma_{AM.I}\left(\omega^{probe}\right)}{\sigma_{COOD}\left(\omega^{probe}\right)}\frac{\left(w\left(\beta_{AM.I,LFM}\right)N_{th}(t)+N_{ent}(t)\right)}{N_{COOD}(t=200fs)} = \quad (9.9)$$

and by using eq.9.7 and eq.9.8

$$= c_{th.}\cdot\left(\frac{T_{1,LFM}}{T_{1,COOD}-T_{,LFM}}\right)\left(e^{-t/T_{1.COOD}}-e^{-t/T_{1,LFM}}\right)+c_{ent.}\left(\frac{T_{1.AM.I}}{T_{ent}-T_{1.AM.I}}\right)\left(e^{-t/T_{ent}}-e^{-t/T_{1.,AM.I}}\right) \quad (9.10)$$

where

$$c_{th.}\equiv\frac{\sigma_{AM.I}\left(\omega^{\mathsf{probe}}\right)w\left(\beta_{AM.I,LFM}\right)}{\sigma_{\mathsf{COOD}}\left(\omega^{\mathsf{probe}}\right)}\frac{N_{th}(t=200fs)}{N_{\mathsf{COOD}}(t=200fs)} \quad (9.11)$$

and

$$c_{\mathsf{ent.}}\equiv\frac{\sigma_{AM.I}\left(\omega^{\mathsf{probe}}\right)}{\sigma_{\mathsf{COOD}}\left(\omega^{\mathsf{probe}}\right)}\frac{N_{\mathsf{ent.}}(t=200fs)}{N_{COOD}(t=200fs)} \quad (9.12)$$

T_{ent}, $c_{th.}$and $c_{ent.}$are the only free parameters of the fit to the experimental cross-peak signals of the ν_{COOD} mode and the $\nu_{AM.I}$ mode (amide I mode).The dynamics of the diagonal COOD peak both for the putty state (pH=2.5) and the solution state at pH=2.9 are very similar showing a $T_{1.COOD}$ of 0.65±0.1 ps.

9.5.4 2DIR study of the amide-COO- interaction

We studied the interaction between the amide and carboxylate anion groups with 2DIR spectroscopy. The most intense modes of these two groups, the amide I ($\nu_{AM.I}$) and the anti-symmetric stretching vibrations ($\nu_{ant,COO-}$), absorb at ∼1640 and ∼1608 cm^{-1}, respectively, and overlap in both linear and 2DIR spectra. We studied the $\nu_{AM.I}$-$\nu_{ant,COO-}$cross-peak signal and its pH dependence with two different methods. In the first method, we measure 2DIR spectra with parallel and perpendicular polarization of the excitation and detection pulses at pH=1.9 (with a concentration of COO- <5%), pH=2.5 (with a concentration of COO- of ∼20%), and pH=2.9 (with a concentration of COO- of ∼50%). We construct the isotropic 2DIR spectra at pH=1.9, pH=2.5, and pH=2.9, at a time delay of 0.3 ps (Fig.9.10a-b-c). We then normalize all the 2DIR spectra to the maximum intensity observed for a pump frequency of 1645 cm^{-1} (at this frequency the 2DIR signal is completely dominated by the amide I vibration). We then subtract the 2DIR spectrum at pH=1.9 from the 2DIR spectra at pH=2.5 and pH=2.9. This allows us to compare the diagonal and cross-peak signals involving the $\nu_{ant,COO-}$ mode at pH=2.5 and pH=2.9, as the amide I signal can be assumed to be pH independent. The resulting difference spectra are denoted as sub$_{pH=2.5}$ (Figure 9.10d) and sub$_{pH=2.9}$ (Figure 9.10e). The difference 2DIR spectra show a strong diagonal signal of the $\nu_{ant,COO-}$ mode, and a weaker off-diagonal signal at a pump frequency of ∼1640 cm^{-1} and a probe frequency of ∼1610 cm^{-1}. The diagonal signal is stronger for the sub$_{pH=2.9}$ than for the sub$_{pH=2.5}$ 2DIR spectrum, because of the higher concentration of COO- at pH=2.9. The off-diagonal signal represents the $\nu_{AM.I}$-$\nu_{ant,COO-}$ cross-peak signal. We integrate this off-diagonal signal over a range of pump frequencies between 1637 cm^{-1} and 1650 cm^{-1} to eliminate possible effects of spectral diffusion. The resulting signal is shown as a function of the detection frequency in Figure 9.10f. The signals are normalized to the diagonal signal of the $\nu_{ant,COO-}$ mode at 1610 cm^{-1}. We observe that the cross-peak signal (pumping $\nu_{AM.I}$ at ∼1640 cm^{-1} and probing $\nu_{ant,COO-}$ at ∼1610 cm^{-1}) is stronger at pH=2.5 than at pH=2.9. This difference shows that the interaction between the amide and carboxylate anion groups

is enhanced at pH=2.5 in comparison to pH=2.9.

In a second method we determined the strength of the cross-peak signal at different pH values by subtracting the parallel 2DIR spectrum from three times the perpendicular 2DIR spectrum, both at pH=2.5 (Fig.9.5) and at pH=2.9 (Figure 9.11). This procedure reveals the cross-peak signals of the $\nu_{AM.I}$ and $\nu_{ant,COO-}$ vibrations, as all diagonal signals of $\nu_{AM.I}$ and $\nu_{ant,COO-}$ will be strongly suppressed. From the resulting difference 2DIR spectra we subsequently construct transient absorption spectra, in which we average over the excitation frequency interval between 1600 and 1620 cm^{-1} (excitation of $\nu_{ant,COO-}$). These spectra (shown in Fig.9.5b) contain a clear $\nu_{AM.I}$ - $\nu_{ant,COO-}$ cross-peak signal near 1635 cm^{-1} (detection of $\nu_{AM.I}$). To compare the fraction of COO- groups that interacts with an amide group at pH=2.5 with that at pH=2.9, we normalize the transient absorption signals at pH=2.5 and 2.9 of Fig.9.5b to the diagonal signals of the $\nu_{ant,COO-}$ mode at 1610 cm^{-1} at these pH values (Figs. 9.10d and 9.10e). The cross-peak signal near 1635 cm^{-1} is stronger at pH=2.5 than at pH=2.9, showing the enhanced interaction between the COO- and amide groups at pH=2.5 (putty state).

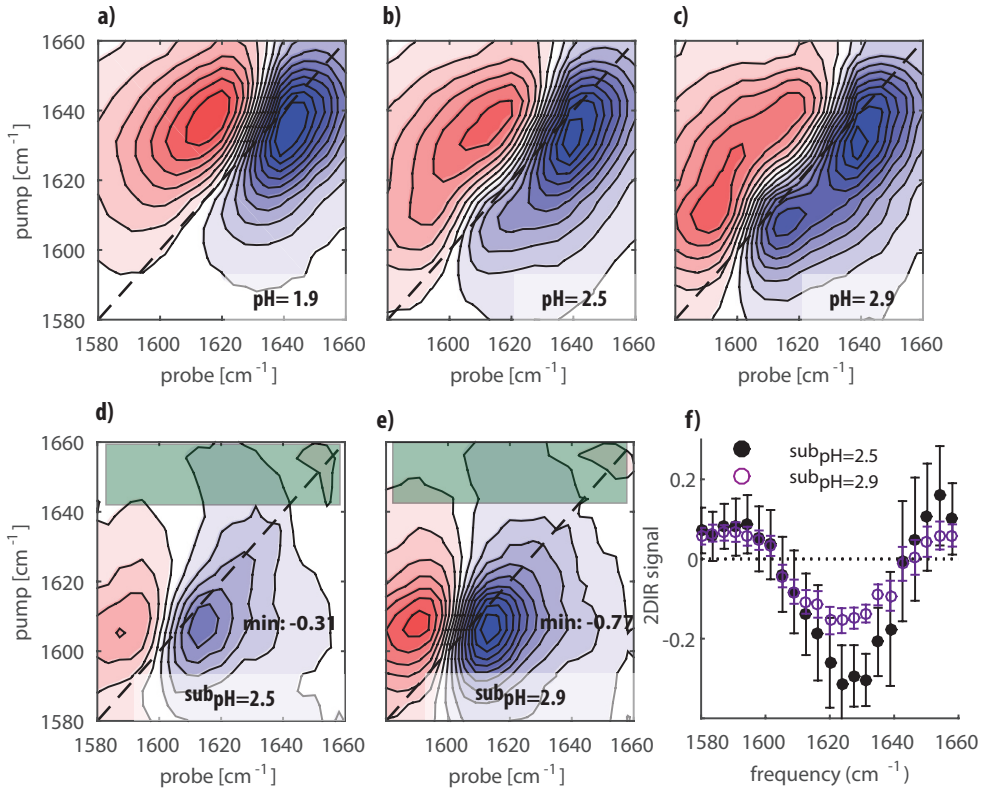

Figure 9.10: 2DIR spectra of hyaluronic acid at a concentration of 20 mg/ml at pH=1.9, pH=2.5 and pH=2.9 in figure a), b) and c). d) and e) are obtained by subtracting a) from b) and a) from c), respectively, after normalizing the 2DIR spectra to the minimum intensity along the pump frequency around 1645 cm^{-1}. We will refer to the subtracted 2DIR spectra in d) and f) as $sub_{pH=2.5}$ and $sub_{pH=2.9}$, respectively. By doing such normalization and subtraction, it is possible to cancel the presence of the intense amide I vibration, and thus to observe more clearly the diagonal signal of the anti-symmetric COO^- mode and possible eventual cross-peak signals of this mode and the amide I mode. In figure f) we report the transient spectra obtained by averaging over the pump frequencies between 1637 cm^{-1} and 1650 cm^{-1} (which is the region highlighted by a dark green rectangle) in the 2DIR spectra shown in figures d) and e). The slices are normalized to the respective bleaches of the COO- vibration at 1610 cm^{-1} of Figures d) and e). At pH=2.5 we observe a larger negative absorption change around 1620 cm^{-1} in comparison to pH=2.9. This larger negative absorption change indicates that more amide and carboxylate anion groups are interacting with each other at pH=2.5 than at pH=2.9.

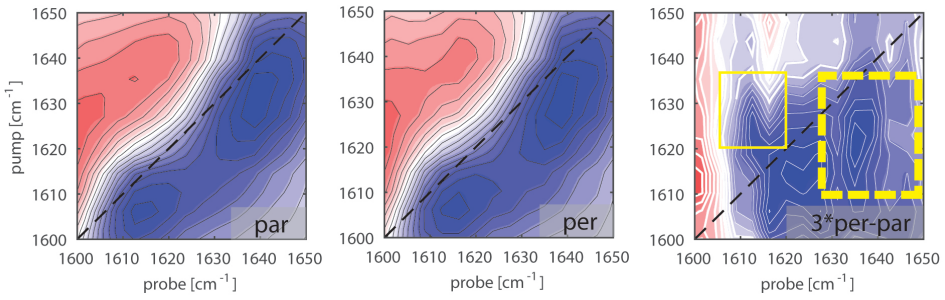

Figure 9.11: 2DIR spectra of a solution of hyaluronic acid at pH=2.9 at a concentration of 20 mg/m at a waiting time of 0.3 ps.

Submitted as:

G.Giubertoni, F.Burla, H.J.Bakker, G.H.Koenderink Connecting the stimuli-responsive rheology of biopolymer hydrogels to the underlying hydrogen-bonding interactions

10

Temperature dependence of the molecular structure and stress relaxation dynamics of hyaluronan hydrogels

Abstract

The viscoelastic properties of hydrogels of responsive biopolymers depend on the interactions between the constituent polymers, which typically include electrostatic and hydrogen-bonding interactions. The connection between the time scale of macroscopic stress relaxation and the molecular-scale structure and dynamics is poorly understood. Here, we study the temperature and pH dependencies of the molecular-scale connectivity and stress-relaxation dynamics of aqueous solutions of the ubiquitous biopolymer hyaluronan by performing 2D-IR spectroscopy and shear rheology. We observe that increasing the temperature does not change the equilibrium density of interchain hydrogen-bond connections. From an analysis of the temperature dependence of the stress relaxation time scale, we find that at pH=2.5 the simultaneous breaking of 5-15 interchain hydrogen bonds, which form the junction point between the segments of the chains, is required for the chain to diffuse, and thus for the network to flow. At pH 7, stress relaxation instead proceeds through polymer reptation. We conclude that an increase in temperature accelerates the dynamics of the polymer network without significantly modifying its structure.

10.1 Introduction

The macroscopic behaviour of hydrogels depends on the motions of the constituent polymer chains, which are restricted by topological entanglements, combined with associative connections. The lifetime of the reversible connections and their density dictate the enhancement of the viscoelastic properties compared to the effect of entanglements alone. Reversible associations can for instance be formed by hydrogen-bonding or hydrophobic interactions. The strength of these interactions is sensitive to temperature, pH and ionic strength, making the hydrogel responsive. This responsiveness can often be tuned by an appropriate molecular design, which makes these hydrogels appealing for an enormous variety of biomedical applications.[34,181,194]

In this chapter, we focus on hyaluronan hydrogels, which are widely found in the animal realm, where they have a critical role in different biological functions, ranging from skin hydration to tissue lubrication.[122,123] Hyaluronan hydrogels are highly responsive to pH changes: by lowering the pH from 7 to 2.5, solutions of hyaluronic acid undergo a liquid-to-gel transition.[36] Hyaluronan is a linear polysaccharide composed of repeating units of N-acetyl-galactosamine and glucuronic acid. The strong change of the mechanical properties of hyaluronan hydrogels at acidic pH is due to the formation of specic intermolecular hydrogen-bonds between adjacent chains. As reported in Chapter 9, at neutral pH all the carboxyl groups are depro-

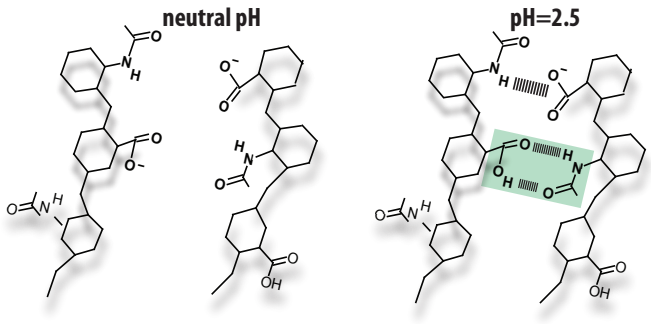

Figure 10.1: Illustration of the hydrogen-bonds formed between adjacent chains, as reported in Chapter 9.

tonated, and thus associative interactions between different polymer chains are prohibited by strong electrostatic repulsion. Hence, at neutral pH, the mechanical properties of hyaluronan solutions are dictated by chain entanglements. By lowering the pH to 2.5, around 80% of the carboxyl groups are protonated, and thus repulsive electrostatic forces between chains are weakened. Adjacent chains can thus form intermolecular hydrogen-bonds between the amide groups and both protonated and deprotonated carboxyl groups, leading to a hydrogen-bonded network as shown in Fig.10.1. The fraction of -COOHs that form intermolecular hydrogen-bonds is around 15% at room temperature. Hydrogen-bonds are often short-lived, forming and breaking on a timescale of a few to tens of picoseconds. Macroscopic stress relaxation in hyaluronan gels at pH 2.5 occurs on much longer time scales, ranging up to minutes. Up to now, the connection between the macroscopic stress relaxation dynamics and the ten orders of magnitude faster molecular dynamics has not been clearly understood.

Here, we study the impact of temperature on the macroscopic mechanical properties of hyaluronan hydrogels and on the density of molecular cross-links by combining rheology and two-dimensional infrared (2DIR) spectroscopy. In 2DIR, we excite the sample with a first, intense beam (pump), and we study the induced vibrational response with a second, weaker probe pulse. In the presence of vibrational coupling, the excitation of one vibrational mode will affect the vibration of other modes, leading to off-diagonal signatures in the 2DIR spectrum, which we refer to as cross-peaks (see Chapter 2). Further information on the molecular interactions can be obtained by measuring the dynamics of the cross-peak signals.

10.2 Results

10.2.1 Temperature dependence of the density of intermolecular interactions

In Figure 10.2 we compare linear infrared absorption spectra of high-molecular weight ($\sim$1.5 MDa) hyaluronan at pH=2.5 at 20 and 40°C. The spectra show an absorption band at 1633 cm^{-1} that we assign to the amide I vibration and

an absorption band at 1725 cm^{-1} that we assign to the carbonyl stretching mode of the protonated carboxylic acid group.[82]

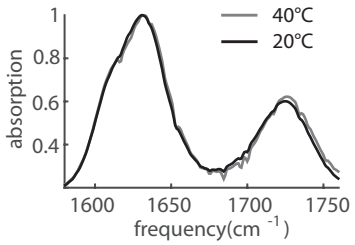

Figure 10.2: Normalized linear infrared spectra for a solution of hyaluronan of 20 mg/ml at pH=2.5 at 20°C and at 40°C. Since the spectral shape does not change by increasing the temperature, we conclude that the fractions of protonated and deprotonated carboxyl groups are constant (∼20%)

At 1607 cm^{-1} we observe an additional shoulder that we assign to the antisymmetric stretch vibration of the carboxylate group anion group. In Chapter 9 we showed that the formation of a hyaluronan hydrogel at pH 2.5 involves the formation of hydrogen bonds between the carboxylic acid, the deprotonated carboxylate anion, and the amide groups of the hyaluronan polymers (Figure 10.1). At pH=2.5 the fraction of deprotonated carboxyl groups (–COO^-) amounts to ∼20%. The comparison of the spectra of Figure 10.2 reveals that a change in temperature by 20°C does not affect the absorption spectrum. Hence, there is no significant change in the percentage of deprotonated carboxylic acid groups.

We also study the effect of temperature on the 2DIR spectrum of hyaluronan at pH=2.5. We excite the amide and carboxyl vibrations with a strong femtosecond infrared pulse pair centred at 1670 cm^{-1} with a bandwidth of 200 cm^{-1} (∼100 fs, 4 μJ per pulse). This excitation induces transient absorption changes that are probed with a weaker (0.35 μJ) single femtosecond probing pulse that is delayed by a time T_w. In Fig.10.3a-b we show the isotropic 2DIR spectra at 5 °C and 4 °C. In both spectra, we observe on the diagonal four distinct spectral signatures. The blue-coloured signatures are negative-going (which we refer to as bleach) and originate from the reduced

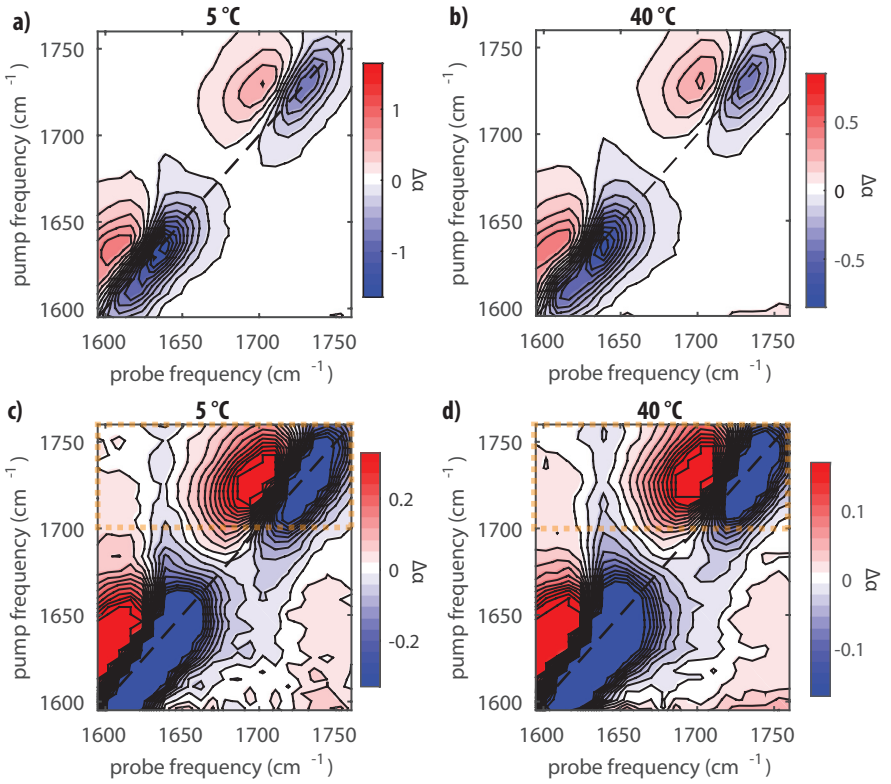

Figure 10.3: a) and b) 2DIR spectra of high molecular weight hyaluronan at pH=2.5 at 5°C and 40°C at a T_w=0.2, respectively. In c) and d) the colour-bar is fivefold magnified to show the off-diagonal peaks.

absorption at the amide I and carboxyl carbonyl frequencies. This reduced absorption is due to the depletion of the fundamental transition (ν =0 to ν =1) and stimulated emission (ν =1 to ν =0) of the amide I and carbonyl pump frequency vibrations. At somewhat lower probing frequencies, we observe red-coloured spectral signatures, which we refer to as excited state absorption or esa. The esa signatures are positive-going and arise because of the vibrational transition from the ν =1 to ν= 2.[43] We observe that the lower-frequency diagonal peak shows a shoulder at 1610 cm^{-1}. This is due to the absorption of the anti-symmetric stretching of the carboxylate group, which at pH=2.5 is present at a significant amount of ~20%. We also observe off-diagonal spectral signatures in the 2DIR spectrum (Fig.10.3c-d).

In the upward off-diagonal regions (exciting around 1725 cm^{-1} and probing around 1630 cm^{-1}), which are indicated by the orange-colored rectangles, we observe 2DIR absorption signals at the probe frequency of the amide I absorption at both temperatures. These cross-peak signals are only visible after multiplication of the signals by a factor of 5, as they are ten-fold weaker than the diagonal signal. In the downward off-diagonal region (exciting around 1630 cm^{-1} and probing around 1725 cm^{-1}) , we observe a bleach signal, which is largely the result of the spectral diffusion of the carbonyl mode, as described in Chapter 9.

Fig. 10.4a reports the 2DIR signals obtained by averaging over the ex-

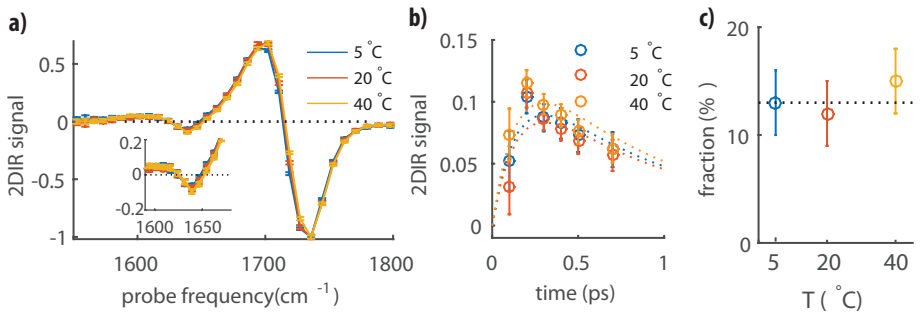

Figure 10.4: a) 2DIR signals at three different temperatures obtained by averaging over the pump region between 1700 and 1760 cm^{-1} . Inset: detail of the 2DIR signal in the absorption frequency of the amide I vibration. b) Cross-peak decay traces for solutions of high molecular weight hyaluronan at a pH=2.5 at 5, 20 and 40 °C. Dashed lines are fits to the relaxation model reported in Chapter 9 Section 9.5.3. c) Extracted fractions of hydrogen-bonded carboxylic acid groups as a function of temperature.

citation frequencies between 1700 and 1760 cm^{-1} (orange rectangle in Fig. 10.3c-d). For every temperature, the 2DIR signal is normalized to the maximum intensity of the carbonyl bleach. In Fig.10.4a we observe again the bleach and the esa of the carbonyl around 1700 cm^{-1}, but also a negative 2DIR signal near 1635 cm^{-1}, which is the vibrational frequency of the amide I absorption. The cross-peak signals between the carbonyl stretching and the amide I vibrations reveals the existence of molecular coupling between these groups at pH=2.5.

To extract the fraction of bonded carboxyl groups, we fit the 2DIR slices

as a function of time in a similar manner as in Chapter 9, by using two different spectral signatures to describe the diagonal and cross-peak spectral signatures, which enables us to resolve the cross-peak signal time dependence. The decay traces of the cross-peak signals are presented in Fig. 10.4b. Since each temperature measurement requires 6-8 hours, it was not possible to collect data at long time delays. As explained in Chapter 9, upon excitation, the carbonyl stretching mode can relax following two different relaxation paths. A fraction of the excited –COOD relaxes by fast energy transfer to the amide I vibration, with a time constant T_{ent} ($\sim$0.150 ps). This energy transfer process leads to the fast rising component that we observe at early time delays. Subsequently, the amide I mode relaxes to the ground state in a time $T_{1AM.I}$ ($\sim$0.65 ps). Another fraction of the excited -COOD vibrations relaxes to low-frequency modes. This process is slower and occurs with a time constant T_{1COOD} ($\sim$0.7 ps). Once populated, the low frequency modes affect the absorption spectrum of the amide I vibration. This latter effect decays with a time constant T_{1LFM}, which is the relaxation time of the low frequency modes. This second mechanism leads to the slowly decaying component of the cross-peak signal, which dominates at time delays larger than 1.5 ps. We therefore fit the dynamics of the cross-peak signal with the kinetic model described in Chapter 9 Appendix Section 9.5.1. The amplitude of the relaxation component due to energy transfer is the only free parameter and represents the fraction of carboxyl groups that form a hydrogen bond to an amide. The amplitude of the second, slower relaxation component is instead constrained around the value reported in Chapter 9. Hence, we extract the amplitude of the relaxation component due to energy transfer, and we find that around 15% of carbonyl groups are directly bonded to the amide groups at pH=2.5. This fraction does not change in the temperature interval between 5 and 40°C. This finding implies that the fraction of carboxyl groups that are engaged in a direct hydrogen-bond with an amide group does not change with temperature.

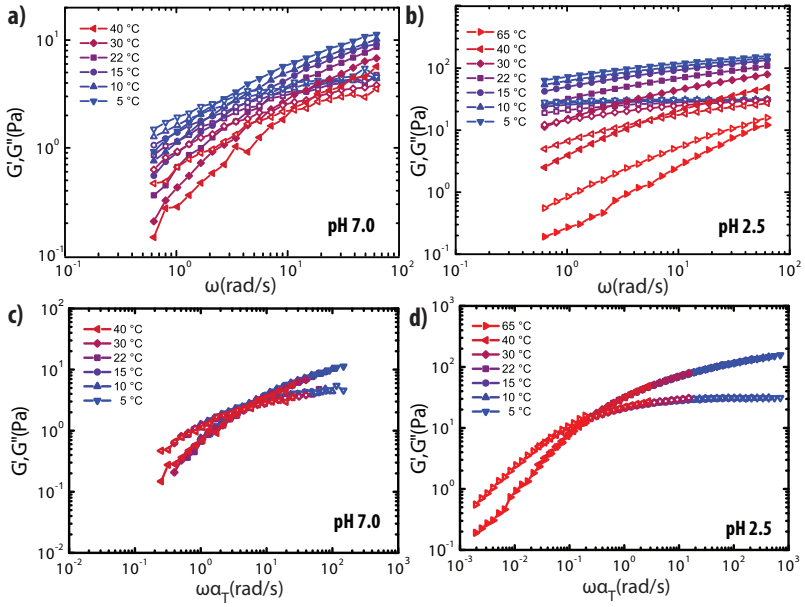

Figure 10.5: a) and b) Temperature dependence of the frequency spectra of the shear moduli of hyaluronan solutions at a concentration of 10 mg/ml, comparing neutral (a) versus acidic pH (b). c) and d) Time-temperature superposition rheology of hyaluronan solutions, comparing neutral (c) versus acidic pH (d). Frequency sweeps for each data set are shifted along the frequency axis onto the measurement at the reference temperature of 22 °C by multiplication with a shift factor a_T. These data were kindly provided by Burla F. Further details can be found in the Ph.D Thesis of Burla F. *Tailoring extracellular mechanics* (Vrije Universiteit, Amsterdam, 2020)

10.2.2 Temperature dependence of mechanical properties[1]

In Fig.10.5 Burla et al. report the shear moduli of solutions of hyaluronan at a concentration of 10 mg/ml at pH=7 (Fig.10.5a) and at pH=2.5 (Fig.10.5b). At this concentration, hyaluronan polymers are found in the semi-dilute entangled regime, meaning that the polymers experience transient topological constraints as a result of the high density.[52,127] The frequency dependence of the shear moduli reveals a transition from a fluid response at low frequencies, where G'<G", to a solid response at high frequencies, where G'>G". The frequency point at which G'=G" is referred

[1]Burla F. (2020), *Tailoring extracellular mechanics*, Doctoral Dissertation, Vrije Universiteit, Amsterdam

to as cross-over point, and marks the liquid-to-gel transition. At both pH values, the elastic and viscous moduli reach a plateau when $\omega > 1/\tau_0$, where τ_0 is a measure for the time needed for equilibration following a step strain. τ_0 is associated to the average lifetime of the interchain entanglements or temporary cross-links[195], and indicates the transition between the terminal regime (time-scales of chain diffusion and network reorganization) to the rubber plateau (time-scales of transient cross-links and entanglements).[196] This spectral shape is typical for entangled polymers, which show a Maxwell-type behaviour with a rubber-plateau that remains till $\omega \simeq 1/\tau_0$, and a terminal regime for $\omega < 1/\tau_0$. At pH 7 we observe at low frequencies that G' scales as ω^2 and G" scales as ω. These frequency dependencies are typical for the terminal regime in solutions of entangled polymers, where the chain diffusion is described by a reptation model, which assumes that the polymer motion is highly restricted by entanglements with surrounding chains.[196] At pH=2.5, it is observed that the cross-over point shifts to lower frequency, indicating that the stress-relaxation has a longer time constant than at neutral pHs. It can furthermore be seen in Fig. 10.5 that the magnitude of the elastic modulus in the plateau regime is higher at pH 2.5 than at pH 7. The changes observed by lowering the pH are consistent with the formation of transient interactions.[197,198] A convenient way to model the viscoelastic behavior of entangled polymers that interact via transient binding between associative groups (referred to as stickers) is the sticky reptation model. Following the sticky reptation model, the stress relaxation time τ_0 is proportional to the effective bond lifetime of the associative interactions, and to the square of the number of stickers per chain.[199]

At both neutral and acidic pHs, it is observed that by increasing temperature, shear moduli become lower. In addition, increasing the temperature leads to an increase of the characteristic frequency at which the terminal regime (i.e., where G"$>$ G') crosses over to the rubber plateau (i.e., where G' $>$ G"), which indicates that the time-scales, in which the hyaluronan hydrogels relieve the stress, become shorter.[197]

In the simplest case that we have only one type of sticker, the sticker life time should show a dependence on temperature given by an Arrhenius acti-

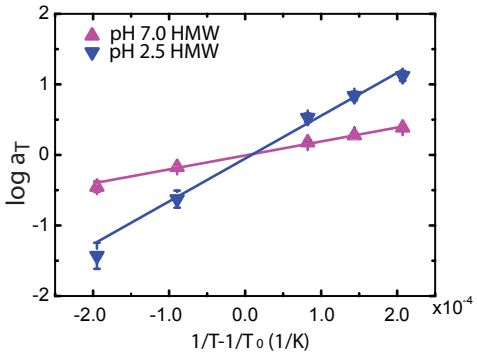

Figure 10.6: Flow activation energy of hyaluronan solutions, comparing neutral and acidic pH. Arrhenius plot showing the shift factors used for constructing the time-temperature superposition data in Fig.10.5c-d as a function of the inverse of the temperature relative to the reference temperature $T_0 = 22^\circ$C. Lines show linear fits whose slopes represent the flow activation energy divided by $2.3R$.

vation energy.[200] To test whether a single chain association mechanism can account for the observed temperature dependence, Burla et al. performed a time-temperature superposition analysis using 22°C as the reference temperature. As shown in Fig.10.5c-d, shifting both the elastic and viscous data along the frequency axis by a temperature-dependent shift factor a_T indeed results in a set of master curves. To retrieve the activation enthalpy E_A for stress relaxation of the hyaluronan hydrogels[201], one can plot the shift factor a_T as a function of the inverse temperature relative to the reference temperature T_0=22°C (295 K) by using the following expression:

$$log(a_T) = -\frac{E_A}{2.3R}\left(\frac{1}{T} - \frac{1}{T_0}\right) \tag{10.1}$$

where R is the universal gas constant and T_0=295 K. As shown in Fig.10.6, Burla et al. obtained straight lines for all data sets, indicating that the relaxation time is controlled by the thermally activated dissociation of bonds between chains. The line slope is higher at pH 2.5 than at pH 7.0, qualitatively consistent with the expectation from the sticky reptation model that pH-induced hydrogen-bonding enhances the friction on the chains. By extracting the activation energy from the curve slope, we obtain for hyaluronan solution at pH=2.5 an activation energy of ∼115 kJ/mol (10 000 cm^{-1}),

corresponding to an activation energy of 50 k_bT at room temperature. In the entangled state at pH 7.0, the activation energy is around ∼30 kJ/mol (∼12 k_BT), consistent with a prior report for high molecular weight hyaluronan.[131,202] We note that this earlier study was carried out at 50 mg/mL, a much larger concentration than studied here (10 mg/ml), suggesting little effect of concentration on the activation energy. For the putty state at pH 2.5, the activation energy is around 50 k_BT for high molecular weight hyaluronan. The values of the activation energy are consistent with typical association energies of hydrogen bonds, which span from a few to tens of k_BT.[203]

10.3 Discussion

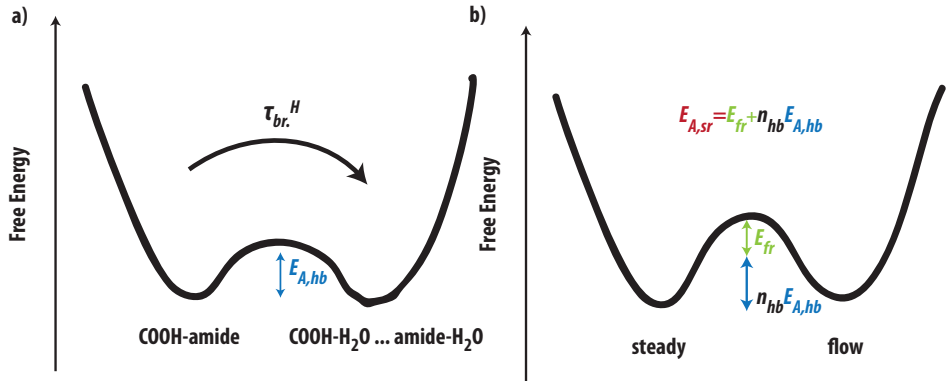

Figure 10.7: a) Schematic representation of the breaking of an hydrogen-bonded complex. We refer to the breakage time of the hydrogen-bonds as τ_H^{br}. The activation energy necessary to break the hydrogen-bonded complex is defined as $E_{A,hb}$. b) Schematic representation of the network dynamics. The flow activation energy $E_{A,sr}$ corresponds to the breaking of n_{hb} hydrogen bonds (stickers).

From our 2DIR measurements, we infer that the fraction of bonded carboxyl groups does not change significantly with temperature between 5 and 40°C, which implies that the formation/breaking time constants change by comparable factors when the temperature is varied. The time-temperature superposition analysis of the rheology likewise reveals that the fraction of bound groups does not change with temperature, since it was only necessary

to apply a horizontal (time) shift factor to superpose the curves. This finding indicates that the sticker density is independent of temperature.[197,204] The fact that the density of hydrogen-bond contacts does not change with temperature indicates that the breaking of an interchain hydrogen bond between a carboxyl group and an amide group results in a state that has about the same overall free energy as the intact hydrogen bond. This state is probably formed by hydrogen bonds between the carboxyl and the amide groups and solvent water molecules. As a result, a change in temperature does not affect the relative fraction of hydrogen-bond between the polymer chains. However, the rates at which the stickers break and reform will depend on temperature as the breaking and reformation will involve an energy barrier $E_{A,hb}$ that will be of the order of the binding energy of a single hydrogen bond, which is typically ∼500-1500 cm^{-1} or 2-7 k_BT (for instance, in protein secondary structure it ranges between 2 and 5 k_BT[205]). In Figure 10.7a, a schematic picture is shown of the free energy potential associated with the intact and broken interchain hydrogen bond.

To understand the acceleration of the network dynamics with increasing temperature, we need to find the relation between the characteristic lifetime of a single hydrogen bond and the characteristic time scale of the stress-relaxation of the hyaluronan solution, as expressed in the frequency dependence of the shear moduli. The typical lifetime $\tau(\tau{=}\tau_{br}^{H})$ of a single hydrogen-bond is on the order of a few to tens of picoseconds. For instance for NMA(N-methyl acetamide) molecules hydrogen-bonded to methanol, the hydrogen-bond lifetime was observed to be tens of picoseconds.[206] The stress relaxation has a characteristic time scale of milliseconds to seconds[195,207,208], much longer than the lifetime of single hydrogen bonds. Such a disparity in time scales is also observed between the acceleration of bond breaking and the acceleration of stress relaxation with increasing temperature. The breaking and the formation rate accelerates by a factor of ∼2 (assuming an activation energy $E_{A,hb}$ of 5 k_BT[205]). This acceleration is quite small in comparison to the acceleration of the stress relaxation by a factor of ∼400 at pH=2.5 ($E_{A,sr}$ = ∼115 kJ/mol (∼50 k_BT)).

The large difference in acceleration factor and the large difference in time

scales of the hydrogen bond and sticker dynamics can be understood from the fact that a certain number of hydrogen bonds n_{hb} needs to be broken at the same time to allow for chain displacement, and consequent network flow. In addition, such a mesoscopic rearrangement involves a frictional barrier due to chain entanglements and to the required displacement of solvent molecules. Hence, the activation energy necessary for the network to flow will be much larger than the activation energy of breaking a single hydrogen bond. Assuming a similar prefactor for the breaking of hydrogen bonds and the friction, the total activation energy for stress relaxation can be written as:

$$E_{A,sr}(pH) = n_{HB}(pH) * E_{A,hb} + E_{fr} \tag{10.2}$$

At pH=7 we assume there are no hydrogen bonds between the hyaluronan polymer chains and thus $n_{hb}(pH = 7) = 0$, which implies that the activation energy will be equal to the frictional barrier energy E_{fr}. At pH=2.5 the density of interchain hydrogen bonds is large enough to cause the formation of an elastic hydrogel. By subtracting the frictional energy E_{fr} to the measured activation energy at pH=2.5, $E_{A,sr}$, we find at this pH that the energy barrier due to the hydrogen-bond formation is of $\simeq$85 kJ/mol ($\sim$ 38 k_BT). This residual activation energy corresponds to $n_{hb}(pH = 2.5) =$ 5-15 hydrogen bonds, which need to be broken in order for the hyaluronan chain to diffuse.

Finally, it should be noted that we have not considered the possible effect of temperature on the frictional energy barrier E_{fr}. This energy barrier will depend on several parameters, such as the intramolecular hydrogen-bonds that stiffen hyaluronan and the mobility of the solvent molecules. A more flexible chain and an increased mobility of water may thus lead to a lowering of E_{fr} with increasing the temperature, which will also lead to faster dynamics of the polymer network.[209] However, the fact that the temperature dependence of the shift factor a_T can be well described with an Arrhenius expression suggests that the value of E_{fr} is quite insensitive to temperature changes within the range we studied.

10.4 Conclusion

We used rheological and two-dimensional IR spectroscopy measurements to measure the effect of temperature on the mechanical properties and molecular structure of entangled networks of hyaluronan polymers at pH=7 and pH= 2.5. The 2DIR results show that at pH=2.5 inter-chain hydrogen bonds between the hyaluronan polymer chains are formed, which results in an elastic (putty) state. Both the 2DIR and the rheological measurements show that the density of cross-links at pH=2.5 does not depend on the temperature (from 20°C to 40°C). Hence the equilibrium structure of the polymer network does not change with temperature. The dynamics of the polymer network does show a strong dependence on temperature. When the temperature is increased, the stress relaxation strongly accelerates. At pH=2.5 this temperature dependence corresponds to an activation energy of ∼115 kJ/mol, at pH=7 to an activation energy of ∼30 kJ/mol. The latter activation energy can be assigned to a frictional energy barrier associated with the motion of the polymer chains along each other and the displacement of the water molecules. The much higher activation energy at pH=2.5 suggests that under these conditions, the simultaneous breaking of 5-15 hydrogen bonds is required for chains to move and, thus, for the network to flow.

Published as:

Giulia Giubertoni, Konrad Meister, Arthur L. DeVries and Huib J. Bakker, Determination of the Solution Structure of Antifreeze Glycoproteins using Two-Dimensional Infrared Spectroscopy, *Journal of Physical Chemistry Letters, 2019*

Submitted as:

Yuling Sun, Giulia Giubertoni, Huib J. Bakker, Manfred Wagner, Arthur L. DeVries, Konrad Meister Structural Basis for the Function of Antifreeze Glycoproteins

11

Determination of the Solution Structure of Antifreeze Glycoproteins

Abstract

We study the solution structure of antifreeze glycoproteins (AFGPs) with linear and two-dimensional infrared spectroscopy (2DIR). With 2DIR we study the coupling between the amide I and amide II vibrations of AFGPs. The measured nonlinear spectral response constitutes a much more clearly resolved amide I spectrum than the linear absorption spectrum of the amide I vibrations, and allows us to identify the different structural elements of AFGPs in solution. We find clear evidence for the presence of polyproline II (PPII) helical structures already at room temperature, and we find that the fraction of PPII structures increases when the temperature is decreased to the biological working temperature of AFGP. We observe that inhibition of the antifreeze activity of AFGP using borate buffer or enhancing the antifreeze activity using sulfate buffer, does not lead to significant changes in the protein conformation,indicating that the effect of the inhibitors and enhancers is likely related to interactions with the disaccharide units. Furthermore, we study the structure of chemically modified AFGPs. We find a strong correlation between the effect of the chemical modification on the relative abundance of the PPII structure, and on the anti-freeze activity.

11.1 Introduction

Antifreeze proteins (AFP) and antifreeze glycoproteins (AFGPs) are a unique class of proteins that inhibit the growth of ice crystals in living organisms and thereby enable their survival in freezing and subfreezing habitats.[14,210] AFGPs were the first antifreeze proteins to be discovered, and are subject to considerably less structural variations than AFPs. The primary structure of an AFGP consists of the repeating tripeptide unit (alanyl-alanyl-threonine) to which a β-D-galactosyl-(1 $\rightarrow$ 3)-α-N-acetyl-d-galactosamine is attached at the threonine side chains, as shown in Figure 11.1a. AFGPs typically occur in isoforms that are grouped into large AFGP1-5 and small AFGP7-8 isoforms.

The secondary structure of AFGP in solution and at the surface of ice has not yet been unambiguously identified. Early circular dichroism (CD) spectra suggested that AFGPs possess an extended random coil structure in solution.[211] Follow-up studies using a combination of NMR and CD experiments proposed a left-handed helical conformation that is similar to a polyproline II helix (PPII).[212,213] The results of later CD, IR, quasi-elastic light scattering and Raman spectroscopic studies all suggested the presence of folded structural elements, but did not allow a definite determination of the structure.[214] Recently, molecular dynamics simulations and a systematic chemical synthesis study of small AFGP isoforms showed that the sugar unit and the PPII structural element play an important role in the binding to ice.[16,215] The uncertainty regarding the solution structure of AFGPs leaves important questions regarding their working mechanism unanswered. It remains for instance unclear which site of the protein binds to ice.

Linear infrared spectroscopy is a widely used method to study the secondary structure of proteins. Structural elements such as alpha-helixes or beta-sheets can be detected from the characteristic frequencies of their amide vibrations. In particular the frequency of the strongly absorbing amide I mode constitutes a clear marker for the presence of specific secondary structural elements.[37,216] Unfortunately, for more complex and (partly) disordered proteins, the linear infrared absorption spectra are often too congested to determine the secondary structure of the protein. Additional information on

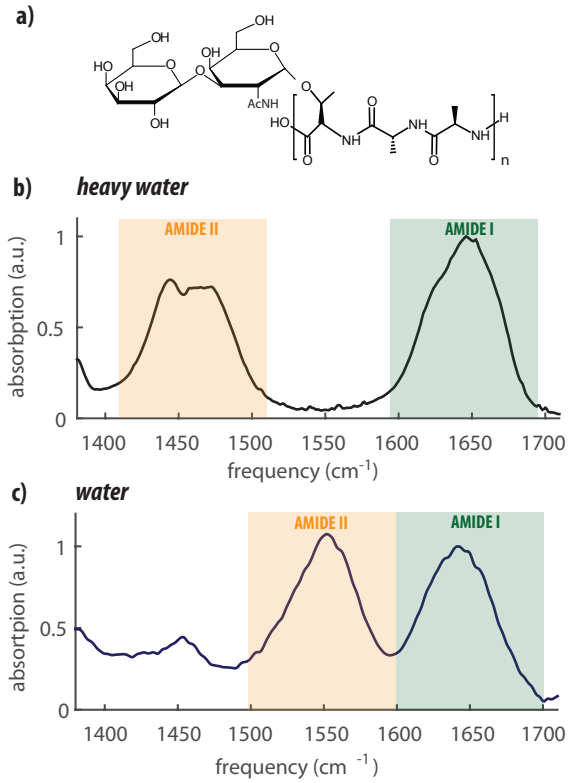

Figure 11.1: a) Chemical structure of a representative antifreeze glycoprotein (AFGP) repeat; n =4-50. b) Normalized FTIR spectrum of AFGP 1-5 at a concentration of 2 wt% in D_2O at room temperature. In c) we report the normalized ATR spectrum of AFGP 1-5 at a concentration of 2 wt% in H_2O. We observe that the amide II modes absorb at lower frequencies in heavy water than in water as a consequence of the isotopic exchange of the N-H proton. Since the amide I is mainly due to the carbonyl stretching vibration, the shift in the absorption frequency of the amide I modes is only a few wavenumbers.

the protein structure can be obtained with two-dimensional infrared spectroscopy (2DIR). 2DIR is a nonlinear spectroscopic technique in which the vibrational response is measured as a function of two frequencies (excitation and probing frequencies). The coupling of different vibrations leads to off-diagonal signals in the 2DIR spectrum.[43] The magnitude of these off-diagonal signals reflects the strength of the coupling, which can provide information on the relative position and orientation of the vibrations, and

thereby on the spatial structure of the studied molecule.[217–219]

Here we use 2DIR to study the coupling between the amide I and amide II modes of AFGPs.[220] We demonstrate that the measurement of this coupling enables a decomposition of the complex amide I solution spectrum of AFGP in subbands that correlate with distinct structural elements. Thereby we can determine the relative fractions of these structural elements of AFGPs in solution as a function of temperature. We also study the effect of chemical modifications of AFGP1-5 on the relative fractions of the structural elements and on the anti-freeze activity. The spectral decomposition of the amide I spectrum using 2DIR also allows us to analyze the linear infrared absorption spectrum of the amide I modes, and to use these spectra to study the effects of the addition of an enhancer (sulfate)[221], an inhibitor (borate),[222,223] and of the chemical modifications on the relative fractions of the different structural elements of AFGP in aqueous solution.

11.2 Results and Discussion

11.2.1 Linear Infrared Spectrum

Fig.11.1b shows the normalized infrared spectrum of a solution of AFGP1-5 in deuterated water (D_2O), between 1380 and 1720 cm^{-1}. We used a concentration of 2 wt% in all our experiments as this was the minimum concentration that provided sufficient absorption to perform 2DIR experiments with a good signal-to-noise. The frequency range between 1400 and 1500 cm^{-1} represents the region of the amide II vibrations, and the frequency range between 1600 and 1700 cm^{-1} represents the amide I region. The amide II vibration is dominated by N-H bending vibrations and the C-N stretching vibrations, whereas the amide I mode is dominated by the stretching of the C=O bond of the amide group. Amide I and amide II modes are strongly coupled by through-bond, mechanical anharmonic interactions.[141] The AFGP spectrum in the amide II region is congested due to the overlap of modes belonging to different protein conformations and the response of the bending mode of residual HDO in the D_2O solvent.[224] The amide I region is also highly congested and consists of a broad band with a maximum around 1645 cm^{-1} and a shoulder around 1620 cm^{-1}. As a result, the different amide

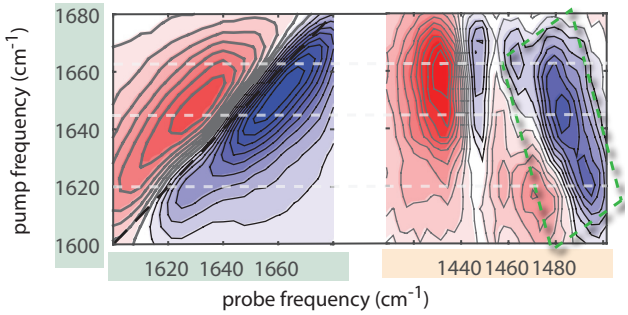

Figure 11.2: Isotropic 2DIR spectra of a 2 wt% AFGP1-5 solution in D_2O at 0°C. The spectra were collected at a delay time T_w of 0.5 ps. The left panel shows the 2DIR spectrum obtained when exciting and probing in the amide I region, the right panel shows the 2DIR spectrum obtained when exciting the amide I region and probing the amide II region. Bleaching (reduced absorption) is indicated in blue, while excited state absorption (increased absorption) is indicated in red.

I subbands and the corresponding structural motifs of the protein cannot be resolved. In Fig.11.1c we show the infrared spectrum obtained by dissolving the protein in water. We observe that the amide II vibrations shift to higher frequency. This blue-shift is due to the isotopic exchange of N-D by N-H. Similar to the heavy water solution, the amide I and amide II regions are observed to be highly congested.

11.2.2 Two-Dimensional Infrared Spectroscopy

We study the vibrational response of the amide I and amide II vibrations and their coupling with two-dimensional infrared (2DIR) spectroscopy. The details of the setup can be found in Chapter 2 Section 2.5. In brief, we excite the amide vibrations with a strong femtosecond infrared pulse pair (∼100 fs, 4 μJ per pulse). This excitation induces transient absorption changes that are probed with a weaker (0.35 μJ) single femtosecond probing pulse that is delayed by a time T_w. In all experiments the excitation pulses are centred at 1630 cm^{-1} with a bandwidth of 200 cm^{-1} in resonance with the amide I vibrations. The probe pulse is centred at 1630 cm^{-1} to measure the response of the amide I vibrations, and at 1450 cm^{-1} to measure the response of the amide II vibrations induced by the excitation of the amide I vibration.

Diagonal two-dimensional infrared spectra

In the left panel of Fig.11.2 we show the isotropic 2DIR spectra obtained by pumping and probing the amide I vibrations (diagonal region) for a solution of a 2 wt% AFGP1-5 solution at 0 °C. The 2DIR spectrum in the diagonal region shows a clear bleaching component (reduced absorption) due to the depletion of the fundamental $\nu = 0$ to $\nu = 1$ transition and induced $\nu = 1$ to $\nu = 0$ stimulated emission. At a slightly lower probing frequency we observe an induced $\nu = 1$ to $\nu = 2$ excited state absorption. The bleaching signal is strongly elongated along the diagonal. The maximum signal is observed at ~1655 cm^{-1} which is slightly higher than the frequency of the maximum in the linear infrared spectrum. The 2DIR spectrum also contains a shoulder at 1620 cm^{-1} that has a higher intensity relative to the main band that is observed in the linear infrared spectrum. This difference can be explained from the fact that the signal in the linear infrared spectrum is proportional to $c|\overrightarrow{\mu}|^2$, where c is the concentration of the species and $|\overrightarrow{\mu}|^2$ is the square of the transition dipole moment of the molecular vibration, whereas the signal of the diagonal 2DIR spectrum is proportional $c|\overrightarrow{\mu}|^4$. Thus, molecular vibrations with a large transition dipole moment will be enhanced in 2DIR spectra.[43] It has been shown that the highly nonlinear dependence of the diagonal 2DIR signal on the transition dipole moment can help in revealing the secondary structure of proteins.[225,226]

Off-diagonal two-dimensional infrared spectra

The right panel of Fig.11.2 shows the isotropic 2DIR spectrum obtained by exciting the amide I vibrations and probing the amide II vibrations. This region of the 2DIR spectrum shows the presence of several off-diagonal features or cross-peaks. The cross-peak signals consist of a bleaching component at higher frequencies and an induced absorption component at lower frequencies. At probe frequencies between 1480 and 1500 cm^{-1} we observe an anti-diagonally elongated bleaching band, highlighted by the green

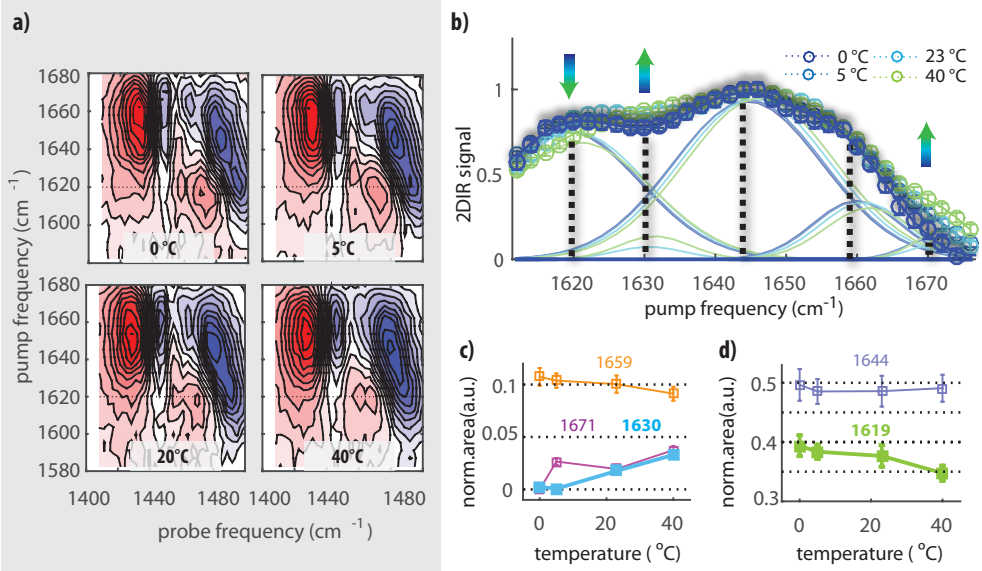

Figure 11.3: a) 2DIR spectra for AFGP 1-5 solutions in heavy water at a concentration of 2 wt%. The 2DIR spectra were collected by starting the measurement at 0 °C and then increasing the temperature. b) Maximum bleaching signal of the amide I-amide II cross-peak region for probing frequencies between 1480 and 1500 cm^{-1} as a function of the excitation frequency, at four different temperatures, for a D_2O solution of AFGP 1-5 at a concentration of 2 wt%. The signal is normalized to clarify the temperature dependence of the spectra. Also shown are the five Gaussian subbands in which the spectrum is decomposed. c) and d) Areas of the five Gaussian bands used to fit the spectra of Figure a, as a function of temperature. The areas are normalized to the total area at each temperature. The error bars represent the standard deviations obtained from the global fit and from the propagation of the experimental errors.

rectangle in Fig.11.2b. In addition, we observe bleaching signals at probe frequencies of 1447 cm^{-1} and 1460 m^{-1} following excitation at ∼1660 cm^{-1}. The linear infrared spectrum shows a peak near 1450 cm^{-1} that has been assigned to the CH3 bending vibration (see Fig.9.1b-c). Hence, we assign the signal near 1447 cm^{-1} to the coupling of the amide I vibrations and the CH3 bending mode.[227]

Fig.11.3a shows the 2DIR spectra obtained at four different temperatures. To analyse the broad anti-diagonal amide II response between 1480 and 1500 cm^{-1}, we plot the maximum of this signal as a function of the exci-

tation frequency in the amide I band. Fig.11.3b shows the resulting spectra at 0°C, 5°C, 23°C and 40°C. The spectrum at 0°C shows a maximum intensity at 1644 cm^{-1} and two shoulders around 1620 and 1660 cm^{-1}. We find that at higher temperatures a significant change of the spectrum occurs. At 40°C, the signal at 1630 and 1670 cm^{-1} increases, while the shoulder at 1620 cm^{-1} becomes less pronounced. It is clearly seen that the measurement of the maximum response of the amide II vibrations as a function of the amide I excitation frequency results in a much better resolved amide I spectrum compared to the linear IR spectrum of the amide I modes. The improved spectral resolution can be explained from the nonlinear character of the signal. The intensity of the signals measured in the cross-peak region is proportional to the product of the squares of the transition dipole moments of the two coupled molecular modes.[43,220] This leads to a strong suppression of all contributions that do not involve a coupling between amide I and amide II. Hence, all contributions of background and contaminations, which lead to congestion of the linear IR spectrum of the amide I modes, are no longer observed in the off-diagonal 2DIR spectrum. The resulting spectrum reveals the presence of five different amide I subbands. We performed a global fit of the spectra at different temperatures using five Gaussian subbands, as shown in Figure 11.3b. In this fit we take the widths of the subbands to be temperature independent and we assume the central frequencies to blue-shift by 0.05 $cm^{-1}/\,°C$ to take into account the effect of an increase in temperature on each of the subbands. From the fit we extract the central frequencies, and the temperature-dependent amplitudes of the five subbands. The obtained frequencies agree very well with frequency values reported in previous studies.[228–230] We assign the modes as follows: the 1619 ± 2 cm^{-1} band is assigned to the PPII structure, the $1630\ \pm2$ cm^{-1} and $1671\pm2 cm^{-1}$ bands to extended structures (or turns), the 1644 ± 3 cm^{-1} band to a random coil structure, and the 1659 ± 3 cm^{-1} band to an α-helical conformation.

The amide I vibration of the sugar unit N-acetyl-d-galactosamine absorbs at 1627 cm^{-1} (see Appendix Sec.11.4.2 and Fig.11.11), and thus overlaps with the band at 1628 cm^{-1} that is assigned to the amide I vibrations of the protein part of AFGP with an extended conformation.[228–230] However, the

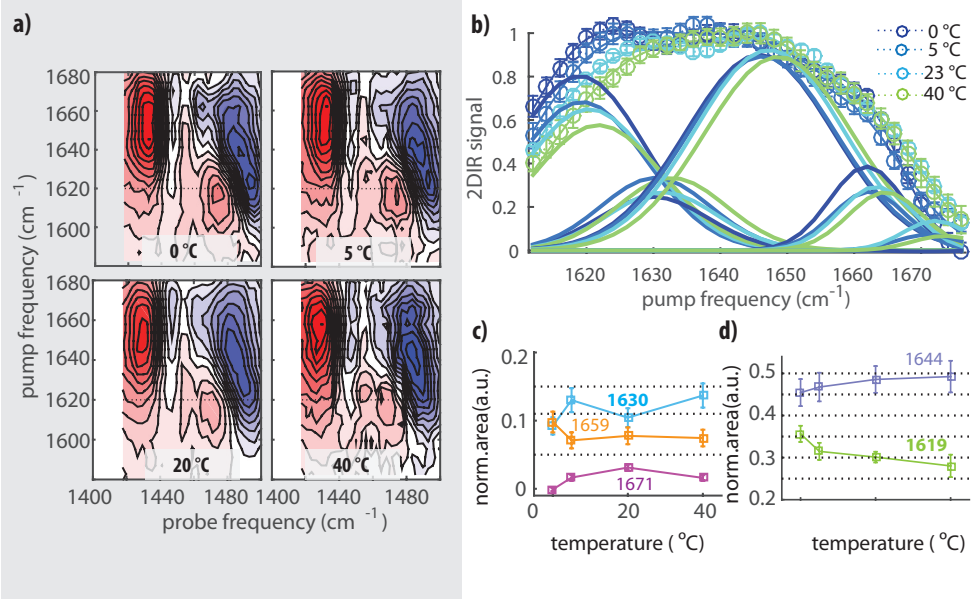

Figure 11.4: a) 2DIR spectra for AFGP 7-8 solutions in heavy water at a concentration of 2 wt%. The 2DIR spectra were collected by starting the measurement at 0°C and then increasing the temperature. b) Maximum bleaching signal of the amide I-amide II cross-peak region for probing frequencies between 1480 and 1500 cm^{-1} as a function of the excitation frequency, at four different temperatures, for a solution of AFGP 7-8 at a concentration of 2%. The signal is normalized to clarify the temperature dependence of the spectra. Also shown are the five Gaussian subbands in which the spectrum is decomposed. c) and d) Areas of the five Gaussian bands used to fit the spectra of Figure a, as a function of temperature. The areas are normalized to the total area at each temperature. The error bars represent the standard deviations obtained from the global fit and from the propagation of the experimental errors.

observed band for AFGP shows a distinct temperature dependence, which is not observed for the amide I vibration of N-acetyl-d-galactosamine Hence, the observed band at 1628 cm^{-1} likely contains contributions from both the amide I vibration of N-acetyl-d-galactosamine, and the amide I vibrations of the protein part of AFGP with an extended conformation. In Fig. 11.3c and 11.3d we present the normalized areas of the five spectral components as a function of temperature. We find that there is no dominant conformation of AFGP in solution, and at all temperatures a mixture of different structural

elements is present. When the temperature is increased to 40 °C, the amplitude of the PPII band (1619 cm^{-1}) decreases from 0.40±0.02 to 0.35±0.02, while the extended structure bands (1671 and 1630 cm^{-1}) increase from 0.00 (+0.01) to 0.04±0.01. The amplitudes of the other two bands show very little change with temperature. We performed the same experiments and data analysis for 2 wt% solutions of AFGP7-8 and obtained similar results (Fig.11.4). For both AFGP 1-5 and AFGP 7-8 we also measured the 2DIR spectra at -5°C, but these spectra do not show significant changes compared to the off-diagonal 2DIR signal at 0°C (Fig.11.5).

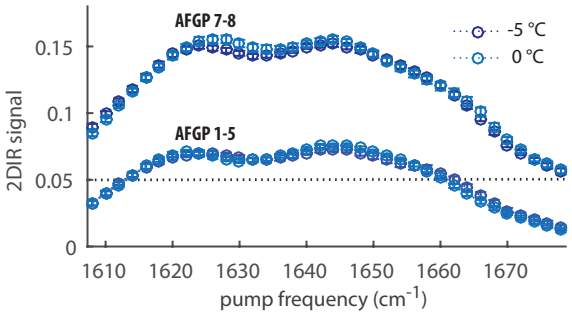

Figure 11.5: Comparison between bleaching signals of the amide I-amide II cross-peak region for probe frequencies between 1480 and 1500 cm^{-1} as a function of the excitation frequency, at 0 and -5 °C, for D_2O solutions of AFGP 1-5 and AFGP 7-8 at a concentration of 2 wt%. It is introduced a offset for comparison (dotted lines)

Comparison of the linear infrared spectra of AFGP 1-5 and AFGP 7-8

In Fig.11.6a we show linear IR spectra of solutions of AFGP1-5 and AFGP7-8 in D_2O at room temperature. We observe that AFGP 7-8 has a stronger absorption in the frequency region between 1580-1620 cm^{-1} in comparison to the larger AFGP 1-5. In comparison to the 2DIR spectra, these spectra show an additional response near 1595 cm^{-1} due to differences in the amino acid composition.[228,231] For the smaller AFGP7-8 isoforms it was shown that alanine is occasionally substituted by proline in some of the re-

peated monomer units.[232,233] The five spectral bands that we obtained from

Center Frequency (cm^{-1})	FHWM (cm^{-1})
1592 ± 2	33 ± 3
1620 ± 3	39 ± 3
1630 ± 2	32 ± 6
1642 ± 2	28 ± 3
1656 ± 3	38 ± 3
1668 ± 2	38 ± 3

Table 11.1: Center positions and widths obtained by globally fitting the linear infrared spectra of AFGP 7-8 and AFGP1-5 as a function of temperature.

the analysis of the cross-peak region (exciting amide I, probing amide II) of the 2DIR spectra can now also be used to analyse the linear IR spectra in the amide I region. We decompose the linear IR spectra in these five bands plus a sixth band centred at 1592 cm^{-1}. The centre frequencies reported in Fig.11.4c-Fig.11.4d are used as input parameters for the linear IR infrared decomposition. We allow the centre frequencies of the six bands to shift slightly to the blue with increasing temperature.[234] The extracted widths and centre frequencies are reported in Table 11.1. Fig. 11.6b shows the linear spectra of solutions of AFGP1-5 in D_2O for different temperatures between 5 °C and 70 °C. We find that the temperature-dependent spectra can be well described with the same bands that we obtained from the 2DIR measurements. In Figure 11.6c we present the normalized areas of the five bands as a function of temperature. We observe that for all temperatures both AFGP 1-5 and AFGP 7-8 do not show a single dominant conformer, indicating that the proteins have a certain structural flexibility. We find that both AFGP7-8 and AFGP1-5 have a significant content of PPII structure, but that at high temperatures the larger AFGP1-5 has less overall PPII content than the shorter AFGP7-8. When the temperature is lowered, the PPII content of AFGP1-5 increases more strongly than for AFGP7-8, but remains smaller for AFGP1-5 than for AFGP7-8 at 5 °C. For both AFGP isoforms, the amplitude of the extended structure band decreases when the temperature is lowered, in agreement with the 2DIR experiments. Figure 11.6c also shows that at all temperatures the shorter AFGP 7-8 isoforms have a

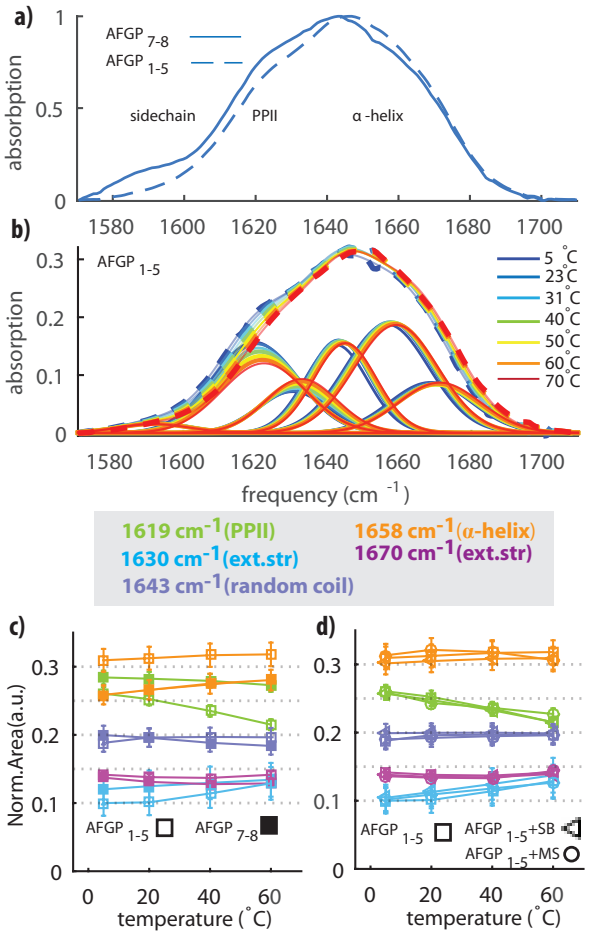

Figure 11.6: a) Normalized linear infrared spectra of solutions of AFGP 7-8 and AFGP 1-5 at a concentration of ∼2 wt% in D_2O respectively at 22 °C. b) Linear infrared spectra of solutions of AFGP 1-5 at a concentration of ∼2 wt %at different temperatures between 5 °C and 70 °C. We also show the decomposition of the spectra in six Gaussian-shaped bands. c) Normalized areas of five Gaussian bands that are used to fit the infrared spectra of Figure b and the temperature-dependent spectra of AFGP7-8 (see Appendix Sec.11.4.1 and Fig.11.9). d) Normalized areas of five Gaussian bands that are used to fit the linear spectra of solutions of AFGP 1-5 (▫) and of AFGP 1-5 in presence of borate(△) or in presence of sufate(○) (see Appendix Sec.11.4.1 and Fig.11.9).

lower α-helix content than the larger AFGP 1-5 isoforms, which likely is a result of their difference in amino-acid composition, i.e. AFGP 7-8 contains more prolines. In fact, proline residues are known to be α-helix breakers.[235] The α-helical content of AFGPs does not show significant changes when the temperature is lowered. We thus find that both AFGP isoforms, and in particular the larger AFGP1-5, tend to form more PPII conformations at the expense of the extended structures as soon as the temperature is lowered to their biological working temperature. This result is in line with a recent molecular dynamics simulation study that showed that PPII structures are important for AFGPs antifreeze activity.[16] The antifreeze activity of AFGP7-8 is known to be lower than for AFGP1-5[236,237], which at first sight may be interpreted as a pure size effect, the larger protein showing an energetically more favourable adsorption to the surface of ice. In view of the present findings, the difference in antifreeze activity between AFGP1-5 and AFGP7-8 may also be partly due to an intrinsic structural difference, the antifreeze activity of AFGP1-5 being higher than that of AFGP7-8 because of its larger α-helix content. The higher α-helix content could for instance be beneficial in the segregation of the hydrophilic and hydrophobic groups of the protein, which is vital for ice binding.

Effect of the addition of an enhancer/inhibitor of the anti-freeze activity

We measured linear infrared spectra as a function of temperature for solutions of AFGP1-5 in D_2O, to which we added 1 M magnesium sulfate or 0.3 M sodium borate.[221,223] Sodium borate is a well-known inhibitor of antifreeze activity and it has been proposed that borate interacts with AFGP by binding to the cis-hydroxyl groups of the β-D-galactopyranosyl group.[223]Magnesium sulfate has been shown to enhance the antifreeze activity of AFGP.[221] The molecular mechanism of this enhancement is unknown. Figure 11.6d shows the normalized areas of the five different Gaussian-shaped bands obtained from a decomposition of the linear spectra (see Appendix Sec.11.4.1 and Fig.11.9). We find that at all temperatures the addition of magnesium sulfate or sodium borate does not lead to a significant change in the distribution

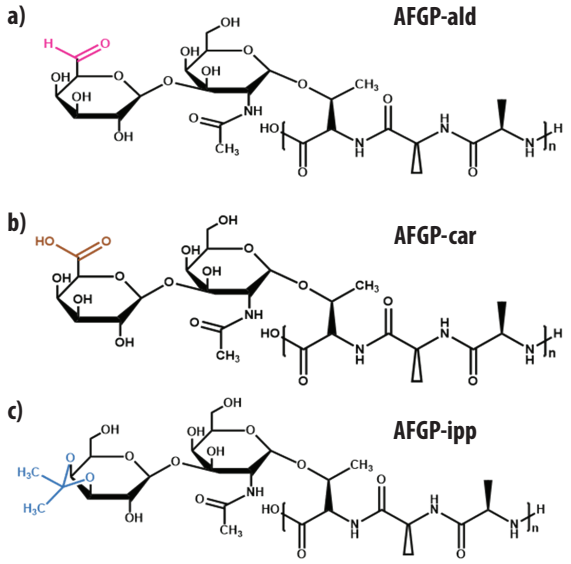

Figure 11.7: Schematic representation of the chemically modified AFGP variants. In the AFGP-ald variant, the C-6 hydroxyl groups of the saccharide were oxidized to aldehyde groups. In the variant AFGP-car, the aldehyde groups of AFGP-ald were oxidized to carboxylic acid groups. In variant AFGP-ipp, an isopropylidene group was attached to the carbohydrate.

of structures of AFGP1-5 in solution. Hence, the addition of enhancers or inhibitors does not change the distribution of the protein structural elements and the temperature dependence of this distribution. This result indicates that the effect of the inhibitors and enhancers is likely related to interactions with the disaccharide units, suggesting that AFGPs bind to ice with the hydroxyl groups of the disaccharide side chains rather than with the hydrophobic groups of the peptide backbone. This binding mechanism agrees with the results of previous studies.[15,238–240] In one of these studies the reorientation dynamics of the hydration water of AFGP was investigated and it was found that inhibiting the antifreeze activity using borate induced no changes in the dynamics of the water molecules.[239] This previous finding suggests that borate primarily interacts with the sugar unit of AFGP, in agreement with the present results.

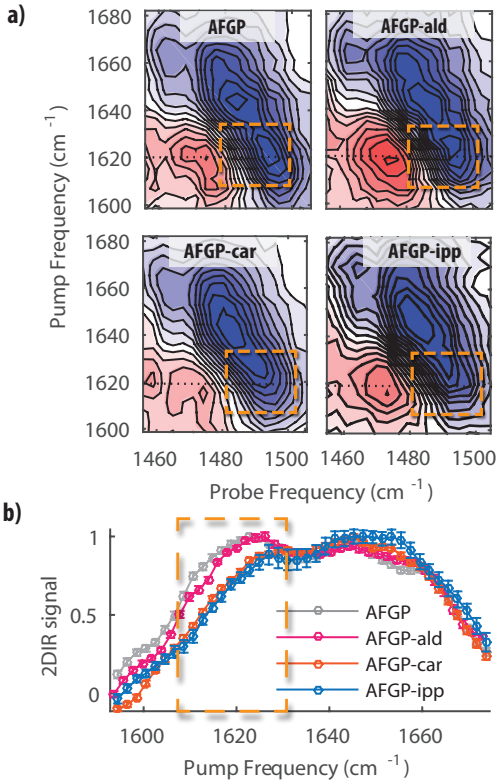

Figure 11.8: a) Perpendicular 2DIR spectra of AFGP and chemically modified AFGPs1-5 at a concentration of 2 wt%. The waiting time T_w is 0.5 ps. The orange rectangles indicate the cross-peak region where we excite the amide I, and probe the amide II at the vibrational frequencies characteristic for PPII structures. b) Anti-diagonal slices taken along the bleaching signal in the spectra shown in a. The intensity of the 2DIR signal at the pump frequency of ∼1620 cm-1 is lower for AFGP-car and AFGP-ipp.

Effect of chemical modification of AFGP on the stucture and activity anti-freeze structure

In order to gain a more comprehensive understanding of the relation between antifreeze activity and the protein structure, we investigated three different chemical modifications of AFGP (Fig.11.7). The AFGP-ald variant was obtained by oxidizing the C-6 hydroxyls of the galactose moieties of the native AFGP isoforms to an aldehyde using galactose oxidase[241]. For the AFGP-car variant the aldehydes of AFGP-ald were oxidized to carboxylic acids using bromine water[241]. The AFGP-ipp variant was prepared by adding an isopropylidene (ipp) group to the galactose part of the sugar residue[241].

In Figure 11.8a we report 2DIR spectra obtained for AFGP1-5 and the three chemically modified AFGPs1-5 at a temperature of 5°C. The delay time

T_w between the excitation and the probe pulses is 0.5 ps. In Figure 11.8b we plot anti-diagonal slices along the bleaching component of the cross-peak signals of Fig.11.8a. We observe that the cross-peak signal obtained when exciting around 1620 cm^{-1}, which represents the PPII structure, is weaker for AFGP-ipp and AFGP-car than for AFGP and AFGP-ald. The 2DIR spectra thus reveal a clear decrease of the relative abundance of the PPII structure for AFGP-ipp and AFGP-car. To quantify the reduction of the intensity of the PPII cross-peak, we decompose the anti-diagonal slices in the same ways as for native AFGP. By assuming that the coupling constant between amide I and amide II is the same for the different conformers and the different chemically modified AFGPs, we find that the PPII cross-peak intensity is decreased by 30-40% in AFGP-ipp and AFGP-car with respect to native AFGP . This decrease of the relative abundance of the PPII structure is also observed confirmed in linear infrared absorption spectra of the different AFGPs. We decompose these linear spectra by representing the amide I vibrations of the different conformers with the same Gaussian bands that we found previously. This decomposition yields to the relative fraction of PPII for the different chemically modified AFGPs (see Appendix Sec.11.4.1 and Fig.11.10). We also included an AFGP-bor variant that is obtained by adding borate ions to AFGP, which form complexes with the cis-hydroxyl groups of the galactose moiety.[242] We find that solutions of AFGP-bor and AFGP-ald contain a similar content of PPII (28$\pm$6% and 27$\pm$4%, respectively). AFGP-car and AFGP-ipp contain a lower fraction of PPII (21$\pm$4% and 24$\pm$5%). Hence, in agreement with the 2D-IR data, the infrared spectra also show a clear reduction of PPII content for AFGP-car and AFGP-ipp.

We also studied the antifreeze activity of the different chemical modifications of AFGP (see Appendix Sec.11.4.3 and 11.12), we find that the activities of AFGP-ald, AFGP-car and AFGP-ipp are reduced by 20%,70 % and 70%, respectively. We thus find that the reduction of the anti-freeze activity is strongly correlated to the reduction of the relative abundance of the PPII content, again indicating that this conformer is crucial for the antifreeze activity of AFGP.

11.3 Conclusion

We used linear infrared spectroscopy and two-dimensional infrared (2DIR) spectroscopy to study the structure of AFGP isoforms in solution. With 2DIR we measure the spectral response of the amide II modes as a function of the excitation frequency of the amide I modes. The obtained response constitutes a much more clearly resolved amide I spectrum than the linear IR amide I absorption spectrum. The improved resolution can be explained from the nonlinear character of the signal, which leads to the suppression of background and/or contamination signals that congest the linear amide I spectrum. The amide II - amide I cross-peak response reveals the presence of five distinct amide I vibrations, which we used to decompose and analyse the linear infrared amide I spectra of AFGP1-5 and AFGP7-8. We assign the 1619 cm^{-1} band to a PPII structure, the 1630 cm^{-1} and 1670 cm^{-1} bands to an extended structure (or turn), the 1644 cm^{-1} band to a random coil structure, and the 1659 cm^{-1} band to an α-helix. We thus identify the different structural motifs and conformations of AFGPs in aqueous solution. Our results demonstrate that AFGPs do not have one preferred secondary structure, and have a high structural flexibility, which make them quite distinct from non-glycosylated AFPs that typically have one preferred conformation and are very rigid.[243,244] We find that AFGPs already adopt a PPII-conformation at room temperature. This PPII content increases as the temperature is lowered. We further observe that the addition of borate, as an inhibitor of antifreeze activity, or sulfate, as an enhancer of antifreeze activity, has a negligible effect on the distribution of AFGP structures in solution, indicating that the effect of the inhibitors and enhancers is likely related to interactions with the disaccharide units. Interestingly, we also find that chemical modifications that lead to a dramatic reduction of the antifreeze activity, also induce a lower PPII content. This outcome shows that the PPII structure is critical for the antifreeze activity of AFGP.

11.4 Appendix

11.4.1 Fitting procedure for 2DIR diagonal signals and infrared spectra

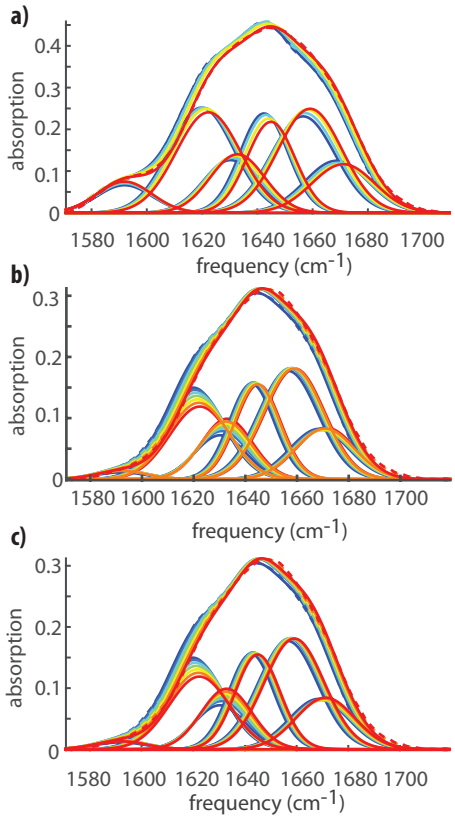

Figure 11.9: a) Linear infrared spectra at different temperature (0-40 °C) of solutions of AFGP 7-8. b) and c) linear spectra for D_2O solutions of AFGP 1-5 with 1 M of magnesium sulfate and AFGP 1-5 with 0.3 sodium borate at a concentration of ∼2 wt%, respectively. The raw data are represented by the dashed lines, and the fits by the solid lines. We also show the six Gaussian-shaped bands used to fit the data.

We fit the 2DIR diagonal signals using a global fitting procedure as a function of frequency and temperature (T_i), which is based on the minimization of the square error

$$\sum_{i,J}(S(\omega_j, T_i) - S^{exp}(\omega_j, T_i))^2 \tag{11.1}$$

where S is the fitted spectrum and S_{exp} the experimental spectrum. By observing the spectral changes in Fig.11.3 we identify the presence of 5

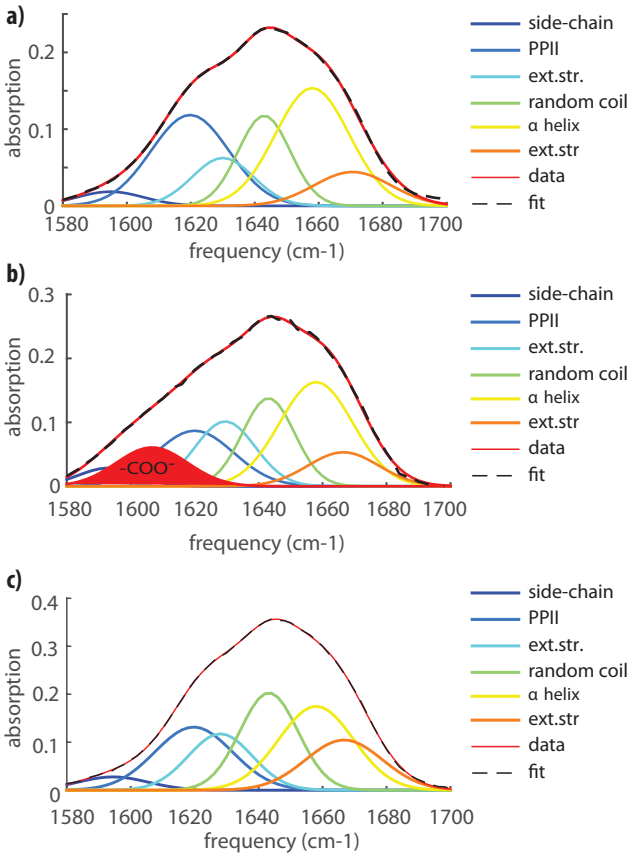

Figure 11.10: a),b) and c) linear IR spectra and fits in heavy water and at a concentration of 2 wt% for AFGP-ald, AFGP-car and AFGP-ipp. The linear IR spectra were measured at a temperature of 5 °C.

different bands. Hence we assume that the experimental spectra are a linear combination of the 5 different Gaussian-shaped bands g, and we expect that

$$\begin{aligned} &\forall i, \text{for } \omega_{min} \leqslant \omega_J \leqslant \omega_{max} \\ &S(\omega_j, T_i) = \sum_{k=1}^{5} c_k(T_i) g_k(\omega_j) \end{aligned} \tag{11.2}$$

where $c_k(T_i)$ are the amplitudes of the five Gaussian bands that account for the spectral changes as a function of temperatures. The Gaussian-parameters, width and the center positions of the bands, are free parameters, which we globally optimize for all the measured temperatures.

The fitting procedure for the linear spectra is similar. However, in this case we make use of the center positions found by fitting the 2DIR signals at different temperatures, and we thus constrain the center positions of the Gaussian-shaped peaks in the linear fit to be similar to the center positions extracted from the 2DIR fit. We use an additional Gaussian-band to describe the absorption band at 1592 cm^{-1}. The spectra and subbands resulting from the fits are reported in Fig.11.9. In fitting the linear spectra of the different chemical modifications of AFGP1-5 variants, we constrain the Gaussian-parameters by using the center positions and widths extracted from fitting the linear spectra of native AFGP1-5 (Fig.11.6b).

11.4.2 Linear spectra of N-acetylgalactosamine

The disaccharide unit of the AFGP protein is composed by N-acetyl-d-galactosamine, which carry an amide group. Fig.11.11 shows the spectrum of a solution of N-acetyl-d-galactosamine dissolved in heavy water at 6 wt%. We observe that the amide I vibration absorbs at 1627 cm^{-1}, and the amide II vibration at 1480 cm^{-1}. When the temperature is increased, the amide I blue-shifts and the amide II red-shifts by a few wave-numbers.

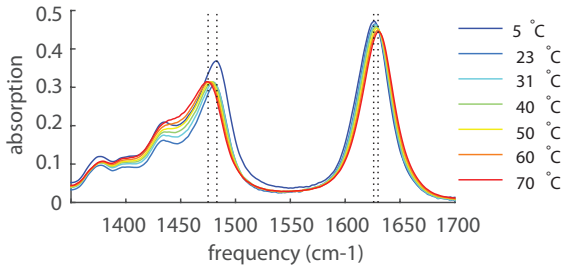

Figure 11.11: Linear infrared spectra of N-acetyl-d-galactosamine at a concentration of 6 wt%. The dashed lines indicate the center positions of the amide II and the amide I vibrations.

11.4.3 Thermal hysteresis measurements

Sun Y. et al. investigated the thermal hysteresis (TH) activity and ice recrystallization inhibition (IRI) activity of the different chemical modifications of AFGP. Figure 11.12a shows the TH activity of natural AFGP, the three chemical modifications, and AFGP in the presence of borate. Sun Y. et al. find that at 10 mg/mL the TH activity of AFGP is $\sim 0.7^{\circ}$C, and that the

TH activities of AFGP-ald, AFGP-car and AFGP-ipp are reduced by ∼20%, ∼70%, and ∼70%, respectively. Similar modifications have previously been shown to diminish the TH activity of AFGPs, and qualitatively agree with these results[241]. The addition of borate to AFGP reduces the TH activity by ∼80% which is also in line with previous studies.[15,239]

AFGPs are known to have an exceptional IRI activity[245]. Figure 11.12b shows the IRI activity for AFGP and the chemical modifications at a concentration of 2 μg/mL. Sun Y. et al. find that the IRI activities of AFGP-ald, AFGP-car and AFGP-ipp are reduced by ∼15%, ∼50%, and ∼63%, respectively. The addition of borate to AFGP leads to a reduction of the IRI activity with ∼60%.

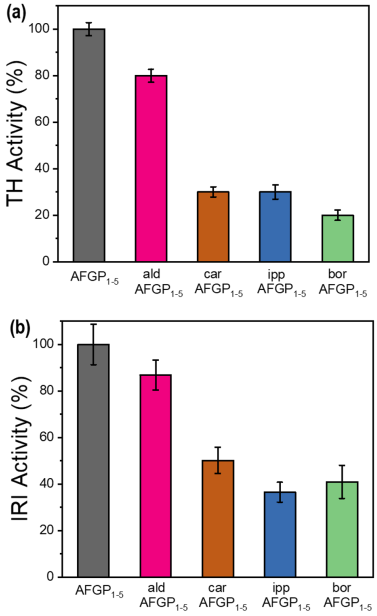

Figure 11.12: Antifreeze activity measurements of AFGP1-5 and modified variants. a) TH activities at 10 mg/ml reveals that the activity of AFGP-ald, AFGP-car, AFGP-ipp and AFGP-bor are reduced by ∼20%, 70%, 70%, and 80%, respectively. b) The IRI activity at 2 μg/ml shows that the activities of AFGP-ald, AFGP-car, AFGP-ipp and AFGP-bor are reduced by ∼15%, 50%, 60%, and 60%, respectively.

Bibliography

Bibliography

[1] Descartes René. *Discours de la methode pour bien conduire sa raison, en chercher la verité dans les sciences Plus La dioptriqve, Les meteores et La Geometrie Qui sont des essais de cete methode*. A Leyde, De limprimerie de I. Maire, 1637.

[2] P. F. Scholander. Oxygen transport through hemoglobin solutions. *Science*, 131(3400):585–590, 1960.

[3] Winslow R. Briggs. *Plant Physiology*.

[4] Jason Gandhi, Anthony C. Antonelli, Adil Afridi, Sohrab Vatsia, Gunjan Joshi, Victor Romanov, Ian V.J. Murray, and Sardar Ali Khan. Protein misfolding and aggregation in neurodegenerative diseases: A review of pathogeneses, novel detection strategies, and potential therapeutics. *Reviews in the Neurosciences*, 30(4):339–358, jun 2019.

[5] Fred E. Cohen. Protein misfolding and prion diseases. *Journal of Molecular Biology*, 293(2):313–320, oct 1999.

[6] D. B. Wetlaufer. Nucleation, rapid folding, and globular intrachain regions in proteins. *Proceedings of the National Academy of Sciences of the United States of America*, 70(3):697–701, 1973.

[7] Philip A. Evans, Christopher M. Dobson, Roger A. Kautz, Graham Hatfull, and Robert O. Fox. Proline isomerism in staphylococcal nuclease characterized by NMR and site-directed mutagenesis. *Nature*, 329(6136):266–268, sep 1987.

[8] Malcolm W. MacArthur and Janet M. Thornton. Influence of proline residues on protein conformation. *Journal of Molecular Biology*, 218(2):397–412, mar 1991.

[9] Caitlin M. Davis and R. Brian Dyer. The Role of Electrostatic Interactions in Folding of β-Proteins. *Journal of the American Chemical Society*, 138(4):1456–1464, 2016.

[10] Daniel G Isom, Carlos A Castañeda, Brian R Cannon, Priya D Velu, and Bertrand García-Moreno E. Charges in the hydrophobic interior of proteins. *Proceedings of the National Academy of Sciences of the United States of America*, 107(37):16096–100, sep 2010.

[11] Bjørn P. Pedersen, Morten J. Buch-Pedersen, J. Preben Morth, Michael G. Palmgren, and Poul Nissen. Crystal structure of the plasma membrane proton pump. *Nature*, 450(7172):1111–1114, dec 2007.

[12] Florian Garczarek and Klaus Gerwert. Functional waters in intraprotein proton transfer monitored by FTIR difference spectroscopy. *Nature*, 439(7072):109–112, 2006.

[13] Peter E. Wright and H. Jane Dyson. Intrinsically unstructured proteins: Re-assessing the protein structure-function paradigm. *Journal of Molecular Biology*, 293(2):321–331, oct 1999.

[14] Arthur L. DeVries and Donald E. Wohlschlag. Freezing resistance in some antarctic fishes. *Science*, 163(3871):1073–1075, mar 1969.

[15] Arthur L. DeVries. Glycoproteins as biological antifreeze agents in Antarctic fishes. *Science*, 172(3988):1152–1155, jun 1971.

[16] Kenji Mochizuki and Valeria Molinero. Antifreeze Glycoproteins Bind Reversibly to Ice via Hydrophobic Groups. *Journal of the American Chemical Society*, 140(14):4803–4811, 2018.

[17] Chris Kiani, Liwen Chen, Yao Jiong Wu, Albert J. Yee, and Burton B. Yang. Structure and function of aggrecan, 2002.

[18] Neha S. Gandhi and Ricardo L. Mancera. The structure of glycosaminoglycans and their interactions with proteins, dec 2008.

[19] Akihiro Onishi, Kalib St Ange, Jonathan S. Dordick, and Robert J. Linhardt. Heparin and anticoagulation. *Frontiers in Bioscience - Landmark*, 21(7):1372–1392, jun 2016.

[20] Ulf Lindahl, Kerstin Lidholt, Dorothe Spillmann, and Lena Kjellén. More to "heparin" than anticoagulation. *Thrombosis Research*, 75(1):1–32, jul 1994.

[21] David H. Small, Victor Nurcombe, Gullveig Reed, Heidi Clarris, Robert Moir, Konrad Beyreuther, and Colin L. Masters. A heparin-binding domain in the amyloid protein precursor of Alzheimer's disease is involved in the regulation of neurite outgrowth. *Journal of Neuroscience*, 14(4):2117–2127, apr 1994.

[22] Jeffrey A. Cohlberg, Jie Li, Vladimir N. Uversky, and Anthony L. Fink. Heparin and other glycosaminoglycans stimulate the formation of amyloid fibrils from α-synuclein in vitro. *Biochemistry*, 41(5):1502–1511, feb 2002.

[23] Rafael S. Aquino, Eui Seung Lee, and Pyong Woo Park. Diverse functions of glycosaminoglycans in infectious diseases. In *Progress in Molecular Biology and Translational Science*, volume 93, pages 373–394. Elsevier B.V., 2010.

[24] Julia Y. Wang and Michael H. Roehrl. Glycosaminoglycans are a potential cause of rheumatoid arthritis. *Proceedings of the National Academy of Sciences of the United States of America*, 99(22):14362–14367, oct 2002.

[25] R. Lever, A. Smailbegovic, and C. Page. Role of glycosaminoglycans in inflammation. In *Inflammopharmacology*, volume 9, pages 165–169, 2001.

[26] Malgorzata Litwiniuk, Alicja Krejner, and Tomasz Grzela. Hyaluronic Acid in Inflammation and Tissue Regeneration, 2016.

[27] Chun-Yu Lin, Constantinos Kolliopoulos, Chung-Hao Huang, Jyrki Tenhunen, Carl-Henrik Heldin, Yen-Hsu Chen, and Paraskevi Heldin. High levels of serum hyaluronan is an early predictor of dengue warning signs and perturbs vascular integrity. *EBioMedicine*, sep 2019.

[28] Torvard C. Laurent, Ulla B.G. Laurent, and J. Robert E. Fraser. Serum hyaluronan as a disease marker, 1996.

[29] Bryan P. Toole. Hyaluronan: from extracellular glue to pericellular cue. *Nature Reviews Cancer*, 4(7):528–539, jul 2004.

[30] Xiao Tian, Jorge Azpurua, Christopher Hine, Amita Vaidya, Max Myakishev-Rempel, Julia Ablaeva, Zhiyong Mao, Eviatar Nevo, Vera Gorbunova, and Andrei Seluanov. High-molecular-mass hyaluronan mediates the cancer resistance of the naked mole rat. *Nature*, 499(7458):346–349, 2013.

[31] Mikhail A. Selyanin, Petr Ya. Boykov, Vladimir N. Khabarov, and Felix Polyak. The History of Hyaluronic Acid Discovery, Foundational Research and Initial Use. In *Hyaluronic Acid*, pages 1–8. John Wiley & Sons, Ltd, Chichester, UK, jan 2015.

[32] Grigorij Kogan, Ladislav Šoltés, Robert Stern, and Peter Gemeiner. Hyaluronic acid: A natural biopolymer with a broad range of biomedical and industrial applications, jan 2007.

[33] Jason A. Burdick and Glenn D. Prestwich. Hyaluronic acid hydrogels for biomedical applications. *Advanced Materials*, 23(12), mar 2011.

[34] Adrianne M. Rosales and Kristi S. Anseth. The design of reversible hydrogels to capture extracellular matrix dynamics. *Nature Reviews Materials*, 1(2):15012, feb 2016.

[35] Maurice N. Collins and Colin Birkinshaw. Hyaluronic acid based scaffolds for tissue engineering - A review, feb 2013.

[36] Endre A. Balazs and Jennifer Cui. The story of hyaluronan putty. *Bioactive Carbohydrates and Dietary Fibre*, 2(2):143–151, oct 2013.

[37] By Samuel Krimm and Jagdeesh Bandekart. Vibrational Spectroscopy and Conformation. *Advances in protein chemistry*, 38:48109, 1986.

[38] Donna Strickland and Gerard Mourou. Compression of amplified chirped optical pulses. *Optics Communications*, 56(3):219–221, dec 1985.

[39] Neil T. Hunt. 2D-IR spectroscopy: ultrafast insights into biomolecule structure and function. *Chemical Society Reviews*, 38(7):1837, jun 2009.

[40] Joseph A. Fournier, William B. Carpenter, Nicholas H.C. Lewis, and Andrei Tokmakoff. Broadband 2D IR spectroscopy reveals dominant asymmetric H5O2+ proton hydration structures in acid solutions. *Nature Chemistry*, 10(9):932–937, sep 2018.

[41] Junrong Zheng, Kyungwon Kwak, John Asbury, Xin Chen, Ivan R Piletic, and M D Fayer. Ultrafast dynamics of solute-solvent complexation observed at thermal equilibrium in real time. *Science (New York, N.Y.)*, 309(5739):1338–43, aug 2005.

[42] Ariel M Alperstein, Joshua S Ostrander, Tianqi O Zhang, and Martin T Zanni. Amyloid found in human cataracts with two-dimensional infrared spectroscopy. *Proceedings of the National Academy of Sciences of the United States of America*, 116(14):6602–6607, 2019.

[43] P.Hamm and M.Zanni. *Concepts and Methods of 2D Infrared Spectroscopy*. Cambridge University Press, 2011.

[44] Yves L. A. Rezus. *Snapshots of water, Orientational dynamics of hydrogen-bonded system*. PhD thesis, University of Amsterdam, 2008.

[45] Oleg Selig. *Ultrasensitive nonlinear vibrational spectroscopy of complex molecular systems*. PhD thesis, University of Amsterdam, 2017.

[46] W. Heisenberg. Über den anschaulichen Inhalt der quantentheoretischen Kinematik und Mechanik. *Zeitschrift für Physik*, 43(3-4):172–198, mar 1927.

[47] G. Lipari and A. Szabo. Effect of librational motion on fluorescence depolarization and nuclear magnetic resonance relaxation in macromolecules and membranes. *Biophysical Journal*, 30(3):489–506, 1980.

[48] Y. L A Rezus and H. J. Bakker. On the orientational relaxation of HDO in liquid water. *Journal of Chemical Physics*, 123(11), 2005.

[49] H. J. Bakker and J. L. Skinner. Vibrational spectroscopy as a probe of structure and dynamics in liquid water. *Chemical Reviews*, 110(3):1498–1517, mar 2010.

[50] S. Woutersen, U. Emmerichs, and H. J. Bakker. A femtosecond mid-infrared pump-probe study of hydrogen-bonding in ethanol. *Journal of Chemical Physics*, 107(5):1483–1490, jun 1997.

[51] Sander Woutersen, Yuguang Mu, Gerhard Stock, and Peter Hamm. Subpicosecond conformational dynamics of small peptides probed by two-dimensional vibrational spectroscopy. *Proceedings of the National Academy of Sciences of the United States of America*, 98(20):11254–11258, sep 2001.

[52] Johan R.C. van der Maarel. *Introduction to biopolymer physics*. WORLD SCIENTIFIC, dec 2007.

[53] Paul J. Flory. *Principles of Polymer Chemistry*. Cornel University Press, 1953.

[54] Gerald S. Manning. Limiting laws and counterion condensation in polyelectrolyte solutions I. Colligative properties. *The Journal of Chemical Physics*, 51(3):924–933, 1969.

[55] Jeffrey I. Seeman. Effect of conformational change on reactivity in organic chemistry. Evaluations, applications, and extensions of Curtin-Hammett Winstein-Holness kinetics. *Chemical Reviews*, 83(2):83–134, apr 1983.

[56] Craig A Taatjes, Oliver Welz, Arkke J Eskola, John D Savee, Adam M Scheer, Dudley E Shallcross, Brandon Rotavera, Edmond P F Lee, John M Dyke, Daniel K W Mok, David L Osborn, and Carl J Percival. Direct measurements of conformer-dependent reactivity of the Criegee intermediate CH3CHOO. *Science (New York, N.Y.)*, 340(6129):177–80, apr 2013.

[57] Sang Tae Park, Sang Kyu Kim, and Myung Soo Kim. Observation of conformation-specific pathways in the photodissociation of 1-iodopropane ions. *Nature*, 415(6869):306–308, jan 2002.

[58] Yuan-Pin Chang, Karol Długołęcki, Jochen Küpper, Daniel Rösch, Dieter Wild, and Stefan Willitsch. Specific chemical reactivities of spatially separated 3-aminophenol conformers with cold Ca+ ions. *Science (New York, N.Y.)*, 342(6154):98–101, oct 2013.

[59] M Kim, L Shen, H Tao, T Martinez, and A Suits. Conformationally Controlled Chemistry: Excited-State Dynamics Dictate Ground-State Reaction. *Science*, 315(March):1561–1565, 2007.

[60] E. G. Robertson and J. P. Simons. Getting into shape: Conforrmational and supramolecular landscapes in small biomolecules and their hydrated clusters. *Physical Chemistry Chemical Physics*, 3(1):1–18, 2001.

[61] Gunter Fischer, Brigitte Wittmann-Liebold, Kurt Lang, Thomas Kiefhaber, and Franz X. Schmid. Cyclophilin and peptidyl-prolyl cis-trans isomerase are probably identical proteins. *Nature*, 337(6206):476–478, feb 1989.

[62] Robert Freedman. Folding into the right shape. *Nature*, 329(6136):196–197, sep 1987.

[63] Franziska Zosel, Davide Mercadante, Daniel Nettels, and Benjamin Schuler. A proline switch explains kinetic heterogeneity in a coupled folding and binding reaction. *Nature Communications*, 9(1):3332, dec 2018.

[64] Kun Ping Lu, Greg Finn, Tae Ho Lee, and Linda K. Nicholson. Prolyl cis-trans isomerization as a molecular timer. *Nature Chemical Biology*, 3(10):619–629, oct 2007.

[65] Franck Ilmain, Toyoichi Tanaka, and Etsuo Kokufuta. Volume transition in a gel driven by hydrogen bonding. *Nature*, 349(6308):400–401, jan 1991.

[66] K. Alba, R. J. Bingham, P. A. Gunning, P. J. Wilde, and V. Kontogiorgos. Pectin Conformation in Solution. *Journal of Physical Chemistry B*, 122(29):7286–7294, jul 2018.

[67] R. Fausto, L. A. E. Batista de Carvalho, J. J. C. Teixeira-Dias, and M. N. Ramos. s-cis and s-trans Conformers of Formic, Thioformic and Dithioformic Acids. *J. Chem. Soc., Faraday Trans. 2*, 85:1945–1962, 1989.

[68] Hajime Hirao. Theoretical study of formic acid: A new look at the origin of the planar Z conformation and C-O rotational barrier. *Chemical Physics*, 344(3):213–220, 2008.

[69] Julianto Pranata. Relative basicities of carboxylate lone pairs in aqueous solution. *Journal of Computational Chemistry*, 14(6):685–690, 1993.

[70] Hirofumi Sato and Fumio Hirata. The syn-ranti-conformational equilibrium of acetic acid in water studied by the RISM-SCFrMCSCF method. *Journal of Molecular Structure Theochem*, 461(462):113–120, 1999.

[71] Mika Pettersson, Ermelinda M.S. Maçôas, Leonid Khriachtchev, Rui Fausto, and Markku Räsänen. Conformational isomerization of formic acid by vibrational excitation at energies below the torsional barrier. *Journal of the American Chemical Society*, 125(14):4058–4059, 2003.

[72] E. M.S. Maçôas, L. Khriachtchev, R. Fausto, and M. Räsänen. Photochemistry and Vibrational Spectroscopy of the Trans and Cis Conformers of Acetic Acid in Solid Ar. *Journal of Physical Chemistry A*, 108(16):3380–3389, 2004.

[73] Ermelinda M. S. Maçôas, Leonid Khriachtchev, Mika Pettersson, Rui Fausto, and Markku Räsänen. Rotational isomerization of small carboxylic acids isolated in argon matrices: Tunnelling and quantum yields for the photoinduced processes. *Phys. Chem. Chem. Phys.*, 7(5):743–749, 2005.

[74] K. Marushkevich, L. Khriachtchev, J. Lundell, A. V. Domanskaya, and M. Räsänen. Vibrational spectroscopy of trans and cis deuterated formic

acid (HCOOD): Anharmonic calculations and experiments in argon and neon matrices. *Journal of Molecular Spectroscopy*, 259(2):105–110, 2010.

[75] Kseniya Marushkevich, Leonid Khriachtchev, Jan Lundell, Alexandra Domanskaya, and Markku Räsänen. Matrix isolation and ab initio study of trans-trans and trans-cis dimers of formic acid. *Journal of Physical Chemistry A*, 114(10):3495–3502, 2010.

[76] Leonid Khriachtchev, Alexandra Domanskaya, Kseniya Marushkevich, Markku Räsänen, Bella Grigorenko, Alexander Ermilov, Natalya Andrijchenko, and Alexander Nemukhin. Conformation-dependent chemical reaction of formic acid with an oxygen atom. *Journal of Physical Chemistry A*, 113(29):8143–8146, 2009.

[77] Peter I. Nagy. The syn-anti equilibrium for the COOH group reinvestigated. Theoretical conformation analysis for acetic acid in the gas phase and in solution. *Computational and Theoretical Chemistry*, 1022:59–69, 2013.

[78] F Génin, F Quilès, and A Burneau. Infrared and Raman spectroscopic study of carboxylic acids in heavy water. *Physical Chemistry Chemical Physics*, 3(6):932–942, 2001.

[79] Jianhan Chen, Charles L Brooks, and Harold A Scheraga. Revisiting the carboxylic acid dimers in aqueous solution: Interplay of hydrogen bonding, hydrophobic interactions and entropy. *Journal of Physical Chemistry B*, 112:242–249, 2008.

[80] Karsten Heyne, Nils Huse, Jens Dreyer, Erik T J Nibbering, Thomas Elsaesser, and Shaul Mukamel. Coherent low-frequency motions of hydrogen bonded acetic acid dimers in the liquid phase Coherent low-frequency motions of hydrogen bonded acetic acid dimers in the liquid phase. *J. Chem. Phys.*, 902(2004):902–913, 2012.

[81] Susy Lopes, Alexandra V. Domanskaya, Rui Fausto, Markku Räsänen, and Leonid Khriachtchev. Formic and acetic acids in a nitrogen matrix:

Enhanced stability of the higher-energy conformer. *Journal of Chemical Physics*, 133(14):1–7, 2010.

[82] Attila Kovács, Balázs Nyerges, and Vladislav Izvekov. Vibrational analysis of N-acetyl-alpha-D-glucosamine and beta-D-glucuronic acid. *The journal of physical chemistry. B*, 112(18):5728–35, 2008.

[83] O. Selig, R. Siffels, and Y. L. A. Rezus. Ultrasensitive Ultrafast Vibrational Spectroscopy Employing the Near Field of Gold Nanoantennas. *Physical Review Letters*, 114(23):233004, jun 2015.

[84] David E Moilanen, Emily E Fenn, Yu-Shan Lin, J L Skinner, B Bagchi, and Michael D Fayer. Water inertial reorientation: hydrogen bond strength and the angular potential. *Proceedings of the National Academy of Sciences of the United States of America*, 105(14):5295–300, apr 2008.

[85] Juddy Mwaura, Zhen Tao, Herbert James, Thomas Albers, Alexander Schwartz, and Christof Grewer. Protonation state of a conserved acidic amino acid involved in Na + binding to the glutamate transporter EAAC1. *ACS Chemical Neuroscience*, 3(12):1073–1083, 2012.

[86] Giovanna Di Nardo, Maximilian Breitner, Andrea Bandino, Debashis Ghosh, Gareth K. Jennings, John C. Hackett, and Gianfranco Gilardi. Evidence for an Elevated Aspartate p K _a in the Active Site of Human Aromatase. *Journal of Biological Chemistry*, 290(2):1186–1196, 2015.

[87] Samuel Z. Hanz, Nicolas S. Shu, Jieni Qian, Nathaniel Christman, Patrick Kranz, Ming An, Christof Grewer, and Wei Qiang. Protonation-Driven Membrane Insertion of a pH-Low Insertion Peptide. *Angewandte Chemie - International Edition*, 55(40):12376–12381, 2016.

[88] M. R. Gunner and E. Alexov. A pragmatic approach to structure based calculation of coupled proton and electron transfer in proteins. *Biochimica et Biophysica Acta - Bioenergetics*, 1458(1):63–87, 2000.

[89] Jayasankar Jasti, Hiroyasu Furukawa, Eric B. Gonzales, and Eric Gouaux. Structure of acid-sensing ion channel 1 at 1.9 Å resolution and low pH. *Nature*, 449(7160):316–323, 2007.

[90] Nate Yoder, Craig Yoshioka, and Eric Gouaux. Gating mechanisms of acid-sensing ion channels. *Nature*, 555(7696):397–401, 2018.

[91] M. Pettersson, J. Lundell, L. Khriachtchev, and M. Rasanen. IR spectrum of the other rotamer of formic acid, cis-HCOOH. *Journal of the American Chemical Society*, 119(48):11715–11716, 1997.

[92] Ermelinda M. S. Maçôas, Leonid Khriachtchev, Mika Pettersson, Rui Fausto, and Markku Räsänen. Rotational isomerization of small carboxylic acids isolated in argon matrices: Tunnelling and quantum yields for the photoinduced processes. *Phys. Chem. Chem. Phys.*, 7(5):743–749, 2005.

[93] Ermelinda M. S. Maçôas, Leonid Khriachtchev, Mika Pettersson, Rui Fausto, and Markku Räsänen. Internal Rotation in Propionic Acid: Near-Infrared-Induced Isomerization in Solid Argon. *The Journal of Physical Chemistry A*, 109(16):3617–3625, apr 2005.

[94] Luigi D'Ascenzo and Pascal Auffinger. A comprehensive classification and nomenclature of carboxyl–carboxyl(ate) supramolecular motifs and related catemers: implications for biomolecular systems. *Acta Crystallographica Section B Structural Science, Crystal Engineering and Materials*, 71(2):164–175, apr 2015.

[95] Richard David Gandour. On the importance of orientation in general base catalysis by carboxylate. *Bioorganic Chemistry*, 10(2):169–176, jun 1981.

[96] Melissa Salmon, Ramesha B. Thimmappa, Robert E. Minto, Rachel E. Melton, Richard K. Hughes, Paul E. O'maille, Andrew M. Hemmings, and Anne Osbourn. A conserved amino acid residue critical for product and substrate specificity in plant triterpene synthases. *Proceedings of the National Academy of Sciences of the United States of America*, 113(30):E4407–E4414, 2016.

[97] Katarzyna Świderek, Iñaki Tuñón, Vicent Moliner, and Joan Bertran. Protein Flexibility and Preorganization in the Design of Enzymes. The Kemp Elimination Catalyzed by HG3.17. *ACS Catalysis*, 5(4):2587–2595, apr 2015.

[98] Brian J. Bahnson, Vernon E. Anderson, and Gregory A. Petsko. Structural mechanism of enoyl-CoA hydratase: Three atoms from a single water are added in either an E1cb stepwise or concerted fashion. *Biochemistry*, 41(8):2621–2629, 2002.

[99] Erik W. Debler, Shuichiro Ito, Florian P. Seebeck, Andreas Heine, Donald Hilvert, and Ian A. Wilson. Structural origins of efficient proton abstraction from carbon by a catalytic antibody. *Proceedings of the National Academy of Sciences*, 102(14):4984–4989, apr 2005.

[100] Adam Eriksson, Charlotte Kürten, and Per-Olof Syrén. Protonation-Initiated Cyclization by a Class II Terpene Cyclase Assisted by Tunneling. *ChemBioChem*, 18(23):2301–2305, dec 2017.

[101] Ilja V. Khavruttski, Jaimee R. Compton, Kayla M. Jurkouich, and Patricia M. Legler. Paired Carboxylic Acids in Enzymes and Their Role in Selective Substrate Binding, Catalysis, and Unusually Shifted p K a Values. *Biochemistry*, page acs.biochem.9b00429, jul 2019.

[102] Kenan Gündoğdu, Jigar Bandaria, Michael Nydegger, William Rock, and Christopher M. Cheatum. Relaxation and anharmonic couplings of the O-H stretching vibration of asymmetric strongly hydrogen-bonded complexes. *Journal of Chemical Physics*, 127(4), 2007.

[103] Ashley M. Stingel and Poul B. Petersen. Couplings Across the Vibrational Spectrum Caused by Strong Hydrogen Bonds: A Continuum 2D IR Study of the 7-Azaindole-Acetic Acid Heterodimer. *Journal of Physical Chemistry B*, 120(41):10768–10779, 2016.

[104] Rumpa Pal, M. B. Madhusudana Reddy, B. Dinesh, Manjunath A. Venkatesha, Simon Grabowsky, Christian Jelsch, and Tayur N. Guru

Row. Syn vs Anti Carboxylic Acids in Hybrid Peptides: Experimental and Theoretical Charge Density and Chemical Bonding Analysis. *The Journal of Physical Chemistry A*, 122(14):3665–3679, apr 2018.

[105] Samantha Hume, Gordon Hithell, Gregory M. Greetham, Paul M. Donaldson, Michael Towrie, Anthony W. Parker, Matthew J. Baker, and Neil T. Hunt. Measuring proteins in H2O with 2D-IR spectroscopy. *Chemical Science*, 10(26):6448–6456, 2019.

[106] Michael R. Peterson and Imre G. Csizmadia. Determination and analysis of the formic acid conformational hypersurface. *Journal of the American Chemical Society*, 101(5):1076–1079, feb 1979.

[107] Kenneth B. Wiberg and Keith E. Laidig. Barriers to rotation adjacent to double bonds. 3. The carbon-oxygen barrier in formic acid, methyl formate, acetic acid, and methyl acetate. The origin of ester and amide resonance. *Journal of the American Chemical Society*, 109(20):5935–5943, sep 1987.

[108] Stephan C. Hammer, Antonija Marjanovic, Jörg M. Dominicus, Bettina M. Nestl, and Bernhard Hauer. Squalene hopene cyclases are protonases for stereoselective Brønsted acid catalysis. *Nature Chemical Biology*, 11(2):121–126, feb 2015.

[109] Maiken Nedergaard, Takahiro Takano, and Anker J. Hansen. Beyond the role of glutamate as a neurotransmitter. *Nature Reviews Neuroscience*, 3(9):748–755, sep 2002.

[110] Jesús Tejero, Ashis Biswas, Zhi-Qiang Wang, Richard C. Page, Mohammad Mahfuzul Haque, Craig Hemann, Jay L. Zweier, Saurav Misra, and Dennis J. Stuehr. Stabilization and Characterization of a Heme-Oxy Reaction Intermediate in Inducible Nitric-oxide Synthase. *Journal of Biological Chemistry*, 283(48):33498–33507, nov 2008.

[111] Marina Sorrentino Hernandes and L. R P Troncone. Glycine as a neurotransmitter in the forebrain: A short review. *Journal of Neural Transmission*, 116(12):1551–1560, 2009.

[112] Kenneth K.S. Ng, Natalia Pendás-Franco, Jorge Rojo, José A. Boga, Àngeles Machín, José M. Martín Alonso, and Francisco Parra. Crystal Structure of Norwalk Virus Polymerase Reveals the Carboxyl Terminus in the Active Site Cleft. *Journal of Biological Chemistry*, 279(16):16638–16645, apr 2004.

[113] Xiuhua Yin, Shengtang Liu, Jose Manuel Perez-Aguilar, Hong Zhou, Qiwen Shao, Zaixing Yang, and Ruhong Zhou. Different protonated states at the C-terminal of the amyloid-β peptide modulate the stability of S-shaped protofibril. *The Journal of Chemical Physics*, 150(18):185102, may 2019.

[114] Giulia Giubertoni, Oleksandr O. Sofronov, and Huib J. Bakker. Observation of Distinct Carboxylic Acid Conformers in Aqueous Solution. *The Journal of Physical Chemistry Letters*, pages 3217–3222, may 2019.

[115] Victoria T Lim, Christopher I Bayly, Laszlo Fusti-Molnar, and David L Mobley. Assessing the conformational equilibrium of carboxylic acid via quantum mechanical and molecular dynamics studies on acetic acid. *Journal of chemical information and modeling*, 2019.

[116] Oleg Selig, Ana V. Cunha, Mark B. Van Eldijk, Jan C.M. Van Hest, Thomas L.C. Jansen, Huib J. Bakker, and Yves L.A. Rezus. Temperature-Induced Collapse of Elastin-like Peptides Studied by 2DIR Spectroscopy. *Journal of Physical Chemistry B*, 122(34):8243–8254, aug 2018.

[117] Nataliya S Myshakina, Zeeshan Ahmed, and Sanford A Asher. Dependence of Amide Vibrations on Hydrogen Bonding.

[118] Hajime Torii, Tomoaki Tatsumi, , Takanori Kanazawa, and † Mitsuo Tasumi*. Effects of Intermolecular Hydrogen-Bonding Interactions on the Amide I Mode of N-Methylacetamide: Matrix-Isolation Infrared Studies and ab Initio Molecular Orbital Calculations. 1998.

[119] Roger N. Hunston, Ioannis P. Gerothanassis, and Juergen Lauterwein. A study of L-proline, sarcosine, and the cis/trans isomers of N-acetyl-L-

proline and N-acetylsarcosine in aqueous and organic solution by oxygen-17 NMR. *Journal of the American Chemical Society*, 107(9):2654–2661, may 1985.

[120] Soohwan Sul, ‡ Denis Karaiskaj, , Ying Jiang, and Nien-Hui Ge*. Conformations of N-Acetyl-l-Prolinamide by Two-Dimensional Infrared Spectroscopy†. 2006.

[121] Jrgen Lauterwein, Ioannis P. Gerothanassis, and Roger N. Hunston. A study of the cis/trans isomerism of N-acetyl-L-proline in aqueous solution by 17O n.m.r. spectroscopy. *Journal of the Chemical Society, Chemical Communications*, (6):367, jan 1984.

[122] Grigorij Kogan, Ladislav Šoltés, Robert Stern, and Peter Gemeiner. Hyaluronic acid: a natural biopolymer with a broad range of biomedical and industrial applications. *Biotechnology Letters*, 29(1):17–25, dec 2006.

[123] Anirudha Singh, Michael Corvelli, Shimon A. Unterman, Kevin A. Wepasnick, Peter McDonnell, and Jennifer H. Elisseeff. Enhanced lubrication on tissue and biomaterial surfaces through peptide-mediated binding of hyaluronic acid. *Nature Materials*, 13(10):988–995, oct 2014.

[124] Uri Raviv, Suzanne Giasson, Nir Kampf, Jean-François Gohy, Robert Jérôme, and Jacob Klein. Lubrication by charged polymers. *Nature*, 425(6954):163–165, sep 2003.

[125] Zhenhuan Zhang and Gordon F. Christopher. The nonlinear viscoelasticity of hyaluronic acid and its role in joint lubrication. *Soft Matter*, 11(13):2596–2603, mar 2015.

[126] Ovijit Chaudhuri, Luo Gu, Darinka Klumpers, Max Darnell, Sidi A. Bencherif, James C. Weaver, Nathaniel Huebsch, Hong-pyo Lee, Evi Lippens, Georg N. Duda, and David J. Mooney. Hydrogels with tunable stress relaxation regulate stem cell fate and activity. *Nature Materials*, 15(3):326–334, mar 2016.

[127] Mary K Cowman, Tannin A Schmidt, Preeti Raghavan, and Antonio Stecco. Viscoelastic Properties of Hyaluronan in Physiological Conditions. *F1000Research*, 4:622, 2015.

[128] Shengfang Wu, Lianzhong Ai, Jie Chen, Ji Kang, and Steve W Cui. Study of the mechanism of formation of hyaluronan putty at pH 2 . 5 : Part I . Experimental measurements. *Carbohydrate Polymers*, (2):1677–1682, nov 2013.

[129] Iuliana Gatej, Marcel Popa, and Marguerite Rinaudo. Role of the pH on hyaluronan behavior in aqueous solution. *Biomacromolecules*, 6(1):61–67, 2005.

[130] D. A. Gibbs, E. W. Merrill, K. A. Smith, and E. A. Balazs. Rheology of hyaluronic acid. *Biopolymers*, 6(6):777–791, jun 1968.

[131] C. Oelschlaeger, M. Cota Pinto Coelho, and N. Willenbacher. Chain Flexibility and Dynamics of Polysaccharide Hyaluronan in Entangled Solutions: A High Frequency Rheology and Diffusing Wave Spectroscopy Study. *Biomacromolecules*, 14(10):3689–3696, oct 2013.

[132] Robert L. Cleland. Viscometry and sedimentation equilibrium of partially hydrolyzed hyaluronate: Comparison with theoretical models of wormlike chains. *Biopolymers*, 23(4):647–666, apr 1984.

[133] * A. Almond, , A. Brass, and J. K. Sheehan. Oligosaccharides as Model Systems for Understanding Water-Biopolymer Interaction: Hydrated Dynamics of a Hyaluronan Decamer. 2000.

[134] J E Scott, F Heatley, and W E Hull. Secondary structure of hyaluronate in solution. A 1H-n.m.r. investigation at 300 and 500 MHz in [2H6]dimethyl sulphoxide solution. *The Biochemical journal*, 220(1):197–205, may 1984.

[135] A Almond, J K Sheehan, and A Brass. Molecular dynamics simulations of the two disaccharides of hyaluronan in aqueous solution. *Glycobiology*, 7(5):597–604, jul 1997.

[136] Andrew Almond, Paul L. DeAngelis, and Charles D. Blundell. Hyaluronan: The Local Solution Conformation Determined by NMR and Computer Modeling is Close to a Contracted Left-handed 4-Fold Helix. *Journal of Molecular Biology*, 358(5):1256–1269, may 2006.

[137] Charles D Blundell, Paul L Deangelis, and Andrew Almond. Hyaluronan: the absence of amide-carboxylate hydrogen bonds and the chain conformation in aqueous solution are incompatible with stable secondary and tertiary structure models. *The Biochemical journal*, 396(3):487–98, jun 2006.

[138] Mary K Cowman, Dennis Cozart, Koji Nakanishi, and Endre A Balazs. 1H NMR of glycosaminoglycans and hyaluronic acid oligosaccharides in aqueous solution: The amide proton environment. *Archives of Biochemistry and Biophysics*, 230(1):203–212, apr 1984.

[139] Christoph Kolano, Jan Helbing, Mariusz Kozinski, Wolfram Sander, and Peter Hamm. Watching hydrogen-bond dynamics in a β-turn by transient two-dimensional infrared spectroscopy. *Nature*, 444(7118):469–472, nov 2006.

[140] S. Woutersen and P. Hamm. Isotope-edited two-dimensional vibrational spectroscopy of trialanine in aqueous solution. *Journal of Chemical Physics*, 114(6):2727–2737, feb 2001.

[141] Lauren P. DeFlores, Ziad Ganim, Sarah F. Ackley, Hoi Sung Chung, and Andrei Tokmakoff. The anharmonic vibrational potential and relaxation pathways of the amide I and II modes of N-methylacetamide. *Journal of Physical Chemistry B*, 110(38):18973–18980, 2006.

[142] Arend G. Dijkstra, Thomas La Cour Jansen, Robbert Bloem, and Jasper Knoester. Vibrational relaxation in simulated two-dimensional infrared spectra of two amide modes in solution. *Journal of Chemical Physics*, 127(19):194505, nov 2007.

[143] M B Mathews and L Decker. Conformation of hyaluronate in neutral and alkaline solutions. *Biochimica et biophysica acta*, 498(1):259–63, jun 1977.

[144] Christopher E. Reed, Xiao Li, and Wayne F. Reed. The effects of pH on hyaluronate as observed by light scattering. *Biopolymers*, 28(11):1981–2000, nov 1989.

[145] K Haxaire, I Braccini, M Milas, M Rinaudo, and S Pérez. Conformational behavior of hyaluronan in relation to its physical properties as probed by molecular modeling. *Glycobiology*, 10(6):587–94, jun 2000.

[146] Robert L. Cleland. Effect of temperature on the limiting viscosity number of hyaluronic acid and chondroitin 4-sulfate. *Biopolymers*, 18(7):1821–1828, jul 1979.

[147] Eric Fouissac, Michel Milas, and Marguerite Rinaudo. Shear-rate, concentration, molecular weight, and temperature viscosity dependences of hyaluronate, a wormlike polyelectrolyte. *Macromolecules*, 26(25):6945–6951, dec 1993.

[148] Joanne M. Hoefting, Mary K. Cowman, Shiro Matsuoka, and Endre Balazs. Temperature Effect on the Dynamic Rheological Characteristics of Hyaluronan, Hylan a and Synvisc®. *Hyaluronan*, pages 103–108, jan 2002.

[149] Artur Krżel and Wojciech Bal. A formula for correlating pKa values determined in D2O and H2O. *Journal of Inorganic Biochemistry*, 98(1):161–166, jan 2004.

[150] David A. Mortimer. Synthetic polyelectrolytes—A review. *Polymer International*, 25(1):29–41, 1991.

[151] Venkata S. Meka, Manprit K.G. Sing, Mallikarjuna R. Pichika, Srinivasa R. Nali, Venkata R.M. Kolapalli, and Prashant Kesharwani. A comprehensive review on polyelectrolyte complexes, nov 2017.

[152] Ioulia Rouzina and Victor A. Bloomfield. DNA Bending by Small, Mobile Multivalent Cations. *Biophysical Journal*, 74(6):3152–3164, jun 1998.

[153] Alexandros Chremos and Jack F. Douglas. Influence of higher valent ions on flexible polyelectrolyte stiffness and counter-ion distribution. *The Journal of Chemical Physics*, 144(16):164904, apr 2016.

[154] Sarah N. Innes-Gold, Philip A. Pincus, Mark J. Stevens, and Omar A. Saleh. Polyelectrolyte Conformation Controlled by a Trivalent-Rich Ion Jacket. *Physical Review Letters*, 123(18), oct 2019.

[155] Arindam Kundagrami and M. Muthukumar. Theory of competitive counterion adsorption on flexible polyelectrolytes: Divalent salts. *Journal of Chemical Physics*, 128(24), 2008.

[156] R J Pelham and Y l Wang. Cell locomotion and focal adhesions are regulated by substrate flexibility. *Proceedings of the National Academy of Sciences of the United States of America*, 94(25):13661–5, dec 1997.

[157] Chun Min Lo, Hong Bei Wang, Micah Dembo, and Yu Li Wang. Cell movement is guided by the rigidity of the substrate. *Biophysical Journal*, 79(1):144–152, jul 2000.

[158] J.J. Kwiecinski, S.G. Dorosz, T.E. Ludwig, S. Abubacker, M.K. Cowman, and T.A. Schmidt. The effect of molecular weight on hyaluronan's cartilage boundary lubricating ability – alone and in combination with proteoglycan 4. *Osteoarthritis and Cartilage*, 19(11):1356–1362, nov 2011.

[159] Michele M Temple-Wong, Shuwen Ren, Phu Quach, Bradley C Hansen, Albert C Chen, Akihiko Hasegawa, Darryl D D'Lima, Jim Koziol, Koichi Masuda, Martin K Lotz, and Robert L Sah. Hyaluronan concentration and size distribution in human knee synovial fluid: variations with age and cartilage degeneration. *Arthritis research & therapy*, 18:18, jan 2016.

[160] Jordan J. Green and Jennifer H. Elisseeff. Mimicking biological functionality with polymers for biomedical applications, 2016.

[161] Vivian R. Feig, Helen Tran, Minah Lee, and Zhenan Bao. Mechanically tunable conductive interpenetrating network hydrogels that mimic the

elastic moduli of biological tissue. *Nature Communications*, 9(1):2740, dec 2018.

[162] D A Gabriel and M E Carr. Calcium destabilizes and causes conformational changes in hyaluronic acid. *The American journal of the medical sciences*, 298(1):8–14, jul 1989.

[163] Phillip Gribbon, Boon Chin Heng, and Timothy E. Hardigham. The analysis of intermolecular interactions in concentrated hyaluronan solutions suggest no evidence for chain–chain association. *Biochemical Journal*, 350(1):329, 2000.

[164] Xinyue Chen and Ralf P. Richter. Effect of calcium ions and pH on the morphology and mechanical properties of hyaluronan brushes. *Interface Focus*, 9(2):20180061, apr 2019.

[165] M A Napier and N M Hadler. Effect of calcium on structure and function of a hyaluronic acid matrix: carbon-13 nuclear magnetic resonance analysis and the diffusional behavior of small solutes. *Proceedings of the National Academy of Sciences of the United States of America*, 75(5):2261–5, may 1978.

[166] Eva Pluhařová, Marcel D. Baer, Christopher J. Mundy, Burkhard Schmidt, and Pavel Jungwirth. Aqueous Cation-Amide Binding: Free Energies and IR Spectral Signatures by Ab Initio Molecular Dynamics. *The Journal of Physical Chemistry Letters*, 5(13):2235–2240, jul 2014.

[167] Halil I. Okur, Jaibir Kherb, and Paul S. Cremer. Cations Bind Only Weakly to Amides in Aqueous Solutions. *Journal of the American Chemical Society*, 135(13):5062–5067, apr 2013.

[168] Jipei Shi and Jianping Wang. Interaction between metal cation and unnatural peptide backbone mediated by polarized water molecules: Study of infrared spectroscopy and computations. *Journal of Physical Chemistry B*, 118(43):12336–12347, oct 2014.

[169] Fouzia Bano, Suneale Banerji, Mark Howarth, David G. Jackson, and Ralf P. Richter. A single molecule assay to probe monovalent and mul-

tivalent bonds between hyaluronan and its key leukocyte receptor CD44 under force. *Scientific Reports*, 6, sep 2016.

[170] Stephan Deublein, Steffen Reiser, Jadran Vrabec, and Hans Hasse. A Set of Molecular Models for Alkaline-Earth Cations in Aqueous Solution. *The Journal of Physical Chemistry B*, 116(18):5448–5457, may 2012.

[171] Elad Project, Esther Nachliel, and Menachem Gutman. Parameterization of Ca+2–protein interactions for molecular dynamics simulations. *Journal of Computational Chemistry*, 29(7):1163–1169, may 2008.

[172] E.A. Carter, Giovanni Ciccotti, James T. Hynes, and Raymond Kapral. Constrained reaction coordinate dynamics for the simulation of rare events. *Chemical Physics Letters*, 156(5):472–477, apr 1989.

[173] Theo Odijk. Theory of Lyotropic Polymer Liquid Crystals. 1986.

[174] Marjolein Dijkstra, Daan Frenkel, and Henk N.W. Lekkerkerker. Confinement free energy of semiflexible polymers. *Physica A: Statistical Mechanics and its Applications*, 193(3-4):374–393, apr 1993.

[175] Adam J. Engler, Shamik Sen, H. Lee Sweeney, and Dennis E. Discher. Matrix Elasticity Directs Stem Cell Lineage Specification. *Cell*, (4):677–689, aug.

[176] Kyle H. Vining and David J. Mooney. Mechanical forces direct stem cell behaviour in development and regeneration, nov 2017.

[177] Hong-pyo Lee, Luo Gu, David J. Mooney, Marc E. Levenston, and Ovijit Chaudhuri. Mechanical confinement regulates cartilage matrix formation by chondrocytes. *Nature Materials*, 16(12):1243–1251, oct 2017.

[178] A B Kayitmazer, A F Koksal, and E Kilic Iyilik. Complex coacervation of hyaluronic acid and chitosan: effects of pH, ionic strength, charge density, chain length and the charge ratio. *Soft Matter*, 11(44):8605–8612, nov 2015.

[179] Gautier Lalevée, Laurent David, Alexandra Montembault, Kevin Blanchard, John Meadows, Sébastien Malaise, Agnès Crépet, Isabelle Grillo, Isabelle Morfin, Thierry Delair, and Guillaume Sudre. Highly stretchable hydrogels from complex coacervation of natural polyelectrolytes. *Soft Matter*, 13(37):6594–6605, sep 2017.

[180] Matthew J. Webber, Eric A. Appel, E. W. Meijer, and Robert Langer. Supramolecular biomaterials. *Nature Materials*, 15(1):13–26, dec 2015.

[181] Adrianne M. Rosales, Sebastián L. Vega, Frank W. DelRio, Jason A. Burdick, and Kristi S. Anseth. Hydrogels with Reversible Mechanics to Probe Dynamic Cell Microenvironments. *Angewandte Chemie - International Edition*, 56(40):12132–12136, sep 2017.

[182] B Chakrabarti and E A Balazs. Optical properties of hyaluronic acid. Ultraviolet circular dichroism and optical rotatory dispersion. *Journal of molecular biology*, 78(1):135–41, jun 1973.

[183] Paul W. Staskus and W. Curtis Johnson. Conformational transition of hyaluronic acid in aqueous-organic solvent monitored by vacuum ultraviolet circular dichroism. *Biochemistry*, 27(5):1522–1527, mar 1988.

[184] I C Dea, R Moorhouse, D A Rees, S Arnott, J M Guss, and E A Balazs. Hyaluronic acid: a novel, double helical molecule. *Science (New York, N.Y.)*, 179(4073):560–2, feb 1973.

[185] J. K. Sheehan, K. H. Gardner, and E. D T Atkins. Hyaluronic acid: a double-helical structure in the presence of potassium at low pH and found also with the cations ammonium, rubidium and caesium. *Journal of Molecular Biology*, 117(1):113–135, nov 1977.

[186] John E. Scott and Frank Heatley. Biological properties of hyaluronan in aqueous solution are controlled and sequestered by reversible tertiary structures, defined by NMR spectroscopy. *Biomacromolecules*, 3(3):547–553, 2002.

[187] Bradley W. Mansel, Che Yi Chu, Andrew Leis, Yacine Hemar, Hsin Lung Chen, Leif Lundin, and Martin A.K. Williams. Zoom-

ing in: Structural Investigations of Rheologically Characterized Hydrogen-Bonded Low-Methoxyl Pectin Networks. *Biomacromolecules*, 16(10):3209–3216, 2015.

[188] Luigi De Marco, William Carpenter, Hanchao Liu, Rajib Biswas, Joel M. Bowman, and Andrei Tokmakoff. Differences in the Vibrational Dynamics of H2O and D2O: Observation of Symmetric and Antisymmetric Stretching Vibrations in Heavy Water. *Journal of Physical Chemistry Letters*, 7(10):1769–1774, 2016.

[189] Pavol Bodis, Matthijs R. Panman, Bert H. Bakker, Aurelio Mateo-Alonso, Maurizio Prato, Wybren Jan Buma, Albert M. Brouwer, Euan R. Kay, David A. Leigh, and Sander Woutersen. Two-dimensional vibrational spectroscopy of rotaxane-based molecular machines. *Accounts of Chemical Research*, 42(9):1462–1469, sep 2009.

[190] Peter Hamm, Manho Lim, and Robin M. Hochstrasser. Structure of the Amide I Band of Peptides Measured by Femtosecond Nonlinear-Infrared Spectroscopy. *The Journal of Physical Chemistry B*, 102(31):6123–6138, 1998.

[191] M. F. DeCamp, L. DeFlores, J. M. McCracken, A. Tokmakoff, K. Kwac, and M. Cho. Amide I vibrational dynamics of N-methylacetamide in polar solvents: The role of electrostatic interactions. *Journal of Physical Chemistry B*, 109(21):11016–11026, 2005.

[192] Ana V. Cunha, Evgeniia Salamatova, Robbert Bloem, Steven J. Roeters, Sander Woutersen, Maxim S. Pshenichnikov, and Thomas L.C. Jansen. Interplay between Hydrogen Bonding and Vibrational Coupling in Liquid N-Methylacetamide. *Journal of Physical Chemistry Letters*, 8(11):2438–2444, jun 2017.

[193] Mary K Cowman, Chiara Spagnoli, Dina Kudasheva, Min Li, Ansil Dyal, Sonoko Kanai, and Endre A Balazs. Extended, relaxed, and condensed conformations of hyaluronan observed by atomic force microscopy. *Biophysical Journal*, 88(1):590–602, jan 2005.

[194] Allan S. Hoffman. Hydrogels for biomedical applications, dec 2012.

[195] Ulf W. Gedde. *Polymer Physics*. Springer Netherlands, 1999.

[196] T P Lodge, N A Rotstein, and S Prager. Dynamics of Entangled Polymer Liquids: Do Linear Chains Reptate?, jan 1990.

[197] Ludwik Leibler, Michael Rubinstein, and Ralph H Colby. Dynamics of reversible networks. *Macromolecules*, 24(16):4701–4707, aug 1991.

[198] Michael Rubinstein and Alexander N. Semenov. Dynamics of entangled solutions of associating polymers. *Macromolecules*, 34(4):1058–1068, 2001.

[199] Michael Rubinstein and Alexander N Semenov. Thermoreversible Gelation in Solutions of Associating Polymers. 2. Linear Dynamics. *Macromolecules*, 31(4):1386–1397, feb 1998.

[200] Motomu Tanaka, Florian Rehfeldt, Matthias F Schneider, Gerald Mathe, Antero Albersdörfer, Klaus R Neumaier, Oliver Purrucker, and Erich Sackmann. Wetting and dewetting of extracellular matrix and glycocalix models. *Journal of Physics: Condensed Matter*, 17(9):S649–S663, mar 2005.

[201] John D Ferry. Viscoelastic properties of polymers, 1980.

[202] Aurélia Charlot and Rachel Auzély-Velty. Novel Hyaluronic Acid Based Supramolecular Assemblies Stabilized by Multivalent Specific Interactions: Rheological Behavior in Aqueous Solution. *Macromolecules*, 40(26):9555–9563, dec 2007.

[203] D Wayne Bolen and George D Rose. Structure and energetics of the hydrogen-bonded backbone in protein folding. *Annual review of biochemistry*, 77:339–362, 2008.

[204] Michael Rubinstein and Ralph H Colby. *Polymer physics*, volume 23. Oxford university press New York, 2003.

[205] Sheh-Yi Sheu, Dah-Yen Yang, H. L. Selzle, and E. W. Schlag. Energetics of hydrogen bonds in peptides. *Proceedings of the National Academy of Sciences*, 100(22):12683–12687, oct 2003.

[206] S. Woutersen, Y. Mu, G. Stock, and P. Hamm. Hydrogen-bond lifetime measured by time-resolved 2D-IR spectroscopy: N-methylacetamide in methanol. *Chemical Physics*, 266(2-3):137–147, may 2001.

[207] Mostafa Ahmadi, Laurence G.D. Hawke, Hadi Goldansaz, and Evelyne Van Ruymbeke. Dynamics of Entangled Linear Supramolecular Chains with Sticky Side Groups: Influence of Hindered Fluctuations. *Macromolecules*, 48(19):7300–7310, 2015.

[208] T. Aida, E. W. Meijer, and S. I. Stupp. Functional supramolecular polymers, feb 2012.

[209] M. Tarek and D. J. Tobias. Role of Protein-Water Hydrogen Bond Dynamics in the Protein Dynamical Transition. *Physical Review Letters*, 88(13):4, 2002.

[210] John G Duman. Antifreeze and Ice Nucleator Proteins in Terrestrial Arthropods. *Annual Review of Physiology*, 63(1):327–357, mar 2001.

[211] F Franks and E R Morris. Blood glycoprotein from antarctic fish. Possible conformational origin of antifreeze activity. *Biochimica et biophysica acta*, 540(2):346–56, may 1978.

[212] C A Bush and R E Feeney. Conformation of the glycotripeptide repeating unit of antifreeze glycoprotein of polar fish as determined from the fully assigned proton n.m.r. spectrum. *International journal of peptide and protein research*, 28(4):386–97, oct 1986.

[213] C. ALLEN BUSH, ROBERT E. FEENEY, DAVID T. OSUGA, SURESH RALAPATI, and YIN YEH. ANTIFREEZE GLYCOPROTEIN. Conformational Model Based on Vacuum Ultraviolet Circular Dichroism Data. *International Journal of Peptide and Protein Research*, 17(1):125–129, jan 1981.

[214] Yin Yeh and Robert E. Feeney. Antifreeze Proteins: Structures and Mechanisms of Function. *Chemical Reviews*, 96(2):601–618, 1996.

[215] Yuki Tachibana, Garth L. Fletcher, Naoki Fujitani, Sakae Tsuda, Kenji Monde, and Shin Ichiro Nishimura. Antifreeze glycoproteins: Elucidation of the structural motifs that are essential for antifreeze activity. *Angewandte Chemie - International Edition*, 43(7):856–862, feb 2004.

[216] Andreas Barth and Christian Zscherp. What vibrations tell us about proteins. *Quarterly Reviews of Biophysics*, 35(4):369–430, nov 2002.

[217] Tianqi O. Zhang, Ariel M. Alperstein, and Martin T. Zanni. Amyloid β-Sheet Secondary Structure Identified in UV-Induced Cataracts of Porcine Lenses using 2D IR Spectroscopy. *Journal of Molecular Biology*, 429(11):1705–1721, 2017.

[218] Biplab Dutta, Bart E. Vos, Yves L.A. Rezus, Gijsje H. Koenderink, and Huib J. Bakker. Observation of Ultrafast Vibrational Energy Transfer in Fibrinogen and Fibrin Fibers. *Journal of Physical Chemistry B*, 122(22):5870–5876, jun 2018.

[219] Megan K. Petti, Justin P. Lomont, Micha Maj, and Martin T. Zanni. Two-Dimensional Spectroscopy Is Being Used to Address Core Scientific Questions in Biology and Materials Science. *Journal of Physical Chemistry B*, 122(6):1771–1780, feb 2018.

[220] Lauren P. Deflores, Ziad Ganim, Rebecca A. Nicodemus, and Andrei Tokmakoff. Amide I-II 2D IR spectroscopy provides enhanced protein secondary structural sensitivity. *Journal of the American Chemical Society*, 131(9):3385–3391, 2009.

[221] Konrad Meister, John G. Duman, Yao Xu, Arthur L. DeVries, David M. Leitner, and Martina Havenith. The role of sulfates on antifreeze protein activity. *Journal of Physical Chemistry B*, 118(28):7920–7924, jul 2014.

[222] Simon Ebbinghaus, Konrad Meister, Benjamin Born, Arthur L. DeVries, Martin Gruebele, and Martina Havenith. Antifreeze Glycoprotein

Activity Correlates with Long-Range Protein-Water Dynamics. *Journal of the American Chemical Society*, 132(35):12210–12211, sep 2010.

[223] A I Ahmed, Y Yeh, Y Y Osuga, and R E Feeney. Antifreeze glycoproteins from Antarctic fish. Inactivation by borate. *The Journal of biological chemistry*, 251(10):3033–6, may 1976.

[224] Pavol Bodis, Olaf F.A. Larsen, and Sander Woutersen. Vibrational relaxation of the bending mode of HDO in liquid D2O. *Journal of Physical Chemistry A*, 109(24):5303–5306, 2005.

[225] Emily B. Dunkelberger, Maksim Grechko, and Martin T. Zanni. Transition Dipoles from 1D and 2D Infrared Spectroscopy Help Reveal the Secondary Structures of Proteins: Application to Amyloids. *Journal of Physical Chemistry B*, 119(44):14065–14075, 2015.

[226] Maksim Grechko and Martin T. Zanni. Quantification of transition dipole strengths using 1D and 2D spectroscopy for the identification of molecular structures via exciton delocalization: Application to α-helices. *Journal of Chemical Physics*, 137(18), 2012.

[227] Andreas Barth. The infrared absorption of amino acid side chains. *Progress in Biophysics and Molecular Biology*, 74(3-5):141–173, jan 2000.

[228] Nelly M. Tsvetkova, Brian L. Phillips, Viswanathan V. Krishnan, Robert E. Feeney, William H. Fink, John H. Crowe, Subhash H. Risbud, Fern Tablin, and Yin Yen. Dynamics of antifreeze glycoproteins in the presence of ice. *Biophysical Journal*, 82(1):464–473, 2002.

[229] J. A. Drewes and K. L. Rowlen. Evidence for a gamma-turn motif in antifreeze glycopeptides. *Biophysical Journal*, 65(3):985–991, 1993.

[230] Andrew N Lane, Lisa M Hays, Nelly Tsvetkova, Robert E Feeney, Lois M Crowe, and John H Crowe. Comparison of the Solution Conformation and Dynamics of Antifreeze Glycoproteins from Antarctic Fish. *Biophysical Journal*, 78:3195–3207.

[231] Yu. N. Chirgadze, O. V. Fedorov, and N. P. Trushina. Estimation of amino acid residue side-chain absorption in the infrared spectra of protein solutions in heavy water. *Biopolymers*, 14(4):679–694, apr 1975.

[232] Vettai S. Ananthanarayanan, Don Slaughter, and Choy L. Hew. Antifreeze proteins from the ocean pout, Macrozoarces americanus: circular dichroism spectral studies on the native and denatured states. *Biochimica et Biophysica Acta (BBA) - Protein Structure and Molecular Enzymology*, 870(1):154–159, mar 1986.

[233] Yuan Lin, John G. Duman, and Arthur L. DeVries. Studies on the structure and activity of low molecular weight glycoproteins from an antarctic fish. *Biochemical and Biophysical Research Communications*, 46(1):87–92, jan 1972.

[234] Krista E. Amunson and Jan Kubelka. On the temperature dependence of amide I frequencies of peptides in solution. *Journal of Physical Chemistry B*, 111(33):9993–9998, 2007.

[235] J Jacob, H Duclohier, and D S Cafiso. The role of proline and glycine in determining the backbone flexibility of a channel-forming peptide. *Biophysical journal*, 76(3):1367–76, mar 1999.

[236] Timothy S. Burcham, Michael J. Knauf, David T. Osuga, Robert E. Feeney, and Yin Yeh. Antifreeze glycoproteins: Influence of polymer length and ice crystal habit on activity. *Biopolymers*, 23(7):1379–1395, jul 1984.

[237] Arthur L. DeVries. The role of antifreeze glycopeptides and peptides in the freezing avoidance of antarctic fishes. *Comparative Biochemistry and Physiology – Part B: Biochemistry and*, 90(3):611–621, jan 1988.

[238] Konrad Meister, Arthur L. Devries, Huib J. Bakker, and Ran Drori. Antifreeze Glycoproteins Bind Irreversibly to Ice. *Journal of the American Chemical Society*, 140(30):9365–9368, aug 2018.

[239] Carien C.M. Groot, Konrad Meister, Arthur L. Devries, and Huib J.

Bakker. Dynamics of the Hydration Water of Antifreeze Glycoproteins. *Journal of Physical Chemistry Letters*, 7(23):4836–4840, dec 2016.

[240] C A Knight, E Driggers, and A L DeVries. Adsorption to ice of fish antifreeze glycopeptides 7 and 8. *Biophysical journal*, 64(1):252–9, jan 1993.

[241] W. Thomas Shier, Yuan Lin, and Arthur L. De Vries. Structure and mode of action of glycoproteins from an antarctic fish. *BBA - Protein Structure*, 263(2):406–413, apr 1972.

[242] Poonam Pandey and Sairam S. Mallajosyula. Elucidating the role of key structural motifs in antifreeze glycoproteins. *Physical Chemistry Chemical Physics*, 21(7):3903–3917, 2019.

[243] Yih-Cherng Liou, Ante Tocilj, Peter L. Davies, and Zongchao Jia. Mimicry of ice structure by surface hydroxyls and water of a β-helix antifreeze protein. *Nature*, 406(6793):322–324, jul 2000.

[244] F. Sicheri and D. S. C. Yang. Ice-binding structure and mechanism of an antifreeze protein from winter flounder. *Nature*, 375(6530):427–431, jun 1995.

[245] Carsten Budke, Axel Dreyer, Jasmin Jaeger, Kerstin Gimpel, Thomas Berkemeier, Anna S. Bonin, Lilly Nagel, Carolin Plattner, Arthur L. DeVries, Norbert Sewald, and Thomas Koop. Quantitative Efficacy Classification of Ice Recrystallization Inhibition Agents. *Crystal Growth & Design*, 14(9):4285–4294, sep 2014.

Summary

What does an anti-freeze protein found in an Antarctic fish have in common with hyaluronan, a long polymer found in the human body?

Both molecules have a flexible structure in aqueous solutions. Proteins can adapt their structure to fulfill their biological functions, such as inhibiting ice growth in organisms exposed to subzero conditions. Hyaluronan is a polysaccharide that can switch on and off intra- and inter-molecular interactions, reshaping its conformation and forming a structured network. To resolve the structural dynamics of both hyaluronan and anti-freeze proteins, we have used in this thesis a state-of-the-art spectroscopic technique, known as two dimensional-infrared spectroscopy (2DIR). In 2DIR we study the molecular vibrations of amide and carboxyl groups of biomolecules, which are important structural markers since their vibrational frequencies are strongly affected by conformational and solvation fluctuations. We excite these vibrations with an intense infrared beam, *pump*, which tags them. We then follow their dynamics on a femtosecond time-scale with a second weaker infrared beam, *probe*. If molecular interactions are present, such as inter-molecular hydrogen-bonds between amide and carboxyl groups, the excitation of the amide modes will affect the vibrations of the carboxyl group. In a 2DIR spectrum, this will lead to the appearance of off-diagonal signatures, which we refer to as *cross-peak*. Cross-peaks also carry information on the relative orientation of the molecular groups, providing important information about the molecular structure. Two-dimensional infrared spectroscopy thus is a unique technique to resolve interactions, and structure at the molecular level.

Resolving the molecular structure of -COOH groups in acids and peptides Many biological functions as well as chemical reactions are based on molecular interactions that involve carboxyl groups. At neutral and alkaline pH, carboxyl groups are deprotonated, and are strong hydrogen-bond acceptors (-COO^-). At acidic conditions, carboxyl groups are protonated (-COOH), and good hydrogen-bond acceptors and donors because of the carboxyl carbonyl (C=O), and carboxyl hydroxyl (O-H) groups. This dual character of carboxyl groups is critical in stabilizing the hydrogen-bonded network of chains of hyaluronans and of pectins, plant polysaccha-

rides widely used in the food industry. The formation of hydrogen-bonded polysaccharide networks can lead to a liquid-to-gel transition, which we usually refer to as acid-gelation.

The chemical properties, which influence the hydrogen-bond strength for instance, depend on the molecular structure of the carboxyl group. In previous works, it has been proposed that in the gas state small acid molecules, such as formic and acetic acid, can adopt two different planar geometries. In the syn-conformer the O-H group is oriented at $\sim 60^{\circ}$ with respect to the C=O group and in the anti-conformer the O-H is anti-parallel to the C=O. Molecular dynamics study also proposed that chemical properties are different among the two conformers. However, since nobody had been able to detect the presence of syn- and anti-conformers in solutions at room temperature, conformational isomerism of carboxyl groups and the possible consequences have never been considered.

In Chapter 4, we show for the first time that the conformational isomerism of carboxyl group exists also in solutions of formic acid at room temperature. We demonstrated that syn and anti conformers are present in apolar (acetonitrile), and polar (heavy water and dimethyl sulfoxide) solutions, and that the anti-conformer is significantly present (25%). In Chapter 5, we demonstrate that conformational isomerism of carboxyl groups is present also in larger molecules, like in peptides. In studying N-acetylaspartic acid in polar solutions, we find that the anti-conformer is again significantly present (25%), indicating that the part of the peptide molecule outside the carboxyl group has a small influence on the conformation isomerism. We additionally implement molecular dynamics simulations to investigate the hydration of these two conformers. We observe that the anti-conformer interacts with water molecules more strongly than the syn-conformer. Both molecular dynamics and experimental results indicate that the anti-conformer indeed is more acidic (lower pK_a) compared to the syn-conformer. In Chapter 6, we study the formation of an intra-molecular hydrogen bond between amide and anti-COOH groups in N-acetylproline. We dissolve N-acetylproline in an apolar solvent such as acetonitrile to mimic hydrophobic micro-environments found inside polypeptide chains. Under such conditions, the anti-conformer

forms a strong intra-molecular hydrogen bond with the nearby amide carbonyl group. The formation of this bond strongly stabilizes the anti structure, leading to a much higher abundance of anti (∼65%) compared to syn (∼35%). In polar solvent, we do not observe the formation of this intra-molecular hydrogen-bond,and the anti-population decreases again to 25%.

Investigation of the molecular structure of hyaluronan at neutral pH Hyaluronan is a natural polysaccharide widely present in Nature and especially important in the human body, where it plays an important role in many biological functions. Hyaluronan has a simple structure that has been mainly studied in water solutions by using molecular dynamics simulations. The repeating block is composed of N-acetyl-glucosamine and glucuronic acid, which contain an amide and a carboxyl group, respectively. Hydrogen bonds of different strengths are formed between N-acetyl-glucosamine and glucuronic acid. The formation of these bonds is largely responsible for the rather large chain stiffness of hyaluronan.

In Chapter 7, we investigate the formation of intra-molecular hydrogen-bonds between the amide and carboxylate groups, which have previously been proposed to stabilize the helical structures of hyaluronan. In our study, we find that less than 10% of these functional groups form an intrachain hydrogen- bond. In this hydrogen bond, the hydrogen atom of the hydrogen-bond donating amide N-H group is positioned close to the line that connects the two oxygen atoms of the carboxylate anion group. We also find that the abundance of this hydrogen-bond is not strongly affected by increasing the temperature and the pH, factors that are well known to lower the chain' rigidity. This finding suggests that hydrogen-bonds between amide and carboxylate groups do not significantly contribute to the stiffening of the hyaluronan chains.

Divalent ion condensation mechanism in hyaluronan Divalent cations have a critical biological role, influencing the structural properties of polyelectrolytes. Ions can indeed loosely bind to charged groups along the polymer chain, inducing local bending, and thus increasing the

flexibility of the chain. Such increased flexibility (or decreased rigidity) has a large impact on the biological functions fulfilled by the polyelectroytes. Though the mechanism of ion condensation is well known, the interactions and the geometry of the complex formed between the charged groups and the divalent ion are largely unclear at the molecular level.

In Chapter 8, we study the ion condensation mechanism of a divalent cation (calcium) with hyaluronan. By combining experiments and molecular simulations, we find that calcium cations sit on the chain of hyaluronan in a selective way because of their space-charge requirements, bridging the carboxylate and amide groups on adjacent saccharides. Interestingly, the amount of amide groups bonded to the cation saturates at low calcium concentration ($\sim$ 100 mM), reaching a maximum fraction of 10%. This saturation suggests that the formation of this complex hinders the formation of additional complexes at neighboring binding sites. Nevertheless, the formation of only a few of these complexes already has a large impact on the intra-molecular hydrogen bonds that stiffen the chain. By performing molecular dynamics simulations, we find that upon calcium condensation the intra-molecular hydrogen bonds drastically weaken. This weakening causes a local bending that in turn leads to a twofold reduction of the chain rigidity, as we measured by using atomic force microscopy, even when only a few percent of the potential binding sites on the hyaluronan chain has bound calcium.

A molecular picture of the macroscopic properties of hyaluronan hydrogels Besides the enormous bio-relevance of hyaluronan, this polymer possesses intriguing material properties. Particularly, the mechanical properties of hyaluronan solution can be tuned by external stimuli such as the pH. By lowering the pH from neutral to 2.5, hyaluronan solutions undergo a liquid-to-gel transition, increasing their elasticity dramatically. Interestingly, a further decrease of the pH suppresses this elastic state again, and a liquid solution is recovered. Such dramatic responsiveness of hyaluronan to external stimuli is an interesting study-case to understand the interaction between cells and the extra-cellular matrix, and to design

novel hydrogels with tunable mechanical properties.

In Chapter 9 we study the molecular interactions leading to the liquid-to-gel transition in hyaluronan solutions at pH=2.5. We find that at this pH the electrostatic repulsive forces between the negatively charged carboxyl groups are reduced, and chains laterally associate by forming inter-molecular connections or stickers. Such connections are due to inter-molecular hydrogen bonds formed between amide and protonated carboxyl groups, COOH, and between amide and deprotonated carboxyl groups, COO^-. We calculate that between 10-20% of carboxyl groups are actively forming such inter-molecular hdyrogen-bonds. By further lowering the pH, and thus by decreasing the amount of COO^-, less strong connections are formed, and the hydrogen-bonded network dramatically weakens, causing a gel-to-liquid transition.

The visco-elastic properties of the hyaluronan elastic state, and of hydrogels of responsive biopolymers in general, depend on the interaction properties between the constituent polymers, such as their density and lifetime. In Chapter 10, we study the effect of temperature on the molecular interactions that lead to the formation of the hydrogen-bonded network at pH=2.5. We find that the fraction of carbonyl groups, which are forming inter-molecular hydrogen bonds and thus associative connections, is not affected by temperature changes. However, we observe that the temporal response of the visco-elastic properties drastically change when the temperature is increased, leading to faster stress relaxation. From the observed temperature dependence , we determine the flow activation energy to be $\sim 50\ k_BT$. This value is 5-15 times larger than the activation energy of breaking a single hydrogen bond, indicating that for the chains to diffuse, and thus for the network to flow, multiple hydrogen bonds must be simultaneously broken. We conclude that an increase in temperature accelerates the dynamics of the polymer network without significantly modifying its structure.

Determination of the secondary structures of anti-freeze glycol protein Anti-freeze glycol proteins (AFGP) are unique proteins able to inhibit ice growth in many organisms. The ice-inhibition mechanism has been largely studied because of possible biomedical and food applications. Despite numerous studies, a series of central questions were still

unanswered: which is the structure of AFGP? Does the protein structure change upon lowering the temperature to the working temperature of the protein? Is a specific structure essential for the ice inhibition properties of AFGP?

In Chapter 11, we study the molecular structure of AFGP by using 2DIR spectroscopy. By exploiting the vibrational coupling between the amide I and amide II modes, we are able to resolve the frequencies of the amide I modes of the different conformations of the protein. Thanks to previous literature, we are able to assign the distinct vibrational frequencies to specific secondary structures. We find that anti-freeze glycol proteins have highly disordered and flexible secondary structures. At room temperature, the anti-freeze proteins adopt PPII, α-helical, random coil and extended structures. By lowering the temperature to the freezing point of water, the PPII content significantly increases at the expense of the extended structure. As suggested by previous literature, a larger presence of PPII structure is essential to segregate the hydrophobic and hydrophylic parts of the proteins, and thus the active binding site to nascent ice crystallites. The introduction of chemical modifications of AFGP lowers the relative abundance of the PPII structure, and reduces the anti-freeze activity. Interestingly, the addition of anti-freeze activity inhibitors or enhancers does not affect the relative abundances of the different secondary structures, indicating that these inhibitors and enhancers have a different working mechanism.

This thesis provides information on the flexible structure of molecules of various sizes and complexities, ranging from carboxyl groups in simple acids to long polymers. Thanks to a combined multi-technique approach, where two-dimensional infrared spectroscopy played a central role, we were able to observe conformational changes in carboxylic acid, in hyaluronan polymers and anti-freeze glycol proteins (AFGP), unhitching the molecular interactions leading to stabilization or destabilization of the molecular structures. In the case of -COOH groups, we showed that two different geometries are possible thanks to stabilizing interactions with surrounding water molecules. In the case of anti-freeze proteins and hyaluronan hydrogel, we studied the

molecular structure in aqueous solutions, enabling us to link macroscopic properties and biological functionalities to particular structural contents.

The obtained detailed molecular pictures of anti-freeze proteins and hyaluronan might have future scientific and technological applications. Understanding the structure of AFGP is critical to proceed with the synthesis of artificial anti-freeze proteins, which can be used to preserve organs for transplant. Tailoring the molecular interactions that lead to changes in the macroscopic properties of hyaluronan is fundamental to comprehend the dynamic, reciprocal interactions between cells and the extracellular matrix, and to design hydrogels with tunable mechanical properties for tailored biomedical applications, such as drug delivery.

All the studies here presented, as always and as it should be, open new scientific questions. Particularly, the discovery of conformational isomerism of -COOH groups of formic acid or peptides, dissolved in aqueous solutions at room temperature, questions our fundamental knowledge even of small molecular systems. Which is the biochemical impact of the presence of syn and anti conformers? This is an issue that we were not able to address, but that we hope will be investigated in future studies.

Samenvatting

Wat hebben een antivries-eiwit van een Antarctische vis en hyaluronan, een lang polymeer dat je kan vinden in het menselijk lichaam, met elkaar gemeen?

Beide moleculen hebben in waterige oplossingen een flexibele structuur. Eiwitten passen hun structuur aan om biologische functies, zoals het verhinderen van de groei van ijs in organismes die blootgesteld worden aan condities van onder nul graden Celsius, uit te kunnen voeren. Hyaluronan is een polysacharide die zich aan en uit kan zetten met het veranderen van vorm middels intra- en intermoleculaire interacties wat leidt tot het vormen van een wel of niet gestructureerd netwerk. Om de structuurdynamiek op te lossen van zowel de hyaluronan en het antivries-eiwit hebben we in deze dissertatie gebruikgemaakt van een state-of-the-art spectroscopietechniek die bekendstaat als tweedimensionale infraroodspectroscopie (2DIR). In 2DIR bestuderen we de moleculaire vibraties van amide- en carboxygroepen van biomoleculen. Dit zijn belangrijke markers voor de structuur, omdat hun trillingsfrequenties sterk worden getroffen door een fluctuatie in conformatie of in solvatie. We wekken deze vibraties op met een infrarood laserstraal van hoge intensiteit, de pump, waardoor ze 'getagd' worden. Vervolgens volgen we door middel van een tweede infrarood laserstraal van minder hoge intensiteit, de probe, hun dynamiek met een tijdschaal van femtoseconden. Als tijdens de excitatietijd moleculaire interacties aanwezig zijn, zoals intermoleculaire waterstofbruggen tussen de amide- en de carboxygroep, zal de excitatie van de amide-vibratiemodus de vibratie van de carboxygroep beïnvloeden. In een 2DIR-spectrum zal je dit zien als de verschijning van niet-diagonale signalen, die we als cross-peaks aanduiden. Daarbij bevatten cross-peaks ook informatie over de relatieve oriëntatie van de moleculaire groepen. Dit verschaft ons belangrijke informatie over de moleculaire structuur in waterige oplossingen. Tweedimensionale infraroodspectroscopie is dus een unieke techniek om interacties en structuren op moleculair niveau te begrijpen.

Het oplossen van de moleculaire structuur van -COOH groepen in zuren en peptiden. Veel biologische functies, alsook

chemische reacties, zijn gebaseerd op moleculaire interacties waarin carboxygroepen zijn betrokken. Bij neutrale en basische pH zijn carboxygroepen gedeprotoneerd en functioneren ze als sterke waterstofbrugacceptoren (-COO^-). In zure pH-condities zijn carboxygroepen geprotoneerd (-COOH) en functioneren vanwege de carboxyl-carbonyl (C=O) en de carboxyl-hydroxyl (OH) groepen als goede waterstofbrugacceptoren én -donoren. Dit tweeledige karakter van de carboxygroep is cruciaal in het stabiliseren van een waterstofbrugnetwerk van ketens hyaluronan of pectine, een in de voedselindustrie veel gebruikte plant-polysacharide. De formatie van zulke waterstofbrugnetwerken leidt tot een vloeistof-tot-gel overgang, die we normaliter als zuur-gelering aanduiden. De chemische eigenschappen, die bijvoorbeeld de sterkte van de waterstofbrug beïnvloeden, worden bepaald door de moleculaire structuur van de carboxygroep. In eerdere literatuur is er voorgesteld dat kleine zuurmoleculen, zoals mierenzuur en azijnzuur, in de gasfase twee verschillende vlakke geometrieën kunnen aannemen. In de syn-conformeer is de O-H-groep $\sim 60^\circ$georiënteerd ten opzichte van de C=O-groep en in de anti-conformeer is O-H antiparallel ten opzichte van de C=O. Daarbij werd in moleculaire dynamicastudies voorgesteld dat de chemische eigenschappen per conformeer verschillend zijn. Echter, omdat niemand de aanwezigheid van de twee syn- en anti-conformeren in oplossing bij kamertemperatuur heeft kunnen detecteren, is conformationele isomerisatie van carboxygroepen en de mogelijke consequenties daarvan nooit overwogen.

In hoofdstuk 4 laten we voor de eerste keer zien dat de conformationele isomerisatie van de carboxygroep ook bestaat in oplossingen van mierenzuur bij kamertemperatuur. We demonstreren dat syn- en anti-conformeren aanwezig zijn in apolaire (acetonitril) en polaire (zwaar water en dimethylsulfoxide) oplossingen en dat de anti-conformeer significant aanwezig is (25%).

In hoofdstuk 5 tonen we aan dat conformationele isomerisatie van carboxygroepen ook aanwezig is in grotere moleculen, zoals in peptiden. Door het bestuderen van N-acetylaspartaam zuur in polaire oplossingen vinden we dat de anti-conformeer weer in aanzienlijke mate aanwezig is (25%). Dit wijst erop dat de overige moleculaire structuur van de peptide maar een kleine invloed heeft op de conformationele isomerisatie. Daarnaast voeren

we moleculaire dynamicasimulaties uit om de hydratatie van deze twee conformeren te onderzoeken. We observeren dat de anti-conformeer sterker met water interacteert dan de syn-conformeer. Beide onderzoeksresultaten, de computationele en de experimentele, wijzen erop dat de anti-conformeer inderdaad zuurder is (lagere pKa) dan de syn-conformeer.

In hoofdstuk 6 onderzoeken we de vorming van een intra-moleculaire waterstofbrug tussen de amide- en anti-COOH-groep in N-acetylproline. We lossen N-acetylproline op in een apolair oplosmiddel, zoals acetonitril, om de hydrofobe micro-omgeving van de binnenkant van een polypeptideketen na te bootsen. In zulke condities vormt de anti-conformeer een sterke intra-moleculaire waterstofbrug met de nabijgelegen amide-carbonylgroep. De vorming van deze binding stabiliseert de anti-structuur krachtig, wat leidt tot een veel hogere aanwezigheid van de anti-conformeer (65%) ten opzichte van de syn-conformeer (35%). In polaire oplosmiddelen, waar we de vorming van intra-moleculaire waterstofbruggen niet zien, neemt de populatie van de anti-conformeer weer drastisch af tot 25%.

ONDERZOEK NAAR DE MOLECULAIRE STRUCTUUR VAN HYALURONAN BIJ NEUTRALE PH Hyaluronan is een natuurlijk veel voorkomende polysacharide en bijzonder belangrijk in het menselijk lichaam waar het een belangrijke rol speelt in veel biologische processen. Hyaluronan heeft een simpele structuur die voornamelijk is onderzocht in waterige oplossingen met behulp van computationele moleculaire dynamische simulaties. De repeterende eenheid is opgebouwd uit N-acetylglucosamine en glucuronzuur, welke respectievelijk een amide- en een carboxygroep bevat. De formatie van deze binding is voor een groot deel verantwoordelijk voor de tamelijk hoge ketenstijfheid van hyaluronan.

In hoofdstuk 7 onderzoeken we de vorming van intra-moleculaire waterstofbruggen tussen amide- en carboxygroepen, waarvan eerder is voorgesteld dat ze de helixstructuur van hyaluronan stabiliseren. In onze studie zien we dat minder dan 10% van de functionele groepen interacteren. De carboxygroep vormt een intra-moleculaire waterstofbrug, waar het waterstofatoom van de waterstofbrugdonerende N-H-groep dicht tegen de lijn is geposition-

eerd die de twee zuurstofatomen van de carboxylaat-aniongroep verbindt. We zien ook dat het voorkomen van de waterstofbindende amide en het carboxylaat niet sterk wordt beïnvloed door een toenemende temperatuur en pH, factoren die bekendstaan om het verlagen van de ketenstijfheid. Deze bevindingen suggereren dat de waterstofbruggen tussen de amide- en de carboxylaatgroepen waarschijnlijk niet significant bijdragen aan het verstijven van de hyaluronanketens.

DIVALENT ION CONDENSATIEMECHANISME IN HYALURONAN. Divalente kationen hebben een cruciale biologische rol door het beïnvloeden van de structurele eigenschappen van polyelektrolyten. Ionen kunnen zich inderdaad losjes binden aan geladen groepen langs de polymeerketen, wat leidt tot lokale buiging en op die manier dus de flexibiliteit van de keten verhoogt. Zo'n verhoogde flexibiliteit (of verminderde stijfheid) heeft een grote impact op de biologische functies die worden vervuld door de polyelektrolyten. Alhoewel het mechanisme van de ionencondensatie bekend is, zijn de interacties en de geometrie van het gevormde complex tussen de geladen groepen en het divalente ion op moleculair niveau nog erg onduidelijk.

In hoofdstuk 8 onderzoeken we het ionencondensatiemechanisme van een divalent kation (calcium) met hyaluronan. Door het combineren van experimenten en moleculaire simulaties zien we dat calcium kationen zich selectief plaatsen op de ketens van hyaluronan, door hun ruimtelijke en ladinggebonden vereisten. Dit koppelt de carboxylaat- en amidegroepen op de aangrenzende sachariden. Opmerkelijk is dat de hoeveelheid kationgebonden amide verzadigd bij een lage calciumconcentratie ($\sim$100 mM), tot een maximum fractie van 10%. Deze verzadiging suggereert dat de vorming van dit complex de vorming van extra complexen bij nabije bindingsplaatsen verhindert. Desondanks heeft de vorming van slechts een aantal van deze complexen al een grote invloed op de intra-moleculaire waterstofbruggen die de ketens verstijven. Door het uitvoeren van moleculaire dynamicasimulaties vinden we dat de calciumcondensatie de intra-moleculaire waterstofbruggen drastisch verzwakt. Door middel van atoomkrachtmicroscopie meten we dat dit een lokale buiging veroorzaakt die leidt tot een tweevoudige vermindering van

de ketenstijfheid, wat zelfs al gebeurt wanneer slechts een paar procent van de functionele groepen van de keten zich heeft gebonden aan calcium.

EEN MOLECULAIR BEELD VAN DE MACROSCOPISCHE EIGENSCHAPPEN VAN HYALURONAN HYDROGELS. Naast de enorme bio-relevantie van hyaluronan heeft dit polymeer intrigerende materiaaleigenschappen. In het bijzonder de mechanische eigenschappen van een hyaluronanoplossing die kan worden 'getuned' door externe stimuli zoals de pH. Door het verlagen van de pH van een neutrale waarde tot 2.5 ondergaat een hyaluronanoplossing een vloeistof-tot-gel-transitie. Dit verhoogt de elasticiteit dramatisch. Opmerkelijk is dat het verder verlagen van de pH de elastische staat onderdrukt en er weer een vloeibare oplossing wordt verkregen. Zo'n dramatische respons van hyaluronan op externe stimuli is een interessante onderzoekscasus om de interactie tussen een cel en een extracellulaire matrix te begrijpen en nieuwe hydrogels met regelbare mechanische eigenschappen te ontwerpen.

In hoofdstuk 9 bestuderen we moleculaire interacties die leiden tot de vloeistof-tot-gel-transitie in hyaluronanoplossingen bij pH=2.5. We zien dat bij deze pH de elektrostatische repulsieve krachten tussen de negatief geladen carboxygroep zijn verminderd. Ketens verbinden zich lateraal door de formatie van inter-moleculaire verbindingen of stickers. Zulke verbindingen ontstaan doordat er zich inter-moleculaire waterstofbruggen vormen tussen de amide- en de geprotoneerde carboxygroepen, COOH, en ook tussen de amide- en de gedeprotoneerde carboxygroepen, COO-. We berekenen dat van de carboxygroepen 10-20% actief zulke inter-moleculaire waterstofbruggen vormt. Wanneer de pH verder wordt verlaagd, en dus bij een verminderde hoeveelheid van COO-, worden minder sterke verbindingen gevormd en wordt het waterstofbrugnetwerk dramatisch verzwakt, wat leidt tot een gel-tot-vloeistof-transitie. De visco-elastische eigenschappen van de elastische staat van hyaluronan, en van hydrogels van responsieve biopolymeren in het algemeen, hangen af van de interactie-eigenschappen tussen de polymeren, zoals hun dichtheid en lifetime.

In hoofdstuk 10 bestuderen we het effect van temperatuur op de molec-

ulaire interacties die leiden tot de vorming van een waterstofbrugnetwerk. We zien dat de fractie carbonylgroepen, welke inter-moleculaire waterstofbruggen vormen en dus associatieve connecties, niet worden beïnvloed door temperatuursveranderingen. Echter, we constateren dat de temperatuurafhankelijke reactie van de visco-elastische eigenschappen drastisch veranderen wanneer de temperatuur wordt verhoogd, leidend tot snellere stress-relaxatie. Aan de hand van de geobserveerde temperatuurafhankelijkheid bepalen we de flow activatie-energie, welke $\sim$50 kBT is. Deze waarde is 5-15 keer groter dan de activatie-energie van het breken van een enkele waterstofbrug, wat een indicatie is dat de ketens diffunderen. Om het netwerk dus te laten vloeien moeten meerdere waterstofbruggen tegelijkertijd worden gebroken. We concluderen dat een verhoging in temperatuur de dynamica van het polymeernetwerk versnelt, zonder significant de structuur aan te passen.

HET VASTSTELLEN VAN DE SECUNDAIRE STRUCTUUR VAN EEN ANTIVRIES-GLYCOL-EIWIT. Antivries-glycol-eiwitten (AFGP) zijn unieke eiwitten die in staat zijn de groei van ijs in veel organismes te verhinderen. Het ijsverhinderingsmechanisme is grondig bestudeerd vanwege de mogelijke biomedische en voedselgerelateerde toepassingen. Ondanks de vele studies is een reeks van centrale vragen nog steeds onbeantwoord: wat is de structuur van AFGP? Verandert het eiwit van structuur bij het verlagen van de temperatuur naar de werkingstemperatuur van het eiwit? Is een specifieke structuur essentieel voor de groei van ijsverhinderende eigenschappen van AFGP?

In hoofdstuk 11 bestuderen we de moleculaire structuur van AFGP met hulp van 2DIR-spectroscopie. Door het exploiteren van de vibrationele koppeling tussen de amide I- en de amide II-vibraties zijn we in staat om de frequenties van de amide I-modi van het eiwit op te lossen. Dankzij eerdere literatuur zijn we in staat de verschillende vibratiefrequenties toe te wijzen aan specifieke secundaire structuren. We zien dat antivries-glycol-eiwitten een hoge ongeordende en flexibele structuur hebben. Bij kamertemperatuur nemen de antivrieseiwitten PPII, alfa-helical, random coil (willekeurige spoel) en verlengde structuren aan. Bij het verlagen van de temperatuur naar het

vriespunt van water wordt de PPII-inhoud significant hoger, wat ten koste gaat van de verlengde structuur. Zoals aangegeven is in eerdere literatuur is een grotere aanwezigheid van PPII-structuur essentieel voor het scheiden van de hydrofobe en hydrofiele delen van de eiwitten en daarmee dus het afzonderen van de actieve bindingsplekken voor ijskristallen in wording. Desondanks zien we dat bij de introductie van chemische modificaties, die de antivriesactiviteit verlagen, de PPII-structuur significant is verminderd. Interessant is dat de toevoeging van antivries-activiteitverminderaars of antivries-activiteitvermeerderaars de secundaire structuur niet beïnvloedt, wat erop wijst dat die een ander werkingsmechanisme hebben.

Deze dissertatie verstrekt informatie over de flexibele structuur van moleculen van verschillende groottes en complexiteiten, reikend van carboxygroepen in simpele zuren tot lange polymeren. Dankzij een gecombineerde multitechniek aanpak, waarbij tweedimensionale infrarood-spectroscopie een centrale rol speelde, waren we in staat om de conformationele veranderingen in carbonzuren, in hyaluronan polymeren en in antivries-eiwitten (AVGE), die de moleculaire interacties loskoppelen, te observeren. Met als gevolg stabilisatie of destabilisatie van de moleculaire structuur. In het geval van -COOH-groepen lieten we zien dat twee verschillende geometrieën mogelijk zijn dankzij de stabiliserende interacties met de omringende watermoleculen. In het geval van de antivries-eiwitten en hyaluronan hydrogel, bestudeerden we de moleculaire structuur in een waterige oplossing. Dit stelde ons in staat om de macroscopische eigenschappen en de biologische functionaliteiten te linken aan de specifieke structurele inhoud. De verkregen gedetailleerde moleculaire beelden van antivries-eiwitten en hyaluronan zouden toekomstige toepassingen kunnen krijgen op wetenschappelijk en technisch gebied. Het begrijpen van de structuur van AVGE is cruciaal voor de synthese van artificiële antivries-eiwitten, die gebruikt kunnen worden om organen voor transplantaties te bewaren. Het op maat maken van de moleculaire interacties die leiden tot veranderingen in de macroscopische eigenschappen van hyaluronan is fundamenteel om de dynamische wederkerigheid te begrijpen tussen cellen en extracellulaire matrix en om hydrogels te ontwikkelen met

afstembare mechanische eigenschappen voor op maat gemaakte biomedische applicaties zoals de aflevering van medicijnen. Alle hier gepresenteerde studies zorgen, zoals het altijd is en zoals het altijd zou moeten zijn, voor nieuwe wetenschappelijke vragen. Voornamelijk, de ontdekking van conformationele isomerisatie van -COOH-groepen van mierenzuur of peptiden opgelost in waterige oplossingen bij kamertemperatuur stelt onze fundamentele kennis van zelfs kleine moleculaire systemen ter discussie. Wat is het biochemische gevolg van de aanwezigheid van syn- of anti-conformeren? Dat is een kwestie waar we ons niet op konden richten en waarvan we hopen dat toekomstige studies in staat zullen zijn om ze te onderzoeken.

Publications

Publications covered by this thesis

1. G.Giubertoni, O.O.Sofronov, H.J.Bakker *Observation of Distinct Carboxylic Acid Conformers in Aqueous Solution*, Journal of Physical Chemistry Letters, 2019

2. O.O.Sofronov, G.Giubertoni,A. Pérez de Alba Ortíz, B. Ensing, H.J.Bakker *Peptide side-COOH groups have two distinct conformations under biorelevant conditions*, Journal of Physical Chemistry Letters, 2020

3. G.Giubertoni, O.O.Sofronov, H.J.Bakker *The effect of inter-molecular and intra-molecular interactions on the stability of syn and anti -COOH conformers*, Communications Chemistry, 2020

4. G.Giubertoni, G.H.Koenderink,H.J.Bakker, *Direct Observation of Intrachain Hydrogen Bonds in Aqueous Hyaluronan*, Journal of Physical Chemistry A, 2019

5. G.Giubertoni, A. Pérez de Alba Ortíz, F.Bano, D.Green,P. DeAngelis, G.H.Koenderink, R.Richter, B.Ensing, and H.J.Bakker, *Strong reduction of the chain rigidity of hyaluronan by selective binding of Ca^{2+} ions*, in preparation

6. G.Giubertoni, F. Burla, C. Martinez-Torres, B. Dutta, G. Pletikapic, E. Pelan,Y.L.A.Rezus, G.H.Koenderink,H.J.Bakker, *Molecular Origin of the Elastic State of Aqueous Hyaluronic Acid*, Journal of Physical Chemistry B, 2019

7. G.Giubertoni, F.Burla, H.J.Bakker, G.H.Koenderink, *Connecting the stimuli-responsive rheology of biopolymer hydrogels to the underlying hydrogen-bonding interactions*, submitted

8. G.Giubertoni, K. Meister, A.L.DeVries, H.J.Bakker *Determination of the Solution Structure of Antifreeze Glycoproteins Using Two-Dimensional Infrared Spectroscopy*, Journal of Physical Chemistry Letters, 2019

9. Y.Sun,G.Giubertoni, H.J.Bakker, J.Liu,M.Wagner, A.DeVries,K.Meister *Structural Basis of Antifreeze Glycoprotein Function*, submitted

Other publications from the author

1. C.Moll,G.Giubertoni,J.Versluis,G.H.Koenderink, H. J. Bakker *The molecular structure of hyaluronan hydrogels at the interface*, in preparation

2. E.P.Van Dam,G.Giubertoni, F,Burla,G.H.Koenderink, H.J.Bakker *Hyaluronan biopolymers release water upon pH-induced gelation*,Physical Chemistry Chemical Physics, 2020

3. N. P Gallop, O. Selig, G.Giubertoni, H. J. Bakker, Y. L.A. Rezus, J. M. Frost, T. L.C Jansen, R. Lovrincic, A. A. Bakulin *Rotational Cation Dynamics in Metal Halide Perovskites: Effect on Phonons and Material Properties*, Journal of Physical Chemistry Letters 2018

4. Hongbo Yuan, Jialiang Xu, Eliane P Van Dam, Giulia Giubertoni, Yves LA Rezus, Roel Hammink, Huib J Bakker, Yong Zhan, Alan E Rowan, Chengfen Xing, Paul HJ Kouwer *Strategies to increase the thermal stability of truly biomimetic hydrogels: combining hydrophobicity and directed hydrogen bonding*, Macromolecules 2017

5. Paola Fermo, M Andreoli, Letizia Bonizzoni, Marzia Fantauzzi, Giulia Giubertoni, Nicola Ludwig, Antonella Rossi, *Characterisation of Roman and Byzantine glasses from the surroundings of Thugga (Tunisia): Raw materials and colours*, Microchemical Journal 2016

Acknowledgments

Hey You!
Thanks to read (or partially read) all this work. Since you arrived (or you just jumped, here) I would like to tell you who got me here.

Like every good story, mine got a bit twisted. Thanks, Yves, my first supervisor, to get me the opportunity to start a Ph.D. and to come back to AMOLF. I am sorry you left before to see what we could do together. I am, however, happy to know that you found your place and your happiness. As a second supervisor, thank you Huib for replacing Yves as my group leader. We did not choose each other, and it has not been an easy road. Nevertheless, I have really appreciated your effort and patience to bring me to the end. You taught me important values such as endurance, creativity, responsibility, and strategy. Thanks, Huib for everything. In all these four years, I had the unique experience to have kind of a secret supervisor, Gijsje. Thanks for all the scientific support, but especially to guide me through complicated moments. Besides your incredible scientific knowledge and curiosity, you have a great humanity that makes you an extraordinary person to work with and for.

> *I know who I am. And after all these years, there's a victory in that.*
>
> True Detective

As every good story worthy of a TV series, I have had the unique opportunity to spend time at work with wonderful, interesting, and enthusiastic people. Thanks to Hinco for solving any problem that came around, and thanks to Jan for saving my PhD life multiple times. Thanks Teresa for all your patience, and your smiles that are highly contagious. And thank you to adopt me in all the times I was waiting or stalking Huib. Thanks to Ale2, for your calmness, your support in all the period of writing this thesis, and

for your help. Bossy, oh Bossy. Four years together went quite quickly by. Dropping by your office to talk and to say hi was one of the reasons that I was happy to come to work. I wish you a lot of success in the future. Robi, Roberto: you brought fun, happiness in the group. Sharing with you all the troubles and all the tears in the last six months together was like breathing underwater. It was highly important to have you, your empathy and humanity close to me. Thanks for that. Lovely O.O.Sofronov, we have been quite a couple you and I. I want to thank you to jump with me on new projects, for the long discussions, for never giving up when everything sucked, for helping me in the lab and in the understanding the dark side of Chemistry. You have been my colleague, my supervisor, my friend, my student all at once. I really do hope that you get to go on in Science and that once I will visit your lab where you will study -syn/anti in biorelevant conditions and in biorelevant samples.Thanks also to the other old, new, present group members: Konrad, Johannes, Andrea, Harmen, Aditi, Balazs, and Rahul. A big thanks also to Bip, with who I went through the supervisor transition. Thanks for all our fights, for our beers, for all the time in the lab, for all the things you taught me. I hope you are happy back in India, and I hope to see you soon, to see how you are doing.

> *You can trust us to stick to you, through thick and thin – to the bitter end. And you can trust us to keep any secret of yours – closer than you keep it yourself. But you cannot trust us to let you face trouble alone, and go off without a word. We are your friends, Frodo.*
>
> Lord of the Rings, J.J.Tolkien

As every good story worthy of *Lord of the Rings*, I have and I have had my Sams. Fe, with you I can fight, laugh, gossip (exchange information), and complain at the same moment. I have the feeling we got stuck with each other long time ago, while we were hiking through Italy. Life is sometimes like that last piece of path to Radicofani: hard, rainy, and tiring, but with you, on my side, it is always easier, funnier, and somehow the destination becomes closer than I thought. And like then, also now, I know, you know

that we have each other backs. No matter what happens on the road, no matter how the sky is, sunny or cloudy, no matter how heavy is the back-bag, no matter if we take for a while different directions, no matter who else we meet during our walk, I got you and you got me. To the next adventures together, Burla. Alessandro Antoncecchi. I still remembered the day I met you 5 years ago, planning with Nicola the trip back to Italy. You have been and are to me kind of a brother, always tripping, laughing, supporting and talking together. Thanks Alejandro for everything. I love you and I swear that I do love you also your hair style. Federico Fanalista, Fava. You and I met years ago, in the weirdest way possible leading to one of the strongest friendships I endure. Thanks for all the time we spent and will spend together, also when you are lost in your world without listening to me :) Paul, every time I see you, it feels like the time does not pass. Thanks for all the chats, thanks for all the aperitivo, thanks for all the laughs. I am so looking forward to have you here back. Nico, it looks yesterday that we were living together, partying as crazy. I do miss you a lot, but not the amount of alcohol we consumed. Thanks for all the grappa together, thanks for being there during my ups and downs, thanks for the patience during my working outburst at home, thanks for being my family, my brother, my home, and for all the smiles, laughs, love we shared and like yesterday we share. Moritzino, Moritzino. Four years we spent to talk to each other from one side to the other of the office. With you there, coming to the office it was like coming home. You were one of my biggest supporter, when at work everything was going down. Thanks for that, for all the time together, for calming me down many times and for the infinite amount of chats and laughs we shared. Caro, first at all, as office neighbor thanks for all the salty sticks and the candies you have provided me during the way. Thanks for the help that you gave me and you give in every situation, for always taking good care of me, and talking to me some sense (wondering if it has worked sometimes). I wish you the best Caro, you deserve it so much. Oleg.Thank you for your continuous support. Thank you for the patience you had while teaching me and for your friendship, which has inspired me many times during this Ph.D. For you, a simple "thank you", though I know

that "thank you" is not nearly enough. Giogio. Giorgio, what would have been a PhD without you? You coming in the office to say hi, to check that I was having breaks, to observe if I was ok, to share your and my frustration. You have been like a good, tasty Spritz after a long day of work. Probably, we imagine differently: you drinking a Spritz in front of a beach, and I in front of a mountain. But this is also what is amazing of you and me, and of our beautiful country.

Contandoli uno a uno non son certo parecchi,
Son come i denti in bocca a certi vecchi,
Ma proprio perché pochi son buoni fino in fondo
E sempre pronti a masticare il mondo

Counting them one by one,
They are like teeth in the mouth of some old people,
But because they are few they are good through and through,
And always ready to chew the world

Gli amici, Francesco Guccini

As a good story worthy of a beautiful, melodic Italian song, during these years I had (and I have) the opportunity to enjoy amazing and wonderful friendship with beautiful people. Marco, thanks for the food we cooked together, for the long chat during the various conferences, for your good mood at every party, for your support during complicated moments. I am looking forward to come to visit you and Ele in Sweden! Vale, oh , Vale. Thanks for everything, for the word "rosicare", for the aperitivo and for the support. And always remember my friend, I have your back! Other Italian friends have been part of this PhD experience: Vane and Lorenzo. Vane, thanks for the chats, for the shared cigarettes when the alcohol was a bit too much. Thanks for your chill, calm and fun mood! Lore, I remember when we met the first time, when we got drunk together at the windmill, when we founded the Sunday lunch club. You and I have recreated our Italian and family traditions together. Thanks Lore for this, and for the other thousands of moments together! Laura, my german friend. What

would have been 4 years without your german hugs? Thanks for sharing with us your life, and your stories. Thanks for all our trips, all our dinner, all the Spritz together. I am so looking forward for the next ones! Douwe, I have known you since a long time, but it seems that time has not passed. Thanks for all the chats, and the advices you gave/give me, and thanks for your contagious calmness. Love you, my blondie dutchie. Flo, really, your support, your honesty, your directness: thank you for that! Thanks for taking care of me and for pushing me to stand up for myself. Thanks for all the chats, the life and love stories shared in front of a Chardonnay. Annemarie, my lovely Dutchie, we met really even before the beginning of this PhD. We met at the beginning of the master thesis, and since then we have walked our way on parallel paths, meeting sometimes when the walk got a bit harder that we expected, swallowing our sorrows in Nachos and beers. I like to think that this will endure, and that together with Flo we will keep resting together when Life will get hard or simply when we will need a good glass of Char...Sauvignon! Niels, oh Niels. Thanks for all the chats, the walks, the help in the lab. My PhD life would have been completely different without your support. Thanks for that, my friend. To the next beer together!

Marloes! My PhD daughter, thanks for your support, for the nice, long chats together where we share ideas, values, and life story. Silviaaaaaa, silvietta, silvia mia. Dio mio, quanto ho riso con te solo le mura dell'ufficio 2.14 lo sanno! Thanks Silvia for all your good mood and the enourmous amount of smiles that you brought in the office. Facing the last year with a fresh you was beautiful! Gianluca, despite Covid-2 divided us before time, I truly enjoyed that working month together, and, as it was promised, thanks for the help to find a title! Parisa, lovely lost and found friend, thanks for the all our chats, and for the next chats we will have! Thanks also to Jenny (< 3), and Agustin to drop by sometimes in the office to talk and sustain me during the thesis writing. Thanks also to Cri, Andrea, Kevin, Mario, Olga, Ciocia Agata for all the beautiful dinner, picnic, barbecue, and brunches we had together. I will keep these memories close to me for a very long time, and I hope to create many more new with you! Lukas, thanks for the

food and all the nice chats together! Alberto, we met through our Latin mafia and we, let me say it, did an amazing work together! Thanks for the nice time, the patience that you showed me while explaining the dark side of computational chemistry and for all the beers! Wam, Tara, and Almer, dank jullie wel voor de tijd samen, voor alle dinertjes en aperitivo, voor al het lachen en voor alle Spritz. Thea, iedere keer als ik naar werk ga of weer thuiskom ben ik gelijk in een goed humeur als je achter het raam staat te zwaaien. Dank je wel om geduldig naar mijn Nederlands te luisteren en voor de gezellige tijd samen!

Yvonne en Jeroen, ik wil jullie bedanken. Jullie hebben mij geaccepteerd als een dochter, misschien omdat ik van prosecco houd? Grapje! Dank jullie wel voor iedere keer dat jullie mij hebben ondersteund, voor al het lachen, en voor alle tijd samen. Ik kijk ernaar uit om dit feestje, en meer feestjes, samen met jullie te vieren! Julia en Natasja ook voor jullie: heel erg bedankt voor alle sushi samen en voor de ondersteuning!

La vera amicizia non é essere inseparabili. É essere separate senza che nulla cambi.

True friendship isn't about being inseparable. It's being separated and nothing changes.

Frozen, Elsa and Anna

Come ogni storia degna di un cartone della Walt Disney (Frozen Cami?), grazie alle mie amichette di una vita, Senza di voi non ce l'avrei mai fatta, sarei stata un albero che il primo forte vento avrebbe spazzato via. Grazie a Dede e Juls per essere sempre pronte per l'aperitivo a due ore dall'atteraggio. Juls e Cami per ricordarmi che la vita e i problemi si affrontano assieme, e che alla fine va davvero tutto bene. Fino a che abbiamo il nostro gin-tonic e siamo assieme, va tutto bene. Leti per prenderti sempre cura di me, come se 10,20,30 anni non siano mai passati. Fra, grazie per farmi respirare con le tue risate, e le nostre passeggiate. Vitto, grazie per rendere divertente ogni momento difficile, soprattutto ora, nel mezzo della quarantena. Fio, il tuo ritorno nel continente é stato uno dei momenti piú felici della mia vita. Dede, ancora te, grazie. Grazie per tutto. Per le serate di Natale a

bere assieme, per il tuo compleanno a bere tisane e a guardare "Malattie Imbarazzanti". Grazie per tutto amiche mie. Ve voio un bene folle.

Un grazie anche a Michi, Anna di Pila and Annuccia. Grazie per condividere con me ad ogni giro un aperitivo e le vostre storie. E a Michi un grazie speciale per tutti i Damiano dalla Nilde!

> *Ogni volta che ti sentirai smarrita, confusa, pensa agli alberi, ricordati del loro modo di crescere. Ricordati che un albero con molta chioma e poche radici viene sradicato al primo colpo di vento, mentre in un albero con molte radici e poca chioma la linfa scorre a stento. Radici e chioma devono crescere in uguale misura, devi stare nelle cose e starci sopra, solo così potrai offrire ombra e riparo, solo così alla stagione giusta potrai coprirti di fiori e frutti.*

> *Every time that you will feel lost, confused, think about the trees, remember of how they grow up. Remember that a tree with a large foliage and few roots is easily uprooted at the first wind, while in a tree with a lot of roots and small foliage the lymph slowly flows. Roots and foliage must grow in equal measure, you must stay in the things and above them, just in this way you will offer shadow and shelter, just in this way you will be able in the right season to cover yourselves of flowers and fruits.*

Susanna Tamaro

Come ogni storia degna della nostra famiglia, grazie a voi, Cugi. Non siete classificati come solo amici, ma con voi condivido del DNA. Con voi al mio fianco sono sempre riuscita ad andare avanti senza paura, e senza nessun timore perché sapevo dove tornare. Martiiiii, grazie. Grazie per le vacanze assieme durante questi 4 anni, per ogni singola battuta, per ogni singolo aperitivo mentre aspettavamo le nostre Vecchie in una piazza in Portogallo o in una piazza in Grecia. Grazie per i dolci, kind of, rimproveri, e

il forte supporto in ogni mia scelta. E soprattutto, grazie per farmi finire il tuo bicchiere di vino o il tuo shot. Grazie Gio per ogni singola birretta, per ogni singola chiaccherata mentre la luna affiorava o il sole tramontava. Grazie a te e a Pippo per il gentile push, e per ripertermi sempre che non c'é nessun problema. Veronica! O cugi mia, ti ho seguito su ogni divano in ogni tua casa. Il tempo continua a passare ma non passa mai fra me e te: quelle lunghe chiaccherate, quelle bottiglie di vino che si svuotavano prima del dovuto, quei sorrisi sono come ieri ancora oggi. Grazie Franci, per quelle lunghe chiaccherate al telefono o a casa, quei momenti dove ci siamo raccontati le nostre paure, i nostri futuri. Condividerle con te ha sempre reso il tutto piú leggero. Mara e Andre. Ogni volta che vi vedo, che con voi parlo, so che sono a casa, no matter what. Grazie di cuore per tutto! Un grande grazie ai miei zii, e specialmente a Zia Iaia, Zio Robi, Zia Franca, Zio Gio,e Zia Anna. Grazie per aspettarmi felici e felici salutarmi ad ogni giro.

Mamma Ebe e Papá Silvio. Per voi, la parola *grazie* non é abbastanza. Non c'é parola che possa esprimere l'amore e la gratitutide che provo per voi. Efrem e Miriam, padre e madre di secondo livello. Ma cosa farei senza di voi? Voi siete il mio supporto in qualunque situazione, di felicitá o di tristezza completa. Non potrei mai immaginare una vita senza di voi. Grazie rompini per esserci, per non andare mai via e per affrontare questa vita assieme.

As every good story worth of a Life, you need a person with who to share and live it, and that's you, Jud, Juditta,Giuditti, Giuditta, Judith. Thanks for the support during these four years, that you have filled in a way that I would have never expected. I always thought I would have been an errant soul, but instead I found you, or you found me. I don't know if it was coincidence, destiny or fate, I just know that I love you immensely.

Everytime I leave my beloved home, my mountains, my friends and my family, I just simply say "See you tomorrow", as no days will pass in between our next encounter. So, to you my friends from different cities, countries

and continents:

A DOMANI, Tot morgen, See you tomorrow Beauties!

Giulia Giubertoni
Amsterdam

About the author

Giulia Giubertoni was born in Borgosesia (Italy) in 1990 and lived in Varallo Sesia, a small village under the shadows of the Monte Rosa, until 2009. She grew up spending her time hiking and pretending to be a shepherd. After losing three goats and leading one calf to a cliff at the age of 12, she understood that such a life was not for her. In 2009, she obtained her high school diploma at *Liceo Classico D'Adda*, where she mainly studied Latin, Greek, and Philosophy. In the same year, she enrolled in Physics at the *Universitá degli Studi* of Milan. In 2014, she moved to Amsterdam to work on her master thesis in AMOLF under the supervision of Dr.Y.L.Rezus. She graduated cum laude in 2015 at the *Universitá degli Studi* of Milan. In 2016, she started her Ph.D. under the supervision of Dr. Y.L. Rezus, and further under the supervision of Prof. Dr. H.J. Bakker and Prof. Dr. G.H. Koenderink. In her free time, she loves to cook, drink with friends and hike in the beautiful, eternal mountains of Valsesia.